

University of Southampton

Faculty of Engineering and the Environment

Energy and Climate Change Division

Microclimate adapted localised weather data generation:
Implications for urban modelling and energy consumption
of buildings.

by

Leonidas Bourikas

Thesis for the degree of Doctor of Philosophy

September 2016

Abstract

Urban and building energy simulation models are usually driven by typical meteorological year (TMY) weather data often in a TMY2 or EnergyPlus Weather data file (EPW) format. In addition, currently, in many countries, weather data files with a TMY format are used for building regulation compliance calculations. However, the locations where these historical datasets were collected (usually airports) generally do not represent the local, site specific micro-climates that cities develop. In this thesis, a humid sub-tropical climate context has been considered. An idealised “urban unit model” of 250m radius is presented as a method of adapting commonly available weather data files to the local micro-climate. This idealised “urban unit model” is based on the main thermal and morphological characteristics of nine sites with residential / institutional (university) use in Hangzhou, China. The area of the urban unit was determined by the region of influence on the air temperature signal at the centre of the unit. Air temperature and relative humidity were monitored and the characteristics of the surroundings assessed (e.g. green-space, blue-space, built form). The “urban unit model” was then implemented into micro-climatic simulations using a Computational Fluid Dynamics – Surface Energy Balance analysis tool (ENVI-met, Version 4). The “urban unit model” approach used here delivered results with performance evaluation indices comparable to previously published work (for air temperature; RMSE <1, index of agreement $d > 0.9$). The micro-climatic simulation results were then used to adapt the air temperature of the TMY file for Hangzhou to represent the local, site specific morphology under three different weather forcing cases, (i.e. cloudy/rainy weather (Group 1), clear sky, average weather conditions (Group 2) and clear sky, hot weather (Group 3)). Following model validation, two scenarios (domestic and non-domestic building use) were developed to assess building heating and cooling loads against the business as usual case of using typical meteorological year data files. A dynamic thermal simulation tool (TRNSYS) was used to calculate the heating and cooling load demand change in a domestic and a non-domestic building scenario. The heating and cooling loads calculated with the adapted TMY-UWP file show that in both scenarios there is an increase by approximately 20%

of the cooling load and a 20% decrease of the heating load. If typical coefficient of performance (COP) values for a reversible air-conditioning system are 2.0 for heating and 3.5 for cooling then the total electricity consumption estimated with the use of the “urbanised” TMY-UWP file will be decreased by 11% in comparison with the “business as usual” (i.e. reference TMY) case. However, this assumes a cooling set-point of 26°C. If a lower set-point is used the predicted energy savings will be lost. Overall, it was found that the proposed method is appropriate for urban and building energy performance simulations in humid sub-tropical climate cities such as Hangzhou, addressing some of the shortfalls (i.e. the representation of the urban micro-climate) of current simulation weather data sets such as the TMY.

Table of contents

Abstract	iii
Table of contents	v
List of figures	ix
List of tables	xvii
Author's declaration	xix
Acknowledgements.....	xxi
Abbreviations	xxiii
Chapter 1 Introduction.....	1
1. Research Overview	1
2. Aims and Objectives	9
3. Research Methodology.....	9
Chapter 2 Scale and the Boundary Layer of cities	13
1. Scales of urban climatology	13
2. Urban boundary layer	15
2.1 Mixed layer	16
2.2 Inertial (surface) sub-layer.....	17
2.3 Roughness sub-layer and the urban canopy layer	19
3. Urban energy balance.....	21
3.1 Role of the energy balance in diurnal building energy consumption.....	22
4. Micro-climate in the urban unit context	25
Chapter 3 Micro-climate modelling	31
1. Micro-scale weather models	31
1.1 Numerical weather prediction models.....	31
1.2 Analytical urban canopy models.....	34
1.3 Empirical urban canopy models.....	38

Table of contents

Chapter 4 Validation dataset	41
1. Local Climate.....	41
2. Urban Context.....	45
3. Measurement equipment and set-up specifications	47
4. Statistical data analysis and data cleaning	53
4.1 Replacement of missing/false values	55
4.2 Statistical forecast modelling	57
5. Results from the value replacement case study	59
6. Conclusions on data cleaning procedure	61
7. Selection of a generic urban unit.....	63
Chapter 5 A simplified model for urban micro-climatic simulations.....	69
1. Introduction	69
2. Land Cover analysis (Step 1)	71
2.1 Datasets	71
2.2. Assessment of the land surface cover	73
2.3 Urban morphological parameters	77
3. Urban classification (Step 2)	87
3.1 Local Climate Zones – urban classification scheme.....	88
3.2 Urban classification results.....	91
4. The idealised “urban unit” model (Step 3)	99
4.1 Morphological characteristics	102
4.2 Construction of the “urban unit” model	105
Chapter 6 Urban weather projections	109
1. Correction of the reference weather data to include the local UHI patterns (local scale) (Part 1).....	109
2. Adaptation of the “localised” TMY data to include the effects of the site specific morphology (local scale + morphology = micro scale) (Part 2)	113

Table of contents	
2.1 ENVI-met set up and configuration	113
2.2 Anthropogenic heat emissions	132
2.3 Solar radiation.....	136
2.4 Meteorological data for the simulations	140
3. Validation of the simulations with the “urban unit model”	143
Chapter 7 Case studies of building energy performance in Hangzhou, China	155
1. Urban weather adapted TMY file	155
2. Case study of a domestic building in Hangzhou, China	157
3. Case study of a non-domestic building in Hangzhou, China	159
4. Results from the case studies	161
Chapter 8 Conclusions.....	165
1. Contribution to knowledge.....	167
2. Further work	169
Appendices.....	I
Appendix A	III
Performance indices for the assessment of the models examined for the replacement of missing air temperature values in weather data files.....	III
Appendix B	V
Sky View factor calculations	V
Appendix C	IX
Local Climate Zones urban classification scheme.....	IX
Appendix D	XXI
Morphology characteristics of the annuli areas in the idealised “urban unit” model.	XXI
Appendix E	XXV
Development of a ANN for the prediction of hourly solar radiation values from typical meteorological parameters	XXV

Table of contents	
E.1 Artificial Neural Network model development	XXVIII
E.2 Data structure and results	XXXI
E.3 Validation of the ANN model and conclusions on its use.....	XXXVI
Appendix F.....	XLV
Main input parameters for the “urban unit model” validation and the simulation of the “urban weather projections”	XLV
Appendix G.....	XLIX
Publication list	XLIX
References.....	LI

List of figures

Figure 1.1. Scales of urban climatology (micro, local and regional) and their mutual dependence.....	2
Figure 1.2. Preview of the Sandia Method used for the creation of the typical meteorological year files. Data Source: ASHRAE (2009), Technical Committee 4.2.5	
Figure 1.3. Southampton UK. Heating demand difference (Heating Degree Days: hours in year that temperature is below a base thermostat setting (Tbase)) between locations in the City Centre, National Oceanographic Centre (NOC) and the airport.	6
Figure 1.4. Left: Annual mean air temperature (°C) difference between the weather stations that have been used for the simulation weather data file for Shanghai. IWEA and CTYW (black and red straight lines) are provided as reference and they do not correspond to the years on the x axis. Right: Official weather stations in Shanghai, China. Distance of Hongqiao (ZSSS)(blue), Pudong (ZSPD) (Green) airports and the WMO 583620 (Red) weather station (CTYW) are shown from the city centre.	7
Figure 1.5. The steps in the methodology for the adaptation of TMY files.....	11
Figure 2.1. Vertical atmospheric layers in the context of the climatic scales. H denotes the average building height. Image adapted from Oke (2006).	13
Figure 2.2. Formation of the “internal” boundary layer plumes of the different land surface types that contribute to the development of the overall urban boundary layer. Image adapted from Foken (2008).	15
Figure 2.3. Wind flow patterns associated with urban morphology as depicted by the H/W aspect ratio. Top: Isolated roughness flow, Middle: Wake interference flow and Bottom: Skimming flow. Source: Oke (1987), Image adapted from Erell et al. (2011).	20
Figure 2.4. The heat fluxes at different urban atmospheric layers. QF (purple arrow) denotes the anthropogenic heat flux, QE is the latent heat flux (blue arrow), Q^* denotes the solar radiation balance, QH is the sensible heat flux and ΔQ_s the net energy stored in the surface. ΔQA is the net energy from advection. Overbars denote the spatial average of the fluxes. Image adapted from Pearlmutter et al. (2007).	21
Figure 2.5. Composition of an urban unit and its relationship to urban configuration.	25
Figure 2.6. The urban street canyon and its main geometrical characteristics. H is the building footprint-area-weighted height, L is the length of the canyon and W is the length averaged width. Image adapted from Erell et al. (2011).	26
Figure 2.7. Depiction of a generic urban unit in Hangzhou, China as selected for analysis in this study (left). The circular footprint is about 200,000 m ² , the radius is r=250 m and the height is adjusted to the building footprint-area-weighted height H (right).	28
Figure 2.8. Description of the main morphological parameters. AF marks the grid block’s averaged area perpendicular to the wind, AT is the total grid box area, H is the building footprint-area-weighted height and L_x and L_y are the mean length and width of the buildings in a grid box respectively. Image adapted from Grimmond et al. (2010).	28

List of figures

Figure 3.1. Function and applications of micro-scale models.	32
Figure 3.2. Computational grid resolution comparison between meso- (purple) and micro- (orange) scale models.....	33
Figure 3.3. Network resistance model for single layer (left), multilayer (middle) and slab (right) urban canopy parameterisation schemes. T_a is the air temperature, T_R is the roof temperature, T_w , T_G and T_S are the wall, ground surface and slab surface temperatures respectively. Image adapted from Kusaka and Kimura (2004).	35
Figure 3.4. The models' lowest level for urban canopy parameterisations according to their turbulence modelling approach. Levels are shown with grey dashed lines. Image adapted from Chen et al. (2011).	36
Figure 4.1. Location of Hangzhou (orange bullet point) and Ningbo (green bullet point) in China. Ningbo is the home of the Centre for Sustainable Energy Technologies (CSET) that owns the networks of air temperature and relative humidity sensors used for model validation (Shen et al., 2014). Background map from Poskanzer (2000).	41
Figure 4.2. Comparison between the daily mean air temperature for Hangzhou typical meteorological year weather files (CSWD and SWERA) and the daily average for the time period from 1998 to 2013. All data are from the same weather station (WMO 584570). Data Source: The Weather Underground (2014a).	42
Figure 4.3. Comparison between the daily mean relative humidity for the Hangzhou typical meteorological year weather data files (CSWD and SWERA) and the daily average for the time period from 1998 to 2013. All data are from the same weather station (WMO 584570). Data Source: The Weather Underground (2014a).	43
Figure 4.4. Comparison between the monthly mean relative dry bulb temperature for the Hangzhou typical meteorological year weather data files (CSWD (red) and SWERA (blue)) and the monthly average for the time periods from 1998 to 2013 (black), 1982 to 1997 (dark yellow) and 1966 to 1981 (dark red). All data are from the same weather station (WMO 584570). Data Source: National Oceanic and Atmospheric Administration (NOAA)-National Climatic Data Center (2014) The Weather Underground (2014a).	43
Figure 4.5. Wind speed distribution and wind rose analysis from observations collected at Mantou Mountain (WMO 584570) reference weather station in Hangzhou. Wind rose outer arc (black) shows frequency and inner arc (red dashed) denotes frequency x wind speed. Data period 1998-2013. Data Source: The Weather Underground (2014a).	44
Figure 4.6. Sensor locations near to large water bodies in Hangzhou and Ningbo (Bottom Right).	45
Figure 4.7. The radiation shield (Left) and the T_{air} / RH sensor (iButton©) used for the observations in China. Images Courtesy of Shen et al. (2013).	47
Figure 4.8. The environmental test chamber in the Centre for Sustainable Energy Technologies (CSET) at the University of Nottingham Ningbo (Left) and the sensors during the calibration (Right). Image Courtesy of Shen et al. (2013).	47
Figure 4.9. Siting of the sensors and the signal source areas.	50
Figure 4.10. The network of sensors in Hangzhou. The boxes give a visual estimation of the annual average albedo (Shen et al., 2013) and the bullet points describe the summer Sky View Factor (SVF) as calculated on site (Bourikas et al., 2013). The	

List of figures

letters nearby the sensors indicate the Land Use type as given in the Local Planning maps (Ningbo Urban Planning Bureau, 2003; Design, 2006).....	53
Figure 4.11. Consecutive outlier values (left, shown with circles and stars) that can be associated with the weather trend of the week before or after (right, the consecutive outliers in day 7 are shaded with orange).	54
Figure 4.12. Outliers (left, shown with red circles) examined in relation to the weather conditions (right). The black vertical reference line (Hr=115, right) shows the time that the outliers were noticed.	54
Figure 4.13. Locations of the sensors used in the case study. The target location for the case study is marked as 1. The blue points denote locations with a SVF similar to that of the target size. The Mantou Mountain, National Principle Weather station's location is marked as 9. Image Source: Google Earth (2013).	56
Figure 4.14. Goodness-of-fit of the air temperature (left) and relative humidity (right) estimations from the methods in the case study (Cases 1 to 8) to the observations from the target site's sensor. Cases 1 to 3 are the statistical forecast models. Cases 4, 5B, 6B & 7 replace missing data with mean values from different sources. Cases 5A and 6A are using the results of linear interpolation and Case 8 is a direct replacement with reference data. The methods adopted for use in this study are shaded with orange.	60
Figure 4.15. Mean absolute difference (i.e. Observed – Estimated) between the air temperature (°C) (left) and relative humidity (%) (right) estimations and the observed weather conditions for each case. The methods adopted for use in this study are shaded with orange.	60
Figure 4.16. The location of the sensors in Hangzhou participating in the analysis for the determination of the urban unit (Top left, bullet points colour corresponds to curves in Figure 4.18 and Figure 4.19). Top right: The three different views from the location of sensor 5 (orange bullet). The views are numbered from one to three and the image is outlined with colours respectively (middle and bottom left). Bottom right (d): Full frame circular fisheye image (taken at a height of 1.5m above ground in May 2013) of the sky dome available to the sensor.	64
Figure 4.17. The vegetated surface area at different concentric (sensor lays at the centre) annuli areas. The vegetated surface area is shown with the polygons (opaque green). The annuli areas are marked with different colours (transparent). Their inner circle border radius (r) and the outer circle radius (R) from the centre outwards are r-R=0-10m; 10-25m; 25-50m; 50-100m; 100-150m; 150-200m; 200-300m ;300-400m ;400-500m.	65
Figure 4.18. The percentage green space in the annuli areas for each sensor in the group participating to the urban unit determination analysis. The legend shows the mean summer Tair (°C) departure for each sensor from the group mean. The location of the sensor is quoted in parentheses.	66
Figure 4.19. Regression lines of the percentage vegetated area in each annulus area on the distance from the centre (i.e. the sensor).	67
Figure 5.1. The digital elevation model and the land cover were built upon the aerial image (Left). Four land surface types had been identified and their surface area was estimated by the model. The sensor was located at the centre of a disk of 250m radius (Right).....	70
Figure 5.2. Error determination in the visual assessment of buildings' height. Artistic representation - images provide a high accuracy approximation (+/- 1 floor level) of the real conditions.	73

List of figures

Figure 5.3. Road vegetation reservations are planted with short bushes and medium height deciduous trees with a distinctive crown.	75
Figure 5.4. Determination of the error in street dimensions measurements based on aerial images (method used for this study) from Google Earth (Google Earth, 2013)	76
Figure 5.5. Assessment of the error in the determination of building footprint area from aerial images (top). Floor height measurement of a residential (student housing) building with a retail shop at the ground floor. UNNC: University of Nottingham in Ningbo, China.....	77
Figure 5.6. Estimation of the error in the building height measurement for a mixed use skyscraper in Hangzhou, China. Image sources as referenced in figure labels.	79
Figure 5.7. Estimation of the error in the building height measurement of a skyscraper with an office use in Hangzhou, China. Image sources as referenced in figure labels.	80
Figure 5.8. Calculation of the frontal area for the urban unit (top). A section cut was made (orange dashed line with arrows, top) perpendicular to the wind's direction. The footprint of the buildings in the projected onto the section cut area (green double arrows, bottom) was estimated and multiplied by the building height h . H denotes the building footprint-area-weighted height.	83
Figure 5.9. Comparison between Chinese (red star), US (red/blue square) residential districts and European (blue/white cross) central districts. European residential districts are expected to have smaller frontal area ratios to these shown but retain the high planar area ratios. Data source references as shown in Table 5.3.	84
Figure 5.10. Calculation of the seasonal and average Sky View Factor (SVF). The original circular fish-eye (left), black and white for the summer (middle) and adjusted for winter (right) images used for the SVF estimation respectively.	86
Figure 5.11. The nine urban units (sensor locations, marked with blue bullets) in Hangzhou classified into Local Climate Zone 5. The Mantou Mountain, National Principle Weather station's location is marked as NP.	92
Figure 5.12. Land cover analysis for Sites 1, 2 (top) and 4, 7 (bottom) in Hangzhou (see Figure 5.11). The buildings are marked with black, vegetation with green, water with blue and the residual area is considered impermeable surface (e.g. pavement, asphalt, dry soil).....	92
Figure 5.13. Analysis of the morphological parameters for each annulus area two of the nine "LCZ5" sites .Site numbers refer to locations in Figure 5.11.	93
Figure 5.14. Distribution of the building footprint surface to area ratio Fr . The annular areas in the diagram correspond to the annular areas in the urban unit with the core (0-50m) being at the centre of the disk.	94
Figure 5.15. Distribution of the pervious surface to area ratio Pr . The annular areas in the diagram correspond to the annular areas in the urban unit with the core (0-50m) being at the centre of the disk.	95
Figure 5.16. Distribution of the impervious surface to area ratio Ir . The annular areas in the diagram correspond to the annular areas in the urban unit with the core (0-50m) being at the centre of the disk.	96
Figure 5.17. Distribution of the mean floor plan area weighted H . The annular areas in the diagram correspond to the annular areas in the urban unit with the core (0-50m) being at the centre of the disk.	97

List of figures

Figure 5.18. Typical building floor plans (left) and residential urban forms (right) in Shanghai. Figure redrawn from Yang et al. (2011).	100
Figure 5.19. Residential urban forms in Hangzhou. Primary streets are marked with red, secondary with yellow and tertiary with blue. Tall buildings (top left) form an interspersed site layout while medium rise buildings (bottom left) are built in a linear / long linear form. The relative size of the streets and the aspect ratios of street canyons are shown in the street level images (top and bottom right). The camera view is marked with dotted lines (left side maps).	101
Figure 5.20. Pervious surface to area ratios (%) for different values of floor plan surface to area ratios (%) for the nine studied sites. A 1:1 reference line is shown on grey and dotted.....	103
Figure 5.21. The building floor plan surface to area ratio (%) per annulus. Solid lines with percentages show the median of the distribution.	104
Figure 5.22. The pervious surface to area ratio (%) per annulus. Solid lines with percentage values show the median of the distribution.....	104
Figure 5.23. Typical grid (top), adaptive grid (middle) and the “urban unit” model (bottom) method to divide a city into regions and represent their geometry with an idealised model. Image adapted from Millward-Hopkins et al. (2013).	106
Figure 5.24. Top plan view (left) and a 3D perspective view (Top right) of the idealised “urban unit” model for the studied “LCZ5” sites. A 2D view of the computational grid is shown in the left image (grid cell horizontal dimensions 8m x 8m).	107
Figure 6.1. Methodology flowchart of the model’s validation and the generation of the adapted weather dataset.....	110
Figure 6.2. The location of the 10 “sample” sites (purple bullets) used for the assessment of generic UHI patterns in Hangzhou, China in relation to the 9 studied (LCZ5, blue bullet points) sites.	112
Figure 6.3. Overview of the ENVI-met model. Data Source: Bruse (2008e).....	114
Figure 6.4. Simulations data flow and main outputs. T_{air} , T_{surf} and T_{soil} [K] denote the air, surface and soil temperature respectively. U [m/s] is the wind speed in the three directions, q [g/kg] is the specific humidity of air, RH [%] is the relative humidity of air, TKE [m^2/s^2] is the turbulent kinetic energy and SVF is the sky view factor [0-1]. Q_H denotes the sensible heat flux and Q_E is the latent heat flux [W/m^2]. Data source: Bruse (2008d).	114
Figure 6.5. The 3D computational domain and the vertical grid layout in this study. .	116
Figure 6.6. Fit of the building geometry to the predefined computational grid. The building (marked as orange) has a square base of 8m x 8m that cannot be allocated to an integer number of the 3m x 3m grid cells.....	117
Figure 6.7. Hourly weather conditions (Left) and the prevalent normalised wind direction (wind speed x frequency) (Right) for the winter scenario (11 th January 2013, Top) and the summer scenario (10 th August 2013, Bottom). Data Source: The Weather Underground (2014a).	120
Figure 6.8. Sensitivity of simulated air temperature to computational grid resolution of 8m (red circle), 6m (black square) and 3m (black x).....	122
Figure 6.9. Sensitivity of simulated relative humidity to computational grid resolution of 8m (red circle), 6m (black square) and 3m (black x).	123
Figure 6.10. Distribution of the vegetated surface area in the urban unit for the cases considered in Scenario 1 of the green-space sensitivity analysis.....	124

List of figures

Figure 6.11. The different percentages of vegetated surface area in the “urban unit” for the cases in Scenario 2 of the green-space sensitivity analysis. Top plan view of the computational domain (Right) for the cases with $Pr = 0.2$ and $Pr = 0.4$	124
Figure 6.12. The computational modelling domain and the boundary conditions. H (m) denotes the average building footprint-area-weighted height over the urban unit.	126
Figure 6.13. The computational grid of the generic circulation model for the region of Hangzhou (major cities outlined with white). The centre of each grid box (model output available) is marked with an orange bullet. The dashed orange lines show the four grid boxes closest to Hangzhou.	129
Figure 6.14. Ground surface types used in the simulations with the “urban unit model”.	130
Figure 6.15. The 3 nodes model for the calculation of the wall/roof surface temperature and the internal building air temperature. T_o is the node at the outer surface, T_w at the middle and T_i at the internal surface of the building element. Image Adapted from Huttner (2012).	131
Figure 6.16. The monthly anthropogenic heat emissions as calculated for Hangzhou with the LUCY model. Data Source: Allen et al. (2011), Lindberg et al. (2013)....	135
Figure 6.17. Schematic representation of the solar radiation net energy Q^* balance at the ground surface. Shortwave and longwave radiation are denoted with k and L respectively. Image modified from Foken (2008).	136
Figure 6.18. Comparison of the hourly global horizontal solar radiation (GHR) [$W\ m^{-2}$] for the winter scenario between different datasets. ENVI-met estimations (black cross), NCEP/NOAA model (yellow points) output, TMY (WMO 584570) file (green square) and the ANN results (red triangle) for Hangzhou are shown respectively. Data Source: Bruse (2004), NCEP/NCAR US (2000).	138
Figure 6.19. Comparison of the hourly global horizontal solar radiation (GHR) [$W\ m^{-2}$] for the summer scenario between different datasets. ENVI-met estimations (black cross), NCEP/NOAA model (yellow points) output, TMY (WMO 584570) file (green square) and the ANN results (red triangle) for Hangzhou are shown respectively. Data Source: Bruse (2004), NCEP/NCAR US (2000).	139
Figure 6.20. Comparison of the observed (black line) and the modelled air temperature (left) and RH (right) at 3.5m above ground for the 3 days in January 2013 (winter) representative for the weather forcing groups. (Time given in China Standard Time – CST: GMT+8).....	144
Figure 6.21. Comparison of the observed (black line) and the modelled air temperature (left) and RH (right) at 3.5m above ground for the 3 days in May 2013 (spring) representative for the weather forcing groups. (Time given in China Standard Time – CST: GMT+8).....	147
Figure 6.22. Comparison of the observed (black line) and the modelled (red line) air temperature (left) and RH (right) at 3.5m above ground for the 3 days in June 2013 (summer) representative for the weather forcing groups. (Time given in China Standard Time – CST: GMT+8).	149
Figure 6.23. Comparison of the observed (black line) and the modelled (red line) air temperature (left) and RH (right) at 3.5m above ground for the 3 days in October 2013 (autumn) representative for the weather forcing groups. (Time given in China Standard Time – CST: GMT+8).	150

List of figures

Figure 7.1. The air temperature trend line (24 hr moving average) for the reference TMY file (TMYref, blue, 584570_CSWD) and the TMY file adapted for the urban weather projections (TMY-UWP, red).	155
Figure 7.2. The importance of hourly air temperature profiles in cooling demand. The air temperature difference in August between the reference TMY file (TMYref, blue, 584570_CSWD) and the local - specific TMY file (TMY-UWP, red) is in the range of 2°C and above at noon and during night. The 27°C thermostat set point for cooling is shown with a black line.	156
Figure 7.3. The monthly (top) and daily (week day) (bottom) heating (red) and cooling (blue) profile for the domestic apartment case study in Hangzhou. Data source: Hu et al. (2013).	158
Figure 7.4. The monthly (top) and daily (week day) (bottom) heating (red) and cooling (blue) profile for the non-domestic apartment case study in Hangzhou.	160
Figure 7.5. Comparison of the degree days in the reference TMY (TMY reference, gray; 1598 HDD, 207 CDD) with the TMY overlaid with the bulk “city” UHI effect (TMY+UHI, orange; 1495 HDD, 243 CDD) and the micro-scale “urban weather projections” (TMY-UWP, red; 1383 HDD, 279 CDD). T_{base} is the temperature threshold used for the calculation of the HDD and CDD. The area with the light blue background marks the cooling period.	162
Figure E.1. Feed forward ANN model architecture. X_i refers to the input parameters. $W_{ijhidden}$ and $W_{joutput}$ denote the synaptic weights between the input and the output. The black lines represent the synaptic weights (here equal for display purposes). Data Source: Gershenson (2003), Bosch et al. (2008).	XXVII
Figure E.2. The neural network function and the training process. SCG denotes the Scale conjugate gradient algorithm. Grey dashed arrows mark the training loop. Bold black arrows show the end of the loop and the final output.	XXIX
Figure E.3. Location of the cities (marked as red triangles) used for the development of the ANN model. Blue lines give an approximation of the +/-2 degrees latitude distance to Hangzhou (marked as orange bullet point). Background Image source: Google Earth (2013).	XXXIII
Figure E.4. The ANN optimisation in different stages during its development. Grey dashed arrows mark the training loop. Bold black arrows show the end of the loop and the output.	XXXV
Figure E.5. Comparison of the ANN (MLP model) GHR results for Hangzhou with the observed daily GHR from Hangzhou TMY file (TMY WMO 584570) for 365 days (a year).	XXXIX
Figure E.6. Comparison of the ANN (MLP model) results for Shanghai (Hongqiao, WMO 583670) with the total daily GHR observations from Baoshan Shanghai(WMO 583620) for 4 days in each month in 2012.	XL

List of figures

List of tables

Table 4.1. Statistical analysis of the calibration results at specific time intervals. Background Data Source: Shen et al. (2013).	48
Table 4.2. Summary of the general guidelines for the site selection and installation of urban weather stations.....	49
Table 4.3. Comparison between the results from temperature measurements with two different types of radiation shields. Source: (Cheung et al., 2010)	51
Table 4.4. Summary of the methods investigated for the replacement of missing data in urban weather datasets. The best performing cases adopted by this study are highlighted with orange.	57
Table 4.5. The Root Mean Square Error (RMSE) of the results from the statistical forecast model when trained with different number of days.	58
Table 4.6. The Mean Absolute Error (MAE) of the results from the statistical forecast models for 4 different cases of model training.	58
Table 5.1. Analysis of the morphological parameters for each annulus area from a site with a LCZ5 classification (site 2 in Figure 5.11)	71
Table 5.2. Floor to floor height assumption for different building uses. f denotes the number of floors.	78
Table 5.3 Comparison of morphological characteristics between urban sites in China, Europe and the USA.	84
Table 5.4. The Urban Climate Zone classification scheme. Table adapted from Oke (2006).	89
Table 5.5. The main classification parameters from the Local Climate Zones scheme. Adapted from Stewart and Oke (2012).	90
Table 5.6. Overview of the median and the (range) of 80% of the observations for key morphological parameters.....	102
Table 6.1. Case studies for the assessment of the solution's sensitivity to grid resolution.	119
Table 6.2. Summary of the two scenarios used for the grid sensitivity analysis. Data Source: The Weather Underground (2014a)	119
Table 6.3. Boundary conditions of the 3D computational domain. Table adapted from (Ashie & Kono, 2011).	127
Table 6.4. Ground surface material properties used in the simulations with the "urban unit model".	130
Table 6.5. Comparison of population density and climate classification between the cities in Sailor and Lu (2004) and this study.	133
Table 6.6. Anthropogenic heat flux reference values for Hangzhou, China and Philadelphia, U.S.A..	134
Table 6.7. Overview of key forcing for the validation simulations and the "urban weather projections" generation. An example is shown for June, weather forcing Group 2.....	141
Table 6.8. Model performance indices determined for the heating season simulations with the novel urban unit model.	145
Table 6.9 Model performance indices determined for the cooling season simulations with the novel urban unit model.	148
Table 7.1. Thermal properties of the building elements in the domestic building case study. Data source: Chow et al. (2013).	157

List of tables

Table 7.2. Main characteristics of the TRNSYS model for the heating and cooling load simulations in the domestic building case study.	159
Table 7.3. Thermal properties of the building elements in the non-domestic building case study (Shen et al., 2014).	159
Table 7.4. Main characteristics of the TRNSYS model for the heating and cooling load simulations in the non-domestic building case study.....	161
Table E.1. Model architecture of the ANN for the generation of global solar radiation time series.	XXX
Table E.2. Cities and the TMY origin weather stations used for the development of the ANN.	XXXII
Table E.3. Input parameters and ANN architecture used for the prediction of global solar radiation.	XXXIV
Table E.4. Input data and variables for the final ANN model and its performance at hourly GHR prediction for each month.....	XXXVII
Table E.5. Comparison of the mean absolute percent error (MAPE) in this study with other models in the literature.	XXXVIII
Table E.6. ANN modelling results for different input variables.	XLI
Table E.7. ANN modelling results for different input variables.	XLII
Table E.8. ANN modelling with different random number generator starting points.	XLIII

Author's declaration

I, Leonidas Bourikas declare that this thesis and the work presented in it are my own and has been generated by me as the result of my own original research.

Thesis title:

Microclimate adapted localised weather data generation: Implications for urban modelling and the energy consumption of buildings.

I confirm that:

1. This work was done wholly or mainly while in candidature for a research degree at this University;
2. Where any part of this thesis has previously been submitted for a degree or any other qualification at this University or any other institution, this has been clearly stated;
3. Where I have consulted the published work of others, this is always clearly attributed;
4. Where I have quoted from the work of others, the source is always given. With the exception of such quotations, this thesis is entirely my own work;
5. I have acknowledged all main sources of help;
6. Where the thesis is based on work done by myself jointly with others, I have made clear exactly what was done by others and what I have contributed myself;
7. Either none of this work has been published before submission, or parts of this work have been published as:

Journal articles

Bourikas L., James P.A.B., Bahaj A.S., Jentsch M.F., Shen T., Chow D.H.C., Darkwa J. (2016) Transforming typical hourly simulation weather data files to represent urban locations by using a 3D urban unit representation with micro-climate simulations. *Future Cities and Environment*, vol. 2, p.p. 1-23

Author's declaration

Jentsch M.F., James P.A.B., Bourikas L. and Bahaj A.S. (2013) Transforming existing weather data for worldwide locations to enable energy and building performance simulation under future climates. *Renewable Energy*, vol. 55, p.p. 514-524

Bourikas L., Shen T., James P.A.B., Chow D.H.C., Jentsch M.F., Darkwa J. and Bahaj A.S. (2013) Addressing the Challenge of Interpreting Microclimatic Weather Data Collected from Urban Sites. *Journal of Power and Energy Engineering*, vol. 1, p.p. 7-15. First presented to the 2nd International Conference on New Energy and Sustainable Development (NESD 2013), 29 Nov – 1 Dec 2013, Sanya, China.

Conference articles

Bourikas L., James P.A.B., Bahaj A.S., Jentsch M.F., Shen, T., Chow D.H.C. and Darkwa, J. (2015) A simplified 3D urban unit representation for urban microclimate simulations: A case study in China's 'Hot Summer and Cold Winter' climate zone. In *SET2015: 14th International Conference on Sustainable Energy Technologies*, 25-27 Aug 2015, Nottingham, UK

Signed:

Date:

For my wife Anastasia and my son Zisis Orion without whom
this thesis would have been impossible to complete

Acknowledgements

This work is part of the activities of the University of Southampton's Energy and Climate Change Division and the Sustainable Energy Research Group (www.energy.soton.ac.uk) on cities and infrastructure. Leonidas has been supported during his research by the Faculty of Engineering and the Environment in the University of Southampton funded PhD programme.

Leonidas would particularly like to single out his supervisors at the University of Southampton, Prof. P.A.B. James and Prof. A.S. Bahaj for their excellent support, cooperation, wise counsel and guidance during the period of his PhD research.

He would also like to give special thanks to Mr. Ian Galloway for his valuable feedback and for proof-reading this thesis. Special thanks are also due to parents and friends for putting up with me all this time.

Acknowledgements

Abbreviations

ANN	Artificial Neural Network
AR	Aspect Ratio
ARIMA	Autoregressive Integrated Moving Average
ASHRAE	American Society of Heating, Refrigerating and Air-Conditioning Engineers
BEP	Building Effect Parameterisation scheme
CAD	Computer Aided Design
CAT	Canyon Air Temperature model
CDD	Cooling Degree Day
CDF	Cumulative Distribution Function
CFD	Computational Fluid Dynamics
CIBSE	Chartered Institution of Building Services Engineers
COAMPS	Coupled Ocean/Atmosphere Meso-scale Prediction System
CSET	Centre for Sustainable Energy Technologies
CSI	Climatic Severity Index
CSWD	Chinese Standard Weather Data
CTYW	Chinese Typical Year Weather
DBT	Dry Bulb Temperature
DEM	Digital Elevation Models
EPC	Energy Performance Certificate
GHR	Global Horizontal Radiation
HDD	Heating Degree Days
HVAC	Heating, Ventilation and Air Conditioning systems
IS	Inertial Sub-layer

Abbreviations

IWEC	International Weather for Energy Calculations
LCZ	Local Climate Zones urban classification scheme
LES	Large Eddy Simulation
MAE	Mean Absolute Error
MAPE	Mean Absolute Percent Error
MBE	Mean Bias Error
MEMO	Meso-scale Model
METAR	Meteorological Terminal Aviation Routine Weather Report
ML	Mixed Layer
MLP	Multi-Layer Perceptron
MOST	Monin-Obukhov Similarity Theory
MSE	Mean Squared Error
NDVI	Normalised Difference Vegetation Index
NOAA	National Oceanic and Atmospheric Administration
NOC	National Oceanographic Centre
NREL	National Renewable Energy Laboratory
RANS	Reynolds Averaged Navier-Stokes
RH	Relative Humidity
RMSE	Root Mean of Squared Error
RS	Roughness Sub-layer
SC	Sky Cover
SCG	Scaled Conjugate Gradient
SEB	Surface Energy Balance
SUEWS	Surface Urban Energy and Water balance Scheme
SUMM	Simple Urban energy balance Model for Meso-scale Simulations
SVF	Sky View Factor
SWERA	Solar and Wind Energy Resource Assessment

Abbreviations

TEB	Town Energy Balance model
TKE	Turbulent Kinetic Energy
TMY	Typical Meteorological Year
TRY	Test Reference Year
TRY-ROW	Test Reference Year - Rest Of World
UBL	Urban Boundary Layer
UCL	Urban Canopy Layer
UCM	Urban Canyon Model
UCP	Urban Canopy Parameterisations
UCZ	Urban Climate Zones urban classification scheme
UHI	Urban Heat Island
UHII	Urban Heat Island Intensity
URANS	Unsteady Reynolds Averaged Navier-Stokes
WMO	World Meteorological Organisation
WRF	Weather Research and Forecasting model
WS	Wind Speed
WYEC	Weather Year for Energy Calculations

Abbreviations

Chapter 1 Introduction

1. Research Overview

Increasing urbanisation has led to an expansion of urban footprints and the emergence of large urban agglomerations worldwide. While the urban land area remains just a fraction of the Earth's land surface (3% of the land mass, (Liu et al., 2014)), it is notably where an unprecedented consumption of resources including energy is taking place. Increasing energy demand puts pressure on the exploitation of more and more varied sources with concomitant financial and environmental cost.

At the same time, urban culture has shifted away from dense mixed-use city cores to loose urban agglomerations with residential suburbs and crowded office districts. Skyscrapers along with highly glazed buildings are erected as a symbol of power and a statement of welfare (Bahaj et al., 2008). It is becoming more obvious than ever before that a sustainable future depends on the decrease of demand through a behavioural shift and the ability of engineers, scientists and planners to optimise the energy efficiency of buildings instead of just serve them.

The expansion of urban footprint changes the land use and land surface characteristics of the newly developed areas. This results in the creation of a surface energy balance distinctive to the urban environment (Oke, 1982). The development and properties of the urban surface energy balance $Q_{(t)}$ in relation to time are a function of the urban fabric properties (e.g. albedo, emissivity, thermal capacitance, thermal conductivity), the site's morphology (e.g. height of buildings to width of streets aspect ratios, frontal area λ_f and planar area λ_p ratios, pervious and impervious surface areas), the external regional weather forcing (e.g. wind velocity, net shortwave and longwave solar radiation, air temperature, relative humidity and precipitation) and anthropogenic heat emissions (Erell & Williamson, 2006; Piringner et al., 2007; Memon et al., 2009) (Eq. 1.1).

$$Q_{(t)} = f(\text{materials, morphology, weather, emissions}) \quad (1.1)$$

It should be noted that there is a mutual dependence between regional (i.e. city with immediate surroundings – scale) weather, urban sites' micro-climate (i.e. hourly averaged weather within the urban canopy), urban design, building design and energy consumption (Figure 1.1).

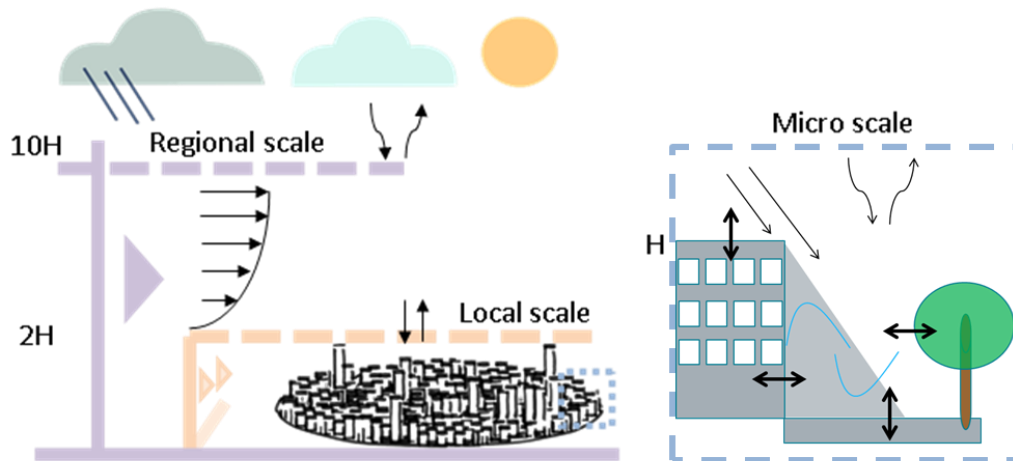


Figure 1.1. Scales of urban climatology (micro, local and regional) and their mutual dependence.

Engineering and urban design practices often rely on thermal simulation modelling in order to achieve regulatory compliance. Such practices support decision making on urban and building design, as well as the size of building energy systems and so directly affects energy consumption.

Heating, ventilation and air conditioning (HVAC) systems are often oversized in order to reduce design risk by ensuring that the system will cope with loads above the design day estimations (Thomas & Moller, 2006). This causes the HVAC system to operate in “short cycles” (Burdick, 2011) that affect the energy consumption of the building, potentially the thermal comfort of the users and the indoor air quality (e.g. low air circulation, excess humidity), whilst at the same time increasing the cost of operation and possibly maintenance by building services (Burdick, 2011). Another issue pertaining to the estimation of the energy use is the so called “energy performance gap”. The energy performance gap refers to the discrepancy between the energy use predictions in compliance modelling and the actual energy use of the building (The Carbon Trust, 2012). Reasons for the performance gap for example include technical issues (poor build quality, poor commissioning), occupancy and user behaviour or a change of use (Hirst & Brown, 1990; Jaffe & Stavins, 1994; Zero Carbon Hub, 2014). Occupancy profiles and user behaviour are a major concern in energy efficiency policy

recommendations because of a notable rebound effect that is responsible for a 20% to 50% share of the performance gap (Haas & Biermayr, 2000; Dimitriou et al., 2014).

Another common concern in the above two cases (oversizing of energy systems for buildings and the performance gap) is the way that energy use is estimated, more specifically the heating, cooling, dehumidification and mechanical ventilation loads.

Currently, in many countries, weather data files with a typical meteorological year (TMY) format are used for building regulation compliance calculations (Crawley, 1998). Several organisations have introduced different TMY formats (e.g. WYEC2 from the American Society of Heating, Refrigerating and Air-Conditioning Engineers (ASHRAE), TMY2 from the U.S. National Renewable Energy Laboratory (NREL), Test Reference Year (TRY) for the UK from the Chartered Institution of Building Services Engineers (CIBSE); for an explanation of the abbreviations *see Abbreviations or below*). Common typical weather year formats have the form of a synthetic year with months representative of the average climatic conditions for the site of interest (Hacker et al., 2009). The weather data used are actual historical observations usually from a source period of 15 to 30 years (Forejt et al., 2006).

The CIBSE Test Reference Year (TRY, 2016 release) for the United Kingdom is based on data collected between 1983 and 2013 (Virk & Eames, 2016). The selection of the typical months is driven by dry bulb temperature, global solar radiation falling on a horizontal surface and wind speed observations (Hacker et al., 2009). The cumulative distribution probability (CDF - cumulative distribution function) of the daily mean values is compared between these three parameters with the use of the Finkelstein-Schafer statistic (a goodness-of-fit measure which sums the absolute difference between the daily values in a month's CDF and the CDF for all same months in the data source period) in order to select the most average - "typical" months (Levermore & Parkinson, 2006; Hacker et al., 2009; Jentsch et al., 2014). In order to assess the overheating risks, especially in natural ventilated buildings, CIBSE develops the Design Summer Year (DSY) weather file. In contrary to the Test Reference Year, DSY is a single year and not a compilation of months. It represents the "near-extreme" third hottest summer observed (average temperature from April to September) in a period of 21 years (Eames, 2016). It should be noted that the most widely used weather file formats (TRY-UK, the Test Reference Years for the rest of the world (TRY-ROW) other than the USA, the Typical Meteorological Year version 2 (TMY2) (update to TRY-US and TMY),

the Weather Year for Energy Calculations version 2 (WYEC2) and the ASHRAE (see below) International Weather for Energy Calculations (IWEC)) have all been derived with the same method. Their main differences are in the statistical weighting of the weather variables for the assessment of the 'typicality' of each month. This methodology, also known as the Sandia method, is part of the ISO standard 15926-4 (American Society of Heating Refrigerating and Air-conditioning Engineers (ASHRAE). Technical Committee 4.2, 2009). The stages (ASHRAE (2009), Technical Committee 4.2) for the construction of a typical year weather file in brief are as follows (Figure 1.2):

1. The accounting of four weather variables¹: dry bulb temperature, global solar radiation, dew point temperature and wind speeds (last two with lower weights). Initially the daily means are calculated for each month. In IWEC data files the weights are 30% for the average dry bulb temperature, 40% for the daily global solar irradiation and 10% for wind speed (Levermore & Parkinson, 2006). (¹nine variables when the maximum, minimum and mean dry bulb and dew point temperatures and max, mean wind speed statistics are considered)
2. The estimation and ranking for every month of the cumulative distribution probability for the daily mean of each parameter.
3. The calculation for the complete dataset of the overall cumulative distribution probability of the daily mean of each parameter.
4. The calculation of the Finkelstein-Schafer (F-S) statistic for each month and the selection of the 5 months with the lower weighted sum of the F-S statistics. These months are ranked in order of closeness to the long term mean and median value of the weather variables.
5. The further refinement of the selection with criteria to exclude months with extreme events.
6. The concentration of the 12 selected months. Smoothing is applied to the last and first 6 hours in each month.

However, compliance with the UK (e.g. Part L & F) and Chinese (e.g. JGJ134-2010) building regulations does not necessarily coincide with occupants' satisfaction or with the real operating conditions of the building services. One important consideration for the use of the typical year weather time series in energy consumption predictions and simulations is the representativeness of the location where the source data have been collected. Many of these locations are due to

historical data (minimum of 8 years but typically around 20 years (Jentsch et al., 2014)), availability and are often airports near large cities (World Meteorological Organisation, 2014).

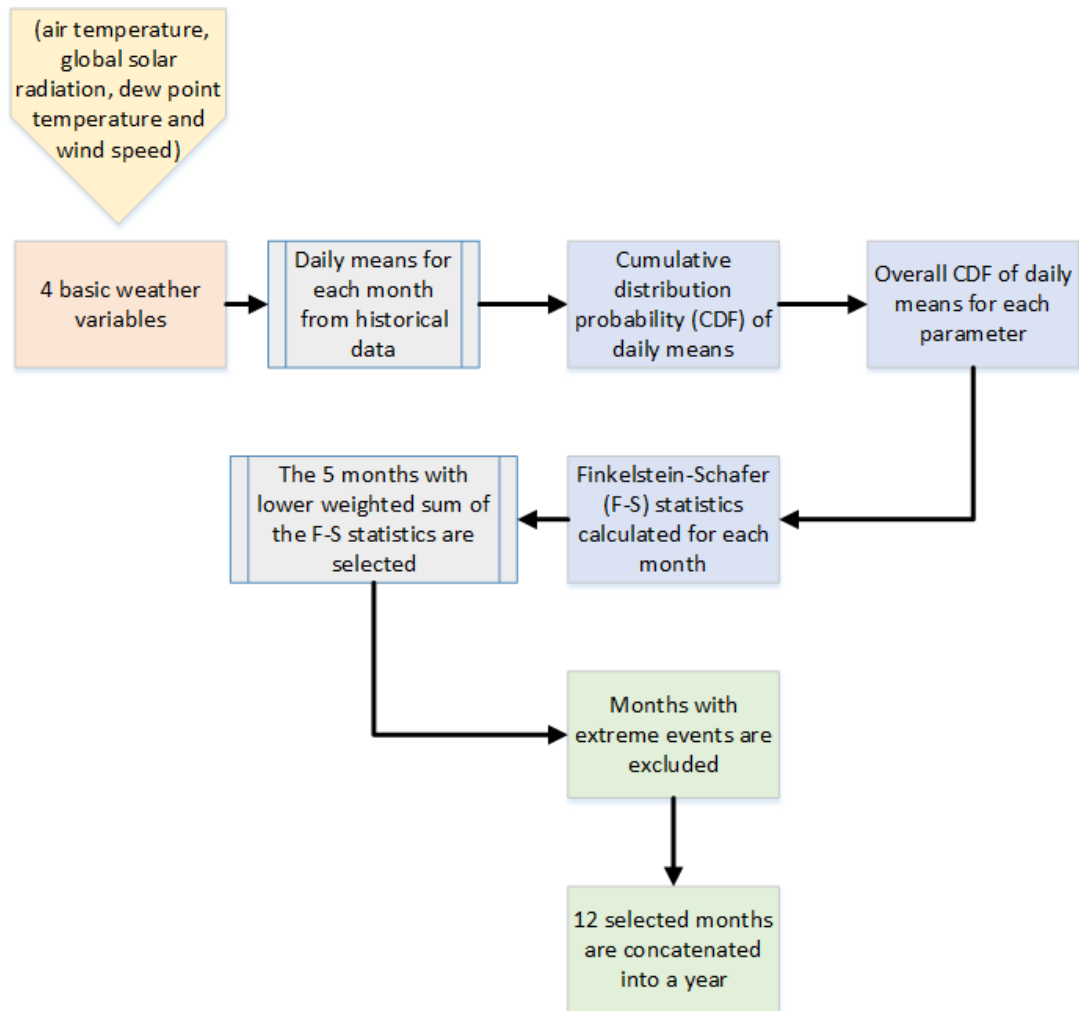


Figure 1.2. Preview of the Sandia Method used for the creation of the typical meteorological year files. Data Source: ASHRAE (2009), Technical Committee 4.2.

Over recent decades many cities expanded rapidly through higher building densities, larger building heights and expansion towards suburban and rural areas. This expansion resulted in changes to the balance of the urban energy budget (Oke, 1982) which consists of the radiation, sensible, latent and anthropogenic heat fluxes and the roughness caused by the built environment (detailed description in the section *Urban Energy Balance*) (Oke, 1982). These features of the built environment's energy and mass equilibrium will cause atmospheric forcing which alters the local weather conditions (Collier, 2006) and contributes to the development of distinctive local

micro-climates specific to a site's characteristics and morphology. The microclimatic factor with the most noticeable variation regarding changes in the energy budget is the air temperature (Taha et al., 1999). The urban air temperature (T) difference from the regional non-urban temperature (i.e. airport sites) is defined as the urban heat island (UHI) and the magnitude of this difference is known as the urban heat island intensity (UHII) (Memon et al., 2009). The UHII is widely used as a projection of the background urban microclimate's effect that is responsible for the UHI's creation and development.

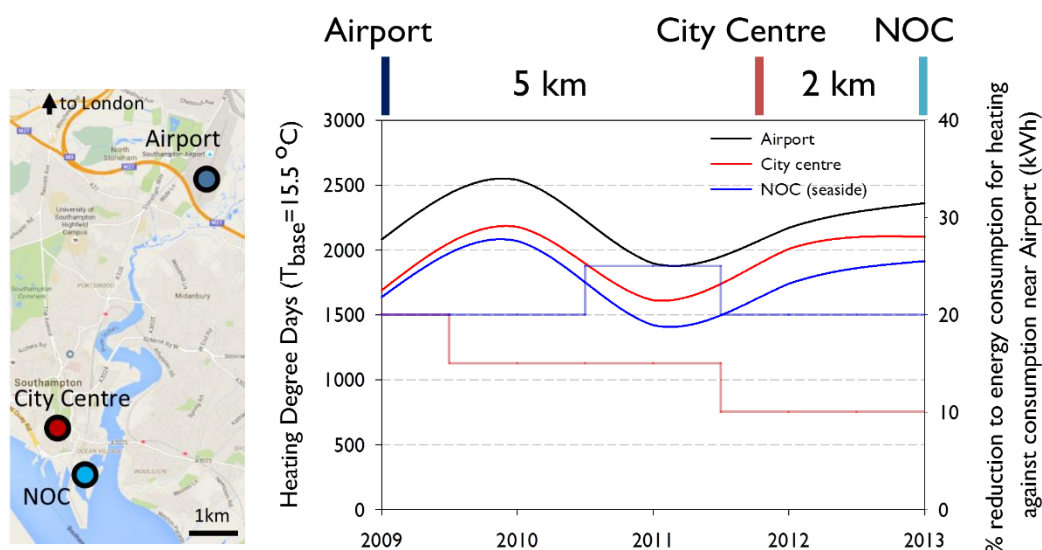


Figure 1.3. Southampton UK. Heating demand difference (Heating Degree Days: hours in year that temperature is below a base thermostat setting (T_{base})) between locations in the City Centre, National Oceanographic Centre (NOC) and the airport.

It is expected that the typical meteorological year (TMY) weather files largely underestimate the urban microclimate's development and are not representative locations within a city (Watkins et al., 2002; Kolokotroni et al., 2006; Mylona, 2012) (Figure 1.3; Figure 1.4). Figure 1.3 shows the heating degree days ($T_{base}=15.5^\circ\text{C}$) calculated for Southampton, UK with air temperature data collected from three different stations in the city. Southampton is at the South coast of the UK (50.9°N , 1.4°W) about 100km South-West of London. The airport (blue circle, top) is the location of the Southampton reference weather station. The National Oceanography Centre (NOC) is 7km to the South next to the sea and 2km away from the city centre. The results from the comparison of the heating degree days are indicative of the urban heat island effect and the influence of the sea to the location-specific climate even at short distances of a few kilometres within the same city.

Chapter 1 Introduction

The airport weather data unrepresentativeness of the urban conditions is much more prominent in the rapidly expanding large cities of China. For example, in Shanghai (31.2°N, 121.5°E), the city centre (orange circle in Figure 1.4) is at least 15km away from all the airport weather stations that have been used for the creation of simulation-ready weather data files. The Pudong International airport (green triangle in Figure 1.4) has a lower average annual air temperature than the airports (red and blue triangles) closer to the city centre indicating the effect of urbanisation and the expansion of the city towards the suburbs. In particular the air temperature in the CTYW source weather station area (red triangle) does not follow the trend of the other stations after 2009. That could be a result of a radical change in the morphology of the surrounding areas (Figure 1.4).

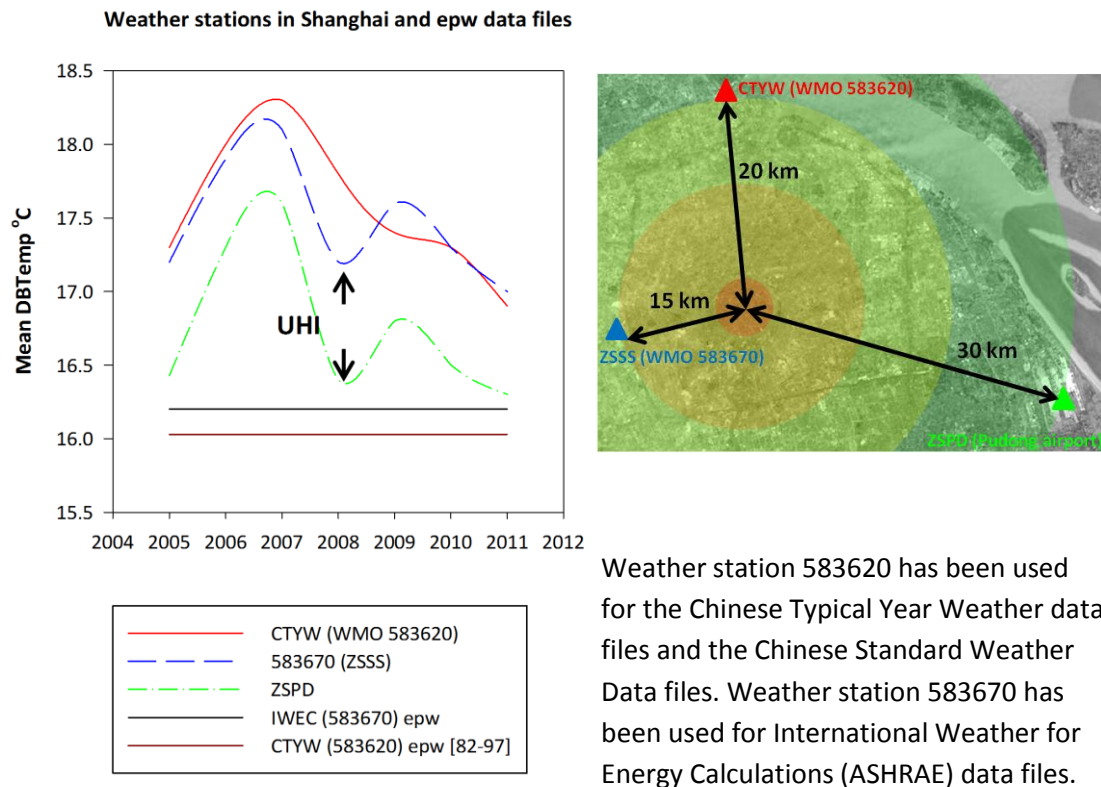


Figure 1.4. Left: Annual mean air temperature (°C) difference between the weather stations that have been used for the simulation weather data file for Shanghai. IWEW and CTYW (black and red straight lines) are provided as reference and they do not correspond to the years on the x axis. Right: Official weather stations in Shanghai, China. Distance of Hongqiao (ZSSS)(blue), Pudong (ZSPD) (Green) airports and the WMO 583620 (Red) weather station (CTYW) are shown from the city centre.

The context of this study is rapidly growing cities with a humid-subtropical climate. Best example of such cities are large cities such as Shanghai and Hangzhou in China where the urban form is often highly uniform and city expansion develops distinct

Chapter 1 Introduction

location-specific micro-climates that are poorly represented by the reference weather stations used for the creation of “typical” weather simulation-ready data files (e.g. airports and other semi-urban/rural locations).

2. Aims and Objectives

This thesis investigates methodologies for the adaptation of typical year simulation weather files to replicate the urban, location-specific micro-climate. The aim is to provide a comprehensive methodology that allows for an integration of urban micro-climate conditions into standard weather datasets such as the TMY. The potential improvements in the estimation of building energy consumption will be assessed against the business as usual case of applying typical meteorological year data files in places with a humid sub-tropical climate such as the case study city of Hangzhou in China.

The research objectives are to:

- a) Determine the characteristics of urban sites and analyse their land cover in view of micro-climate development, urban classification schemes and energy performance simulation requirements.
- b) Introduce a simplified 3D “urban unit model” for use in urban micro-climate simulations.
- c) Examine the local specific air temperature and relative humidity development at street level under different weather forcing for the prevalent urban class in the case study city.
- d) Generate a set of rules for the adaptation of typical meteorological year weather data files to the local micro-climate of urban sites and link these rules to the rural reference weather forcing and the urban morphological characteristics.
- e) Assess the potential impacts of the micro-climate adapted weather data sets on building energy consumption simulation.

3. Research Methodology

This thesis takes the reference weather data file (e.g. airport, non-urban locations) then applies (i) a bulk urban heat island correction and (ii) a specific local micro-climate adjustment. A further climate change projection (iii) may be applied to the local

weather file. These different stages are also detailed in published work (Bourikas et al., 2013; Jentsch et al., 2013; Bourikas et al., 2015; Bourikas et al., 2016).

In order to achieve this, this thesis introduces an idealised “urban unit model” (on a 250m radius) that represents the main thermal and morphological characteristics of urban sites at street level on the neighbourhood scale. This model, which was produced with statistical land cover and urban morphology analysis, can be used with simulations as a method of adapting commonly available weather data files to a local specific micro-climate. This methodology is used to adapt air temperature from the TMY file to the effects of local site-specific morphology on urban weather development. The “urban weather projections” resulting from this adaptation were then used for calculating the heating and cooling loads for the duration of a year.

An important issue for the successful application of any existing micro-climatic model are the input data prerequisites. However, detailed information on the surface materials’ properties, morphological and other modelling parameters is not always readily available in architectural and engineering practice. There is a need for simple models to estimate the weather conditions within urban areas as a function of time and urban morphology (Arnfield, 2003; Bouyer et al., 2011). The “urban unit model” referred to above has, therefore, been designed to be as general and simple as possible in order to facilitate widespread use in thermal simulation of buildings and urban design simulations. Ideally, a visual evaluation (or an automated geographical information system (GIS) platform) would be used to decide the urban class for the site of interest. This would be enough to enable offsetting of the reference (TMY or real time non-urban) hourly air temperature (T) and relative humidity (RH) for the selected urban class for different seasonal weather forcing.

A method is proposed (Figure 1.5) for the micro-climatic adaptation of typical simulation weather data files. The methodology has four key aspects:

- a) The application of a widely accepted urban classification scheme (i.e. Local Climate Zones (Stewart & Oke, 2012; Stewart et al., 2014)) in a case study for the urban micro-climate development in Hangzhou, China. The potential air temperature and relative humidity development in the urban canopy layer were analysed for the prevalent Local Climate Zone in the case study city. The city of Hangzhou is part of the street level air temperature and relative humidity measurement network of the University of Nottingham in Ningbo,

China (Bourikas et al., 2013; Shen et al., 2014). Data loggers were installed at 26 sites across the city. All sites have been categorised into a Local Climate Zone.

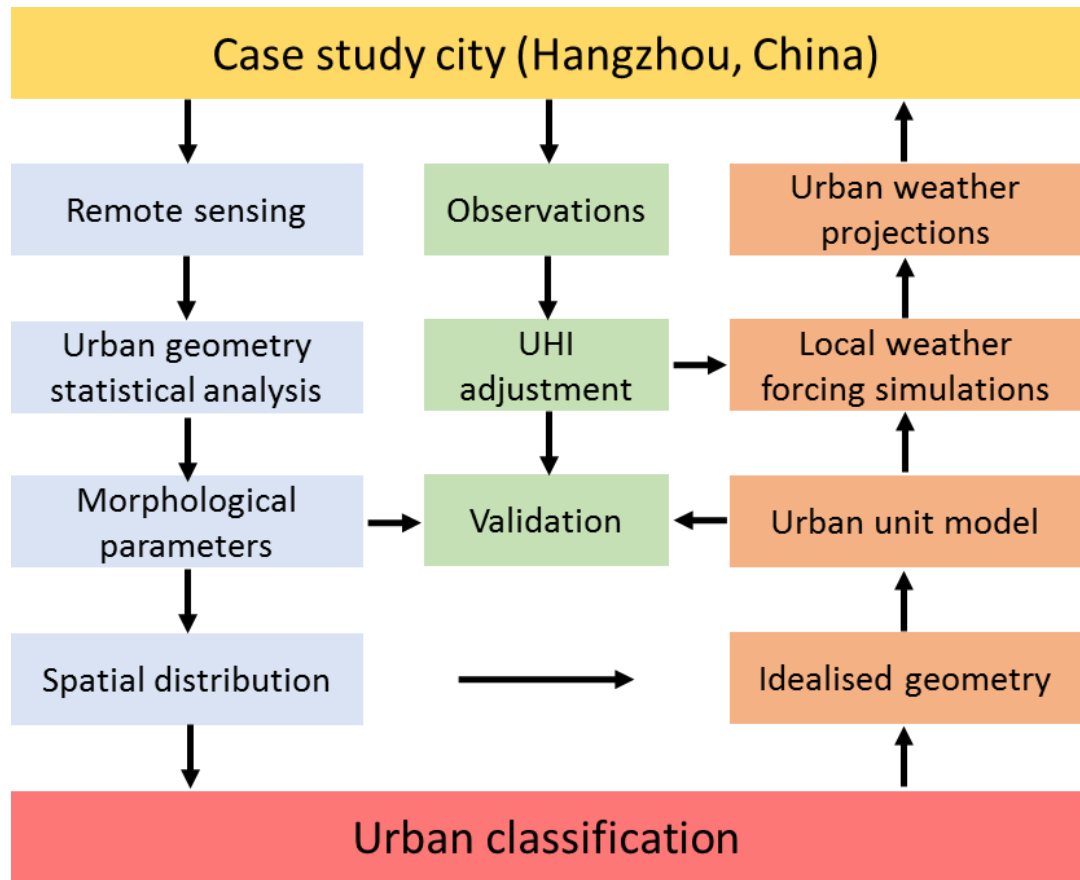


Figure 1.5. The steps in the methodology for the adaptation of TMY files.

- b) The introduction of a simplified, idealised model representative of the prevalent Local Climate Zone morphology. The idealised “urban unit model” has similar-‘typical’ morphological characteristics and it is thermally equivalent to the average characteristics of the real sites with sensors classified into the prevalent Local Climate Zone.
- c) The use of the “urban unit model” in the simulation of the urban micro-climatic development under different regional weather conditions. The typical meteorological year for Hangzhou (WMO 584570, TMY source data) was used to estimate the 25th and 75th percentile of the hourly daytime global solar radiation levels for each month in a year. The days in a month were classified into three bins (1. below the 25th centile, 2. from the 25th to the 75th centile and 3. above the 75th centile) according to their hourly global radiation fit. Statistics from each bin (i.e. mean air temperature and relative humidity; wind

directions normalised with mean wind speed) were used as the hourly weather forcing for the simulations. The three distinctive weather forcing groups were created in order to account for different weather forcing in each month. It was assumed that these three bins reflect three generic weather conditions (i.e. cloudy/rainy weather (Group 1), clear sky, average weather conditions (Group 2) and clear sky, hot weather (Group 3).

- d) The generation of the “urban weather projections” that results from the combined urban classification and simulation modelling and the assessment of the potential impact of their use in building energy consumption simulations. The “urban weather projections” incorporate the adaptation of the reference weather data set for the generic urban heat island whole city aggregate effect (local scale) and for the effect of the urban morphology at street level (local scale + morphology = micro-scale).

There are three key parts to the methodology for generating the “urban weather projections” that result from the combined urban classification and simulation modelling (Figure 1.5): The creation of the idealised “urban unit model” for the sites of interest (in this study 9 sites; Chapter 5); The correction of the reference weather data with the local monthly UHI patterns for different weather forcings (Chapter 6 Correction of the reference weather data to include the local UHI patterns (local scale)); The adaptation of the UHI adjusted hourly air temperature to account for the effect of the site specific generic morphology at street level at the neighbourhood scale (Chapter 6 Adaptation of the “localised” TMY data to include the effects of the site specific morphology (local scale + morphology = micro scale)).

Chapter 2 Scale and the Boundary Layer of cities

1. Scales of urban climatology

In urban climatology the reference scale sets the context for the prevalent physical phenomena and defines the horizontal extents and the vertical atmospheric levels of interest (Figure 2.1). Regardless of the scale the atmospheric layers are diabatic and in perpetual interaction. Weather events in the macro-scale will affect the weather conditions near the ground surface while a city can influence the weather development in the meso-scale level (Collier, 2006).

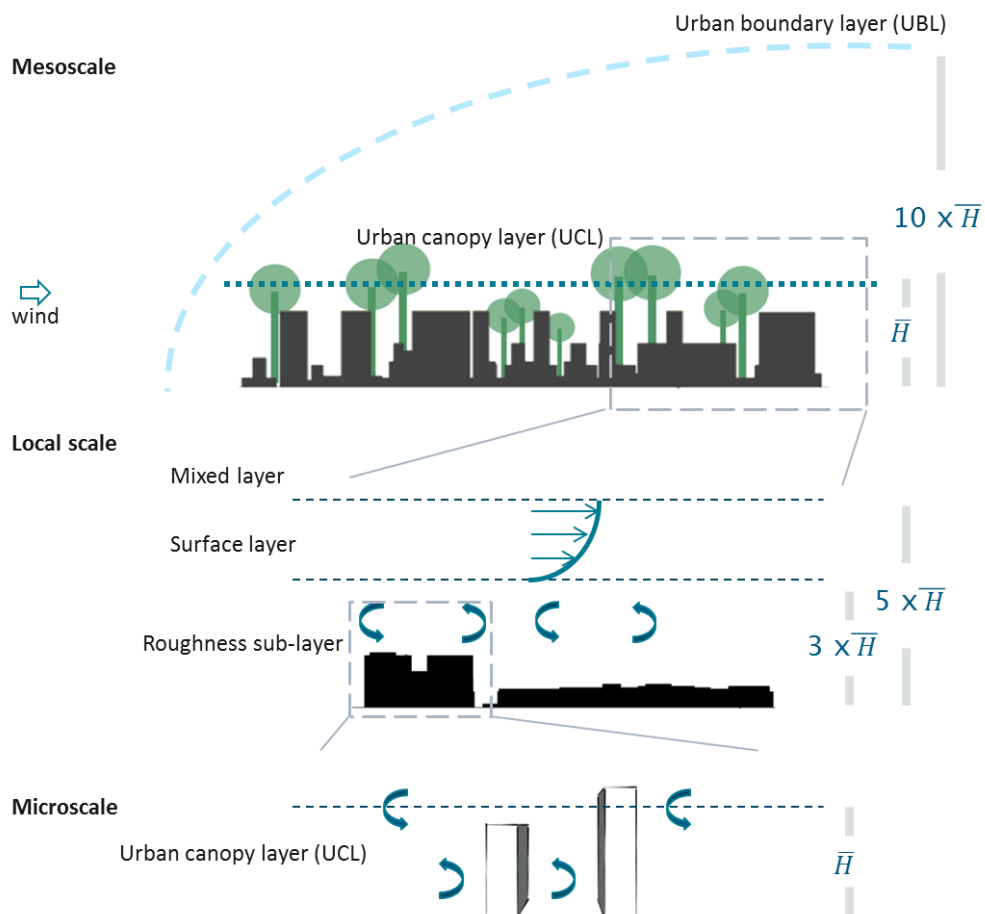


Figure 2.1. Vertical atmospheric layers in the context of the climatic scales. \bar{H} denotes the average building height. Image adapted from Oke (2006).

The size of an urban unit changes according to the scale of the horizontal and vertical atmospheric extent where the respective physical phenomena are in play. The

reference urban unit size in the *macro-scale* is a whole city including any built up surroundings and farmland. In this scale, weather modelling considers only the generic impact on the atmosphere from the land terrain that has been changed by human activity. Weather events relevant to the macro-scale develop with a time resolution of days up to weeks (Orlanski, 1975).

The *meso* (or *regional*) scale weather phenomena are influenced by the city and the anthropogenic processes in it. The effect of individual urban features cannot be distinguished. The impact of the city on this level of the atmosphere is represented with a single aggregated area average of the heat and momentum fluxes (Erell et al., 2011). Regarding the vertical extent in the meso-scale, a notional grid box would contain the urban boundary layer and any distinct internal boundary layers upwind and downwind of the city. The time scale of the weather development is in the range of a day or less (Orlanski, 1975). Most of the numerical weather forecasting models currently in use estimate the turbulent fluxes and wind field development on this scale.

The *local*-scale describes physical processes prevalent at horizontal distances from a few hundred metres to several kilometres. Typical urban units in this scale have the size of a neighbourhood and can reach the size of a town (Figure 2.1). At the local scale the effect of single urban elements is evident on the atmospheric processes. This is the reference scale for several existing energy balance models (Martilli et al., 2002; Dandou et al., 2005; Oleson et al., 2008; Grimmond et al., 2010; Loridan et al., 2010) that have been developed based on urban parameterisations in order to provide the lower boundary conditions for operational weather forecasting models (Baklanov et al., 2010).

The *micro-scale* has the highest horizontal spatial resolution with typical urban units in this context having an area of a single building and up to the area of several building blocks. The vertical layer where heat and momentum exchanges take place extends from the ground surface up to a level 2-3 times the average buildings' height (Grimmond & Oke, 2002; Erell et al., 2011).

This thesis approached the modelling of urban climate with a horizontal spatial resolution of 500m (i.e. diameter of the circular "urban unit model") in the micro to local-scale. In this scale domain, the processes of energy and mass transfer are extremely variable with time and space. It is suggested that this variability can be

hourly averaged across the total urban unit. The simulated weather development at street level has been related to the urban unit's generic morphology (through a local-scale surface classification scheme) and different regional (meso-scale) weather forcing (Erell & Williamson, 2006; Oke, 2006; Stewart et al., 2014).

2. Urban boundary layer

The urban elements exchange large amounts of energy with the adjacent air. Terrain and thermal heterogeneity cause changes to the surface roughness and the local specific temperature profiles. These changes result in the creation of internal boundary layers (Foken, 2008). The internal boundary layers extend as a plume in the local downwind direction; they merge and mix creating a region of high turbulence, large wind velocity and thermal gradient variation with time and space (Foken, 2008) (Figure 2.2).

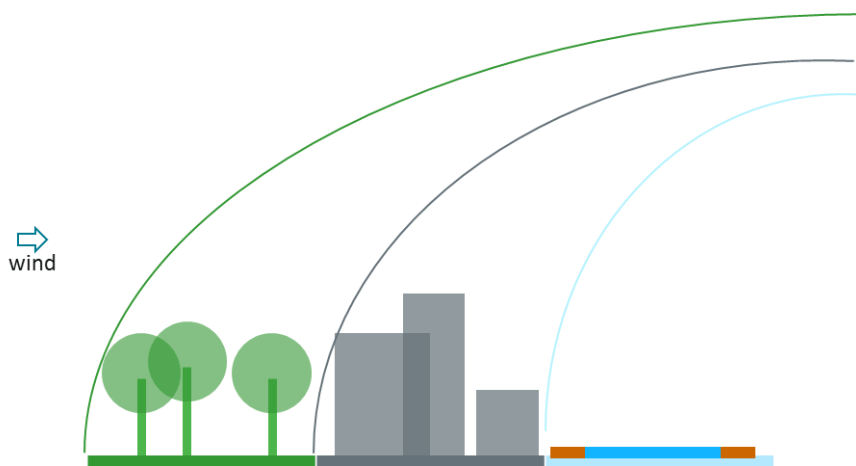


Figure 2.2. Formation of the “internal” boundary layer plumes of the different land surface types that contribute to the development of the overall urban boundary layer. Image adapted from Foken (2008).

The interaction between these successive internal boundary layer plumes form the urban boundary layer (Harman, 2003). The top of the urban boundary layer is approximately ten times the city's average height above ground (Erell et al., 2011). The magnitude, strength and shape of this disturbance field follow a highly variable diurnal profile (Piringer et al., 2007; Foken, 2008). This profile is shaped by the urban morphology and regional climatic factors (i.e. wind velocity, relative humidity, soil moisture) (Martilli, 2002; Rotach et al., 2005; Collier, 2006). Specifically, high wind

speeds during the day, delay the development and peak of the boundary layer's height. During the night, the stability of the incoming air to the urban environment's wind flow field affects the wind velocity within the urban boundary layer and the height and strength of the night time capping inversion (Martilli, 2002).

Different degrees of inertial and buoyant forces and heat fluxes govern the energy and mass transfers in the urban boundary layer (Arnfield, 2003). In general, the vertical structure of the urban boundary layer is distinguished by 3 regions/layers according to the energy and momentum flux gradients' change and the wind flow properties (Oke, 2006; Foken, 2008). These three layers are the Mixed layer (ML), the Surface layer or Inertial sub-layer (ISL) and the Roughness sub-layer (RSL) (Erell et al., 2011). The Urban Canopy layer (UCL) is the lowest part of the roughness sub-layer and the one where human activity takes place (Figure 2.1). The stratification of the boundary layer plays a significant role in the validity of key assumptions made by numerical weather prediction models and in the representativeness of urban weather observations (Foken, 2008).

2.1 Mixed layer

In rural environments during daytime, the incoming solar radiation increases the turbulent heat flux from the ground surface (Foken, 2008). Convective cells of warm buoyant air move with high vertical wind speeds through the atmosphere creating a well-mixed turbulent layer (Foken, 2008). The boundary layer stratification becomes unstable and the night time capping inversion is replaced by an entrainment zone (Foken, 2008). When solar radiation forcing is weak (i.e. cloudy days, winter) the boundary layer is less turbulent and more stable. On these days, the mixed layer's development might not destroy the residual night time layer above (Foken, 2008).

In urban boundary layers, the energy stored by the urban elements will delay the generation of the large convective cells during daytime. At night, the release of the stored energy back to the atmosphere and the anthropogenic heat emissions will increase the turbulence and the depth of the boundary layer (Collier, 2006). It remains unclear if this layer of the atmosphere develops into a mixed layer above urban terrain or if it retains a stable stratification (Rotach et al., 2005). Experimental findings suggest the conditional existence of strong "convective updraft - downdraft rolls" (Miao et al.,

2009). Collier (2006) argues that in urban sites, surface heterogeneity which leads to the development of the mixed layer, prevails over local scaling (significant above relatively homogenous areas) which promotes a stable stratification.

2.2 Inertial (surface) sub-layer

The development of the Inertial sub-layer relies on the sufficient fetch distance (downwind distance from a point of roughness or thermal change) that will allow the blending of the effects of individual urban elements on the atmosphere (Erell et al., 2011). There are two key assumptions common in urban canopy parameterisation models that are only met within the Inertial sub-layer; a) within this region the vertical mean flow follows a logarithmic profile and b) the turbulent fluxes are constant with height (Harman, 2003; Foken, 2008; Erell et al., 2011). The validity of these assumptions is very important because they make possible the estimation of sensible and latent heat fluxes and mean wind speeds (Erell et al., 2011).

The idea for the existence of a layer that has nearly constant neutral stability belongs to Monin and Obukhov. In the case of urban boundary layers, the only region where the Monin Obukhov Similarity Theory (MOST) is valid is the Inertial sub-layer (Foken, 2008; Yamada & Koike, 2011). MOST has been largely applied in meso-scale studies in order to represent the urban fluxes (Atkinson, 2003; Martilli, 2007; Baklanov et al., 2010). It is a scheme that allows the urban impact on wind flow (turbulent kinetic energy) to be represented with an urbanisation adjustment to roughness and to other surface characteristics (Mirzaei & Haghighat, 2010a). The Monin-Obukhov dimensional scales such as the friction velocity u_* (velocity scale) and the Obukhov length L (length scale) are incorporated into the description of the logarithmic wind profile (American Meteorological Society, 2013b).

Friction velocity, u_* , is defined by:

$$u_* = (\tau_0 / \rho)^{1/2} \quad (m\ s^{-1}) \quad (2.1)$$

While the Obukhov length, L , is given by (Harman, 2003):

$$L = \frac{-u_*^3}{\kappa(g/Ts)(H/\rho c_p)} \quad (m) \quad (2.2)$$

where τ_0 is the Reynolds stress, ρ is the density of air (kg m^{-3}), κ (≈ 0.4) is the von Kármán's constant, g is the gravitational acceleration, Ts is the area-averaged surface temperature (K), H is the area-averaged sensible heat flux (W m^{-2}) and c_p ($\text{J kg}^{-1} \text{K}^{-1}$) is the specific heat capacity of air at constant pressure.

For a rural terrain and unstable atmospheric conditions the Obukhov stability length can be rewritten as a function of sensible heat flux H (W m^{-2}) with the inclusion of the water vapour's effect (Brutsaert, 1982) :

$$L = \frac{-u_*^3 \rho}{\kappa g [(H/T_a c_p) + (0.61 E)]} \quad (m) \quad (2.3)$$

where T_a (K) is the mean air temperature near the surface and E is the actual evaporation rate (mm s^{-1}).

The Obukhov length is the height where the production ($L < 0$) or loss ($L > 0$) of turbulent kinetic energy (TKE) by buoyant forces becomes equal to the shear TKE production (Foken, 2008; Erell et al., 2011). A physical explanation of the Obukhov length is possible with the approximation of atmospheric stability. Negative length ($L < 0$) corresponds to unstable atmosphere, $L \rightarrow \infty$ corresponds to neutral stability and positive values ($L > 0$) correspond to stable atmospheric conditions (Erell et al., 2011).

The vertical logarithmic profile of the wind speed in height z (m) above ground within the inertial sub-layer and for atmospheric stability other than neutral reads as (Bitter & Hanna, 2003):

$$u_z = \frac{u_*}{\kappa} \left[\ln \left(\frac{z-d}{z_0} \right) - \psi_m \left(\frac{z}{L} \right) \right] \quad (m s) \quad (2.4)$$

ψ_m is a stability function for momentum and z_0 is the roughness length; a measure of surface roughness and the hypothetical height where the wind speed is equal to zero under the assumption that the logarithmic wind profile is extrapolated downwards into regions that this logarithmic relationship does not apply (Erell et al., 2011). The

zero-plane displacement d is a notional ground displacement due to the effect of urban geometry. It is an index of the vertical height where the mean drag force acts on an area-averaged surface. The roughness length z_0 is measured above that notional level (Erell et al., 2011).

Rotach (2001) noted that the existence of the surface layer depends on the characteristics of roughness elements and the boundary layer height, linking in that way the inertial sub-layer with the urban morphology. Despite the importance of the surface layer to boundary layer modelling and energy balance estimations, its existence is questioned (Cheng & Castro, 2002b; Flagg & Taylor, 2011). High roughness and thermal heterogeneity will prevent the development of the surface layer because they do not allow a sufficiently uniform fetch distance where blending can occur (Cheng & Castro, 2002a; Britter & Hanna, 2003).

2.3 Roughness sub-layer and the urban canopy layer

In comparison to the inertial sub-layer, the roughness sub-layer's depth is not affected by the wind direction or the existence of long enough horizontal distance downwind for the plumes to develop (Cheng & Castro, 2002b). This layer's depth is mostly a function of the surface roughness and the height of the urban elements. Typical depth values for the roughness sub-layer are in the range of 1.85 to 3 times the average height of the roughness elements (Roth, 2000; Cheng & Castro, 2002b).

The lowest part of the roughness sub-layer in urban climatology is usually referred to as the urban canopy layer. The urban canopy layer extends to a height up to the average building's height. One of its significant characteristics is the existence of strong shear at the level of buildings' roof tops or directly above where turbulence production takes place (Harman, 2003; Hamlyn & Britter, 2005). The wind field inside the urban canopy layer is composed of the wakes and plumes from individual urban elements with zones of recirculation, pressure differences along the urban elements and vortex formation in the space between them (Britter & Hanna, 2003; Hamlyn & Britter, 2005; Erell et al., 2011).

A primary qualitative analysis distinguishes the wind flow field with respect to the aspect ratio of the height (H) of the buildings to the width (w) of the space between them into three prevalent patterns (Figure 2.3). The first regime, known as

the *isolated roughness flow* has been observed for H/w aspect ratios ≤ 0.5 (Oke, 1987). The isolated flow regime is characterised by low wind velocities close to the ground, regions of air recirculation and down-flow into the street of the air above the street canyon (Erell et al., 2011) (Figure 2.3).

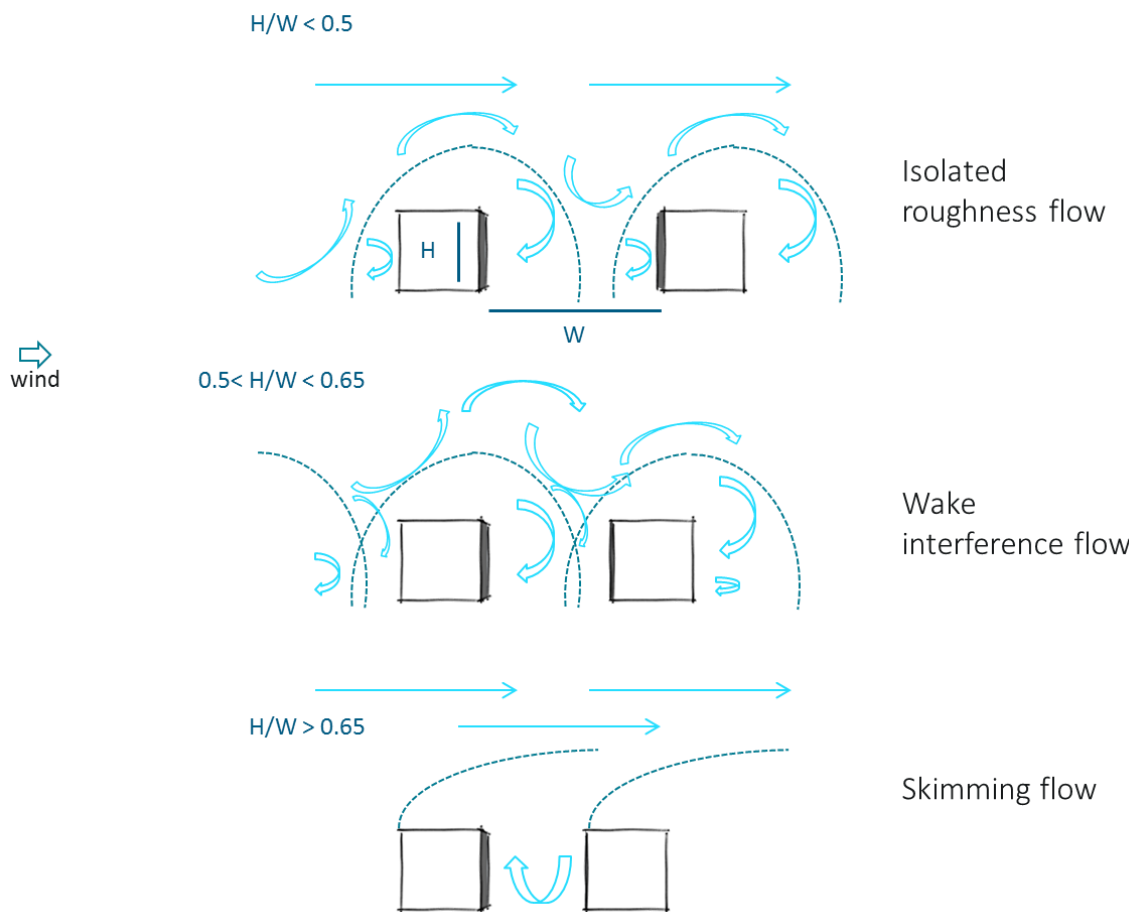


Figure 2.3. Wind flow patterns associated with urban morphology as depicted by the H/W aspect ratio. Top: Isolated roughness flow, Middle: Wake interference flow and Bottom: Skimming flow. Source: Oke (1987), Image adapted from Erell et al. (2011).

In urban settings with H/w aspect ratios $0.5 < (H/w) < 0.65$, the *wake interference regime* denotes a wind flow state of high turbulence. The eddies formed inside the street canyon are reinforced due to the interference of the wakes from the urban elements downwind (Erell et al., 2011).

Lastly, *skimming flow* applies to very dense morphology with H/w aspect ratios greater than 0.65. The main air flow remains above the buildings' rooftops level and there is only one circulatory vortex formed inside the street canyon as a result of the momentum exchange (Erell et al., 2011).

3. Urban energy balance

The weather development in the micro-scale is considered to be the outcome of continuous interactions between the energy fluxes that are regulated by the surface geometry, the elements' physical properties and incoming energy levels (Arnfield, 2003). The 'urban energy budget' was initially proposed by Oke (1982) in an attempt to study and explain the variation in urban temperature with time and space in order to study the urban heat island (UHI) and its diurnal development.

The urban heat island describes the tendency of the urban surface and air within the urban canopy to be warmer on average (colder in some cases, e.g. cities in desert environment) than the immediate rural (reference) surroundings (Oke, 1973). The urban heat island exhibits a diurnal and a seasonal cycle (Yongzhu et al., 2010). Diurnal fluctuation is mainly governed by the solar radiation and the capacity of the urban fabric to reflect, store and re-emit it (Coutts et al., 2007). Seasonal changes are better explained by the impact of regional climatic factors (such as wind velocity, cloud cover and hours of daylight) (Oke, 1982).

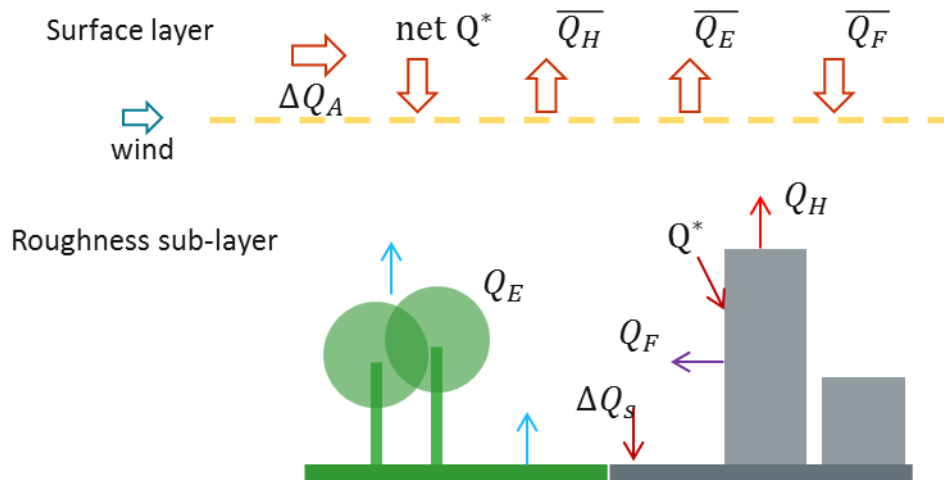


Figure 2.4. The heat fluxes at different urban atmospheric layers. Q_F (purple arrow) denotes the anthropogenic heat flux, Q_E is the latent heat flux (blue arrow), Q^* denotes the solar radiation balance, Q_H is the sensible heat flux and ΔQ_s the net energy stored in the surface. ΔQ_A is the net energy from advection. Overbars denote the spatial average of the fluxes. Image adapted from Pearlmutter et al. (2007).

Urban surface is closely related to the development of turbulence and the mean wind profile in the urban boundary layer (Raupach, 2001). Atmospheric stability and the turbulence profile affect the intensity of heat and moisture exchange between

the elements' surfaces and the atmosphere (Raupach, 2001; Harman, 2003; Barlow et al., 2004) (Figure 2.4). The energy exchange between the surfaces and the air in the urban canopy layer can be considered through a volumetric averaging approach (Oke (1988) cited in (Arnfield, 2003)) (Figure 2.4). The rural surface energy balance (SEB) is adapted to the urban setting; (1) with the addition of a term, Q_F , for the heat from anthropogenic activities (including heat losses from buildings), (2) the account of net heat storage, ΔQ_S , in the ground surface and buildings and (3) the net horizontal transfer of heat due to air movement, ΔQ_A , (advection – advective flux) through the vertical boundaries of a notional air volume ($W m^{-2}$) (Harman, 2003) (Eq. 2.5).

$$Q^* + Q_F = Q_H + Q_E + \Delta Q_S + \Delta Q_A \quad (W m^{-2}) \quad (2.5)$$

where Q^* is the net solar radiation at ground surface ($W m^{-2}$), Q_H is the sensible heat flux ($W m^{-2}$) and Q_E is the latent heat flux (evapotranspiration) ($W m^{-2}$).

The largest part of the advective heat flux, ΔQ_A , takes place over the urban canopy layer where the wind flow is less obstructed and wind speeds are higher (Santamouris et al., 2008). In dense urban canopies heat and momentum transfer by advection is mainly diminished due to wind obstruction by buildings and the uniformity in building density with the surrounding areas (Santamouris, 2001b). That uniformity implies similar temperature and pressure conditions across and outside the notional air volume's borders which neutralise any horizontal mass transfer processes. However, micro-scale advection remains significant in the case of urban sites bordering parks, large open spaces, built-up areas of lower density and rural sites (Santamouris, 2001b; Arnfield, 2003).

3.1 Role of the energy balance in diurnal building energy consumption

The energy balance has a diurnal and a seasonal profile that is directly associated with the local specific morphology and the properties of urban elements. Soil moisture, water vapour and cloud cover can offset maximum temperature values by stirring the energy partitioning towards strong latent heat flux that will consequently decrease the sensible heat flux (Kassomenos & Katsoulis, 2006; Papangelis et al., 2012). The amount and types of vegetation can reduce the incoming solar radiation that reaches the solid

surface (walls, streets) and enhance the latent heat flux due to plant transpiration (Memon et al., 2008; Bowler et al., 2010).

High albedo values correspond to high solar reflectivity from the urban canopy which decreases the amount of solar radiation input. As a result, there is less energy input to the balance and all the local energy fluxes will be smaller. High wind speeds in the urban canopy layer strengthen the air mixing and the convective heat exchanges between air and urban surfaces (Morris et al., 2001). The heat storage in the urban canopy and the rate of convective cooling during night are correlated with the height to width (H/w) aspect ratio and the sky view factor (Yang et al., 2010). The increase of an urban canyon's aspect ratio is followed by a decrease of convective heat exchanges. However, increasing levels of street shadowing due to high H/w aspect ratios in combination with high surface albedos can improve pedestrian thermal comfort and the buildings' cooling potential during daytime (Santamouris, 2001b). At night, high urban densities which result in low street sky view factors are associated with excessive heat entrapment within the urban canopy and restricted surface cooling through radiative heat exchange with the atmosphere. This radiation entrapment effectively is an increase of the net radiation in the urban energy balance (Johansson, 2006).

Trapped heat in the urban canopy layer affects the air stratification while the wind flow in the street canyons is usually disconnected from the wind flow above the rooftops (Memon et al., 2010). Vehicular heat emissions, building thermal losses and heat rejected from building service systems can contribute to the development of heat stress conditions and increase the cooling loads of buildings (Santamouris, 2001a). In addition, the heat rejected by building mounted air conditioning units can cause an increase in air temperature close to the building surface that will subsequently deteriorate their performance (Papadopoulos, 2001). Nevertheless, the significance of the anthropogenic heat flux is often greater in winter when the heat flow from anthropogenic activities can be 2 to 25 times larger than the incoming solar radiation (Offerle et al., 2006; Hamilton et al., 2009).

The seasonal variation of the sensible heat flux Q_H follows the net solar radiation profile for the largest period of the year (Offerle et al., 2006). However the seasonality in energy fluxes is not always obvious in places with significant solar radiation intensity and dry conditions (Loridan & Grimmond, 2011). The seasonal

effect of vegetation on the energy balance can be represented by the Bowen ratio, which is the ratio of sensible Q_H to latent Q_E heat flux (Grimmond & Oke, 2002). The Bowen ratio is higher in urban sites with limited vegetation and limited permeable surface area. In this case, the sensible heat flux remains positive (i.e. energy transfer from surface to atmosphere) for longer than in rural sites and even after sunset (Grimmond & Oke, 2002).

4. Micro-climate in the urban unit context

In this thesis the terms ‘urban element’, ‘urban geometry’, ‘urban morphology’ and ‘urban configuration’ are specifically used to denote certain aspects of the surface layout and its characteristics (Figure 2.5). The urban elements are the structural units of the urban environment. Their geometry defines the morphological characteristics. The combination of elements in different quantities and forms creates distinctive layouts that are described under the general loose term of urban configurations.

Urban element is used to describe the different parts of the urban environment and can be reduced to the structures that form the surface cover (e.g. buildings, trees and river).

Urban geometry denotes the geometrical attributes of the elements (e.g. height) and the space formed between them, as for example the height of the different elements and the width of a street (Harman, 2003).

Urban morphology is used to denote the form of the space as a whole and it is directly associated with the segregation of space and the effect of aggregate geometry characteristics on wind flow, heat and momentum fluxes.

Urban configuration is any urban layout that results from the arrangement of elements in different forms and combinations.

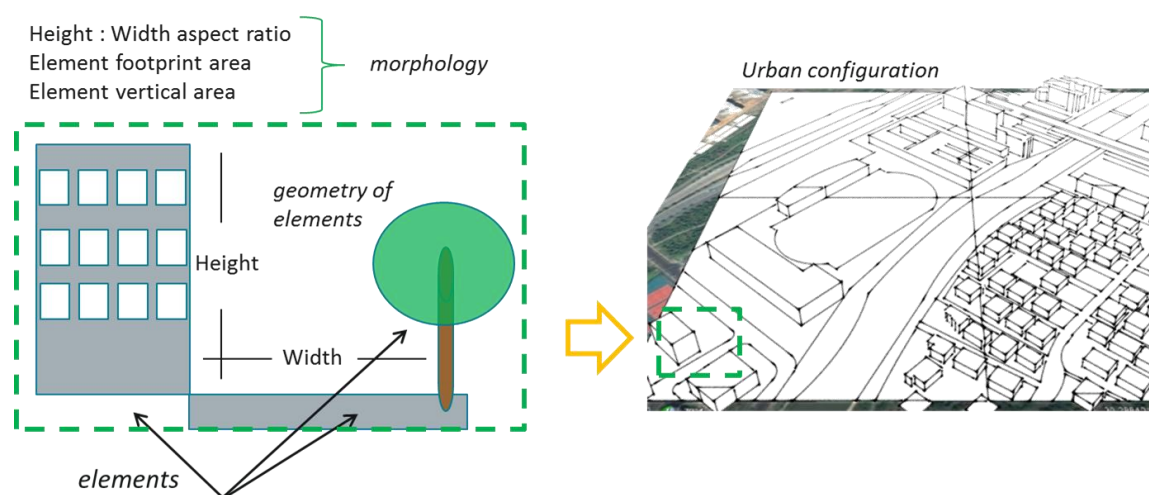


Figure 2.5. Composition of an urban unit and its relationship to urban configuration.

The development of micro-climatic conditions will be different in each urban configuration. This is the issue this thesis looks to address. The surface energy balance is responsible for the development of the weather conditions within the urban canopy layer (i.e. the lowest part of the urban boundary layer that extends up to the average building height). Subsequently, the urban micro-climate can be defined as the long term (a few hours in relation to weather in the micro-scale) area-averaged effect of the urban energy balance on a finite air volume that encloses and is contained by the generic urban unit of interest.

Existing qualitative models for the air flow and the energy balance in the urban canopy layer are mainly based on experimental observations and numerical simulations. In these models, surface morphology has been typically represented with an urban canyon approximation (Figure 2.6) (Pearlmutter et al., 1999; Georgakis & Santamouris, 2008) and three dimensional cubes in regular (cube dimensions equal to their separation) or staggered arrays (Cheng & Castro, 2002b; Martilli & Santiago, 2007; Santiago et al., 2007). Nevertheless, the results cannot be generalised for real city layouts with an unstable atmosphere (Martilli & Santiago, 2007). It still remains unclear what the minimum surface morphology and geometry configuration requirements are in order to approximate reality with acceptable accuracy when using a model (Martilli, 2007; Baklanov et al., 2009; Grimmond et al., 2010).

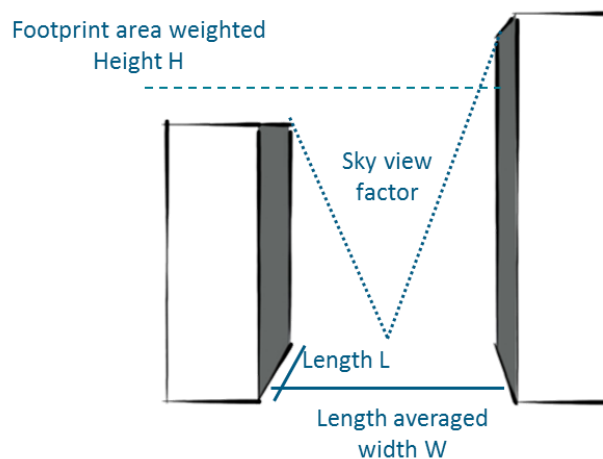


Figure 2.6. The urban street canyon and its main geometrical characteristics. \bar{H} is the building footprint-area-weighted height, L is the length of the canyon and W is the length averaged width. Image adapted from Erell et al. (2011).

The selection of a generic urban unit is dictated by the scale and the purpose of the study (Erell et al., 2011). The urban street canyon has been extensively used as the

urban morphological unit in several studies covering a variety of research fields from the estimation of urban energy fluxes to the simulation of air conditioning loads (Pearlmutter et al., 1999; Kusaka et al., 2001; Papadopoulos, 2001). It is defined by the buildings' vertical boundaries to the street and the linear space lying between them (Figure 2.6).

Two characteristic urban geometry features of street canyons are the height (H) of the vertical faces of the urban elements and the width (W) of the space between them. The aspect ratio for the canyon is defined as the ratio of the bordering buildings footprint averaged Height (H) to the length averaged distance (w) spacing them apart. Different urban geometries can be represented by the height to width (H/w) aspect ratio (AR) and the sky view factor (SVF) where SVF is an index (0 to 1) of the unobstructed sky area which can be seen from a given point in an urban street canyon (Figure 2.6). The geometry of the street canyon can affect the thermal comfort and building cooling potential during daytime (Santamouris, 2001b), the intensity of convective fluxes that can cool down the surface during night (Johansson, 2006), the diurnal air temperature change (Memon et al., 2009) and the air stratification inside the urban canopy (Memon et al., 2010).

In practice it is difficult to build street canyon geometry models representative of complex urban geometry (Bohnenstengel et al., 2011). In addition, surface energy fluxes are likely to have a larger footprint area than a single canyon's area and they cannot be realistically estimated with the geometrical characteristics of street canyons (Oke, 2006; Bohnenstengel et al., 2011).

An urban unit in the neighbourhood scale is selected as more appropriate for the objectives of this study. At this scale, the energy fluxes are described with morphological parameters relevant to the total surface area. The model grid box is defined as the space enclosed by a grid box with a circular base area equal to $\sim 200,000 \text{ m}^2$ ($\pi \times r^2 = \pi \times 250^2 \text{ m}^2$) (see Chapter 4.7 *Selection of a generic urban unit*) and height equal to 3 times the mean building height weighted for the building footprint area (Figure 2.7). The selection and characteristics of the urban unit are described in detail in 'Chapter 4. Selection of a generic urban unit'. The urban morphology in each grid box is commonly parameterised with the use of indices based on the geometrical attributes of any urban configuration. The planar area, λ_p , is an index of the proportion of the total area which is covered by the main elements that cause roughness to the

air flow (i.e. buildings) (Grimmond & Oke, 1999). The planar area index is estimated in this study as the ratio of the buildings' (large man made constructions such as telecommunication towers included) floor area to the total urban unit area.

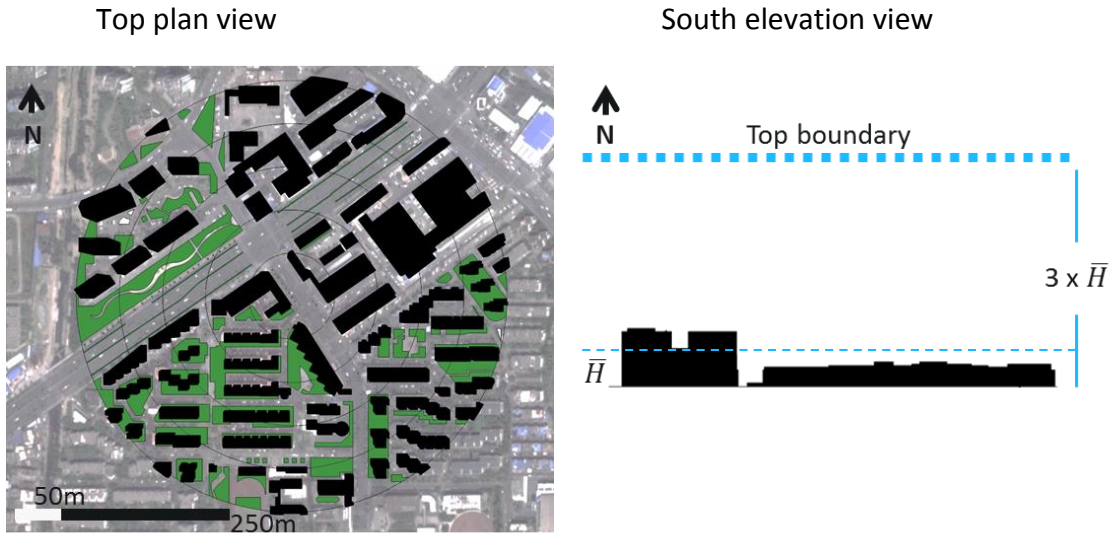


Figure 2.7. Depiction of a generic urban unit in Hangzhou, China as selected for analysis in this study (left). The circular footprint is about 200,000 m², the radius is $r=250$ m and the height is adjusted to the building footprint-area-weighted height \bar{H} (right).

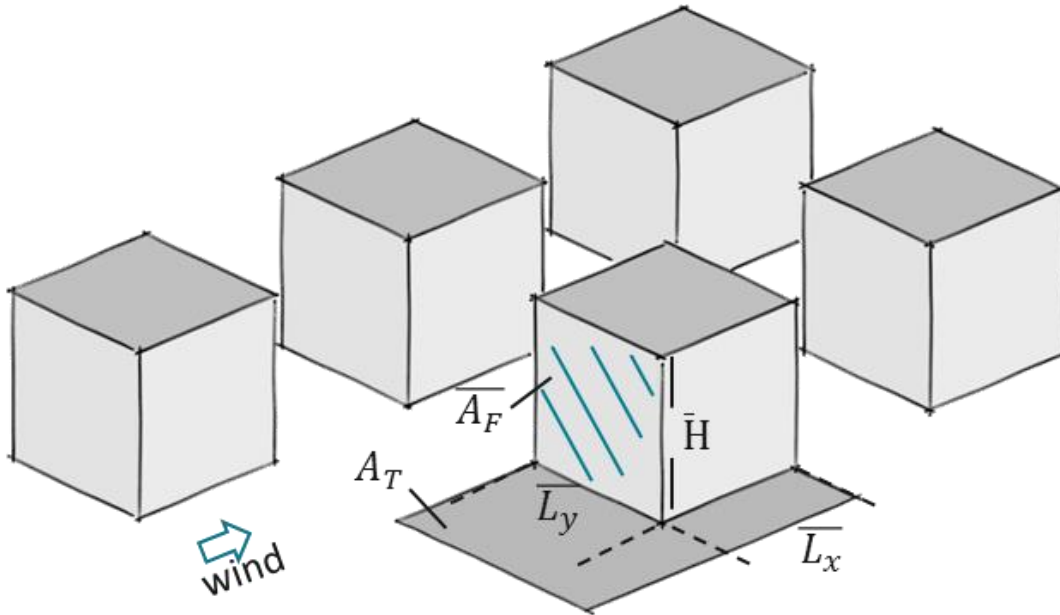


Figure 2.8. Description of the main morphological parameters. \bar{A}_F marks the grid block's averaged area perpendicular to the wind, \bar{A}_T is the total grid box area, \bar{H} is the building footprint-area-weighted height and \bar{L}_x and \bar{L}_y are the mean length and width of the buildings in a grid box respectively. Image adapted from Grimmond et al. (2010).

Pedestrian walks, trees, short vegetation and other small roughness elements have not been incorporated in the estimation of λ_p . If $\overline{L_x}$ and $\overline{L_y}$ are the mean length and width of the buildings in a grid box respectively, the planar area index λ_p is simply $\overline{L_x L_y} / A_T$ (Bohnenstengel et al., 2011) (Figure 2.8). The frontal area index λ_f is the ratio of the total building surface projection on a vertical plane perpendicular to the wind flow to the total area for each wind direction. It can be written as $\lambda_f = \overline{A_F} / \overline{A_T} = \overline{H L_y} / \overline{A_T}$ where $\overline{A_F}$ is the grid block's averaged area perpendicular to the wind, and \overline{H} is the average height of the surface area perpendicular to the wind flow (Figure 2.8). The grid block's averaged area perpendicular to the wind $\overline{A_F}$ is defined according to the wind's direction.

One of the hypothesis of this work is that a local scale land cover classification based on common urban morphometric parameters can be directly associated with typical micro-climatic development patterns (see Chapter 6 *Urban weather projections*). The challenge is to estimate and aggregate the “micro-weather” conditions which are highly variable with time (Bouyer et al., 2011).

Chapter 3 Micro-climate modelling

1. Micro-scale weather models

Micro-scale weather models are divided into numerical, analytical and empirical according to the approximations they follow for the description of the physical processes inside the urban canopy layer. Each modelling category has different requirements for representing the urban surface and setting up the initial and boundary conditions.

1.1 Numerical weather prediction models

In recent approaches related to engineering practice the urban boundary layer is modelled with the use of computational fluid dynamics (CFD) models (Flagg & Taylor, 2011). CFD models resolve the wind flow and turbulence (directly or statistically) with very high spatial and time resolution (Sanderse et al., 2011). The impact of urban geometry and vegetation on turbulent kinetic energy and the energy exchanges between the surface and the atmosphere can be parameterised and integrated into these models in the form of source and sink terms (Bruse & Fleer, 1998).

CFD models have been extensively used across a range of studies (Figure 3.1) looking at air pollution dispersion in streets (Li et al., 2006; Baik et al., 2009), natural ventilation assessment of buildings (Cheung & Liu, 2011; Ramponi & Blocken, 2012) and pedestrian thermal comfort (Huang et al., 2005; Mochida & Lun, 2008; Mirzaei & Haghighat, 2010b). Bouyer et al. (2011) established a CFD - Building energy simulation coupling procedure on a single simulation platform to assess the impact of the micro-climate on the thermal simulation of buildings. The results indicate improvements in the estimation of the heat gains, the convective heat fluxes and moisture transport (Bouyer et al., 2011). In an urban design application, Gaitani et al. (2011) coupled a CFD model with thermal simulation software to suggest micro-climatic improvements on a city square with inhomogeneous wind profile and high air temperature.

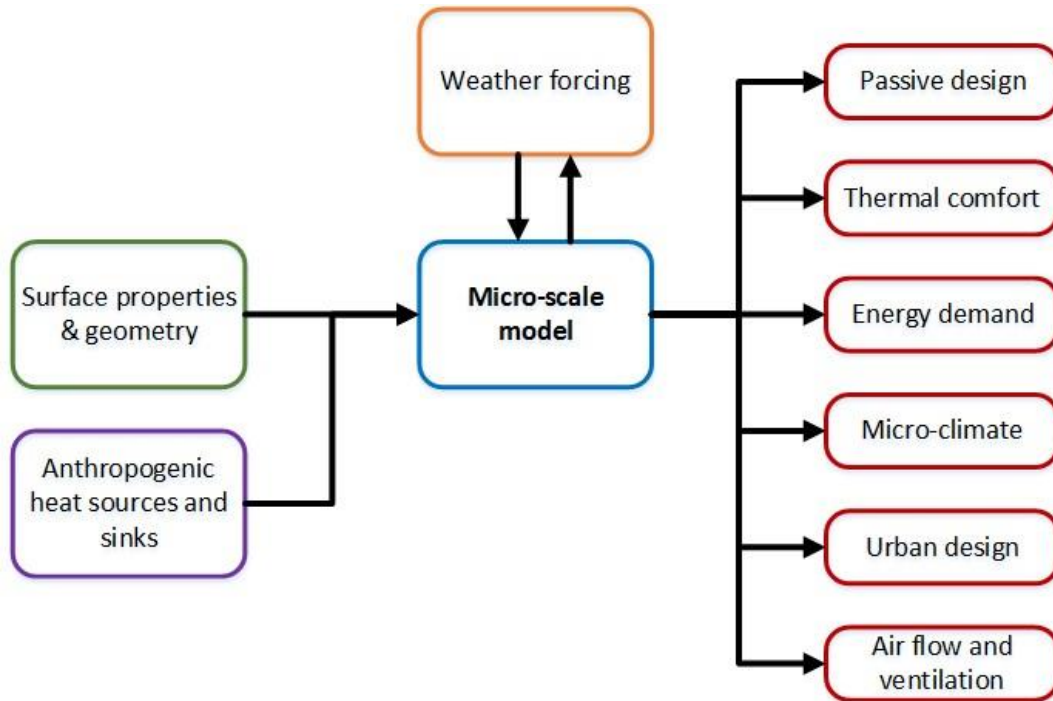


Figure 3.1. Function and applications of micro-scale models.

The applications with the biggest relevance to this study come from the urban heat island research. Ashie and Kono (2011) used a Reynolds Averaged Navier-Stokes (RANS) model with an horizontal computational grid resolution of 5m in their simulation study. The simulation results suggest that the urban air temperature is positively correlated with building density while on the other hand the wind speed is negatively correlated with air temperature and consequently with building density (Ashie & Kono, 2011). The Urban Canyon model (de la Flor & Domínguez, 2004) estimates the heat fluxes and the air temperature distribution in an urban street canyon configuration. It introduces a zonal model that divides the air volume between the buildings into cells where the heat and mass balance can be estimated for each cell (de la Flor & Domínguez, 2004). The results have been used to introduce the climatic severity index (CSI) that can assess the impact of the street canyon morphology on the heating and cooling demands of locally based buildings (de la Flor & Domínguez, 2004).

In a very interesting development, meso-scale weather forecasting and CFD models were coupled in order to predict the micro-scale weather development in wind farms and urban environments (Chen et al., 2011; Yamada & Koike, 2011). In those coupling schemes, the numerical weather prediction models were downscaled in order

to provide the initial and boundary conditions for the micro-scale models (Tewari et al., 2010) (Figure 3.2).

Meso-scale weather prediction models (e.g. WRF, MEMO, COAMPS) can resolve the wind flow and energy conservation equations (COMET® Cooperative Program for Operational Meteorology Education and Training, 2002) at typical horizontal resolutions of ~1km (Baklanov et al., 2009). The lower atmospheric level of these models ranges between 200m and 2km height above ground (Mirzaei & Haghighat, 2010a) (Figure 3.2). The initialisation of the meso-scale models requires large datasets to set up the initial and boundary conditions that are usually available only to specialists and to meteorological offices. Otherwise, the existence of a fully developed inertial sub-layer is assumed (Chapter 2, Section 2.2) which facilitates the application of a logarithmic wind profile at this layer, with stable wind speed forcing used at the boundary layer's borders (Yamada & Koike, 2011). The results from meso-scale weather prediction models are sensitive to the land surface type at the bottom boundary and to the scale of the surface terrain representation (Flagg & Taylor, 2011).

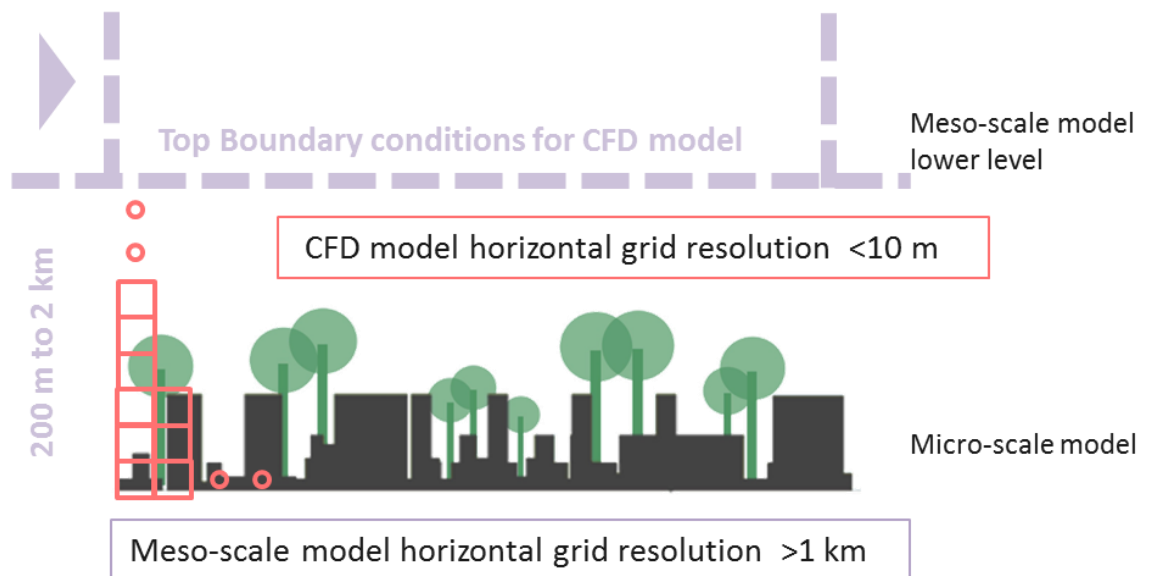


Figure 3.2. Computational grid resolution comparison between meso- (purple) and micro- (orange) scale models.

Despite the benefits from coupling meso- to micro-scale models, the differences in the horizontal and vertical scales and the time resolution between these models pose a challenge to their widespread successful application. The grid size differences and sub-scale grid implications regarding the physical processes at play are often a threat to the analysis of the results and their correct physical interpretation (Schlünzen,

2010). In addition, numerical models are computationally demanding in terms of both power and time. Therefore, their use in micro-scale modelling is usually restricted to small domains and relatively simple geometries (Baklanov et al., 2010).

1.2 Analytical urban canopy models

A more common approach is the coupling of numerical weather prediction models with analytical micro-scale models. The analytical urban canopy models estimate the energy balance development and momentum transfer in relation to the urban canopy's morphology and produce single area-averaged values in order to be used as forcing in the scale (typically meso) that the weather prediction model resolves (Martilli & Santiago, 2007).

The sensitivity of numerical weather prediction models to the surface representation led to the development of urban canopy parameterisations (UCP) with different surface geometry characteristics and different approaches to energy flux modelling (Grimmond et al., 2010). In general, UCP schemes are categorised into bulk, single and multilayer models according to the levels of interactions in the solution of the energy budget (Souch & Grimmond, 2006; Grimmond et al., 2011) (Figure 3.3). Bulk (slab approach) schemes require the smallest input and their function is based on the adaptation of the surface's roughness length, moisture availability, albedo and drag coefficient to represent the urban characteristics (Best, 1998; Taha et al., 1999; Best, 2005; Dandou et al., 2005). However, bulk models fail to represent three-dimensional properties of the urban elements such as the heat storage, the differential heating of wall and street surfaces and their effect on wind flow (Salamanca et al., 2011). In order to address these issues, a single layer model with three distinct surfaces has been proposed by Kusaka et al. (2001) that includes the diurnal variation in shading. The Town Energy Balance (TEB), a single layer model, introduced for the same purpose a street canyon geometry with three distinct surfaces (i.e. roof, wall, floor) that resolve the energy budgets with respect to each surface type (Masson, 2000; Masson et al., 2002).

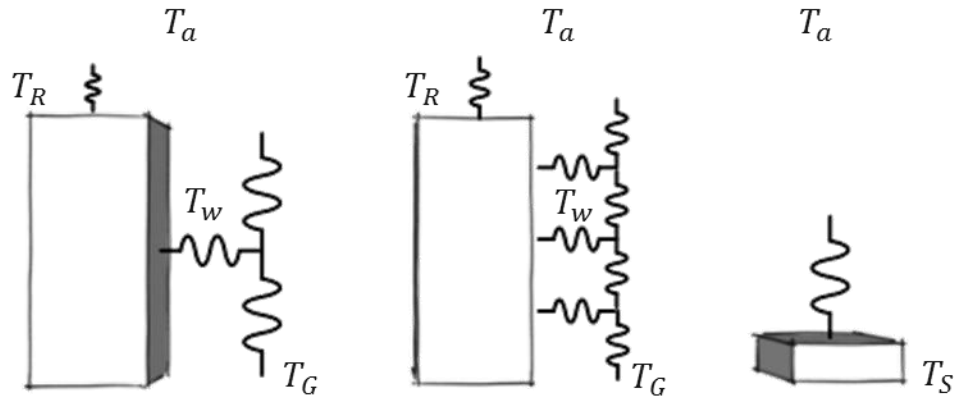


Figure 3.3. Network resistance model for single layer (left), multilayer (middle) and slab (right) urban canopy parameterisation schemes. T_a is the air temperature, T_R is the roof temperature, T_w , T_G and T_S are the wall, ground surface and slab surface temperatures respectively. Image adapted from Kusaka and Kimura (2004).

The number of layers in each model denotes the vertical atmospheric level where the mean thermal fluxes and the turbulent kinetic energy (TKE) profile are estimated (Dupont et al., 2004) (Figure 3.3). Single layer schemes usually model the turbulent kinetic energy production and dissipation with a roughness approach by adopting the Monin-Obukhov Similarity Theory (MOST) (Dupont et al., 2004). MOST permits the representation of urban surfaces with roughness length, an initial temperature and a surface moisture value for each grid cell (Martilli et al., 2002). In this case, the model's lowest level is above the top height of the canopy layer and within the surface layer (Figure 3.4).

Conversely, multilayer models are most likely following a drag force approach where the lowest level of the models is at ground level, inside the urban canopy layer (Martilli et al., 2002; Dupont et al., 2004; Kondo et al., 2005) (Figure 3.4). In the drag force approach, the drag of the urban elements on the wind flow is incorporated into the energy transfer equations with the addition of a sink term for momentum and a source term for the turbulent kinetic energy (Dupont et al., 2004; Martilli, 2007). The surface energy balance can be resolved for each surface (or any parts of it) (Masson, 2006). The added complexity makes the coupling of these models with meso-scale models more difficult and they are more computationally intensive than the single layer schemes (Masson, 2006).

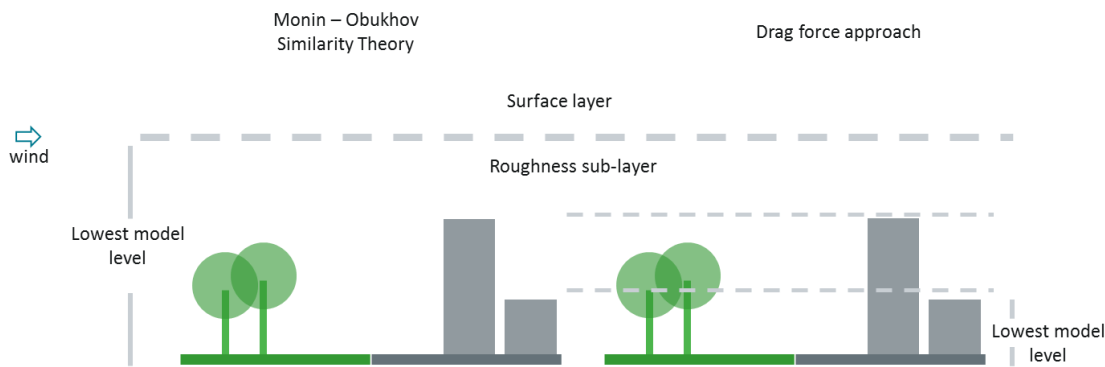


Figure 3.4. The models' lowest level for urban canopy parameterisations according to their turbulence modelling approach. Levels are shown with grey dashed lines. Image adapted from Chen et al. (2011).

The Building Effect Parameterisation scheme (BEP) introduced a further advancement in the form of a hybrid drag approach (Martilli et al., 2002). According to this hybrid approach, any source and sink terms of turbulent kinetic energy and momentum are vertically distributed across the model's vertical layers (Martilli et al., 2002; Salamanca et al., 2011). In addition, BEP takes into account the variation in building heights by assigning a probability of building height to grid cells according to an urban classification of the cells in the model (Martilli et al., 2002). In a similar approach, the Simple Urban energy balance Model for Meso-scale simulations (SUMM) estimates a theoretical value for the heat transfer coefficient in the surface layer by using the Monin-Obukhov similarity theory and in a second step distributes individual values into six surface types (i.e. roof, floor and four vertical walls) in a block array (Kanda et al., 2005).

Most of the urban canopy models reviewed above can be used in stand-alone mode (i.e. not integrated into a weather prediction model). The Surface Urban Energy and Water balance Scheme (SUEWS) (Järvi et al., 2011) is an extensive energy balance model that requires common surface morphology parameters and weather forcing data in order to estimate the surface temperature, energy storage, sensible and latent heat fluxes. It accounts for the effects of soil moisture and vegetation and it can estimate the water run-off and the evaporation along with other parameters such as the surface and aerodynamic resistances (Järvi et al., 2011). Despite its simplicity, the weather data forcing requires knowledge of air temperature, wind speed and incoming shortwave solar radiation in the surface layer while the area-averaged output applies at the same level, well above the urban canopy layer. The derivation of air

temperature from surface temperatures inside the urban canopy layer would be possible only if the wind speed profile near the surfaces or the surface convective heat exchange coefficients were known (Erell & Williamson, 2006; Offerle et al., 2007).

Regarding the application of bulk and single layer urban canopy models in this study, there is an additional difficulty in the validation of the results with real meteorological observations. It is well established that weather observations at urban sites should be made at a sufficient height (in the surface layer) in order to avoid the “noise” in the observations from the impact of individual elements (Rotach et al., 2005; Oke, 2006). However, practical implications such as the height of the measurement masts indicate that the meteorological data collected during field measurements are in several cases from the roughness sub-layer and not the surface layer (Cheng & Castro, 2002b). This is also the case for some of the data collected from Chinese cities used in this study.

Relevant to this thesis, TEB and an integrated building energy model have been coupled with other schemes (i.e. rural station, vertical diffusion and urban boundary layer model) and they have been used for the adaptation of rural air temperature and relative humidity hourly values to the urban heat island effect (Bueno et al., 2012). The so-called Urban Weather Generator requires a large number of initial parameters that vary from construction elements properties and characteristics (e.g. albedo and initial temperature) to the urban (e.g. façade to site ratio) and reference rural site morphology (Ramamurthy et al., 2014; Massachusetts Institute of Technology, 2015). The land cover analysis for the creation of the simplified “urban unit model” can provide most of the required parameters for the initialisation of the Urban Weather Generator. The use of the 3D “urban unit model” in numerical simulation modelling was chosen instead as it can provide an approximation of the vertical development of air temperature and relative humidity in the roughness sublayer and it can capture the majority of the transient physical processes at street level.

With a similar approach to the Urban Weather Generator, the Canyon Air Temperature (CAT) model can modify reference rural (i.e. fields outside the main city, airports inclusive) air temperature data for the local specific weather conditions in the urban canopy layer (Erell & Williamson, 2006). The CAT model is based on the assumption that the temperature of two sites located within the same meso-scale region (i.e. inside the city and its immediate rural surroundings), will be an aggregation

of a shared common background temperature (i.e. a common temperature in the absence of any urban features) and the effect of the site specific morphology on this temperature (Erell & Williamson, 2006). The concept of the common meso-scale initial background temperature implies that the model is not valid in the case of proximity to large water bodies or mountainous areas (Erell & Williamson, 2006). In addition, the simplicity of the model is largely attributed to several empirical parameters which were calibrated with observations from the same region as the validation dataset in Adelaide, Australia. The generality and transferability of the model results have to be further examined in order to conclude its wider applicability (Erell & Williamson, 2006). The methodology introduced in this work is using considerable less data than the CAT model as input. In addition the data required for the creation of the “urban unit model” can be easily acquired by remote sensing observations and online resources. Another difference between the two models is that this work suggests a method for the adaptation of typical meteorological year simulation-ready data files. Finally, CAT is an analytical model that solves the energy balance for the surfaces in an urban canyon and it has not been tested at urban canyons with surface and morphology characteristics different to these found in Adelaide, Australia (Erell & Williamson, 2006).

1.3 Empirical urban canopy models

Field observations and experimental measurements have been used by various researchers in order to create algorithms for the adaptation of weather data to local specific morphologies (Kolokotroni et al., 2007; Jusuf, 2009). In Hong Kong, urban heat island intensity observations were used in order to adapt a weather data file and use it in cooling load simulations (Chan, 2011). In a field study, Wong et al. (2011) pointed out that density, the ratio of building height to building footprint area and especially the green surface area (vegetation) can substantially influence the development of the micro-climate. Summertime temperature observations in London suggest additional correlations of UHI intensity with the distance from a thermal hotspot and wind direction (Watkins et al., 2002). More recently, a model was introduced for the estimation of the UHI intensity in urban centres and the modification of weather data files in the UK (Kershaw et al., 2010). This model is based on the statistical analysis of

temperature data from UK based weather stations from the period 1961 to 2006. The urban thermal centres were defined by assigning thresholds to predefined urban fraction parameters for each UK grid cell and its surroundings (Kershaw et al., 2010). The urban fraction limits were calibrated with visual inspection of the fit of calculated ranges for the urban fraction parameters to real UK cities (Kershaw et al., 2010). Therefore, in order to apply this methodology in places other than the UK, this method should be repeated for similar or equivalent local land cover types and temperature data spatial resolution under the same baseline assumptions of urban fraction limits.

Empirical models have limited universal applicability and the reliability of their results is usually a derivative of the data collection methods and duration. Field studies are an excellent data source for successful verification and validation of simulation studies both by comparing the simulation results with the in situ observations and by correctly interpreting different model functions.

This study departs from empirical models in order to increase scientific understanding regarding the capabilities of micro-scale models and the generalisation of their results for urban classes with different morphology. The novel “urban unit model” was implemented into micro-climatic simulations using a Computational Fluid Dynamics – Surface Energy Balance analysis tool (ENVI-met, Version 4). Empirical observations were used for the initialisation and the validation of the simulations at different stages of this study. Full details of the ENVI-met and the “urban unit model” approach are given in Chapters 5 & 6.

Chapter 4 Validation dataset

1. Local Climate

The micro-climate simulation results were validated against air temperature and relative humidity observations collected from urban sites in Hangzhou (30°15'N 120°10'E) in Zhejiang Province, China (Shen et al., 2014) (Figure 4.1).

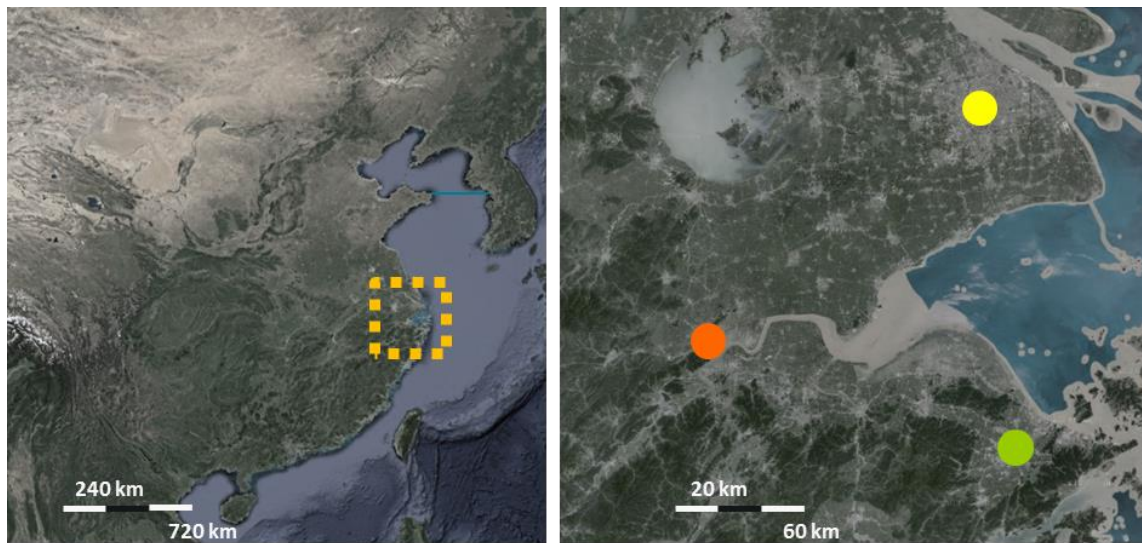


Figure 4.1. Location of Hangzhou (orange bullet point) and Ningbo (green bullet point) in China. Ningbo is the home of the Centre for Sustainable Energy Technologies (CSET) that owns the networks of air temperature and relative humidity sensors used for model validation (Shen et al., 2014). Background map from Poskanzer (2000).

The measurement network consists of 55 air temperature and relative humidity sensors installed at a height of 3 to 5 metres above ground level. Both Hangzhou and Ningbo have a humid sub-tropical climate with a Cfa classification in the Köppen-Geiger climate system (Rubel & Kottek, 2010). The Cfa classification denotes a warm temperate (C), fully humid (f) climate with hot summer (a) (Rubel & Kottek, 2010). In 2011 these two cities combined had a total urban population of 6.65 million people with a mere 7.85 million documented in the broader Municipality areas (Hangzhou Statistical Bureau, 2011; Ningbo Municipal Statistics Bureau, 2012).

The comparison of the daily average air (dry bulb) temperature in Hangzhou with the typical meteorological year files (CSWD: Chinese Standard Weather data; SWERA: Solar and Wind Energy Resource Assessment) for the period from 1998 to

2013 (Figure 4.2) shows a similar trend between the three datasets. The large daily differences can be attributed to the characteristics of the typical meteorological year (not to be confused with TMY as a format) datasets.

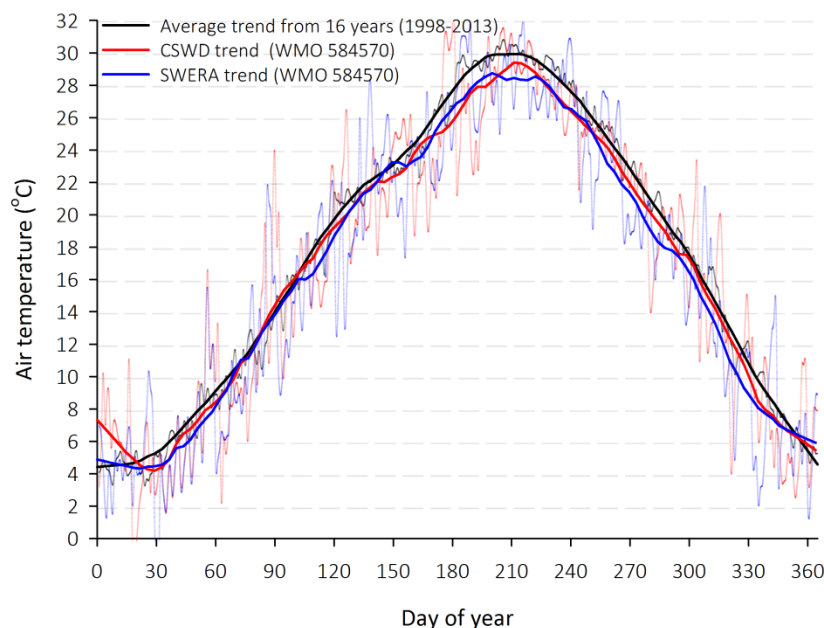


Figure 4.2. Comparison between the daily mean air temperature for Hangzhou typical meteorological year weather files (CSWD and SWERA) and the daily average for the time period from 1998 to 2013. All data are from the same weather station (WMO 584570). Data Source: The Weather Underground (2014a).

These datasets are derived from statistically analysed ‘typical’ months, they are not based on individual days (different data file formats are based on different time periods of data and statistical analysis). Conversely, the long-time mean air temperature (black in Figure 4.2) has been smoothed by the averaging process.

The relative humidity in the typical meteorological year weather files shows a +/- 20% deviation from the 16 year mean values (Figure 4.3). This deviation could be explained, similarly to the air temperature case, by the RH value smoothing due to the averaging of the daily historical data. From both Figure 4.2 and Figure 4.3 it is clear that the selection of the weather dataset to be used in simulations can have big implications for the accuracy of the final results.

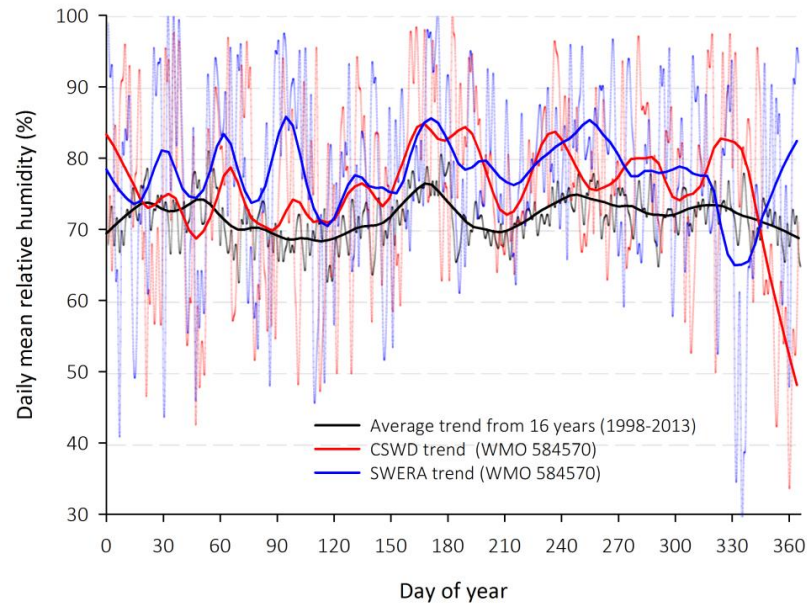


Figure 4.3. Comparison between the daily mean relative humidity for the Hangzhou typical meteorological year weather data files (CSWD and SWERA) and the daily average for the time period from 1998 to 2013. All data are from the same weather station (WMO 584570). Data Source: The Weather Underground (2014a).

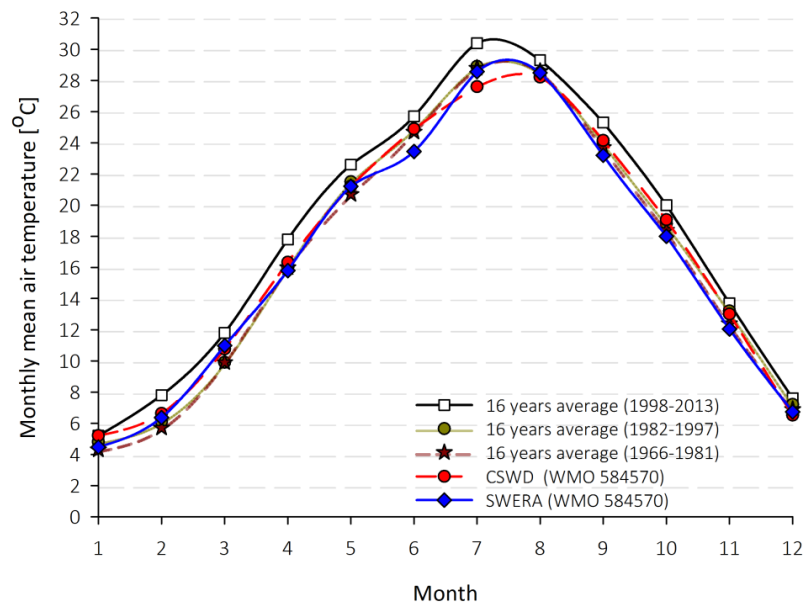


Figure 4.4. Comparison between the monthly mean relative dry bulb temperature for the Hangzhou typical meteorological year weather data files (CSWD (red) and SWERA (blue)) and the monthly average for the time periods from 1998 to 2013 (black), 1982 to 1997 (dark yellow) and 1966 to 1981 (dark red). All data are from the same weather station (WMO 584570). Data Source: National Oceanic and Atmospheric Administration (NOAA)-National Climatic Data Center (2014) The Weather Underground (2014a).

In turn, the monthly mean air temperature from three historical periods was compared to the two typical meteorological year data files available for Hangzhou

(Figure 4.4). The mean air temperature from the typical meteorological years (red and blue lines in Figure 4.4) fits well, as was expected, to the temperature observations in the historical periods from 1966 to 1981 (dark red) and 1982 to 1997 (dark yellow). However, it is noticed that the monthly mean temperature in the last 16 years (black line) shows an increasing trend in comparison to the previous time periods. This could be the result of the combined effect of urbanisation and climate change on air temperature observations (Jentsch et al., 2013).

In conclusion, the air temperature and relative humidity analysis shows that Hangzhou has four seasons with average air (i.e. dry bulb) temperatures ranging from 0°C in winter to 30°C in summer (Figure 4.2). Therefore, it exhibits both a heating and a cooling season. The daily average RH remains constantly high at the level of 70% (Figure 4.3) which emphasises the need for correct air conditioning sizing (Burdick, 2011).

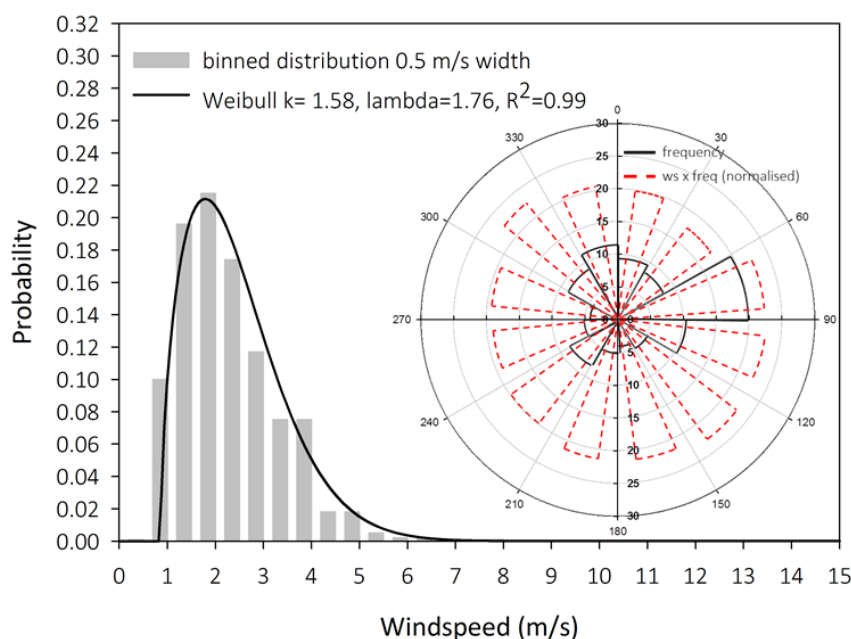


Figure 4.5. Wind speed distribution and wind rose analysis from observations collected at Mantou Mountain (WMO 584570) reference weather station in Hangzhou. Wind rose outer arc (black) shows frequency and inner arc (red dashed) denotes frequency x wind speed. Data period 1998-2013. Data Source: The Weather Underground (2014a).

The average wind conditions can be considered as calm to light breeze with the wind speeds below 3 m/s having a cumulative probability of 80% (Figure 4.5). Therefore, the horizontal energy transfer (advection) between different neighbourhoods (urban) is expected to be weak (Harman, 2003; Santamouris et al., 2008). The most important impact though could be a decoupling between the air flow

above and within the urban canopy layer (Santamouris et al., 2008). The prevailing wind direction is from the East by North-East (60° - 90° angular degrees clockwise) (Figure 4.5). The wind rose analysis indicates that the wind speed normalised for the frequency (red dashed line in Figure 4.5) is almost equally distributed to all directions. There is a predominant 120° arc from the Easterly to Southerly direction (60° to 180°).

2. Urban Context

Recent urbanisation trends in combination with a climate change induced warming effect have led to a noticeable temperature rise in developed Chinese cities (Information Office of the State Council of the People's Republic of China, 2008).

Hangzhou. West Lake
(view from sensor's location)



Hangzhou. XiXi Wetland
(sensor's location marked with arrow)



Hangzhou. West Lake
(view from sensor's location)



Ningbo. The Old Bund
(view from sensor's location)



Figure 4.6. Sensor locations near to large water bodies in Hangzhou and Ningbo (Bottom Right).

According to China's national meteorological statistics for the period 1981 to 2010, Hangzhou experienced on average 27.2 days per year with average

temperatures higher than 35 °C. Since 2003, this figure has increased to more than 35 days annually, making Hangzhou the third hottest city in China (Best News, 2013; China Daily, 2013).

From an urban planning perspective, Hangzhou's urban grid spans across 3,070 km² (Hangzhou Statistical Bureau, 2011) and contains two large water bodies, namely the West Lake close to the city centre and Xixi Wetland (Figure 4.6). Ningbo occupies an area of 2,460 km² (Ningbo Municipal Statistics Bureau, 2012) and is characterised by three main rivers, the Fenghua, Yao and Yong Rivers, which meet in the city centre (Figure 4.6).

3. Measurement equipment and set-up specifications

Air temperature (T_{air}) and relative humidity (RH) was recorded with miniature data loggers (Maxim Integrated, 2013). The sensors were positioned in radiation shields and installed on lamp posts (Figure 4.7). The data loggers recorded hourly values for air temperature at 11-Bit (0.0625°C) resolution and relative humidity at 12-Bit (0.04%) resolution (Maxim Integrated, 2013). The manufacturer stated air temperature accuracy is $\pm 0.5^{\circ}\text{C}$ and the RH accuracy is $\pm 5\%$ RH points (Maxim Integrated, 2013).



Figure 4.7. The radiation shield (Left) and the T_{air} / RH sensor (iButton©) used for the observations in China. Images Courtesy of Shen et al. (2013).



Figure 4.8. The environmental test chamber in the Centre for Sustainable Energy Technologies (CSET) at the University of Nottingham Ningbo (Left) and the sensors during the calibration (Right). Image Courtesy of Shen et al. (2013).

The memory capacity of 8kb allows up to 110 days of hourly data to be stored. At the end of a 110 day period the data were downloaded to a PC and the sensors were repositioned at the same location to continue recording the weather conditions. All sensors were calibrated prior to installation and their readings were inter-

compared in an environmental test chamber at the Centre for Sustainable Energy Technologies (CSET) in the University of Nottingham Ningbo (Figure 4.8).

For calibration purposes air temperature ($^{\circ}\text{C}$) and RH (%) readings within 1 minute intervals were compared to the readings of two separate thermo couples at chamber ambient air temperatures of -10°C , 0°C , 10°C and 30°C (Shen et al., 2013). The results showed that all the sensors operate within the reported accuracy margin and fit well to the thermocouple measurements (not shown) (Shen et al., 2013).

The standard deviation of the air temperature ($^{\circ}\text{C}$) at any specific time was in the range of 0.1°C to 0.8°C . In low temperature (10°C) and low relative humidity (30%) conditions the scatter of the sensors' readings was within the reported accuracy of $\pm 0.5^{\circ}\text{C}$ (Table 4.1). This was not the case when the temperature approached 30°C and the relative humidity was in the range of 20%. Under these conditions there was a maximum difference of 3°C between the sensors' minimum and maximum readings. The standard deviation in this case was 0.8°C . The standard deviation of relative humidity (RH) measurements was larger than the standard deviation of temperature observations. The difference between the RH minimum and maximum readings was in the range of 2% to 15% RH. The sensor's specifications note that the "saturation" drift becomes larger at 70% RH and above (Maxim Integrated, 2013). High RH levels are typical in the region of the field measurements. Therefore, it is expected that in some cases the accuracy of the RH readings will be lower than the $\pm 5\%$ RH units accuracy stated by the manufacturer.

Table 4.1. Statistical analysis of the calibration results at specific time intervals. Background Data Source: Shen et al. (2013).

Chamber ambient Temp. $^{\circ}\text{C}$	-10°C	0°C	10°C	30°C
$T_{\text{air}} [^{\circ}\text{C}]$	mean: -9.2	mean: 1.2	mean: 10.7	mean: 31.0
	min: -9.3	min: 1.1	min: 10.6	min: 29.8
	max: -9.0	max: 1.6	max: 11.1	max: 32.7
	σ : 0.05	σ : 0.09	σ : 0.06	σ : 0.77
RH [%]	mean: 91	mean: 86	mean: 29	mean: 20
	min: 85	min: 77	min: 28	min: 18
	max: 100	max: 95	max: 30	max: 21
	σ : 3.29	σ : 3.83	σ : 0.46	σ : 0.57
RH: relative humidity, σ : standard deviation				

There are extensive guidelines (Table 4.2) available for the selection of representative locations and on-site installation of weather stations at urban sites (World Meteorological Organisation, 1996; Oke, 2006). The installation and maintenance of the sensor network in Hangzhou and Ningbo had to strike a balance between being representative of the urban canopy and at the same time ensuring accessibility to the site and easy maintenance (Shen et al., 2013).

Table 4.2. Summary of the general guidelines for the site selection and installation of urban weather stations.

Guidelines for the installation of weather stations at urban sites. Following the principles of Oke (2006) and World Meteorological Organisation (2008).	
<ul style="list-style-type: none"> Circle of influence on a screen level (~1.5 m) temperature or humidity sensor: 0.5 km Select a location in the Urban Canopy Layer (UCL) surrounded by the 'average' for the site of interest urban morphology. Sensors installation height can be greater (3 to 5 m) in the UCL than typical screen height with negligible impact on measurements. North – South orientation is favoured for long time measurements in streets. 	<ul style="list-style-type: none"> Urban stations in parks, playing fields and over short grass are not representative of urban locations. Radiation shielding and ventilation of the shield should be carefully considered. Distance from walls or other obstructions should be at least twice the height of the object. Otherwise, forced shield ventilation may be required.

According to Oke (2006) air temperature and relative humidity observations in the surface layer (3x above average building height) can be expected to be representative of an area ranging from 100m to several hundred metres in a direction upwind and around each sensor. However, it is expected that most of the sensors were collecting measurements in the roughness sub-layer and not in the surface layer (Cheng & Castro, 2002b) (

Figure 4.9). The location of the measurement sites was carefully selected to have characteristics as homogeneous as possible in a large city. The sensors were installed at sites with a reasonable distance to the fringe of different surface types. The radiation shield design and the sensors were tested to ensure that the logged air temperature data were reliable and similar within an accepted accuracy to data

Chapter 4 Validation dataset

collected with a commonly used Stevenson screen design (Cheung et al., 2010) (Table 4.3). A detailed comparison of hourly temperature observations between the sensors design used here inside a Stevenson screen and the radiation shield used for the sensors in this study is available in the original paper from Cheung et al. (2010).

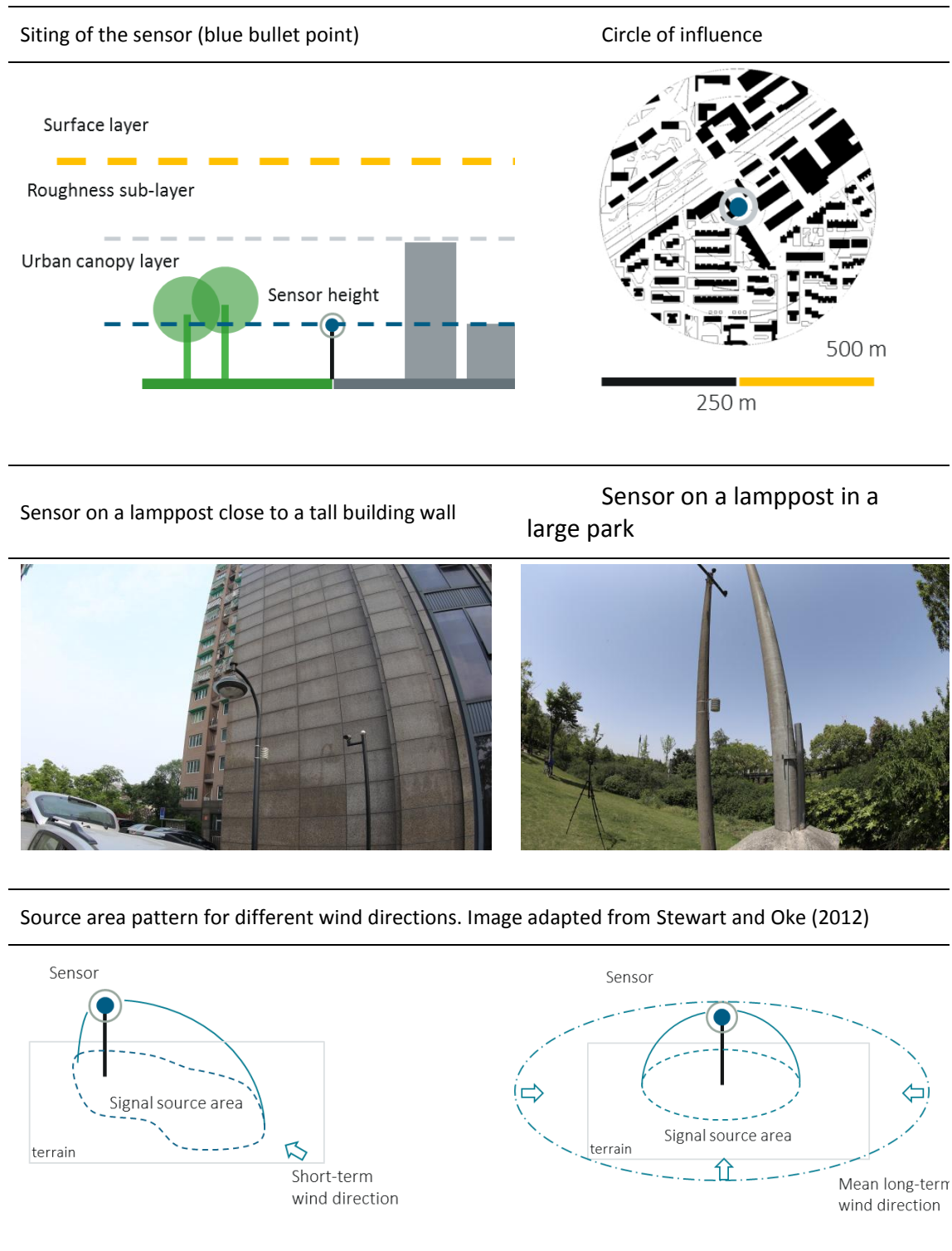


Figure 4.9. Siting of the sensors and the signal source areas.

Table 4.3. Comparison between the results from temperature measurements with two different types of radiation shields. Source: (Cheung et al., 2010)

Shield type	Mean (°C)	Standard deviation (°C)
Stevenson screen	14.86	2.30
Radiation shield (used for the sensors in China)	14.92	2.37

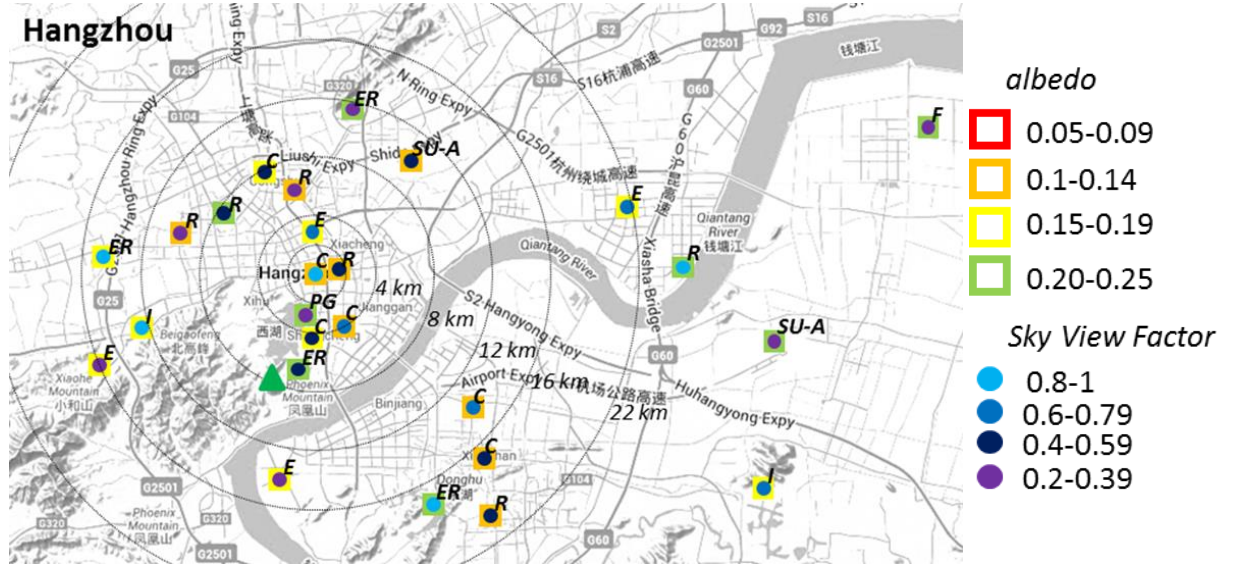
The difficulty in convincing the authorities and private owners to allow the use of lamp posts for sensor mounting in conjunction with easy access and free of obstructions make the current selection of sites the best possible choice (Bourikas et al., 2013). However, there are some cases where the sensors had to be positioned very close to airflow obstructions or in open-park locations (

Figure 4.9) and their readings may not represent the typical weather conditions of the urban environment.

It is considered that the urban unit's size, as defined in this study, covers the footprint of thermal and humidity sources for the sensors' measurements in both urban and modified rural (i.e. urban parks) sites. The footprint or source area of a sensor is the surface area that has the largest impact on the sensor measurement and it is the source of the signal that the sensor receives (Schmid & Oke, 1990; Oke, 2006; Stewart & Oke, 2012). The shape of the footprint and its size depends on the height of the sensor (in this study 3 to 5 metres above ground), the surface geometry and the nearby urban elements, the atmospheric conditions and the wind profile (Kljun et al., 2002; Stewart & Oke, 2012).

4. Statistical data analysis and data cleaning

The weather data time series collected from the sensors' network were, as a first step, examined to identify outliers in the datasets. It was found that relative humidity (RH) values were often above 100% regardless of the sensor and its location. A simple algorithm (i.e. *if* $RH > 100\% = 100\%$) was applied to cap the RH values at 100% levels. The scatter and frequency of the erroneous RH data indicates that the most probable cause of sensors short term drift was due to pollution or water spray (Bourikas et al., 2013). The drift was reset and there was not a permanent effect on the measurements. Boxplots of the hourly air temperature distribution per week were created with IBM SPSS Statistics Ver.19 (IBM Corp, 2010) for each sensor's location in Hangzhou (Figure 4.10).



Letter Index: C = commercial, R = residential, PG = public green, E = educational, I = industrial, ER = Ecological Reserve, F = Farmland, SU-A = Special use-Airport.

Figure 4.10. The network of sensors in Hangzhou. The boxes give a visual estimation of the annual average albedo (Shen et al., 2013) and the bullet points describe the summer Sky View Factor (SVF) as calculated on site (Bourikas et al., 2013). The letters nearby the sensors indicate the Land Use type as given in the Local Planning maps (Ningbo Urban Planning Bureau, 2003; Design, 2006).

All outliers (i.e. values that are at least 1.5 times higher / lower than 50% of values in the sample “box height in boxplots”) were investigated in detail. Outliers (Figure 4.11, left) that showed up in consecutive hours or that were common to all sensors' observations at a specific time and day were not treated as potential errors (Bourikas et al., 2013). Those values deviate largely from the weekly mean, more than

the other data, but they represent the hottest and coldest days of a week. However, these high values were not errors as they represent the following week's air temperature development (Figure 4.11; orange vertical reference line to the right). Weather conditions have radically changed during the week and the identified outliers (left, shown with circles and stars) were the highest air temperature values in the week under examination. This means that they appeared as outliers only due to the selection of a week as the time period for the analysis but the abnormality was explained by the weather change between the two weeks.

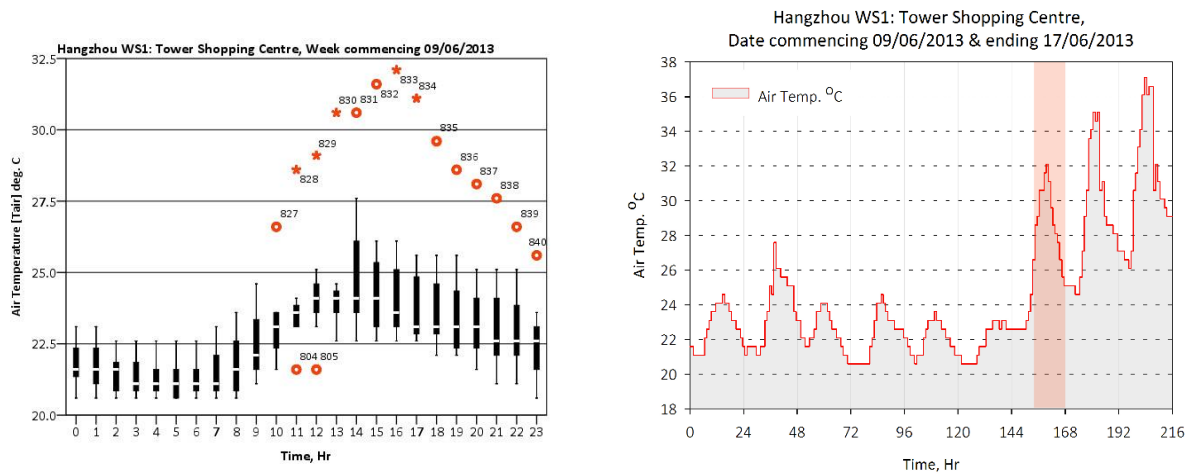


Figure 4.11. Consecutive outlier values (left, shown with circles and stars) that can be associated with the weather trend of the week before or after (right, the consecutive outliers in day 7 are shaded with orange).

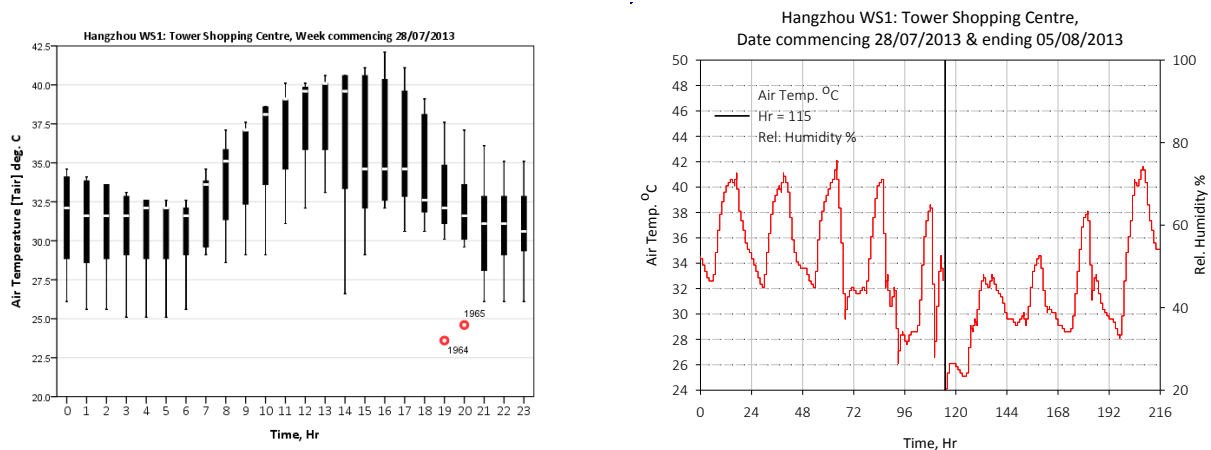


Figure 4.12. Outliers (left, shown with red circles) examined in relation to the weather conditions (right). The black vertical reference line (Hr=115, right) shows the time that the outliers were noticed.

The interpretation of the observations in the context of consecutive days can justify the selection of a week (Sunday to Saturday) as the time unit for this analysis instead of a random number of days from randomly generated samples for each month. It

shows also the importance of the interpretation of weather data in their urban context. Outliers should be examined in relation to the urban context, weather forcing and in comparison to measurements from other sensors (Figure 4.12).

In Figure 4.12 (left) the air temperature values marked with red circles are a cause of concern for the sensor's operative conditions. A closer look reveals that the sudden temperature drop (Figure 4.12, right) is strongly related to the relative humidity (Figure 4.12, blue dots) spikes (i.e. rain after a dry period) while comparison with observations from other sensors in the city returned similar results (not shown here). Outliers such as these were not classified as erroneous data. The continuity of days and weeks is an integral part of urban datasets. Random selection of days or hours would increase the uncertainty and decrease the validity of any conclusions about the micro-climate development. The range of hourly changes in the measurements from each measurement site was also compared with the hourly changes in weather data collected from the reference weather station at Mantou Mountain, National Principle weather Station (30°13'N, 120°26'E, elevation 43m, see Figure 4.13).

4.1 Replacement of missing/false values

Eight cases (Table 4.4) have been investigated for replacing false data readings and missing values in urban weather measurements. The first three cases involved the use of statistical prediction models trained with the existing dataset and application of these models to estimate the few hours of missing data (Cases 1-3 in Table 4.4). These models estimate the level, seasonal change and trend for the data that are put into the models and predict the time series' development (IBM Corp, 2010). In the other three cases, missing values were replaced with the mean value of the two hours before and two hours after the missing data (Case 4 in Table 4.4), the mean temperature from locations with similar to the target site's sky view factor (SVF) (marked with blue points in Figure 4.13) (Case 5B in Table 4.4) the mean temperature from the nearest sites to the target site's location (marked as 2, 7, 8 in Figure 4.13) (Case 6B in Table 4.4). In Cases 5A and 6A the missing values were replaced using linear interpolation of the average temperature in locations with a SVF similar to that of the target site and linear

interpolation of the average temperature of the three nearest sites respectively. Case 7 examined the case of filling gaps in the dataset with the 10 year-long average temperature values from data collected at Mantou Mountain National Principle Station (marked as 9 in Figure 4.13). Case 8 assessed the filling of missing values with data collected at the same date from the reference National Principle weather Station at Hangzhou.

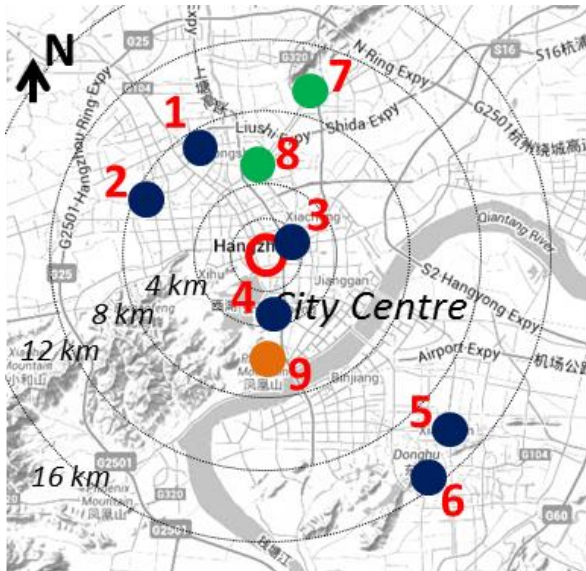


Figure 4.13. Locations of the sensors used in the case study. The target location for the case study is marked as 1. The blue points denote locations with a SVF similar to that of the target size. The Mantou Mountain, National Principle Weather station's location is marked as 9. Image Source: Google Earth (2013).

The goodness-of-fit of the estimated values to the observed data was examined under two scenarios; the prediction and replacement of 6 subsequent hours during night-time (00:00 – 05:00) (Scenario 1) and daytime (12:00 – 17:00) (Scenario 2). The selected target sensor (marked as 1 in Figure 4.13) is located in a commercial area 8 km North West of Hangzhou's commercial city centre.

There were two days selected in the scenarios; one cold cloudy day in January (13/01/2013) and one warm sunny day in March (09/03/2013). On the 13th of January the sky conditions at Mantou Mountain's National Principle weather Station were reported as mostly cloudy with light rain showers while the winds were blowing from a North by North-West direction with speeds from 1 to 3 m/s. The 9th of March was the fifth day in a row with a clear sky, the wind at Mantou Mountain was blowing from a South West-South direction with speeds from 1 to 4 m/s (The Weather Underground, 2014a).

Table 4.4. Summary of the methods investigated for the replacement of missing data in urban weather datasets. The best performing cases adopted by this study are highlighted with orange.

Cases	Estimation Method	Dataset from sensors (Fig. 3.14)	Scenarios
Case 1	Forecast model	1	1 (00:00 to 05:00) 2 (12:00 to 17:00) Days 13/01/2013 09/03/2013
Case 2	Forecast model	1 to 6	
Case 3	Forecast model	2,7,8	
Case 4	Mean (2 hours before and after missing data)	1	
Case 5A	Linear Interpolation	Average from sensors 1 to 6	
Case 5B	Mean	Average from sensors 1 to 6	
Case 6A	Linear Interpolation	Average from sensors 2,7,8	
Case 6B	Mean	Average from sensors 2,7,8	
Case 7	Long-time Mean (10 years)	Average from National Principle station	
Case 8	Direct replacement	National Principle station, WMO listed	

4.2 Statistical forecast modelling

Three prediction models were created with historical observations from the target sensor (marked as 1 in Figure 4.13, Case 1), the average temperature from locations with approximately the same summer time SVF (blue bullets in Figure 4.13, Case 2 in Table 4.4) and the average temperature from the three sites nearest to the target sensor location (marked as 2, 7 & 8 in Figure 4.13, Case 3 in Table 4.4).

Hourly weather observations for short periods of time (hours to days) cannot be considered as stationary (statistical properties such as the mean and variance would be time independent (NIST/SEMATECH)) with respect to the time scale of weather development within the urban canopy layer. For this reason autoregressive integrated moving average (ARIMA) models were excluded from the SPSS built-in forecasting procedure. Only seasonal exponential smoothing models have been considered and the best fitting one was selected according to the results of the Expert Modeler component of IBM SPSS Ver. 19 (IBM Corp, 2010).

Control tests were carried out with 7, 5, 3 and 2 day period samples training of model for January, February and March. Results from this analysis show that for the specific case studies the statistical models should be built with data from 7 days in January and 5 days in March (Table 4.5 and Table 4.6). The results with the lowest Root Mean Square Error (RMSE) indicate the best fit of the predicted values to observed data. Mean Absolute Error (MAE) is an additional indication of the goodness-of-fit of model prediction to real data where the lowest MAE shows the best fit.

Table 4.5. The Root Mean Square Error (RMSE) of the results from the statistical forecast model when trained with different number of days.

RMSE	Model - 2 days data	Model - 3 days data	Model - 5 days data	Model - 7 days data
January	2.361	2.014	1.654	1.442
February	1.179	0.619	1.006	0.870
March	1.950	1.464	1.374	1.643

Table 4.6. The Mean Absolute Error (MAE) of the results from the statistical forecast models for 4 different cases of model training.

MAE	Model - 2 days data	Model - 3 days data	Model - 5 days data	Model - 7 days data
January	2.10	1.73	1.35	1.08
February	0.98	0.52	0.89	0.80
March	1.70	1.16	1.11	1.26

As it would be expected, it has been found that the weather conditions in the last few days before the missing values have a larger effect on the model's output than the monthly weather trend. A stable, homogeneous weather conditions pattern and a strong diurnal signal in the prediction dataset (models' training dataset) seem to increase the accuracy of the first few forecast hours and give a 24-hour periodicity trend to the results.

5. Results from the value replacement case study

The goodness-of-fit of all methods was evaluated with the fit of the predicted values to the 6 hours of observations (Figure 4.14, Appendix A – model performance indices) that were deemed as ‘missing’ in the scenarios (Table 4.4). Results showed that the replacement of the missing urban air temperature (T_{air}) and relative humidity (RH) observations with the long-term average temperature from the nearby airport will lead to large deviations from reality. In the case of a hot day, such as the one studied in March, the error can be as large as 16 °C for temperature and 50% for relative humidity (Figure 4.15). Therefore this hypothesis – scenario was discarded. The 10 °C to 16 °C air temperature (30% to 50% RH) (Case 7, Figure 4.15) difference between the temperature and RH observations from the National Principle reference weather station and the temperature and RH observed at the weather station in the city strengthen the view that historical datasets collected at non-urban sites such as airports do not represent locations within the city where a distinctive micro-climate develops.

In Cases 5B and 6B, the missing air temperature values from location 1 were replaced by direct substitution with the mean temperature from sensors across the city that have a similar Sky View Factor (SVF) and from sensors within a small distance (< 4 km) to the site of interest. It is pointed out that on a day with clear sky (Mar_Day marked as green bar) both methods performed well at noon and early afternoon, during the air temperature’s peak point. The large daily variation of air temperature during warm days and the associated high air temperature values at noon could not be satisfactorily predicted by the statistical forecast models (Cases 1 to 3 in Table 4.4) and linear interpolation methods (Cases 5A and 6A in Table 4.4). Generally, these methods appear to be applicable only during days with small diurnal temperature differences and they were not applied in this study.

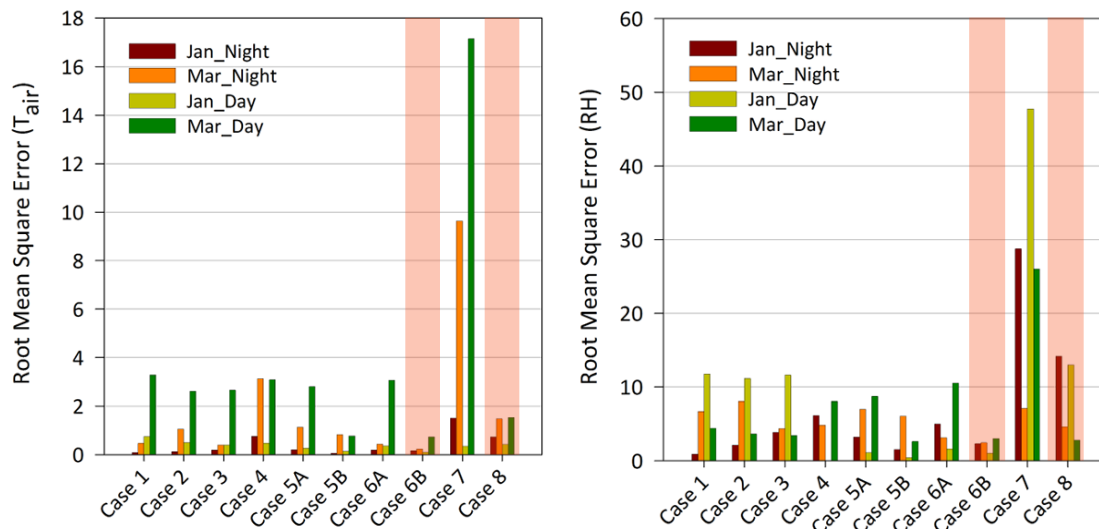


Figure 4.14. Goodness-of-fit of the air temperature (left) and relative humidity (right) estimations from the methods in the case study (Cases 1 to 8) to the observations from the target site's sensor. Cases 1 to 3 are the statistical forecast models. Cases 4, 5B, 6B & 7 replace missing data with mean values from different sources. Cases 5A and 6A are using the results of linear interpolation and Case 8 is a direct replacement with reference data. The methods adopted for use in this study are shaded with orange.

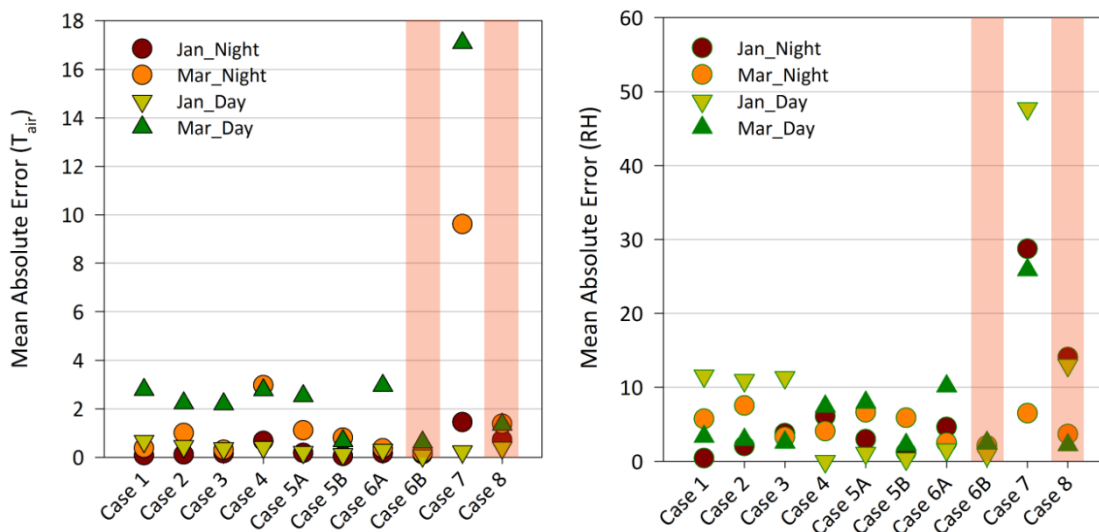


Figure 4.15. Mean absolute difference (i.e. |Observed – Estimated|) between the air temperature ($^{\circ}\text{C}$) (left) and relative humidity (%) (right) estimations and the observed weather conditions for each case. The methods adopted for use in this study are shaded with orange.

Figure 4.14 shows that all the methods had a similar performance in air temperature estimation during the mostly cloudy day that was studied in January. Even Case 4 that replaces the missing values with the mean temperature data of the 2

hours before and after the gap in the dataset returns results close to the observed weather conditions. However, in Case 4 all 6 missing values are replaced with the same mean value. Therefore, this method should only be used when a single value is missing and there is not a big change in the values before and after. This is also the case in the RH estimation for Case 4 during daytime in January. Humidity remained constantly high throughout the day and the replacement with the mean of the two hours before and after the missing data returned the best results. In Case 8 the data are directly replaced with data from the local reference weather station (National Principle station). The absolute error is consistently low across all cases and it could indicate that the reference weather station at Mantou Mountain (marked with 9 in Figure 4.13) can be affected by the city's boundary layer development.

6. Conclusions on data cleaning procedure

In both scenarios (day-time and night-time) the largest temperature difference between the city centre (location 1 in Figure 4.13) and the official reference weather station (location 9 in Figure 4.13) is during clear sky, warm weather. That could be a result of anthropogenic heat emissions, the latent heat flux on the mountain where the reference weather station is located or the surface properties at the city sensor's location in the city. The latter is the most likely reason as the relative humidity levels are similar (Case 8 in Figure 4.15) and the air temperature difference is constant with time (day – nighttime, Case 8 in Figure 4.15).

Eight methods for replacing missing values were evaluated for their performance in the context of urban measurement datasets. It was observed that the replacement of missing and false values with the mean from nearby sites and with the mean from sites with characteristics similar to those of the target location returns equally good results and is better than the direct replacement with data from the local reference weather station. There were not any significant differences in the performance of these two methods during day-night time and on cold-warm days. However, the night-time temperature estimates during calm weather with clear skies; when the urban temperature difference to the rural surroundings is expected to be larger (Oke, 1987; Basara et al., 2008); show that the mean of the nearby sites is the best fit to the measured data. This might be due to the night cooling potential of

remote sites, away from the city centre that were included in the dataset of Case 5 when they had a SVF similar to one of the sites of interest. Nevertheless, weather data from multiple sites in the city are not usually available. In that case the replacement with data from the reference weather station (Case 8) for the same time is a better choice than statistical prediction models, especially considering the expertise and time required to build and run them. This analysis concluded that the most appropriate methods for the replacement of erroneous and missing weather data are (1) the replacement with the average value from observations collected at locations near the place of interest (Case 6B) and (2) with direct replacement with data collected from the reference weather station even if it is not representative of the urban location (Case 8). These two cases were adopted for use in this study.

7. Selection of a generic urban unit

The urban unit's size, i.e. the radius of the disk around the "centre of a neighbourhood", has been determined by assessing the vegetation cover's influence on air temperature. For this, twelve urban sites were selected across the city centre of Hangzhou, North of the Qiantang River. The locations for the twelve sensors participating in this pre-analysis are shown in Figure 4.16 (top left).

The surface area covered by vegetation has been estimated from aerial and street images and on site field observations. Different views from the location of sensor 5 are shown as an example (Figure 4.16, middle and bottom). Each sensor was considered to be the centre of concentric circles at radii of 10m, 25m, 50m, 100m, 150m, 200m, 300m, 400m and 500m. The footprint of the vegetated surface was estimated and apportioned to these annular areas (Figure 4.17). The detailed procedures for the calculation of the morphological parameters in the final urban unit are described in a following section.

The ratio of green space to the total unit area ratio (% green space) is expected to have a negative correlation with air temperature (Yang et al., 2013a). There are cases though where the tree obstruction of wind flow can lead to limited street ventilation (Yang et al., 2013a). In these cases, the temperature of stagnant air could increase with the increase of vegetated area (trees) (i.e. heating due to limited ventilation prevails over cooling through evapo-transpiration and lower surface temperatures due to shading) (Park et al., 2012).

It is to be expected that the influence of green space is larger when closer to the sensor and diminishes if it is more towards to the outer annuli areas. This is shown in Figure 4.19. It is hard to isolate the influence of vegetated space from other parameters that may be affecting the air temperature. The long seasonal average and the selection of stations in proximity to each other and away from large water bodies confine the cooling effect to the vegetated surface area and its micro-climatic impacts on the air temperature signal.

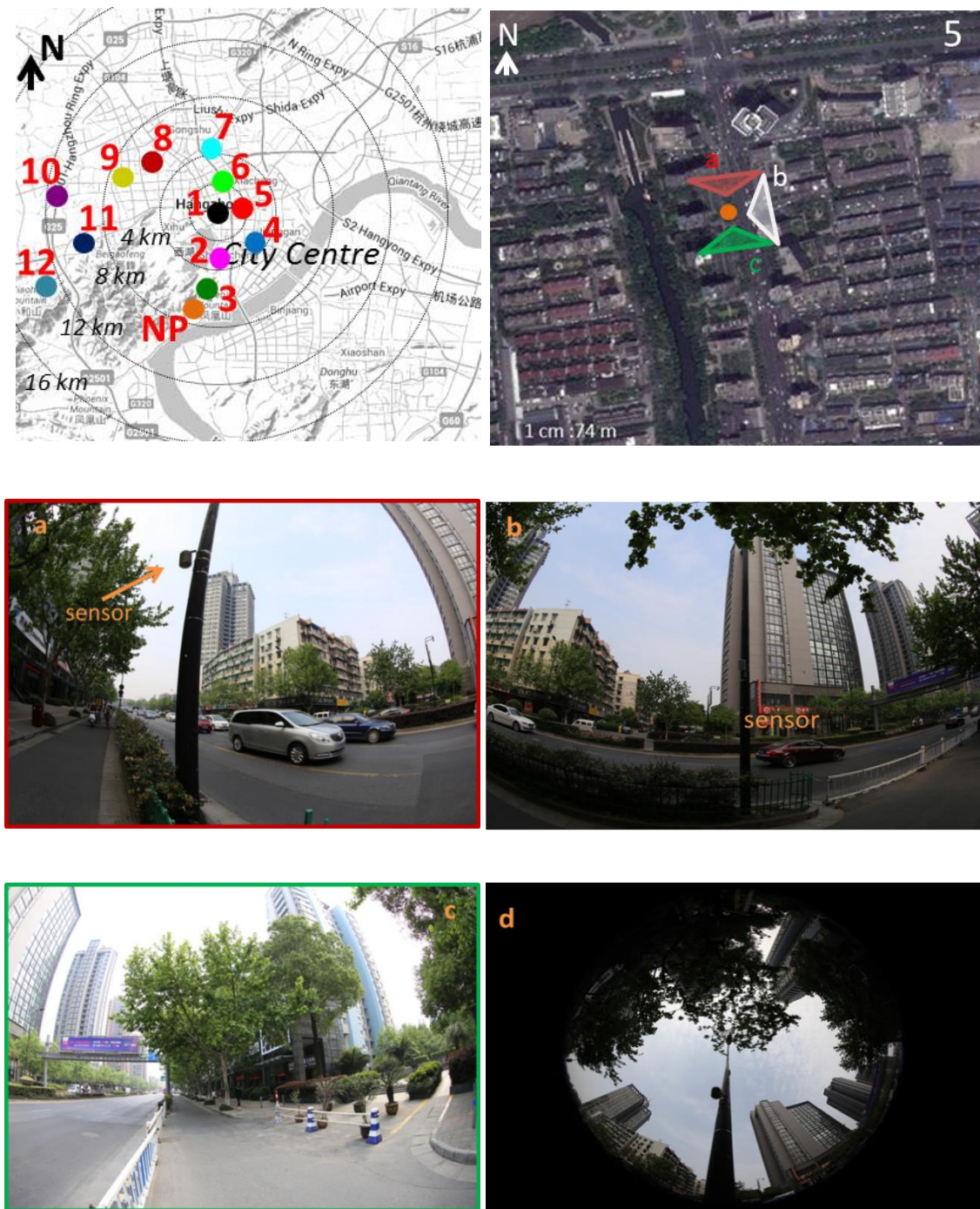


Figure 4.16. The location of the sensors in Hangzhou participating in the analysis for the determination of the urban unit (Top left, bullet points colour corresponds to curves in Figure 4.18 and Figure 4.19). Top right: The three different views from the location of sensor 5 (orange bullet). The views are numbered from one to three and the image is outlined with colours respectively (middle and bottom left). Bottom right (d): Full frame circular fisheye image (taken at a height of 1.5m above ground in May 2013) of the sky dome available to the sensor.

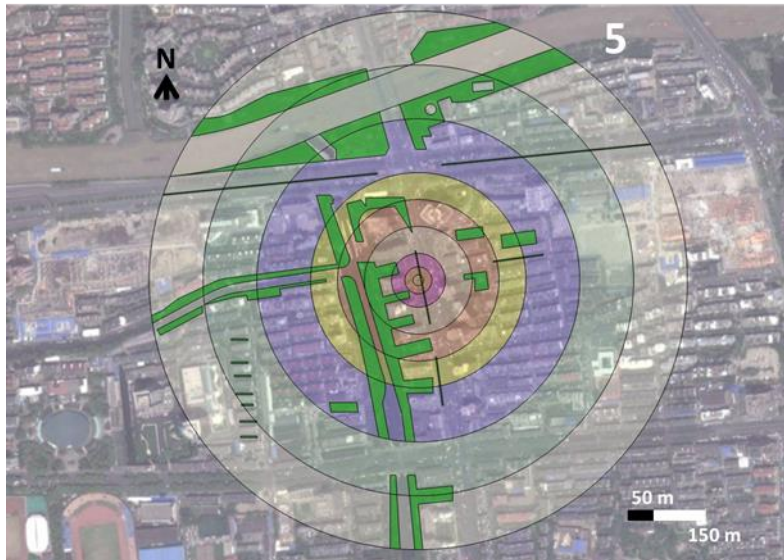


Figure 4.17. The vegetated surface area at different concentric (sensor lays at the centre) annuli areas. The vegetated surface area is shown with the polygons (opaque green). The annuli areas are marked with different colours (transparent). Their inner circle border radius (r) and the outer circle radius (R) from the centre outwards are r - R =0-10m; 10-25m; 25-50m; 50-100m; 100-150m; 150-200m; 200-300m ;300-400m ;400-500m.

The strong influence of vegetated areas close to the sensor is evident from the first peak of a vegetated surface area in comparison to the general trend in the group of sensors. The locations of sensors 3 (dark green; -1.4°C) and 10 (purple; -0.4°C) have a lower than the group average air temperature and their vegetated surface area is large with an early peak within the first 100 metres from the sensor (Figure 4.18). Interestingly, sensor 12 (dark cyan; -1.0°C) which also shows a negative temperature departure from the group mean has a small vegetated area in the first 150 metres away from the sensor, comparable with those at locations with higher than the group average temperature. Its negative trend can, however, probably be explained with the steep rise in vegetated surface area at the annuli area from 150 to 200 metres, showing that the influence of vegetation remains strong at this distance (Figure 4.18).

Further evidence comes from the comparison between sensor 1 (black, $+0.5^{\circ}\text{C}$) and sensors 2, 5 and 9 (pink, red, gold; $+0.2^{\circ}\text{C}$). The regression trend lines indicate that the location where sensor 1 resides is warmer than the locations of sensors 2, 5 and 9 despite the larger vegetated surface within a 0 to 100 m radial distance from the sensor (Figure 4.19). In the case of sensors 2, 5 and 9 the vegetated surface area peaks occur later at distances from 100 to 150 metres showing the persistent impact of the green space area. In addition, site 5 (red; $+0.2^{\circ}\text{C}$) has a similar vegetated surface area

to site 1 (black; +0.5 °C) with the only difference being a delay of the peak, that is seen at distances 50 to 100m farther outwards.

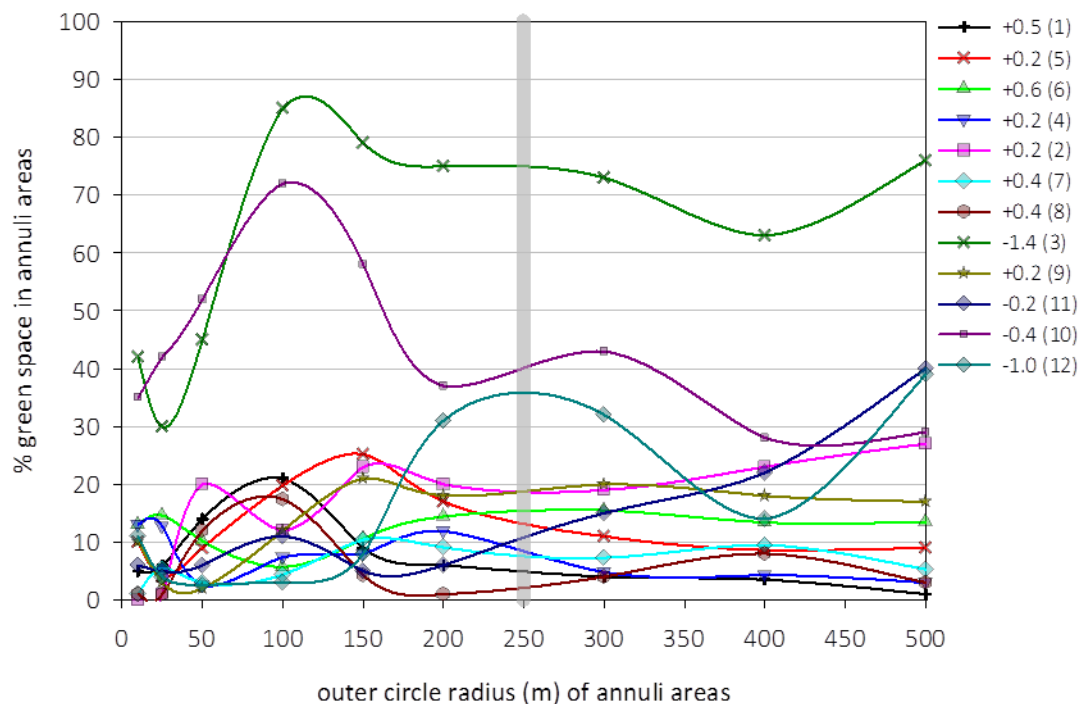


Figure 4.18. The percentage green space in the annuli areas for each sensor in the group participating to the urban unit determination analysis. The legend shows the mean summer T_{air} (°C) departure for each sensor from the group mean. The location of the sensor is quoted in parentheses.

Sensor 11 (dark blue, -0.2 °C) has a lower air temperature than the group average but the green space percentage peak occurs after the 250 m radius border (Figure 4.19). However, in this case the low air temperature is mainly attributed to the site's proximity to a large wetland (i.e. Xixi).

It has been shown that the impact of vegetation is strong at distances of up to 200 metres away from the sensor. The trend lines for sensors 3 (dark green) and 12 (dark cyan) seem to peak a bit farther (Figure 4.19), still under the influence of the vegetated surface area estimations for the annuli area at 200 to 300 m. Based on these results an estimate is therefore made for a representative circular "urban unit" with a 250 m radius. It is expected that the total area of 200,000 m² (250 m radius) surrounding the sensor will be the representative part of the source area for the air temperature and relative humidity signal. The size of the proposed urban unit also agrees with other studies on the windward distance from a point of roughness or

thermal change (~200-500m) and the internal boundary layer extent in zones within local climate classification schemes ($r \sim 200-500$ m) (Stewart & Oke, 2012)

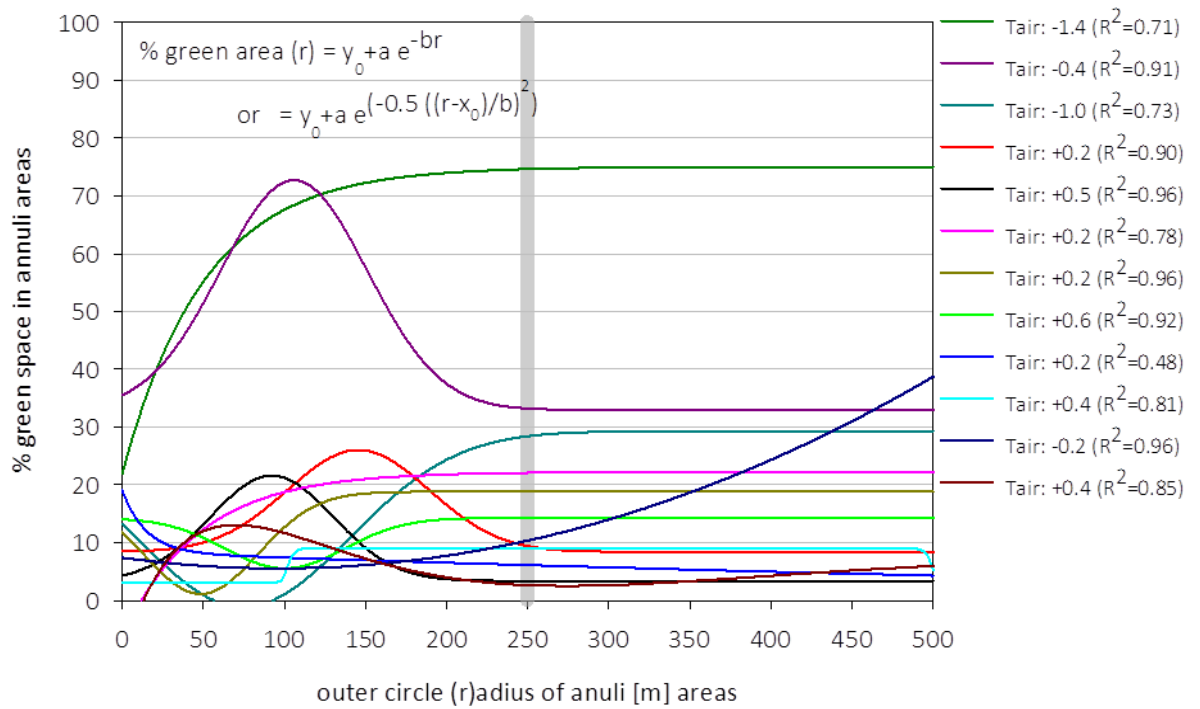


Figure 4.19. Regression lines of the percentage vegetated area in each annulus area on the distance from the centre (i.e. the sensor).

Chapter 5 A simplified model for urban micro-climatic simulations

1. Introduction

The way surface morphology is represented in weather prediction models can strongly influence their function (Baklanov et al., 2008). The minimum surface detail requirements are defined by the purpose of the model. For example, the assessment of pedestrian thermal comfort and air pollution dispersion within a specific urban setting would require a higher degree of surface detail than an urban canopy model that parameterises the urban energy fluxes in the surface layer (Baklanov et al., 2009). In this study, the modelled urban environment is based on the conservation of the main thermal and morphological characteristics of the actual studied sites. Martilli (2009) defines the similarity of the total fluxes of heat and momentum as a requirement for the representativeness of a simplified morphology. That determines three basic rules for the equivalency of thermal models to reality (Kanda, 2006; Martilli, 2009):

- Models should have the same percentages of horizontal and vertical surfaces (e.g. roof, wall) to the real site. This can be interpreted as the same planar area, frontal area and building height.
- Each individual surface should have the same energy balance to the real one.
- The modelled surface should emit the same levels of long-wave radiation during the night.

The generation of the “urban unit model” was based on the following steps: (Step 1) - The land cover analysis started with the inspection and selection of an aerial image of the sensor’s location in Google Earth (Google Earth, 2013). The image with the best orthographic projection and quality was selected (ideally, a clear top plan view image). It was then processed with SketchUp (Trimble Navigation Limited, 2013), computer aided design software, using the urban unit described above with the temperature sensor at the centre of the 250m circular area (Figure 5.1).

A selection of metadata (e.g. high resolution images taken on site) was used in combination with the aerial view to draw polygons for the vegetation (green colour), water (blue colour) and built-up (black colour) surfaces (Figure 5.1). The residual was designated as other impermeable surface (white colour) and includes street and pavement surfaces. A set of morphological parameters was then calculated for each site including: the mean building height \bar{H} , the roughness length z_0 , the height to width aspect ratio, the frontal area ratio λ_f to the total surface, the building surface fraction F_r , the impervious surface fraction I_r and the pervious surface fraction P_r .

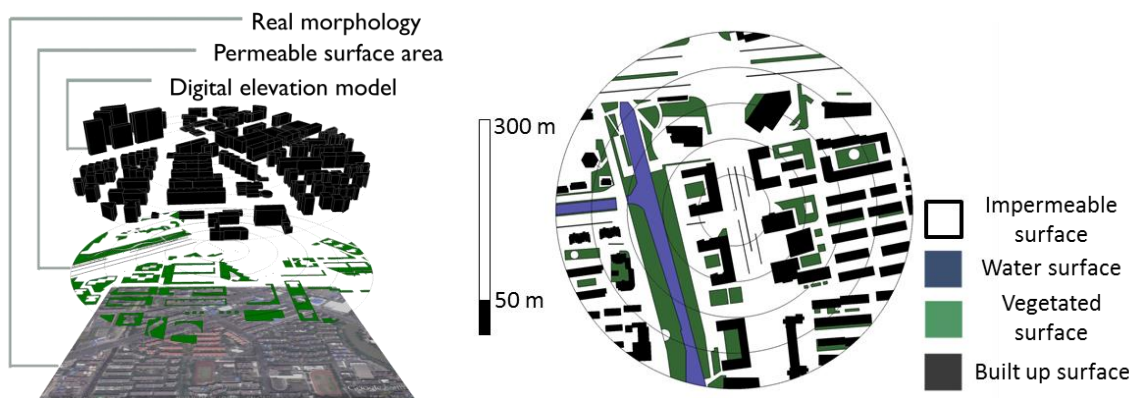
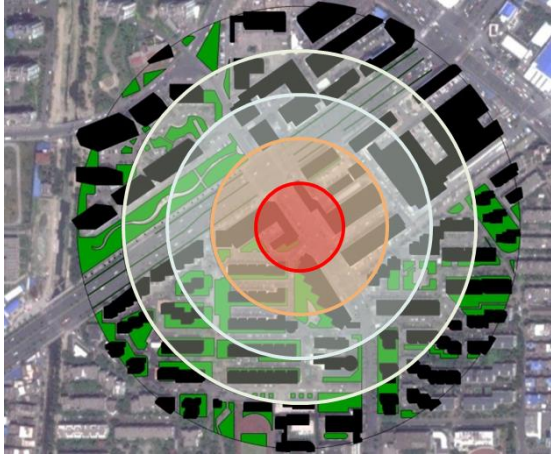


Figure 5.1. The digital elevation model and the land cover were built upon the aerial image (Left). Four land surface types had been identified and their surface area was estimated by the model. The sensor was located at the centre of a disk of 250m radius (Right).

(Step 2) - Each urban site was classified according to the land cover analysis into a “Local Climate Zone” following an urban classification scheme developed by Stewart and Oke (2012). Each zone (i.e. thermally homogenous region of uniform surface characteristics) in the scheme exhibited a distinctive diurnal temperature development profile at sensor height (~ 1.5 to 3 m) at the local scale (Stewart & Oke, 2012). The resulting Local Climate Zones (LCZs) describe 17 generic environments consisting of 10 zones for built-up (e.g. open high-rise) and 7 for non-urban land cover types (e.g. scattered trees) (Stewart & Oke, 2012). Each zone was represented by a set of ten morphological parameters and a descriptive definition of the typical location and use of the urban sites classified into a zone. Nine urban sites out of a total of 26 investigated areas in Hangzhou were classified as “Local Climate Zone 5” (LCZ5) which denotes mid-rise buildings at a medium density arrangement (Stewart & Oke, 2012). This study focused on these nine sites classified as “LCZ5”.

The urban morphology of these sites was further analysed for 5 annular areas. The annular rings' periphery had been defined at radii of 50 m, 100 m, 150 m, 200 m and 250 m.

Table 5.1. Analysis of the morphological parameters for each annulus area from a site with a LCZ5 classification (site 2 in Figure 5.11)

Site 2.	R-r (m)	P_r	I_r	F_r	z_0	σ_H/\overline{H}
	0-50 (red)	0.05	0.64	0.31	1.5	0.52
	50-100 (orange)	0.11	0.62	0.27	1.3	0.45
	100-150 (blue)	0.17	0.56	0.27	1.2	1.08
	150-200 (green)	0.16	0.60	0.24	1.7	0.99
	200-250 (outer)	0.19	0.56	0.25	2.1	0.87

P_r = pervious surface fraction, I_r = impervious surface fraction, F_r = building surface fraction, z_0 = roughness length, σ_H/\overline{H} standard deviation of the building height adjusted for the area weighted average height

Urban morphological parameters and descriptive statistics were then calculated for all the annular areas (which represent doughnut shape like disks, (i.e. 0-50m (red), 50-100m (orange), 100-150m (blue), 150-200m (green), 200-250m (outer) as shown in Table 5.1, for an example of one of the nine studied sites).

(Step 3) - The generic, idealised “urban unit model” was constructed to have a similar planar area ratio and mean weighted (footprint) building height to the nine studied sites. The individual surface energy balances were represented in the model by the pervious, impervious and building footprint surface area ratios.

2. Land Cover analysis (Step 1)

2.1 Datasets

The metadata sources for the land cover classification and urban zoning were : a) Google Earth images for Hangzhou (4/10/2010, 20/5/2011, 30/7/2011) and Ningbo

(12/3/2010, 3/4/2012, 10/7/2013), b) street level on site images taken on May 2013, c) hourly meteorological data from the National Principle weather station (WMO 584570), d) hourly observations of relative humidity and air temperature from the sensors' network (Shen et al., 2013), e) three dimensional street view maps of the urban terrain in Hangzhou and Ningbo (Sogou maps, 2014) and f) real view images at street level (Tencent, 2013).

The meteorological data were supplemented with weather event descriptions and sky observations from the National Oceanic and Atmospheric Administration (NOAA) database (National Oceanic and Atmospheric Administration (NOAA)-National Climatic Data Center, 2014) and online METAR weather data reporting resources (METAR is a standardised format for reporting weather data mainly used by pilots and meteorologists) (The Weather Underground, 2014b). The typical meteorological year hourly simulation weather files had an Energy Plus weather format (.epw) (U.S. Department of Energy, 2012). Please note that although the National Principle weather station (WMO 584570, TMY source data) reports weather data for Hangzhou with the 4 letter international airport code (i.e. ZSHC), in reality it is not located at any of the city's airports. A topographic estimation of the location and the relative location to the airports and the city centre can be seen in Figure 5.11. This location (Mantou Mountain) was cross checked and confirmed with the authors of the TMY files for Hangzhou (Shen et al., 2013).

The three dimensional maps (Sogou maps (2014), data source by Edushi) provided important information for the estimation of buildings' heights. Sogou maps provide a high resolution artistic representation of the buildings and the streets (Figure 5.2).

In order to validate the number of the floors shown in the three dimensional maps several buildings were identified and their number of floors compared across the art style 3D maps, photo images on site and images uploaded on Google Earth by users. It was concluded that the floors counted across the images (typically 6 floors) were accurate to +/- 1 floor level that is an acceptable error for that kind of building height analysis. Real street view images were also used for the assessment of buildings' heights (floor count) and of the vegetated area (Tencent, 2013) (Figure 5.2, left).

Street view image. (Tencent, 2013)



Art style view of the city. (Sogou maps, 2014)

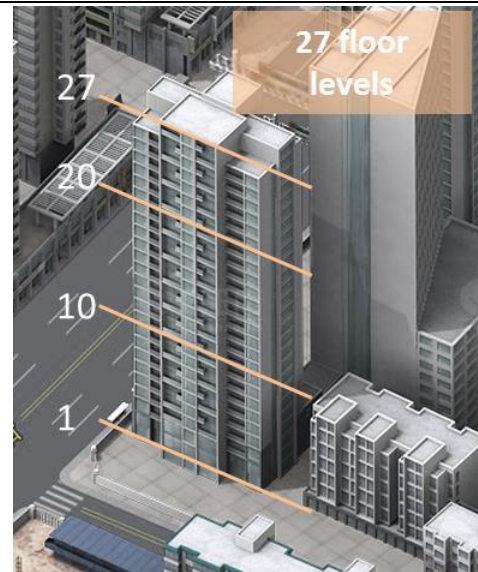


Figure 5.2. Error determination in the visual assessment of buildings' height. Artistic representation - images provide a high accuracy approximation (+/- 1 floor level) of the real conditions.

2.2. Assessment of the land surface cover

Four main land surface types have been identified through the analysis. The land cover was distinguished by vegetated (green), built, water and impermeable surfaces. All the vegetated surface area was grouped into a single category designated as green. That category was subdivided into grass and trees. An under-the-canopy approach was followed to identify the fractions of each surface at ground level (Akbari et al., 2003; Zhao et al., 2011). It was considered that the tree canopy and foliage are prone to short term and seasonal changes. These changes could impact the surface categorisation and increase the error in the classification procedure. A different approach would have required classifying the urban unit's surface cover for each season (Stewart & Oke, 2012). However, there were not enough data regarding the species, size and age of the trees that would have allowed the detailed seasonal categorisation. A random number of deciduous trees was included in the model in order to include their effect on the local specific seasonal weather conditions.

Land cover is usually analysed using remote sensing techniques (i.e. aerial and satellite images in different spectral regions). The Normalised Difference Vegetation

Index (NDVI) has been used for the assessment of surface urban heat islands and the investigation of local climate zones (Bechtel, 2011; Ji et al., 2011; Li et al., 2011). Zhao et al. (2011) used an automated technique that applied a square grid over a disk area (500m radius) of a sample site and categorised each grid box according to the land cover of its midpoint. That technique was favoured in their study because it produced a lower error than random sampling methods and the results could be easily visualised (Zhao et al., 2011).

This study did not use an automated method for the land cover analysis on the grounds of limited accuracy and poor description of the air temperature and relative humidity source area at the micro-scale. A visual inspection of aerial and eye view images was considered to suit the scale of the analysis well.

Land cover polygons were created with SketchUp (Trimble Navigation Limited, 2013), using the urban unit described above with a circular area of 250m radius. The radius of 250m was found to be representative of the impact of vegetation with distance from the sensor. A selection of metadata (e.g. high resolution images taken on site) was used in combination with the aerial view to draw polygons for the vegetation (green colour), water (blue colour) and building (black colour) surface (Figure 5.1). The polygons of the buildings' footprint area were based on roof outlines and aerial images in Google Earth. They were manually ortho-corrected by fitting the polygons to the actual borders of the buildings' base footprint. The polygon areas for each surface type had been summed and the green, built, water and impermeable area percentages of the total area ($\sim 200,000 \text{ m}^2$) were calculated. The residual was designated as other impermeable surface (white colour) and it included street and pavement surfaces. More analytically the land cover percentages are:

Vegetated space ("green") ratio (G_r): the ratio of the total under-the-canopy area covered by vegetation (grass, shrub, trees) to the total surface area of the urban unit (Zhao et al., 2011).

Total building plan (floor) area ratio (F_r): the ratio of the total building floor area to the total surface area of the urban unit. It is equivalent to the Building area fraction and the planar area ratio λ_p (but not the impermeable area fraction) and was calculated as (Di Sabatino et al., 2010) :

$$F_r = \lambda_p = \frac{\sum_{i=1}^N A_{p,i}}{A_T} \quad (5.1)$$

where $A_{p,i}$ is the floor plan area of the i_{th} building and A_T is the total plan area of the urban unit or its annulus depending on the aims of the analysis.

Water area ratio (W_r): the ratio of the area covered by water (fountains, streams, rivers, lakes, sea) to the total surface area of the urban unit.

Pervious area ratio (P_r): the sum of the green and water area ratios; $P_r = G_r + W_r$.

Impervious area ratio (I_r): The residual of the total surface area after the subtraction of the floor, green and water area ratios; $I_r = 1 - (F_r + G_r + W_r)$.

These estimations were used in the classification of the urban unit as different percentage ranges were considered to be class parameters in the Local Climate Zones scheme (Stewart & Oke, 2012). The assumptions for the width of planted road reservations and the building footprint were based on and validated with on-site measurements. A Devon LM50 digital laser distance meter by Nanjing Chervon Industry CO (Devon, 2010) was used for the measurement of typical street widths and building heights in Hangzhou and Ningbo, China. The laser distance meter has a 2 mm manufacturer-stated accuracy (Devon, 2010). Images of a road vegetation reservation near the sensor located at West Lake, Hangzhou can be seen in Figure 5.3.



Figure 5.3. Road vegetation reservations are planted with short bushes and medium height deciduous trees with a distinctive crown.

The area calculation error in the image processing method was estimated by comparing area calculations with observations from pedestrian pavements, streets in Hangzhou (Figure 5.4) and student housing in Ningbo, China (Figure 5.5). The results

showed a distance and area measurement accuracy in the range of +/- 5% of the measured sample dimensions of streets and buildings.

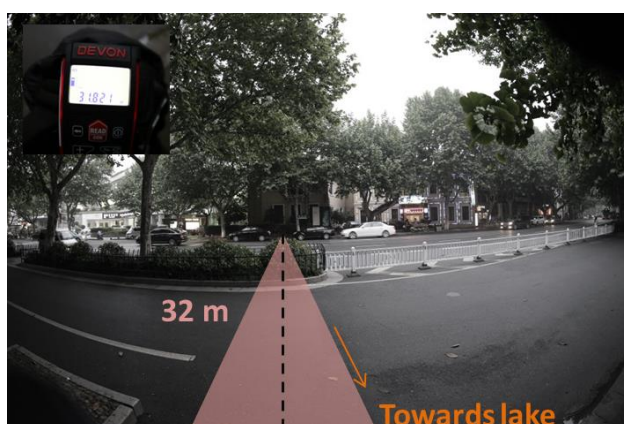
On site length measurement in Hangzhou China (May 2013).



Length measurement based on an aerial image of the same site from Google Earth. Similar aerial images were used for the land cover analysis.



Street width measurement in Hangzhou. West Lake.



Tree leaf canopy increases the difficulty (and the error) of measuring the street width on the aerial image from the same site.



Figure 5.4. Determination of the error in street dimensions measurements based on aerial images (method used for this study) from Google Earth (Google Earth, 2013)

Building length measurement in UNNC campus.

Length estimation from an aerial image of the same site.



Building floor height measurement in UNNC campus.

Street view at the same site.

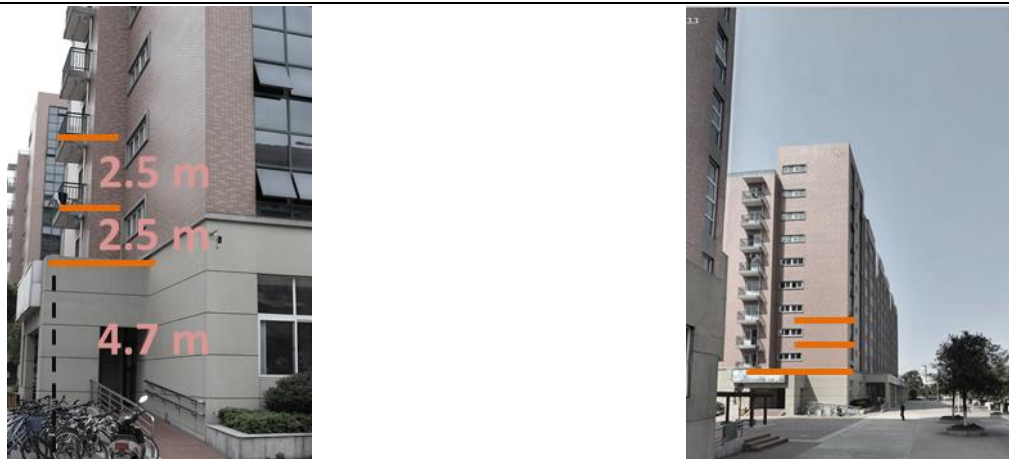


Figure 5.5. Assessment of the error in the determination of building footprint area from aerial images (top). Floor height measurement of a residential (student housing) building with a retail shop at the ground floor. UNNC: University of Nottingham in Ningbo, China.

2.3 Urban morphological parameters

A critical part of the spatial analysis in this study was the calculation of the morphological parameters for the monitored sites. The minimum distance (e.g. distance for adequate natural light access, fireproof distance) between buildings is a key urban planning indicator in China (Zhao et al., 2011). The width of the streets and the height of the buildings play a critical role in pollution dispersion and street ventilation (Ratti et al., 2006). In addition, urban canopy roughness affects the wind speed in urban sites and has direct implications for natural ventilation and the

application of renewable energy sources in buildings (Georgakis & Santamouris, 2008; James et al., 2010; Drew et al., 2013).

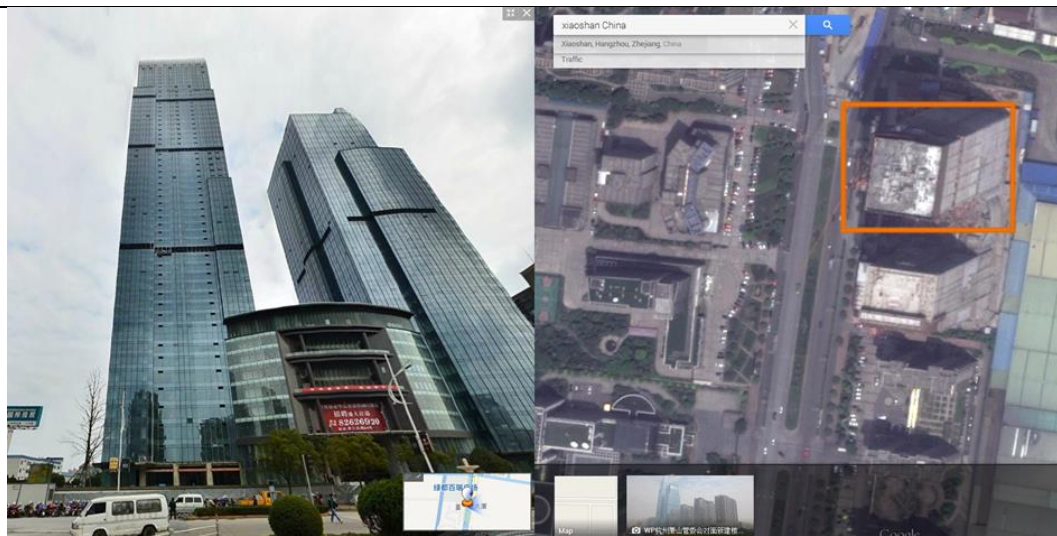
This study used the planar area ratio λ_p and the frontal area ratio λ_f as they had been defined before. The frontal area index was initially calculated over 8 main orientations with 45 degrees azimuth difference and $360^\circ = 0^\circ$ marking the true North. Initial results confirmed previous studies that showed that the frontal area ratio for one wind direction is almost equal to the one of the opposite direction ($\lambda_{f(45)} \approx \lambda_{f(225)}$; $\lambda_{f \text{ North-easterly}} \approx \lambda_{f \text{ South-westerly}}$) (Evans, 2009; Drew et al., 2013). Therefore the frontal area ratio was estimated for 4 main wind directions from 0° (North) to 135° (Southeast). In order to calculate the frontal area ratio the building height was calculated with the assumption of a floor to floor height of 3.1 metres for residential buildings, 3.9 metres for office and 3.5 metres for mixed and unknown use buildings respectively (MIT Building Technology Group, 2000; Council on Tall Buildings and Urban Habitat, 2014). Buildings with more than 14 floors were treated as “tall buildings” and their height was estimated with the Tall Building Height Calculator by the Council on Tall Buildings and Urban Habitat (2014) (Table 5.2).

Table 5.2. Floor to floor height assumption for different building uses. f denotes the number of floors.

Building use	Height assumption (floor to floor) [m]
Residential (houses, hotels)	3.1
Office, commercial	3.9
Mixed, unknown	3.5
Residential – tall (>14 floors)	$H_{res} = 3.1 \times f + 7.75 + 1.55 \times (f/30)$ (Council on Tall Buildings and Urban Habitat, 2014)
Office – tall (>14 floors)	$H_{office} = 3.9 \times f + 11.7 + 3.9 \times (f/20)$ (Council on Tall Buildings and Urban Habitat, 2014)
Mixed – tall (>14 floors)	$H_{mixed} = 3.5 \times f + 9.625 + 2.625 \times (f/25)$ (Council on Tall Buildings and Urban Habitat, 2014)

The error in height calculations was assessed by comparing the height estimations from the images with height measurements on site and building height estimations published online on the Emporis GmbH public website (Emporis GMBH, 2014) (Figure 5.6 and Figure 5.7).

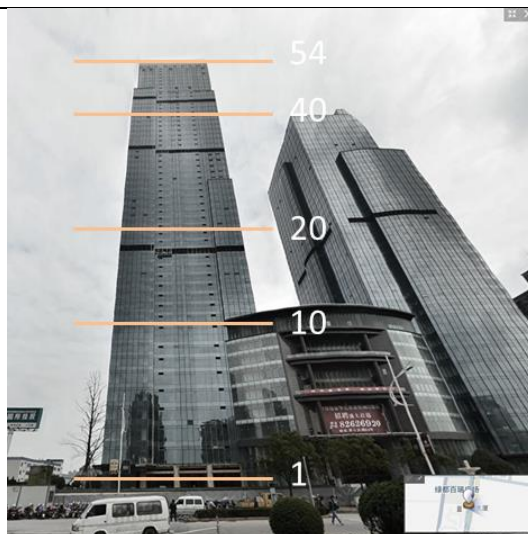
Street (left) (Tencent, 2013) and top plan view (right) of the Radisson Hotel plaza Towers in Hangzhou, China.



Mixed use. Estimated Height = 204 m

Architectural Height = 258m
(Emporis GMBH, 2014).

Error: 20%



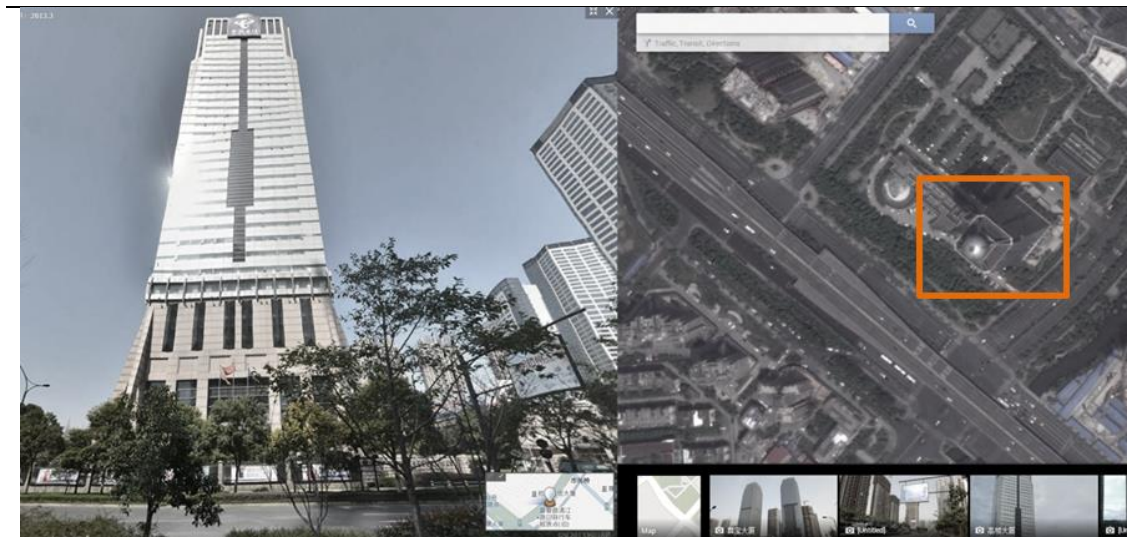
54 floor levels.

Figure 5.6. Estimation of the error in the building height measurement for a mixed use skyscraper in Hangzhou, China. Image sources as referenced in figure labels.

The error in the height calculation was in the range of 20% in the case of tall buildings (>14 floors) and a similar error is to be expected in the case of shorter buildings. However, in the case of tall buildings the height was underestimated while in the case of shorter buildings (<14 floors) this was overestimated. This had been the case when the architectural features of the building facades made difficult to count the number of floors. In buildings with less than 14 floors the height had often been

overestimated because in reality the height assumption of the 3.1 m might have been introducing a systematic error in the height calculation.

Street (left) (Tencent, 2013) and top plan view (right) of the No. 2 Telecom Hub in Hangzhou, China.



Office use. Estimated Height = 159.1 m

Roof Height = 209.1 m (Emporis GMBH, 2014).

Error: 24%



36 floor levels

Figure 5.7. Estimation of the error in the building height measurement of a skyscraper with an office use in Hangzhou, China. Image sources as referenced in figure labels.

Adjustments were applied to the heights of buildings when real data or measures of logical comparison were available. However, the average building footprint-area-weighted height of the total urban unit is expected to have a lower

error than the error for individual buildings due to the averaging of the overestimated and underestimated heights.

In addition, it was considered that the height underestimation of tall buildings will not affect the air flow property assumptions because the roughness length was determined by analysis for the total urban unit. In the idealised urban unit model the mean building footprint-area-weighted height of the buildings in each annuli area was calculated by the overall statistics from the land cover analysis for the studied “LCZ5” sites with the sensors. Lastly, the maximum height of specific tall buildings could have been much higher than the mean building footprint-area-weighted height. The height of these buildings could vary between different locations but it was considered that the air flow properties in the urban unit would remain similar for tall building heights in the range of 100 to 200 m and above. This assumption agrees partially with the results from the Al-Sallal et al. (2001) wind tunnel experiment. Their study concluded that in the case of a staggered array with 2 rows of buildings: 1. The airflow at the top of the front row was not affected by the height difference between the buildings at the front and rear row and 2. When the building at the front row reached and surpassed the height of the building at the rear row, the air velocity at the top of the rear building remained constant and equal to 45% of the upstream velocity (Al-Sallal et al., 2001). The maximum height of the buildings in the urban unit was not included in the simulation modelling due to: 1. the limits of the computational model’s vertical grid size, 2. the unrepresentativeness of single specific tall buildings and 3. the main focus of this thesis on the air temperature development and not on the airflow where the maximum height would have had the largest impact.

The building height h was estimated by counting the floors from the three-dimensional maps and photo images. The use of the building was either implied by the trade signs, its façade views and structural materials or it was described by the Sogou maps’ address directory. The mean building footprint-area-weighted height \bar{H} is (Salamanca et al., 2011) :

$$\bar{H} = \frac{\sum_{i=1}^N A_i h_i}{\sum_{i=1}^N A_i} \quad (m) \quad (5.2)$$

The building height distribution was assessed with the standard deviation of the footprint area weighted building height (e.g. Di Sabatino et al. (2010)):

$$\sigma_H = \sqrt{\frac{\sum_{i=1}^N (h_i - \bar{H})^2}{N-1}} \quad (5.3)$$

The standard deviation of the area weighted height is associated with the influence of height variation on the roughness length z_0 and the displacement height d of the urban unit (Millward-Hopkins et al., 2013). Millward-Hopkins et al. (2013) suggest that σ_H is positively correlated with building density (effectively the λ_p) and there is a linear (non-linear for z_0) relationship between the increase in d (z_0) and the increase in standard deviation of building heights.

The frontal area ratio λ_f was calculated from the area of buildings and urban elements (including trees but excluding bushes and short vegetation) projected onto a section cut along the urban unit's diameter and perpendicular to each of 4 main wind directions with $\hat{\varphi} = 45^\circ$ azimuth difference between them and $\hat{\varphi} = 0^\circ$ marking the true North (Figure 5.8, Equation 5.4). The total projected area was divided by the total surface plan area of the urban unit (A_T) and the frontal area ratios were averaged over the 4 wind directions.

$$\lambda_f = \frac{\sum_{\hat{\varphi}=0^\circ}^{135^\circ} L_{y,\varphi} \times H}{A_T} \quad (5.4)$$

where $L_{y,\varphi}$ is the footprint of the projected area along the disk's diameter at a section cut perpendicular to the wind direction for the 4 main wind directions ($\hat{\varphi} = 0^\circ$, $\hat{\varphi} = 45^\circ$, $\hat{\varphi} = 90^\circ$ and $\hat{\varphi} = 135^\circ$ with $\hat{\varphi} = 0^\circ$ marking the true North). A_T is the total surface area of the urban unit's disk (200,000 m²). The relative percentage error of the symmetry assumption for orientations with a clockwise azimuth difference of $\hat{\varphi} = 180^\circ$ was calculated to be less than 5%.

The calculated frontal areas compared well with the results from other studies (Table 5.3). It is noted that comparison of the frontal area ratio λ_f (and hence z_0) has only meaning to a first approximation of the order of λ_f . A direct comparison was not possible due to the different size and shape characteristics of the urban unit in this study. The studies in Lecce, London and Toulouse (Table 5.3) use an urban unit with a square plan area of 160,000 m² (400m x 400m) (Ratti et al., 2006; Di Sabatino et al., 2010). In this study the urban unit had a circular plan area of $\sim 200,000 \text{ m}^2$ ($\pi * 250^2 \text{ m}^2$).

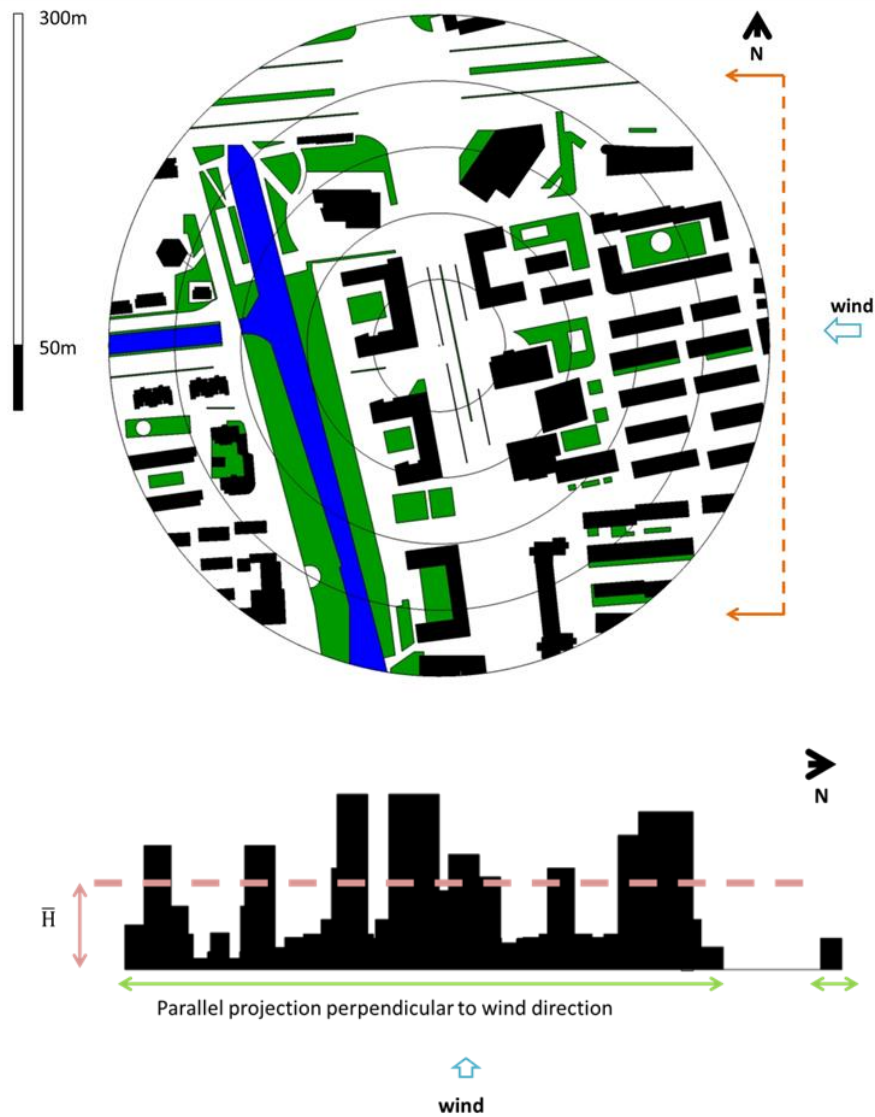


Figure 5.8. Calculation of the frontal area for the urban unit (top). A section cut was made (orange dashed line with arrows, top) perpendicular to the wind's direction. The footprint of the buildings in the projected onto the section cut area (green double arrows, bottom) was estimated and multiplied by the building height h . \bar{H} denotes the building footprint-area-weighted height.

The comparison between the planar area ratios (λ_p) (Table 5.3) showed that density in the Chinese residential districts is similar to the US urban layout (i.e. dispersed buildings into an open space) and does not follow the European paradigm of densely built districts with narrow streets (Figure 5.9) (Di Sabatino et al., 2010). The average height (footprint area weighted) approximated the height of city centre in commercial European districts with tall buildings. However, the skyline in the Chinese

districts is less homogenous with large height variability as shown by the σ_H/\bar{H} in Table 5.3 (Di Sabatino et al., 2010).

Table 5.3 Comparison of morphological characteristics between urban sites in China, Europe and the USA.

DEM Model (reference)	\bar{H} (m)	σ_H/\bar{H}	λ_f	λ_p	d (m)	z_0 (m)
Site 2 (this study)	18	0.76	0.08	0.26	9.1	0.70
Site 3 (this study)	17	0.39	0.06	0.25	8.5	0.40
Site 4 (this study)	24	0.89	0.11	0.21	10.0	1.80
Lecce 1 (Di Sabatino et al., 2010)*	20	0.40	0.55	0.44	14.7	1.37
Berlin (Ratti et al., 2000)**	19	0.23	0.23	0.35	11.4	1.08
Toulouse (Ratti et al., 2000)**	15	0.40	0.32	0.40	10.3	0.89
London (Ratti et al., 2000)**	14	0.37	0.32	0.55	11.0	0.29
Salt Lake City (Ratti et al., 2000)	16	0.87	0.11	0.22	11.6	0.94
Los Angeles (Burian et al., 2002)***	10	na	0.12	0.27	5.7	0.74

* Commercial district; ** Central districts; *** Residential district

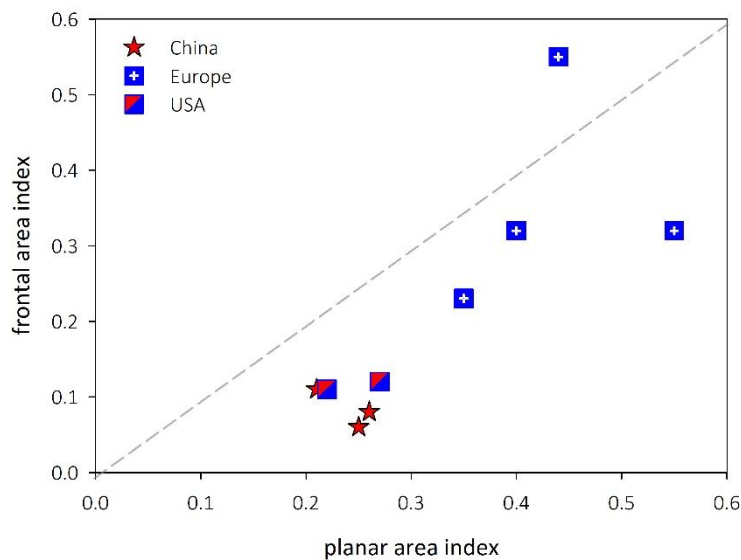


Figure 5.9. Comparison between Chinese (red star), US (red/blue square) residential districts and European (blue/white cross) central districts. European residential districts are expected to have smaller frontal area ratios to these shown but retain the high planar area ratios. Data source references as shown in Table 5.3.

This conclusion points out the difficulties in the selection of a homogenous urban site for urban weather measurements. It is expected that the urban unit model generated in this study included the largest effect of the surrounding urban morphology to the micro-climatic development at the studied sites with sensors.

In the case that digital elevation models are available for the region of interest, a recent study proposed the use of an adaptive grid that divides the city into homogenous cells-“neighbourhoods” according to the calculated morphological parameters (Millward-Hopkins et al., 2013). The adaptive grid approach could not be applied to this study because; 1) digital elevation models for the region of study were not available, 2) the model proposed by Millward-Hopkins et al. (2013) estimates only the aerodynamic parameters and not the weather development, 3) the transferability and validity of their methodology is currently limited to cities with similar characteristics to Leeds, UK and $\lambda_p > 0.5$ and 4) the locations of the sensors had been pre-selected. However, their conclusions on the importance of height variability to the estimation of the aerodynamic properties of urban sites were taken into consideration and the standard deviation of building height σ_H (Di Sabatino et al., 2010; Millward-Hopkins et al., 2013) was included as a parameter in the site analysis.

Following the calculation of the frontal area ratios, the height to width (H/w) aspect ratio averaged over the urban unit was then calculated as a function of the frontal and the planar area indices (Bohnenstengel et al., 2011):

$$\overline{H}/\overline{w} = \pi \lambda_f / 2 (1 - \lambda_p) \quad (5.5)$$

where the factor $\frac{\pi}{2}$ represents the averaging over all orientations (Porson et al., 2010; Bohnenstengel et al., 2011).

The aspect ratios of the street canyons where the sensors were located were individually estimated according to the length (along the street side dimension) weighted height of buildings bordering the street and the street’s width. This estimation was essential for the correct classification of the locations because a) the generic aspect ratio of the urban unit was not always representative of individual streets and b) the sensors were located at low height levels at the sides of streets.

The standard deviation σ_H and the variance of the building footprint-area-weighted height were used as indicators of the buildings’ height variation (Grimmond & Oke, 1999).

The sky view factor (SVF) exhibits a seasonal variation trend due to the trees’ leaf canopy. Although all the trees in the under-the-canopy method followed in this study were substituted with an assumption for the plot area of the street planted

verges (typically 0.5 to 2 metres width) or the park that contained them, the sky view factor at the location of the sensor was calculated for the cases of both bare trees and trees covered with leaves. The average value of the two was used in the urban classification process when needed.

Full frame high resolution, circular fisheye images of the sky dome were taken at a height of 1.5 metres (using a tripod for consistency between measurements) above ground on the sites with a sensor. In most images the lamppost where the sensor was located was at the centre of the image and it had to be manually removed. The pictures were taken in May 2013 when the tree canopy was at its full extent. In order to assess winter conditions, all trees were considered to be deciduous and the leaves were removed through image processing (Figure 5.10). The SVF was calculated with the Sky View Factor Calculator, Version 1.1. The calculator follows the methods of Holmer et al. (2001) and Johnson and Watson (1984). Under the assumption of an adequately homogenous urban unit the average SVF value of the two methods and seasons was selected as the one representative of the annual local specific conditions. A list with the seasonal SVF values and the annual estimation can be seen in Appendix B.

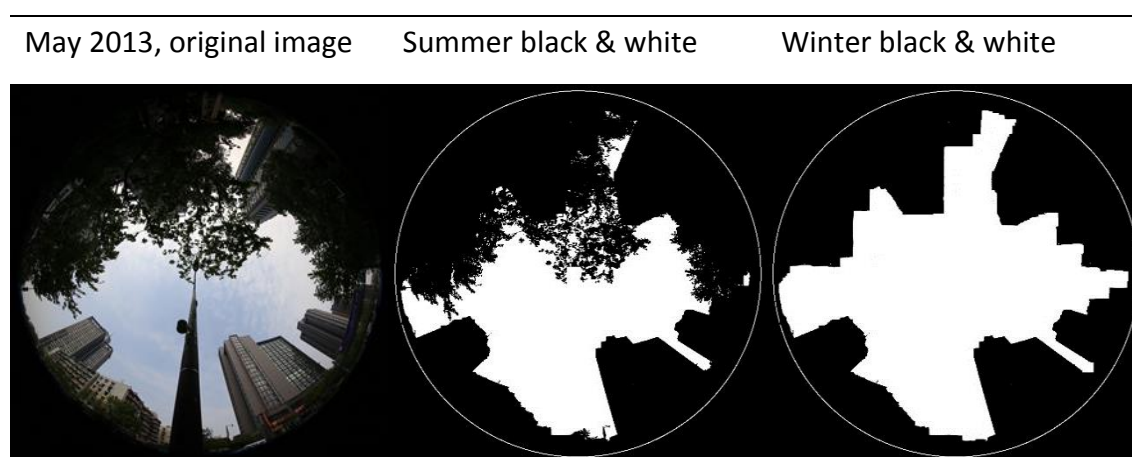


Figure 5.10. Calculation of the seasonal and average Sky View Factor (SVF). The original circular fish-eye (left), black and white for the summer (middle) and adjusted for winter (right) images used for the SVF estimation respectively.

The aerodynamic characteristics of the urban environment as described with the zero-plane displacement (d) and the roughness length (z_0) are important for the modelling of wind flow and turbulence within the urban canopy and above (Grimmond & Oke, 1999). This study followed a morphological approach to the estimation of z_0

and d (Britter & Hanna, 2003; Drew et al., 2013) with the use of the expressions introduced by Macdonald et al. (1998) and described by Drew et al. (2013) :

$$\frac{z_0}{H} = \left(1 - \frac{d}{H}\right) \exp \left\{ - \left[0.5 \beta \frac{C_D}{\kappa^2} \left(1 - \frac{d}{H}\right) \lambda_f \right]^{-0.5} \right\} \quad (5.6)$$

$$\frac{d}{H} = 1 + A^{-\lambda_p} (\lambda_p - 1) \quad (5.7)$$

where C_D is the drag coefficient which has a value of 1.2 based on the mean-square wind over the face of a cube in shear flow (ESDU, 1980; Macdonald et al., 1998; Drew et al., 2013). β is a correction factor for the specific form and shape of the obstacles and A is an experimental coefficient. In this study the values $A = 4.43$ and $\beta = 1$ used in the analysis were representative of a staggered array of obstacles (Drew et al., 2013). The equations (Equations 5.6 & 5.7) by Macdonald et al. (1998) generally underestimate the roughness length in the case of cities with large building-height variability (Di Sabatino et al., 2010). The inclusion of building height-variability increases the estimated values and there are strong indications that a detailed height distribution analysis is important for the prediction of the aerodynamic parameters in real urban areas (Millward-Hopkins et al., 2013). The simplistic approach by Macdonald et al. (1998) was selected over more detailed methodologies because a) most neighbourhoods in China have a uniform building height distribution according to their use and location, b) the selected method facilitated the generation of the idealised urban unit model and c) roughness length and displacement height were used in conjunction with the rest of the morphological parameters and they were only presented as an initial estimation of the aerodynamic properties for the urban unit.

The outcomes of the urban morphology analysis were used with the information on the use of the sites in Hangzhou in order to categorise them into classes in the Local Climate Zones scheme.

3. Urban classification (Step 2)

In urban micro-scale models, the lower boundary conditions are usually provided by an explicit description of the surface geometry and the physical properties of the

materials. In meso-scale weather models land use classifications retain information about the aggregated aerodynamic properties of the surface and its area averaged thermal properties (Baklanov et al., 2008). Meso-scale models often include an urban canopy parameterisation that turns the overall effects of the urban canopy's features on the local energy budget into single area-averaged values (Martilli & Santiago, 2007). However, urban canopy parameterisations cannot adequately describe the weather development within the roughness sub-layer as they are mainly aiming at the estimation of area-averaged variables at the top of the respective grid cell (Martilli & Santiago, 2007). Conversely, detailed description of the surface cover requires significant computational power and time (Baklanov et al., 2010). Furthermore, simulation results are valid only for the specific modelled surface and they have rather limited generality and transferability to different urban morphologies.

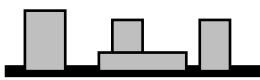
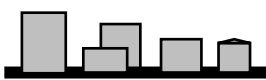





Building on the urban unit and the morphology analysis of the sites with a sensor as described before, this study developed a method for the estimation of local specific weather development based on a combination of a local urban classification scheme and the micro-climatic simulations with the use of an idealised urban unit model for sites with a residential / institutional (university, college) use and a humid sub-tropical climate. The main advantage of using such a surface classification scheme is that it provides generic input data for the simulation model (Stewart & Oke, 2012) and the simulation results can be attributed back to typical urban morphology characteristics.

3.1 Local Climate Zones – urban classification scheme

Ellefsen (1991) has developed a detailed urban classification based on the observation of aerial photographs and on site measurements in ten U.S. cities. His classification scheme, the Urban Terrain Zones, contains a dense information matrix of the urban forms' layout and construction characteristics (Ellefsen, 1991). However, that scheme is based on empirical data from U.S. cities and its applicability is rather restricted to locations with a similar architectural and building tradition (Baklanov et al., 2008). Nonetheless, the classification was tested in several cities worldwide with good evidence of a universal generalisation (Oke, 2006). Following from the work of Ellefsen, Oke (2006) introduced the Urban Climate Zones' classification scheme. In his work, the

urban morphology has been grouped into 7 distinct classes according to parameters such as the height to width aspect ratio, ground permeability, height and use of buildings and urban density in a generic urban unit (Oke, 2006) (Table 5.4).

Table 5.4. The Urban Climate Zone classification scheme. Table adapted from Oke (2006).

Urban Climate Zone, UCZ	Image	Roughness class	Aspect ratio	% Built (impermeable)
1. Detached close-set high rise buildings with cladding		8	>2	>90
2. High density urban, 2-5 storeys, attached or very close often with brick or stone		7	1 – 2.5	>85
3. Medium density urban, terraced and detached houses and flats		7	0.5 – 1.5	70 - 85
4. Medium to low density, low buildings with parking plots (e.g. warehouses)		5	0.05 - 2	70 - 95
5. Low density suburban with 1 to 2 storeys		6	0.2 – 0.6, Up to >1 with trees	35 - 65
6. Mixed use, large buildings in open landscape (e.g. airport)		5	0.1 – 0.5, depends on trees	<40
7. Semi-rural, houses in natural or agricultural areas (e.g. farms)		4	>0.05, depends on trees	<10

Building upon the Urban Climate Zones, Stewart and Oke (2012) have proposed a detailed urban classification based on the micro-climatic properties of different urban – land types. Each zone (i.e. thermally homogenous region of uniform surface characteristics) in the scheme exhibits a distinct diurnal temperature development profile at “screen” height (~1.5 to 3m) at the local scale (Stewart & Oke, 2012). The resulting Local Climate Zones (LCZs) as they are called in the scheme describe 17

distinct generic environments consisting of 10 classes for built (e.g. open high-rise) and 7 for land cover types (e.g. scattered trees) (Stewart & Oke, 2012; Stewart et al., 2014).

Table 5.5. The main classification parameters from the Local Climate Zones scheme. Adapted from Stewart and Oke (2012).

LCZ	Zone name
<i>Zone Definition</i>	
Form	Building geometry and materials, land cover, vegetation and human activity.
Function	Most likely land uses. Location in a city (e.g. periphery, city core)
<i>Zone properties</i>	
Aspect Ratio H/W [0 – 3 ⁺]	Mean Height to Width ratio of the street canyon where the sensor is. In the case of sparsely built areas it is equal to building spacing. Affects airflow characteristics and amount of solar radiation to and from building surfaces.
Mean building height \bar{H} [0 – 50+ m]	Area weighted average of building heights. Affects the exposure of surfaces to solar radiation, air flow and heat dispersion above ground.
Terrain roughness class [1 – 8]	According to Davenport et al. (2000) effective terrain roughness classification scheme (based on the roughness length z_0). Affects the exposure of surfaces to solar radiation, air flow and heat dispersion above ground.
Building surface fraction F_r [0-100%]	Proportion of ground surface covered by buildings. Affects the exposure of surfaces to solar radiation, air flow and heat dispersion above ground.
Impervious surface fraction I_r [0-100%]	Proportion of ground surface covered by roads, rock and pavements. Affects the exposure of surfaces to solar radiation, air humidity and heating/cooling potential.
Pervious surface fraction P_r	Proportion of ground surface covered by soil, vegetation and water. Affects the exposure of surfaces to solar radiation, air humidity and heating/cooling potential.

Each Zone is represented by a set of ten morphological parameters and a descriptive definition with illustrations of the location and the use of typical urban sites

classified into this zone. A full list of the Local Climate Zones with their properties and description is available in Appendix C. The complete datasheets with illustrations are available at the original paper from Stewart and Oke (2012).

Each urban site in Hangzhou (i.e. site with a sensor) was classified according to the land cover analysis into a “Local Climate Zone”. The main morphology parameters used for the classification of the monitored sites were: the canyon aspect ratio, the neighbourhood average aspect ratio, the mean building footprint-area-weighted building height, terrain roughness class, the building surface fraction, the impervious surface fraction and the pervious surface fraction. A detailed description of the main parameters from the classification scheme can be seen in Table 5.5. Parameters that exhibit a seasonal trend such as the Sky View Factor (SVF) and the albedo were not taken into consideration. This conformed to the guidelines for site classification (Stewart & Oke, 2012).

The recommended by the classification scheme urban unit is a disk with a minimum radius of 200 – 500 m. It is suggested that at this distance the urban unit will contain the source area footprint of the temperature signal which will be representative of the local specific land surface cover (Stewart & Oke, 2012). This assumption was determined by the analysis of the vegetation impact on air temperature in relation to the distance from the centre of the urban unit as presented before.

3.2 Urban classification results

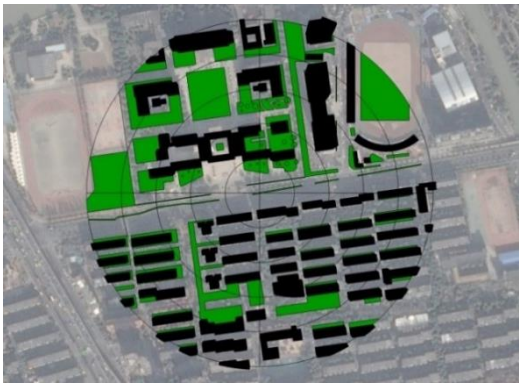
This study had focused on the nine sites in Hangzhou classified as “LCZ5” (Figure 5.11). Three additional sites were initially classified into the “LCZ5” Zone but they were excluded because they were located next to large water bodies or they did not have homogenous characteristics.

The “LCZ5” Zone denotes midrise buildings at a medium density arrangement typically having a residential / institutional (universities) use (Figure 5.12) (Stewart & Oke, 2012). The observed diurnal temperature range and the UHI magnitude at the nine studied sites were further analysed for a selection of cold (i.e. 14 days in January) and warm (i.e. 17 days in July) days.



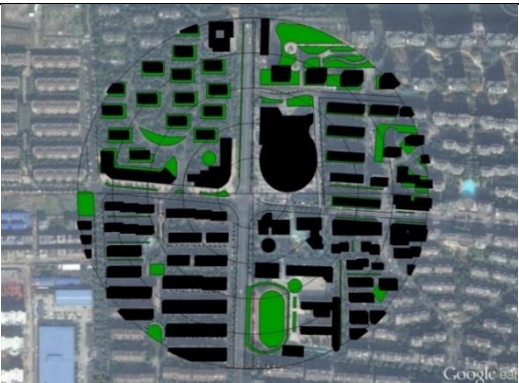
Figure 5.11. The nine urban units (sensor locations, marked with blue bullets) in Hangzhou classified into Local Climate Zone 5. The Mantou Mountain, National Principle Weather station’s location is marked as NP.

Site plans for typical urban units in Hangzhou with a residential/institutional primary use.



Site 1. $P_r : 0.23$ $I_r : 0.57$ LCZ : 5
 $F_r : 0.21$ $z_0 : 1.1\text{m}$

Site 2. $P_r : 0.16$ $I_r : 0.58$ LCZ : 5
 $F_r : 0.26$ $z_0 : 0.7\text{m}$



Site 4. $P_r : 0.12$ $I_r : 0.63$ LCZ : 5
 $F_r : 0.25$ $z_0 : 0.4\text{m}$

Site 7. $P_r : 0.24$ $I_r : 0.54$ LCZ : 5
 $F_r : 0.21$ $z_0 : 0.6\text{m}$

Figure 5.12. Land cover analysis for Sites 1, 2 (top) and 4, 7 (bottom) in Hangzhou (see Figure 5.11). The buildings are marked with black, vegetation with green, water with blue and the residual area is considered impermeable surface (e.g. pavement, asphalt, dry soil).

The most important finding was that the nine sites classified in this study in the “LCZ5” Zone (Figure 5.11) had similar diurnal temperature ranges between each other with an UHI intensity standard deviation $< 1^{\circ}\text{C}$.

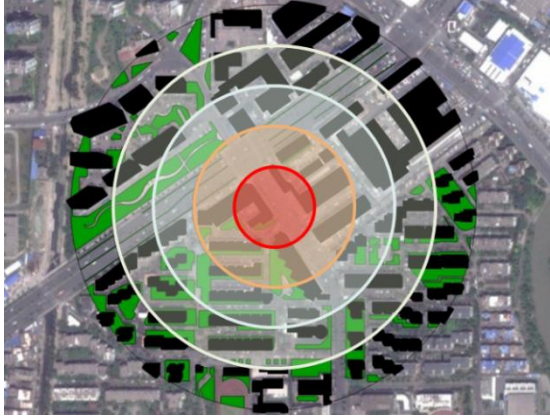
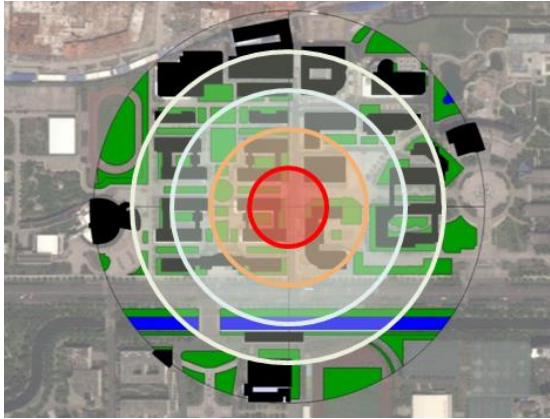
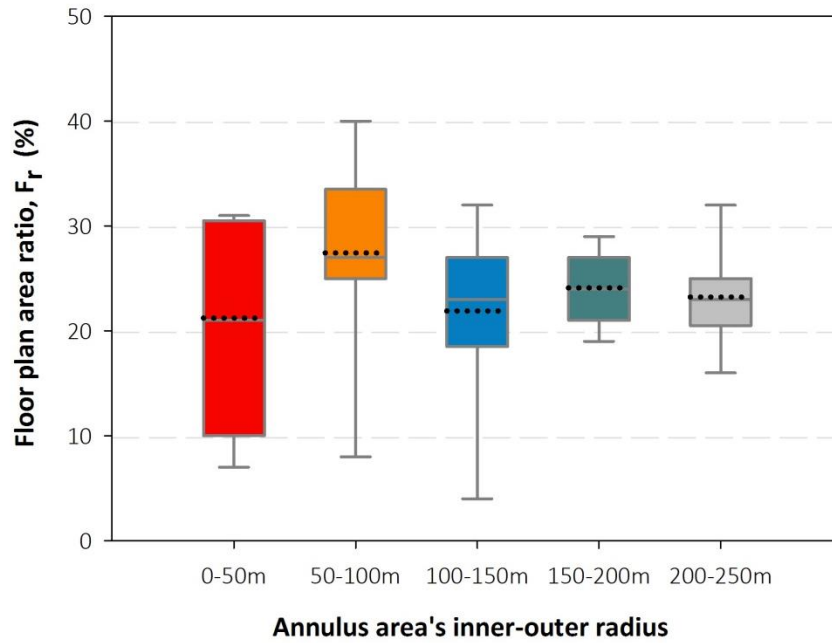
Site 2.	R-r (m)	P_r	I_r	F_r	z_0	σ_H/\bar{H}
	0-50 (red)	0.05	0.64	0.31	1.5	0.52
	50-100 (orange)	0.11	0.62	0.27	1.3	0.45
	100-150 (blue)	0.17	0.56	0.27	1.2	1.08
	150-200 (green)	0.16	0.60	0.24	1.7	0.99
	200-250 (outer)	0.19	0.56	0.25	2.1	0.87
Site 7	R-r (m)	P_r	I_r	F_r	z_0	σ_H/\bar{H}
	0-50 (red)	0.18	0.51	0.31	1.8	0.44
	50-100 (orange)	0.18	0.54	0.28	1.6	0.42
	100-150 (blue)	0.24	0.59	0.17	2.3	0.40
	150-200 (green)	0.24	0.50	0.27	1.2	0.85
	200-250 (outer)	0.28	0.56	0.16	1.4	0.89

Figure 5.13. Analysis of the morphological parameters for each annulus area two of the nine “LCZ5” sites .Site numbers refer to locations in Figure 5.11.

Urban morphological parameters and descriptive statistics were calculated for all the annular areas (i.e. 0-50 m (red), 50-100 m (orange), 100-150 m (blue), 150-200 m (green), 200-250 m (outer) as shown in Figure 5.13).

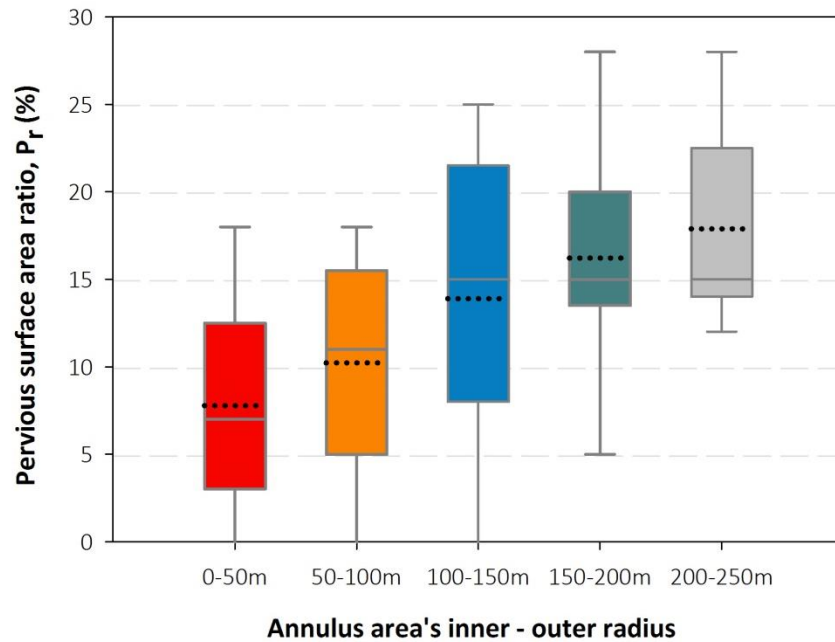


F_r / annulus area	0-50m	50-100m	100-150m	150-200m	200-250m
mean	21.2	27.4	21.9	24.1	23.2
median	21.0	27.0	23.0	24.0	23.0
σ	10.0	9.1	8.1	3.4	4.4
Percentiles	Cut-off values				
2.5	7.0	8.0	4.0	19.0	16.0
25	10.0	25.0	18.5	21.0	20.5
75	30.5	33.5	27.0	27.0	25.0
82.5	31.0	38.5	28.3	27.5	26.8

Figure 5.14. Distribution of the building footprint surface to area ratio F_r . The annular areas in the diagram correspond to the annular areas in the urban unit with the core (0-50m) being at the centre of the disk.

In all sites the impervious surface area I_r exceeded 50% of the total area. The pervious surface to area ratio P_r increased with distance from the centre. The building footprint to the total area (F_r) ratio, the roughness length (z_0) and the standard deviation of the building footprint-area-weighted height (σ_H/\bar{H}), adjusted for the average area-weighted height, remained in the same range. A summary of the results from the urban morphology analysis for the nine studied sites is shown in Figure 5.14, Figure 5.15, Figure 5.16 and Figure 5.17.

The mean building footprint surface to area ratio varied from 20% to 30% and the standard deviation was less than 10% (Figure 5.14). 80% of the building footprint surfaces to area ratio measurements had a value between 5% and 40%.

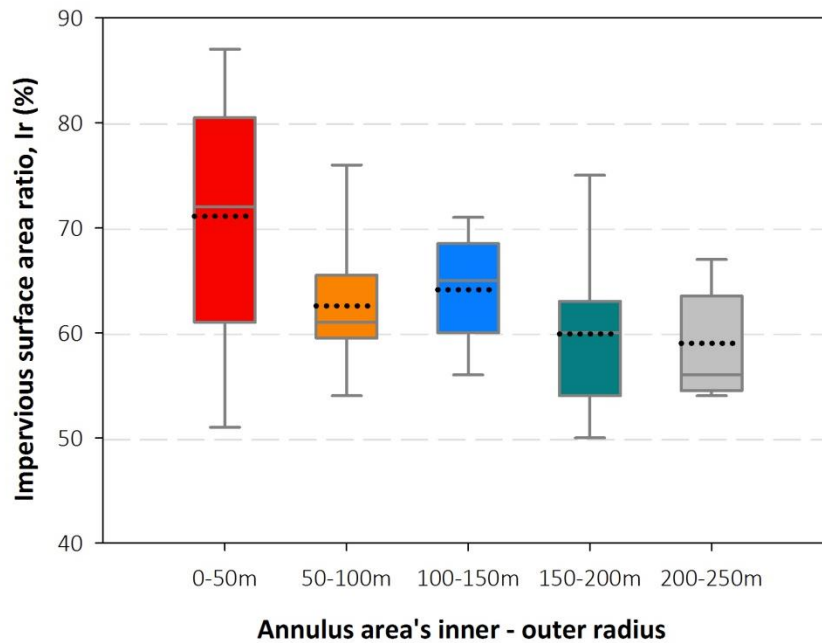


P_r / annulus area	0-50m	50-100m	100-150m	150-200m	200-250m
mean	7.8	10.2	13.9	16.2	17.9
median	7.0	11.0	15.0	15.0	15.0
σ	5.8	6.1	8.3	6.6	5.5
Percentiles	Cut-off values				
2.5	0.0	0.0	0.0	5.0	12.0
25	3.0	5.0	8.0	13.5	14.0
75	12.5	15.5	21.5	20.0	22.5
82.5	14.3	16.5	24.3	25.0	25.0

Figure 5.15. Distribution of the pervious surface to area ratio P_r . The annular areas in the diagram correspond to the annular areas in the urban unit with the core (0-50m) being at the centre of the disk.

The largest range was noted in the second annulus area (50-100m (orange) in Figure 5.14). The distribution of the values was skewed to the right (i.e. the mean is greater than the median in most cases) but the degree of skewness was low (i.e. there is a small difference between mean and median).

The pervious surface to area ratio for the studied sites was in the range of 0% to 30 % for all annular areas. The standard deviation of the ratio was almost the same for all annuli and lower than 10% (Figure 5.15). The difference between the mean and the median values was small with the mean being higher than the median in the annular areas R-r=0-50m (red), 150-200m (green), 200-250m (outer) (distribution skewed to the right).

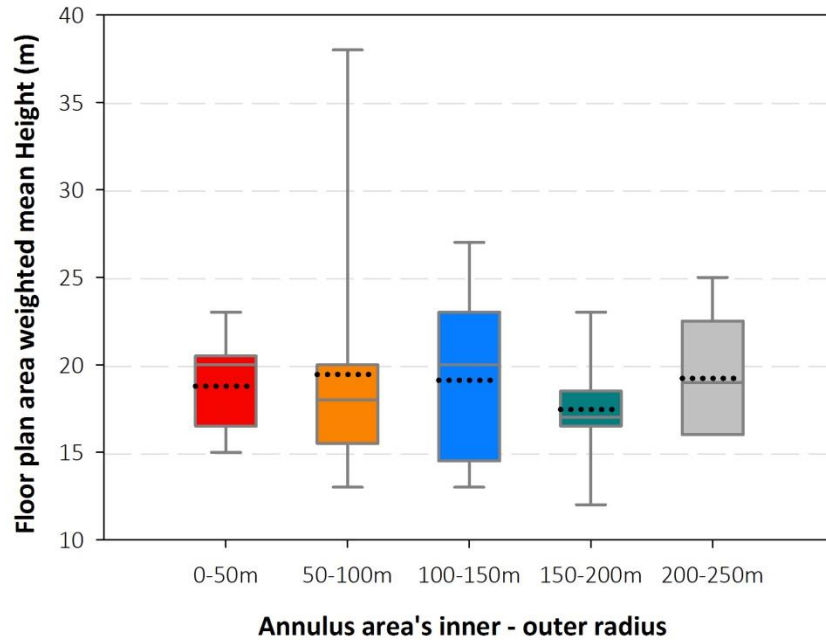


I_r / annulus area		0-50m	50-100m	100-150m	150-200m	200-250m
mean		71.1	62.6	64.1	59.9	59.0
median		72.0	61.0	65.0	60.0	56.0
σ		11.8	6.2	5.0	7.3	5.0
Percentiles	Cut-off values					
2.5		51.0	54.0	56.0	50.0	54.0
25		61.0	59.5	60.0	54.0	54.5
75		80.5	65.5	68.5	63.0	63.5
82.5		84.8	69.3	70.3	66.0	65.5

Figure 5.16. Distribution of the impervious surface to area ratio I_r . The annular areas in the diagram correspond to the annular areas in the urban unit with the core (0-50m) being at the centre of the disk.

The impervious surface to area ratio varied from 50% to 80% with the central annulus area having the larger standard deviation value (Figure 5.16). The difference

between the mean and the median values was again small. The highest ratios were observed in the R-r=0-50m (red) annulus which also had the largest ratio range. This can be explained by the location of the sensors.



\bar{H} / annulus area	0-50m	50-100m	100-150m	150-200m	200-250m
mean	18.7	19.4	19.1	17.4	19.2
median	19.5	18.0	20.0	17.0	19.0
σ	2.6	7.3	4.8	2.9	3.5
Percentiles	Cut-off values				
2.5	15.0	13.0	13.0	12.0	16.0
25	16.5	15.5	14.5	16.5	16.0
75	20.5	20.0	23.0	18.5	22.5
82.5	21.5	24.5	24.0	20.0	24.3

Figure 5.17. Distribution of the mean floor plan area weighted \bar{H} . The annular areas in the diagram correspond to the annular areas in the urban unit with the core (0-50m) being at the centre of the disk.

The requirement for easy access to the sensors and their installation on lamp-posts in most of the cases led to the selection of locations on street verges and central reservations surrounded by roads and pavements. Consequently the impervious

surface to area ratio had often been higher close to the centre of the urban unit than in the outer annuli.

The maximum building height was not one of the primary parameters in the classification process despite its importance for the aerodynamic properties of the unit (Di Sabatino et al., 2010). The height of the buildings in the idealised urban unit model was based on the mean building-footprint-area weighted height. The median building height was about 19m and the standard deviation was below 8m that is the equivalent height of three floors (Figure 5.17). The building footprint-area-weighted height was similar across all the annuli showing good height homogeneity within the studied urban units. The results of the statistical analysis were used for the development of an idealised thermally equivalent urban unit.

4. The idealised “urban unit” model (Step 3)

The typical urban form of residential districts in densely populated Chinese cities consists of blocks with high or mid-rise, multi-storey buildings of flats in an open terrain that contains vegetation and sometimes water features. The buildings are usually built in geometric arrangement and they are uniform in height.

Neighbourhoods share similar generic patterns of building shape and size, street size and vegetation reservations and zones. Yang et al. (2011) classified the city centre of Shanghai into four zones according to the Urban Climate Zones scheme from Oke (2006). Their study recognised four different residential site layouts that are described as Long-linear, Linear, Semi-enclosed and Interspersed and are linked to long rectangular “galley tall buildings”, “tall buildings” and “tower buildings” (Figure 5.18) (Yang et al., 2011). Residential blocks in Hangzhou and Ningbo follow similar urban form patterns to Shanghai with clear similarities in the residential building design (Figure 5.19). The urban form analysis for the studied sites identified a repeated, regular appearance of the long-linear and linear block layouts (Figure 5.18 & Figure 5.19, Bottom). Tall buildings with flats are usually connected with a ground floor galley that has a commercial use. The buildings are typically bounded by patches of vegetation that comprise lawn, short bushes and medium height trees. Tertiary streets (see next paragraph) connect the buildings with the main roads. Street vegetation reservations are typically planted with short bushes.

Streets were classified as primary (arterial), secondary (collector) and tertiary (local) according to their width and use (Salagoor, 1990). Primary, arterial roads (marked as red in Figure 5.19) were multi-lane, wide roads with a minimum of 6 traffic lanes, width of 30 to 60 metres, a central planted reservation, side roads for slower or public transport and planted verges (Figure 5.19). The width of secondary streets (marked as yellow in Figure 5.19) varied from 20 to 30 metres. Secondary streets had usually been connected to the main, primary roads and served the traffic inside the district.

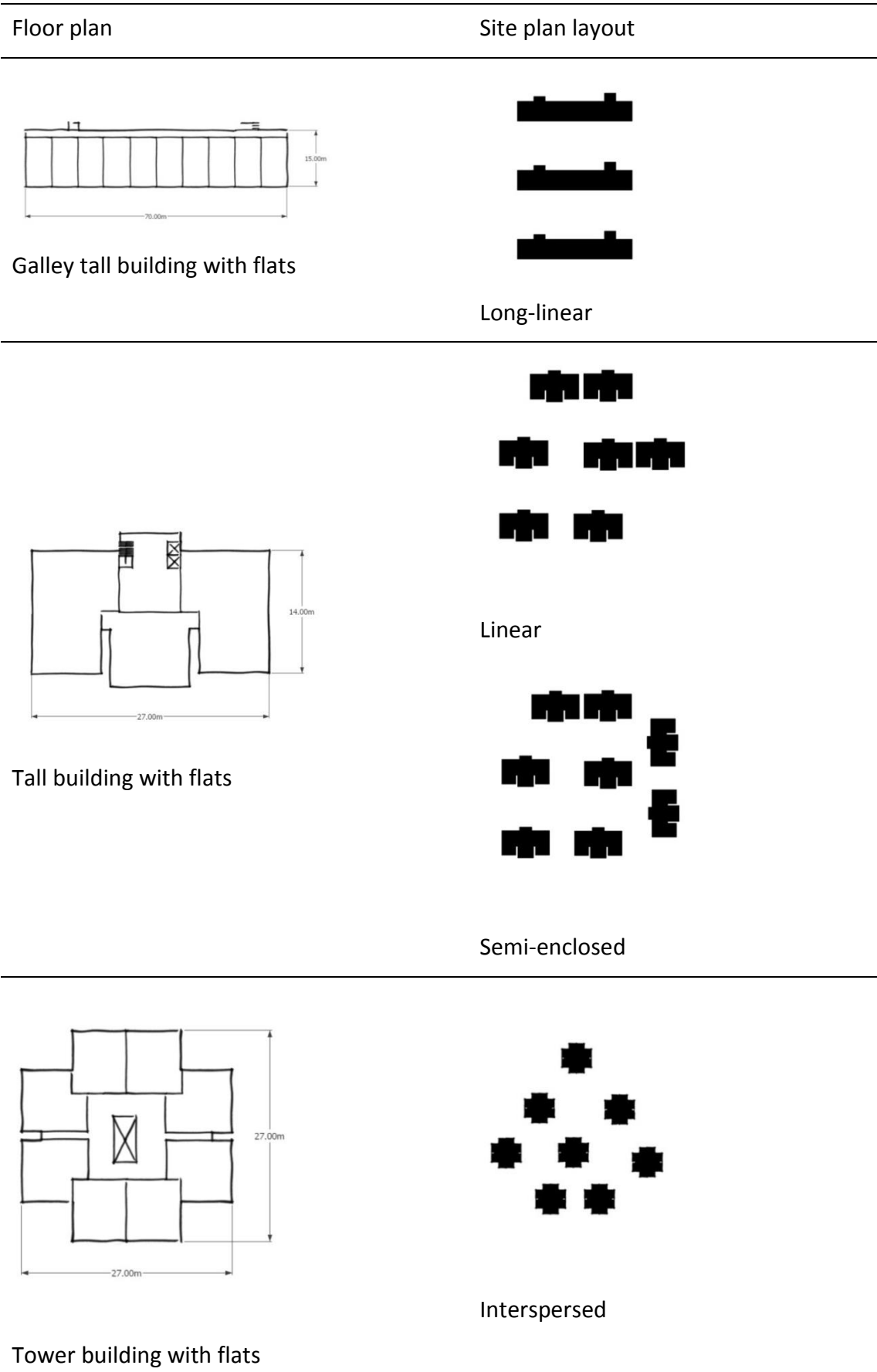


Figure 5.18. Typical building floor plans (left) and residential urban forms (right) in Shanghai. Figure redrawn from Yang et al. (2011).

Secondary streets typically had 4 traffic lanes without a central reservation and the verges were paved to facilitate pedestrian movement and local businesses. Side lanes were sometimes used for car parking. On the pavements, there were areas of vegetation planted with medium height trees that shade the street and the pavements themselves (Figure 5.19).



Figure 5.19. Residential urban forms in Hangzhou. Primary streets are marked with red, secondary with yellow and tertiary with blue. Tall buildings (top left) form an interspersed site layout while medium rise buildings (bottom left) are built in a linear / long linear form. The relative size of the streets and the aspect ratios of street canyons are shown in the street level images (top and bottom right). The camera view is marked with dotted lines (left side maps).

Lastly, tertiary streets (marked as blue in Figure 5.19) typically had 2 lanes and passed through blocks of buildings to connect with secondary roads. The pedestrian pavements were narrow and the street was mainly used by the residents or workers of

nearby buildings. In Hangzhou and Ningbo, tertiary streets were usually shaded in summer by tree canopies from trees planted at the sides.

4.1 Morphological characteristics

The morphological characteristics of each annulus were based on the median value observations from the statistical analysis for the nine LCZ5 urban units (Table 5.6). The median was preferred over the mean because it is not affected by extremely low or high values and the calculated distributions were skewed rather than normal.

Table 5.6. Overview of the median and the (range) of 80% of the observations for key morphological parameters.

Annulus R-r (m)	\overline{H} (m)	P_r (%)	I_r (%)	λ_f (%)	λ_p (%)	d (m)	z_0 (m)
0-50	20 (15-22)	7 (0-15)	72 (50-85)	17 (7-25)	21 (7-30)	6.7 (3.6-11.1)	1.8 (1.3-4)
50-100	18 (13-25)	11 (0-17)	61 (54-70)	15 (6-20)	27 (8-40)	8.9 (3.6-12.9)	1.4 (0.5-3)
100-150	20 (13-24)	15 (0-25)	65 (56-70)	13 (6-20)	23 (4-30)	7.6 (2.0-10.6)	1.8 (0.5-3)
150-200	17 (12-20)	15 (5-25)	60 (50-66)	14 (10-17)	24 (19-28)	8.6 (5.5-9.7)	1.2 (0.7-2)
200-250	19 (16-24)	15 (12-25)	56 (54-66)	13 (10-20)	23 (16-27)	8.3 (5.8-11.3)	1.8 (0.7-3)

The results indicated that the idealised urban unit had a constant floor plan to area ratio (P_r) between 20% and 30% in all the annular areas (Table 5.6). The building floor area-weighted height was highest in the 100-150m annulus but the difference in average height between all the annuli was less than the residential building level height (i.e. 3.1m). The building footprint-area-weighted height \overline{H} was represented in the idealised urban unit model with the buildings of each annulus having the same height as the calculated parameters.

The impervious surface area was four times greater than the pervious one indicating that in the studied sites the prevalent features were buildings, streets and paved surfaces. Water surfaces were included in the pervious surface area with the

exception of water masses that were contained in tanks and pools with artificial, impervious walls.

The high roughness length z_0 (m) was indicative of the roughness of the urban environment. The roughness length has the physical meaning of the height where the assumed logarithmic wind profile in the surface layer above the rooftops has a zero wind speed. In the case of urban environments, this zero wind speed point is calculated at a height above the zero plane displacement height d (m). In practice that would mean a height of approximately 10 metres above street level. ENVI-met allows at the reference point where wind speed was measured a maximum roughness length of 0.1 m otherwise it fails to initialise the 1D boundary layer model. The maximum allowed value was used in the simulations.

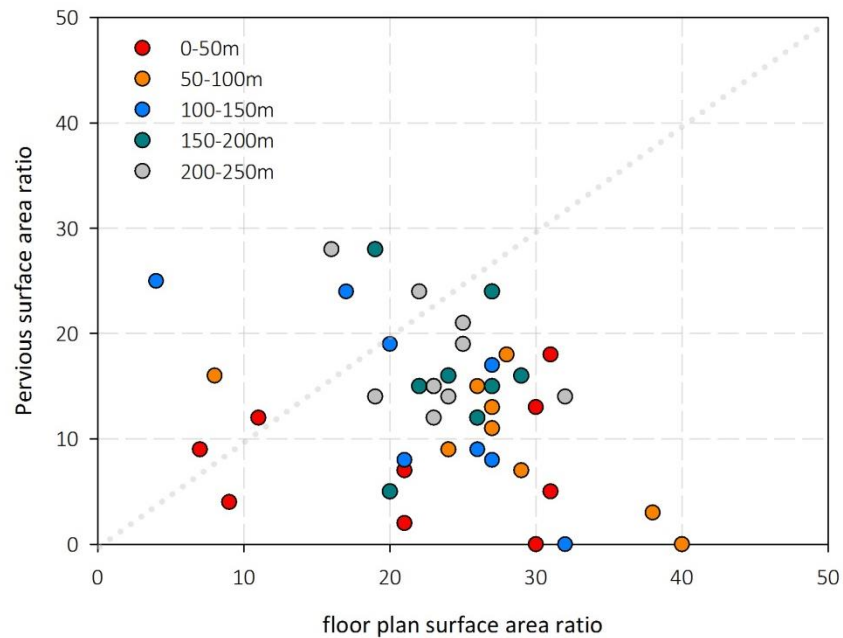


Figure 5.20. Pervious surface to area ratios (%) for different values of floor plan surface to area ratios (%) for the nine studied sites. A 1:1 reference line is shown on grey and dotted.

The correlation between the building floor plan to area ratio and the pervious surface to area ratio was statistically insignificant ($r_s(43) = -0.291 < 0.294$ ($p=0.05$)) (Figure 5.20). Statistically insignificant was also the correlation of the building floor plan to area ratio with the annulus area ($r_s(43) = -0.125 < 0.294$ ($p=0.05$)) (Figure 5.21) and the correlation between the impervious surface to area ratio and the roughness length ($r_s(43) = 0.187 < 0.294$ ($p=0.05$)) (r_s is the Spearman rank correlation coefficient, with 43 degrees of freedom at the 95% confidence level ($p=0.05$)).

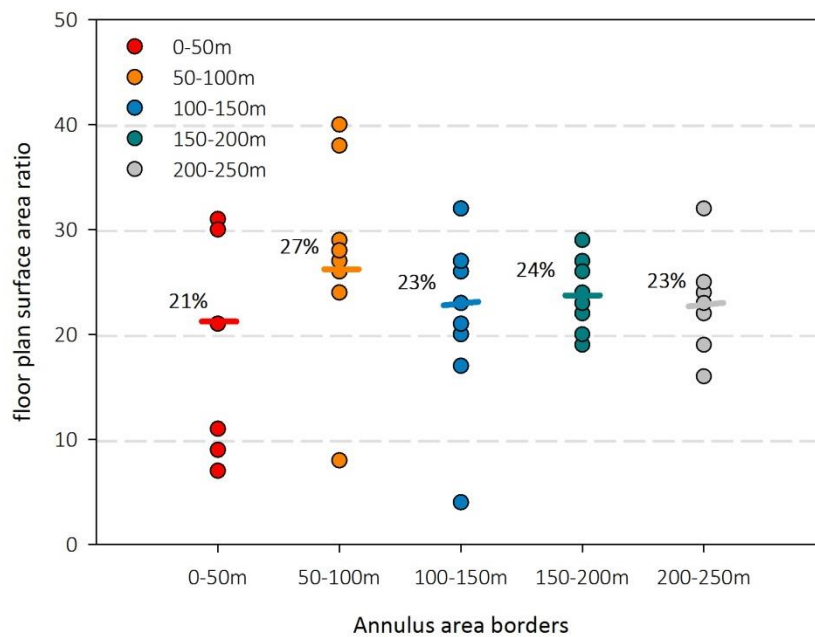


Figure 5.21. The building floor plan surface to area ratio (%) per annulus. Solid lines with percentages show the median of the distribution.

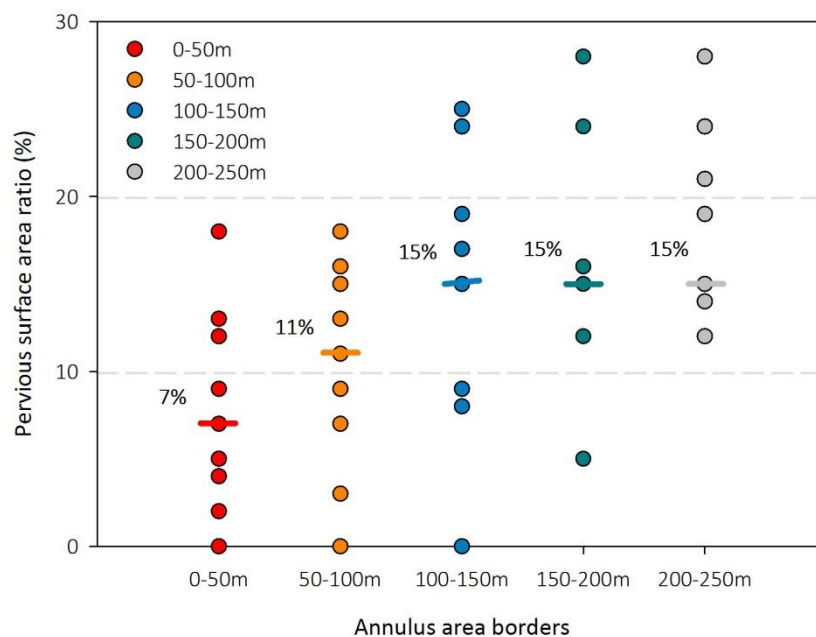


Figure 5.22. The pervious surface to area ratio (%) per annulus. Solid lines with percentage values show the median of the distribution.

The pervious surface to total area ratio increased with the distance from the centre of the urban unit (Figure 5.22). This positive correlation ($(r_s(43)=0.503 > 0.294$ ($p=0.05$)) is strictly location specific (i.e. nine studied sites in Hangzhou) but it was

meaningful for the study of temperature development in relation to ‘green’ space in the context of Hangzhou.

4.2 Construction of the “urban unit” model

In idealised models, building geometry is usually simplified with arrays of cubes. Typical methods use cubes in staggered or aligned arrays (Cheng & Castro, 2002b; Xie & Castro, 2006; Santiago et al., 2007; Kanda & Moriizumi, 2009; Millward-Hopkins et al., 2013). Cubes in regular arrays are spaced at repeated intervals equal in all directions to the cube’s edge length (i.e. aspect ratio = 1). In this study however, the generic “urban unit model” was comprised of square based boxes (i.e. blocks) with a non-uniform height in a staggered irregular array (Figure 5.23, bottom). Each block had a base equal to the computational grid cells’ horizontal dimensions. For example, the minimum building footprint area in this study was 64 m² because the computational grid cells had horizontal dimensions of 8 m (x) x 8 m (y). Regarding the vertical grid dimension (z), any building and vegetation in the urban unit model had a minimum height equal to the height of the first vertical grid cell (i.e. 0.50m). Each block could represent a building (black), vegetated surface (green, grass or tree) or water surface (blue, zero height). The residual space between the blocks represented the impervious surface (grey, e.g. roads, paved areas) (Figure 5.23). The distance between the building blocks in each annulus area was random and the number of blocks representing buildings and vegetation was defined by the estimated F_r and P_r ratios respectively. The distribution of the blocks in each annular area was similar in all notional quarter annuli (i.e. 1/4th of the total annular area). The changes to the packing density and distance between the blocks produced a randomly dispersed layout that is expected to fit better the high spatial inhomogeneity of real cities than a regular staggered cube array.

An illustrated summary of the morphology characteristics of the annular areas in the “urban unit” model is available in Appendix D. The novel “urban unit” model, which was produced with the statistical land cover and urban morphology analysis (Figure 5.24), was implemented into micro-climatic simulations using a CFD – Surface Energy Balance analysis tool (ENVI-met, Version 4).

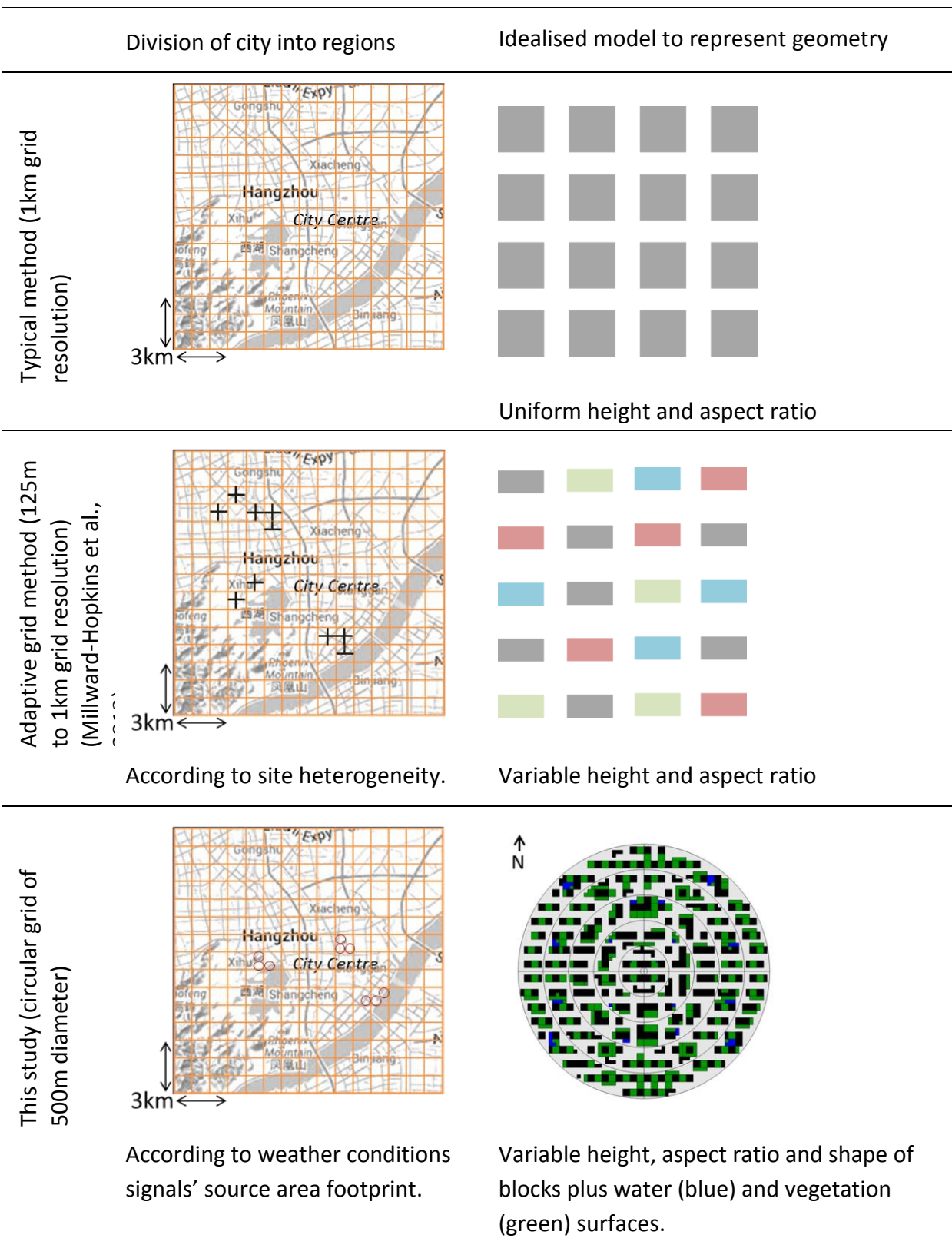


Figure 5.23. Typical grid (top), adaptive grid (middle) and the “urban unit” model (bottom) method to divide a city into regions and represent their geometry with an idealised model. Image adapted from Millward-Hopkins et al. (2013).

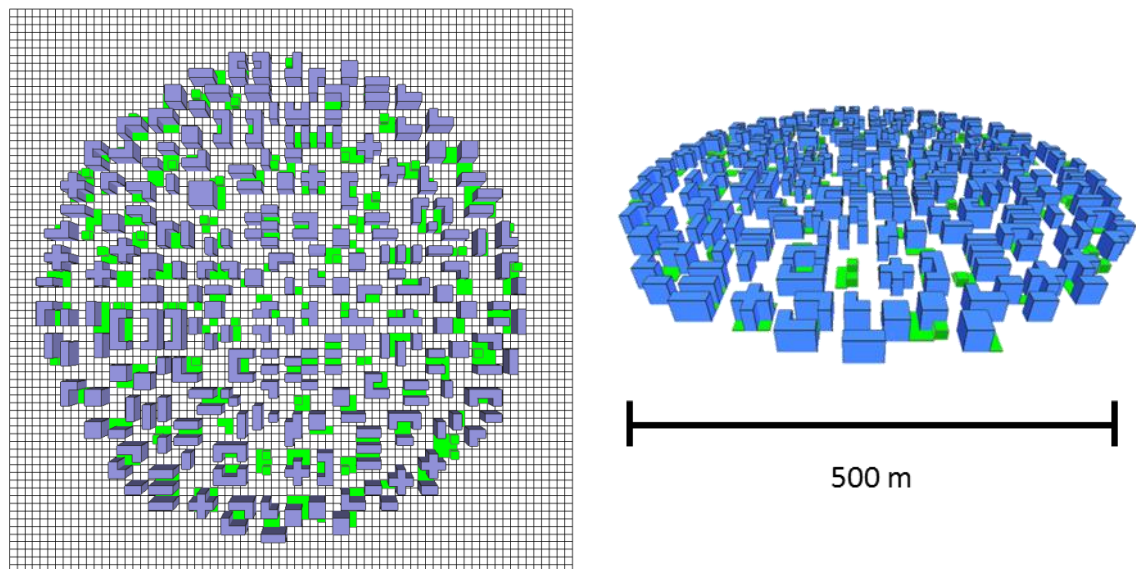


Figure 5.24. Top plan view (left) and a 3D perspective view (Top right) of the idealised “urban unit” model for the studied “LCZ5” sites. A 2D view of the computational grid is shown in the left image (grid cell horizontal dimensions 8m x 8m).

Chapter 6 Urban weather projections

There are two key parts to the methodology for generating the “urban weather projections” that resulted from the combined urban classification and simulation modelling (Figure 6.1): (Part 1) The adjustment of the reference weather data with the local monthly UHI patterns for different weather forcing and; (Part 2) The adaptation of the UHI adjusted hourly air temperature to account for the effect of the site specific generic morphology at street level at the neighbourhood scale. The main components of the overall methodology are described in the following:

1. Correction of the reference weather data to include the local UHI patterns (local scale) (Part 1)

The reference weather station (official, NP in Figure 5.11) for Hangzhou is located at Mantou Mountain (30.23°N, 120.17°E, at an elevation of 42 m). This weather station is the source of the typical meteorological year (TMY) files for Hangzhou and it reports data with Hangzhou international airport’s reference code (ZSHC) and the code 584570 in the World Meteorological Organisation’s (WMO) weather station list. The steps for the adjustment of the reference weather data are as follows:

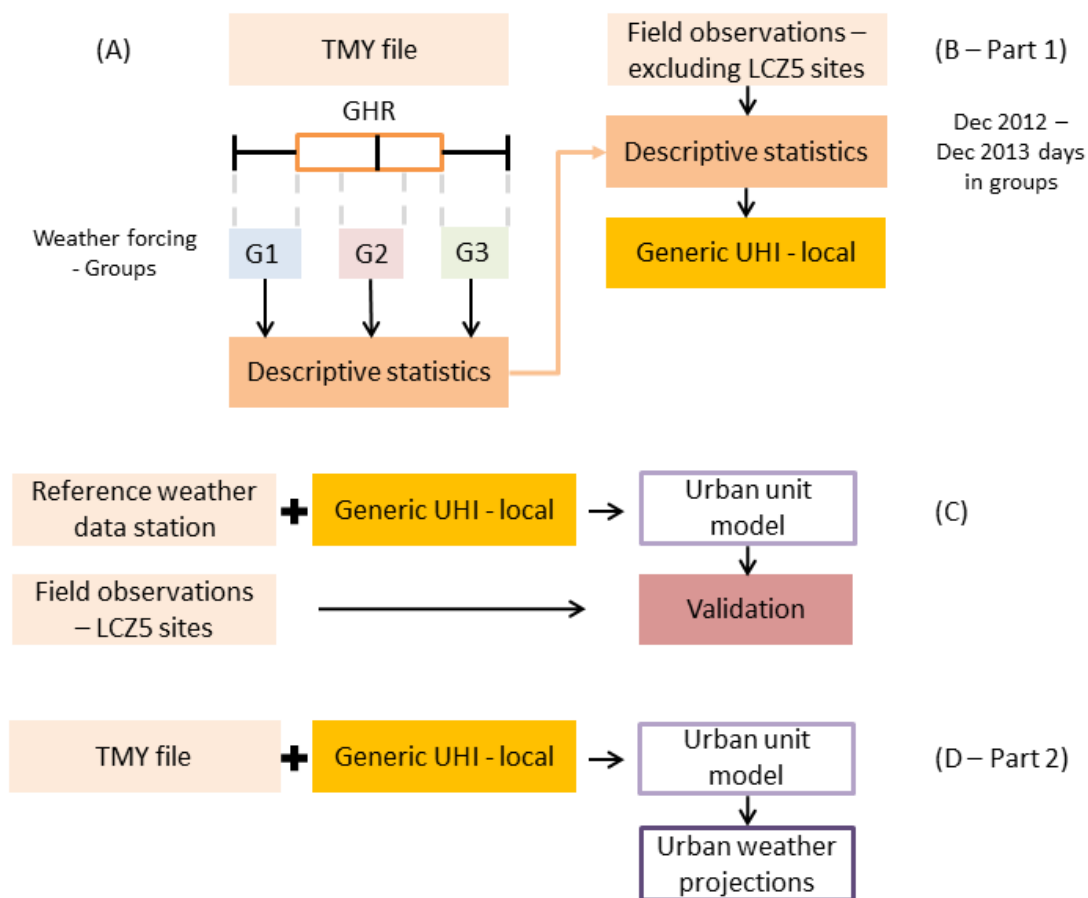
(A) in Figure 6.1 - The global horizontal solar radiation (GHR) from the typical meteorological year (TMY) file (584570_CSWD) was used for creating three distinct groups in order to account for different weather forcing in each month (Figure 6.1);

- Group 1 (G1) represented days with overcast sky conditions and rain events.
- Group 2 (G2) aimed at representing days with clear skies and average or “typical” weather conditions for the month, while
- Group 3 (G3) represented rather warm/hot days with a clear sky.

It was considered that the distribution of the days into three groups would satisfactory represent the three main weather conditions (i.e. overcast, rainy days; clear skies, “normal” temperature; hot days with clear sky) without adding complexity. The distribution of the days into the weather forcing groups was necessary in order to reduce computational time and allow the generalisation of the methodology and its transferability to other cities with similar characteristics and climate. If all the days in

the TMY file were individually simulated then the simulation run time would approach 26,500 hours.

(A) in Figure 6.1 - The 25th and 75th centiles (1st and 3rd quartiles) of the GHR values were used as the cut off points for the categorisation of the hourly TMY data into the groups. Group 1 for a given month contained all the days in that month that have hourly GHR values equal to or less than the 25th centile GHR value for the respective hours (lowest 25% of GHR values).



GHR= Global Horizontal Radiation,
 (A)= Creation of the weather forcing groups and analysis of the descriptive statistics for each group and month,
 (B)= Distribution of the field observations (excluding the LCZ5 studied sites) between Dec 2012 and Dec 2013 into the weather forcing groups and estimation of a generic UHI intensity offset for each group and month,
 (C)= Model validation for days representative of the average conditions for each weather forcing group and season,
 (D)= Generation of the urban weather projections as an hourly air temperature offset for each month and weather forcing group.

Figure 6.1. Methodology flowchart of the model's validation and the generation of the adapted weather dataset.

Similarly, Group 2 contained all the days in a month with hourly GHR values within the interquartile range of the GHR data for the respective hours (50% of GHR values). Therefore, Group 2 is expected to be the most representative TMY-based weather forcing scenario. Group 3 contained days that had most of the hourly GHR values in the upper quartile (highest 25% of GHR values). Here, the definition of “most of the hourly values” in this context relates to days with less than three hours with GHR values that did not fit into the specific group and where these hours are not between 12:00 h and 16:00 h. Following the grouping of the days, descriptive statistics were calculated for the daily mean air temperature, temperature range, daily mean RH and maximum temperature for all the days in each group. The remaining days from the TMY file that did not fit into any category were then distributed into either group 1, 2 or 3 according to their matches of daily mean air temperature, temperature range, daily mean RH and maximum temperature.

The descriptive statistics (i.e. mean T, T range, mean RH, max T) were also calculated for observations from the reference weather station (TMY source) for the period from December 2012 to December 2013 (Figure 6.1). The results were then compared with the descriptive statistics ((A) in Figure 6.1) of the weather forcing groups from the TMY data file. Following this the individual days of the 2012 – 2013 observations from the reference weather station dataset were distributed into the monthly weather forcing groups according to the four criteria (i.e. mean T, T range, mean RH, max T from TMY data analysis) in descending order of weighting. (Note: Data were available for the periods from 17th of December 2012 to 11th of March 2013 and from 7th of May 2013 to 22nd of October 2013 (Bourikas et al., 2013; Shen et al., 2014)).

(B) in Figure 6.1 - The data collected for each day from the sensors of 10 additional (“sample”) sites in Hangzhou (Figure 6.2) were allocated to the weather forcing groups according to the classification of the 2012-2013 observed reference weather station data of the same day (Figure 6.1). Further to this, the observations from the 10 “sample” sites were used to create a generic hourly UHI pattern which relates to the difference of the sample sites’ hourly average observations to the reference weather station data for each month and weather forcing group. The hourly

average observations from the nine studied sites (LCZ5) were then used to validate this method.

(C) in Figure 6.1 - Here we are comparing real measurements of the 9 LCZ5 sites with the simulation results of the “urban unit model” forced with measured data from the reference (TMY source) weather station offset by the generic UHI effect as measured in the 10 “sample” sites. For this reason, the 10 UHI sampling sites did not include any of the 9 studied urban units, i.e. sites with a LCZ5 classification. The 10 UHI “sample” sites included a mix of sites with different morphological characteristics, space use and locations within the city.

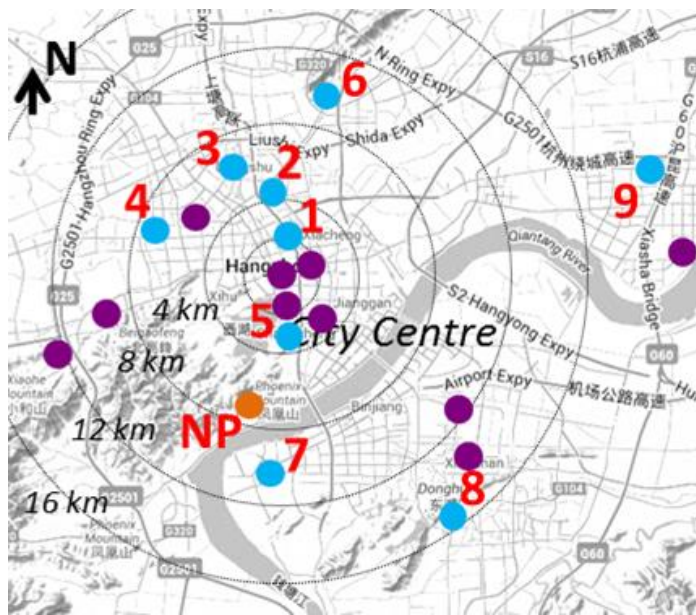


Figure 6.2. The location of the 10 “sample” sites (purple bullets) used for the assessment of generic UHI patterns in Hangzhou, China in relation to the 9 studied (LCZ5, blue bullet points) sites.

The adjustment of the TMY reference weather data with the generic UHI group patterns (T and RH offsets) was based on a simple offset of the hourly mean temperature and RH values for each weather forcing group (Equation 6.1).

$$T(RH)_{urb_{Group,hr}} = T(RH)_{ref_{Group,hr}} + UHI(RH \text{ offset})_{Group,hr} \quad (6.1)$$

Where $T(RH)_{urb}$ is the air temperature (RH) after the adjustment to the hourly UHI (RH offset) pattern, $T(RH)_{ref}$ is the reference air temperature (RH) from the TMY weather file and $UHI(RH \text{ offset})$ is the positive or negative air temperature (RH) offset due to the urban heat island effect for each weather forcing group and hour

respectively. The “bulk”-city UHI profile is independent of location because the 10 “sample” weather stations are across the whole city and the city has multiple thermal centres. The aggregate effect of the local specific micro-climate is included in the “bulk” – city UHI profile. This methodology identified

2. Adaptation of the “localised” TMY data to include the effects of the site specific morphology (local scale + morphology = micro scale) (Part 2)

The idealised “urban unit model” (250m radius) introduced in Chapter 5 was implemented into the micro-climatic simulations using a CFD – surface energy balance analysis tool (ENVI-met Version 4). In this final stage of data processing the hourly “localised” data generated according to the methodology section (Chapter 6, Section 1 (B)) was used to initialise and force the hourly weather conditions in the simulation. The “urban weather projections” resulting from the simulations express the weather change at street level in relation to the baseline-reference weather (e.g. weather at airport sites or non-urban sites) caused by the effect of the site specific morphology in the city. These projections have the format of an additional hourly offset to the “localised” dataset for each weather forcing group.

2.1 ENVI-met set up and configuration

ENVI-met is a three dimensional non-hydrostatic numerical micro-climate model that couples an atmospheric, a soil and a one-dimensional (1-D) vegetation model with the surface energy balance (Figure 6.3). The atmospheric model is based on the incompressible Reynolds averaged Navier Stokes (RANS) equations with a Yamada and Mellor (1975) $k-\epsilon$ turbulence closure scheme and the inclusion of terms for the production and dissipation of turbulent kinetic energy due to wind shear, thermal stratification, buoyancy and vegetation (Bruse & Fleer, 1998).

The wind field is always simulated with an open type boundary (i.e. the values of the closest to the border grid cell are copied to the border (Bruse & Fleer, 1998)). Wind flow in the three dimensional domain is calculated initially with the RANS equations without the pressure. The dynamic pressure field is estimated in a second

Chapter 6 Urban weather projections

stage with the Poisson equation (for details see the original paper of Bruse (2004)). The successive over relaxation method is used for the update of the wind field and for mass convergence. (Bruse & Fleer, 1998). Detailed equations can be found in the paper of Bruse and Fleer (1998).

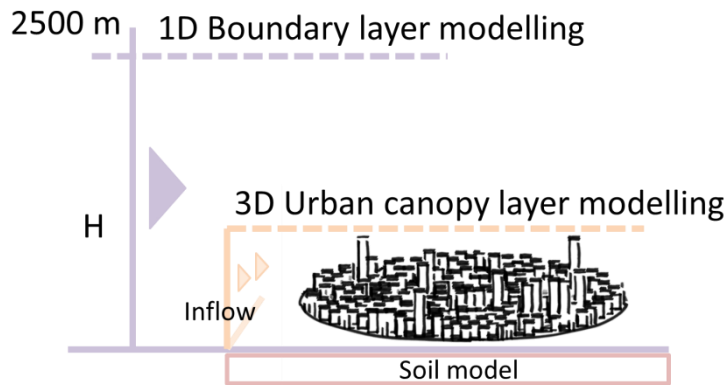


Figure 6.3. Overview of the ENVI-met model. Data Source: Bruse (2008e)

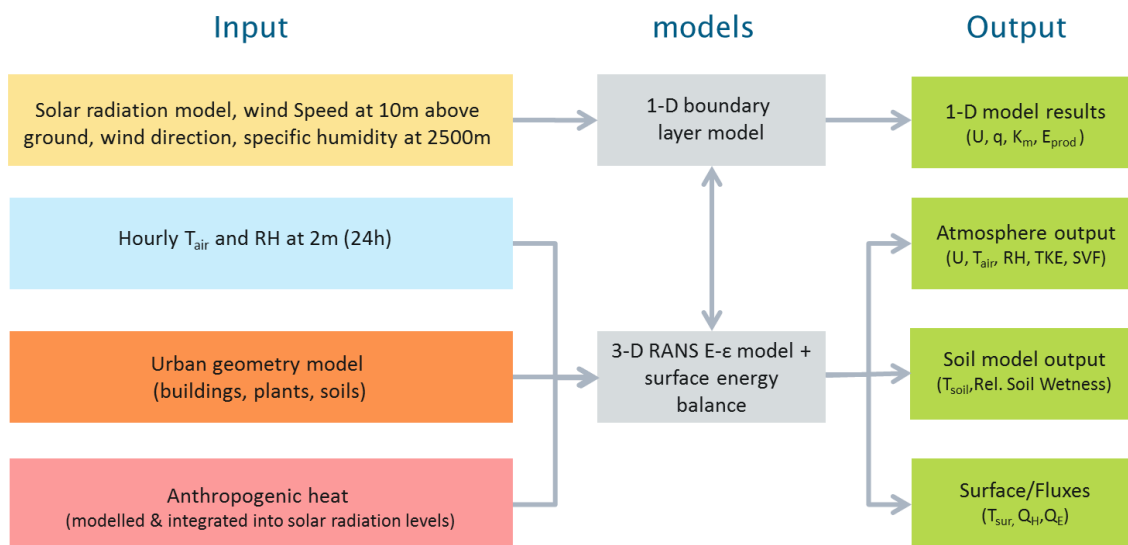


Figure 6.4. Simulations data flow and main outputs. T_{air} , T_{surf} and T_{soil} [K] denote the air, surface and soil temperature respectively. U [m/s] is the wind speed in the three directions, q [g/kg] is the specific humidity of air, RH [%] is the relative humidity of air, TKE [m^2/s^2] is the turbulent kinetic energy and SVF is the sky view factor [0-1]. Q_H denotes the sensible heat flux and Q_E is the latent heat flux [W/m^2]. Data source: Bruse (2008d).

Air temperature (at 2 m above ground) and relative humidity at the inflow boundary were forced with the “localised” (i.e. adjusted with bulk-city UHI) air temperature and relative humidity TMY data on a 24 hourly input. The turbulence field was updated every 10 minutes; solar radiation was modelled with a dynamic time step

(i.e. smaller when solar radiation is near its peak (1 sec) and longer during morning and afternoon (2 sec)); the internal temperature of buildings (free running) is calculated according to the heat transfer through the walls and roofs, where all walls and roofs have the same thermal transmittance and albedo. The spin-up period was set to 4 hours (starting at 20:00 on the day before the simulated day). A list of the main input, output and functions of the model when hourly weather forcing is used can be seen in Figure 6.4.

ENVI-met estimates the surface energy balance for the ground surface and the temperature for the walls and roofs by taking into consideration shading, albedo and heat transmittance from the interior of buildings. The ground surface and the wall/roof system are the lowest boundary for the atmospheric model while the ground surface is the top boundary of the soil model. The turbulent heat, momentum and vapour fluxes at the lowest solid boundary are calculated with respect to thermal stratification as a function of temperature and vapour exchange coefficients between the surface and the first layer above (Bruse, 2004). The temperature and humidity distribution in the canopy layer are based on the wind flow profile and estimation of the local turbulent exchange coefficients from the E- ϵ field (Bruse & Fler, 1998). The temperature of leaves and the vapour exchange with the atmosphere are controlled by a leaf surface energy balance and a CO₂ gas exchange model for plant transpiration. The calculations of the turbulent fluxes in the leaf energy balance include shading and absorption of solar radiation from the other plant layers (Bruse, 2008c).

2.1.1 Computational domain

The computational domain in ENVI-met comprises an equidistant grid that can be compressed / stretched in the vertical (z, height) dimension by using an expansion ratio but there is no option for the local refinement of the horizontal computational grid (Bruse, 2008b). The starting grid cell height, i.e. the height for the cell in contact with the ground surface, was set to 0.5m and the grid remained equidistant below the height of 2.5m with a grid cell spacing equal to $dz=0.5m$ (Figure 6.5). The combination of a 0.5m starting grid cell height with an 18% grid height expansion ratio resulted in a

vertical grid with 16 grid cells at the lower part of the domain (i.e. the lower 20m within the roughness sub-layer).

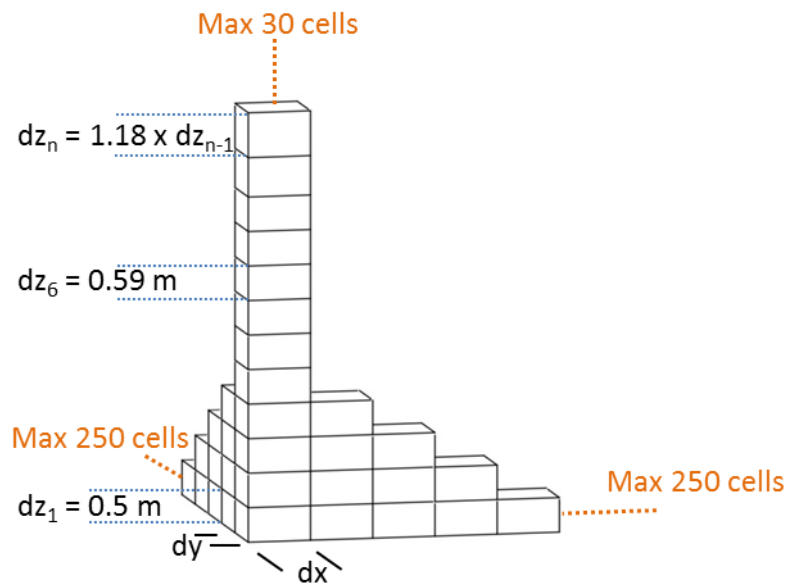


Figure 6.5. The 3D computational domain and the vertical grid layout in this study.

The maximum expansion ratio proposed in the COST Action 732 (2007) guidelines is 20%. The “urban unit’s” 250m radius resulted in 3D computational grids of 72 x 72 x 28 grid cells with a horizontal resolution of 8m. Three additional “nesting grids” were used to achieve a sufficient distance to the boundaries (lateral and top) for the flow to develop. The nesting grid areas have coarser resolution than the main “core” of the computational domain. The nesting grid cell dimensions increase with a linear growth equal to the grid cell dimensions of the “core” model (i.e. horizontal grid cell dimensions increase by 8m in every nesting grid). The nesting grids do not have any objects in them and they receive the average shortwave solar radiation as calculated by the “empty” grid cells in the main model area.

The computational grid cells have a hexahedral (cuboid) shape. Hexahedral cells in equidistant grids are favoured (i.e. against tetrahedral and prismatic cells) because they facilitate the convergence of the iterative solution and reduce any truncation errors (COST Action 732, 2007).

ENVI-met (Version 4.0) is confined to three domain size choices (length, width, height = x, y, z): a) 100 x 100 x 30, b) 180 x 180 x 30 and c) 250 x 250 x 30 grid cells respectively (Figure 6.5). The idealised urban unit has a diameter of 500 m. A horizontal

grid cell size of 2 m x 2 m would mean that the model occupies the total 250 x 250 grid cells available in the largest domain. However, there is a need for adequate distance between the model and the inflow, outflow and lateral boundaries for the flow to develop. Therefore the horizontal grid cell dimensions are expected to be larger than 2 metres. Another limitation that derives from the use of a predefined computational grid is that the modelled geometry must fit to an integer number of grid cells. For example if the grid cell's size is $(dx, dy) = (3 \text{ m}, 3 \text{ m})$ and a building has a square base of 8 m x 8 m then it cannot fit to the grid cells in the computational domain (Figure 6.6).

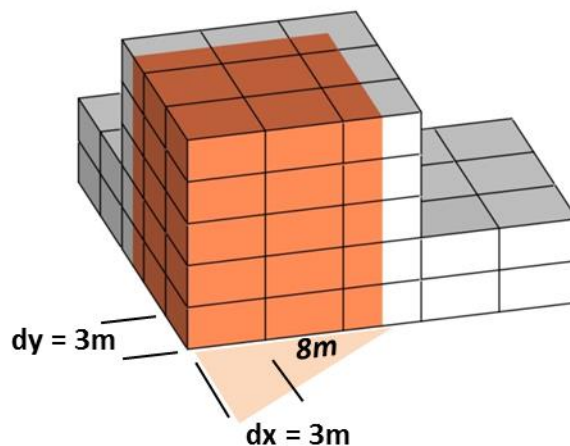


Figure 6.6. Fit of the building geometry to the predefined computational grid. The building (marked as orange) has a square base of 8 m x 8 m that cannot be allocated to an integer number of the 3 m x 3 m grid cells.

Best practice guidelines for the flow simulation in the urban environment propose a minimum grid resolution of 10 grid cells per cube root of building volume and 10 grid cells spatial separation of buildings in any area of interest (COST Action 732, 2007). The minimum building volume in the idealised urban unit for a building with 19 m height is $1,216 \text{ m}^3$ (8 m (L) x 8 m (W) x 19 m (H), the cube root is 10.7 m). The minimum spatial separation of buildings is 8 m. According to the COST Action 732 (2007) recommendations the minimum horizontal grid dimensions should have been 0.8 m. However, the guidelines are indicative of the “flow simulation” in “the area of interest” (COST Action 732, 2007). The detailed wind field simulation close to the building walls would require computational fluid dynamics models with adjustable grid spacing, adequate fine grid cell resolution close to any solid boundaries and explicit calculation of turbulent flow with an unsteady technique such as a Large Eddy

Simulation (LES), an Unsteady RANS (URANS) or Hybrid LES-RANS models (Xie & Castro, 2006).

The aim of this thesis is the adaptation of non-urban air temperature and relative humidity observations to the effect of local specific micro-climates. The estimation of the wind velocity was not a primary objective. The “urban weather projections” are spatially averaged values over the “urban unit” model that represent the impact of the modelled urban morphology. The selection of ENVI-met for the simulations was a trade-off between the accuracy in the flow field simulation and the simulation of the thermal and vegetation effects on local specific (i.e. urban unit) weather development.

ENVI-met has the advantage of using an integrated vegetation, soil and radiation model compared to other numerical models that do not include such representations of physical processes. Vegetation in particular is very important to the approximation of the latent heat flux and in the modelling of the surface energy balance (Grimmond et al., 2010; Flagg & Taylor, 2011).

2.1.2 Sensitivity to computational grid size

A sensitivity study was carried out to assess the magnitude of the dependence of the computational results on the computational grid's resolution. The vertical grid resolution was pre-set and remained constant. Details of the different cases can be seen in Table 6.1. The sensitivity to the vertical grid cell size was not assessed because it was considered important to a) have a solution at the height between 2.5 m and 5 m above the ground (i.e. middle of grid cells, solution at 2.80 m, 3.44 m, 4.20 m and 5.09 m) where the observations have been collected and b) have at least 10 grid cells in the lower 20 m of the domain and an expansion ratio below 20% for the cells above the 20 m threshold.

Three case studies were created with different horizontal grid resolution (Table 6.1). The first case study (Case 1 in Table 6.1) had the finest horizontal grid resolution of $(dx, dy) = (3m, 3m)$. The coarsening ratio r for the grid is defined by (COST Action 732, 2007) :

$$r_{i,i+1} = h_{i+1}/h_i \quad (6.2)$$

where $i = 1$ denotes the fine grid and h is the width of the grid cell.

Table 6.1. Case studies for the assessment of the solution's sensitivity to grid resolution.

Case	horizontal grid resolution (dx,dy) [m]	vertical grid resolution (dz) [m]	computational domain dimensions (x,y,z) [grid cells] (+no of nesting grids)	coarsening ratio $r_{i,i+1}$
Case 1	(3, 3)	first 5 grid cells' height: 0.5 m, from 2.25 m to the top of the 3D domain: $dz_n = 1.18 \times dz_{n-1}$	207 x 207 x 28 (+6)	n.a.
Case 2	(6, 6)	same as Case 1	104 x 104 x 28 (+5)	$r_{1,2} = 2.0$
Case 3	(8, 8)	same as Case 1	72 x 72 x 28 (+ 4)	$r_{2,3} = 1.3$

The coarsening ratio was not constant because of limitations set by the computational domain size and the fixed computational grid (i.e. the modelled geometry should fit to an integer number of grid cells). In addition, it was not possible to assess the grid sensitivity to computational grid dimensions below 3 m x 3 m due to the simulation domain size limitations (i.e. 250 x 250 grid cells maximum). That is because the urban unit has a diameter of 500 m and a number of grid cells in proximity to the domain borders must remain empty. Grid cell resolutions coarser than 8 m were not assessed because they were deemed too low for the purposes of this study.

Table 6.2. Summary of the two scenarios used for the grid sensitivity analysis. Data Source: The Weather Underground (2014a)

	Sky conditions	Mean T (°C)	Mean RH (%)	Mean wind speed (m/s)	Prevalent wind orientation (0° North - 90° East)
Winter					
11/01/13	scattered clouds / clear	4	70	1	240
Summer					
10/08/13	clear	36	45	2	210

Chapter 6 Urban weather projections

Two scenarios were created for the assessment of the solution's sensitivity to the horizontal grid dimensions; one for winter that represents cold clear sky conditions and one for summer that represents hot weather with a clear sky in Hangzhou (Table 6.2). The average weather conditions reported in Table 6.2 are observations from the Mantou Mountain National Principle station (30.23°N, 120.17°E, elevation 43 m, WMO 584570) in Hangzhou. The 11th of January 2013 had an average temperature of 4 °C and 70% RH. The wind was calm (~1 m/s) during the day blowing from a South-West direction (The Weather Underground, 2014a) (Figure 6.7, Top). The sky was obscured by haze. The previous 3 days had been dry with similar maximum, minimum and average air temperature and relative humidity.

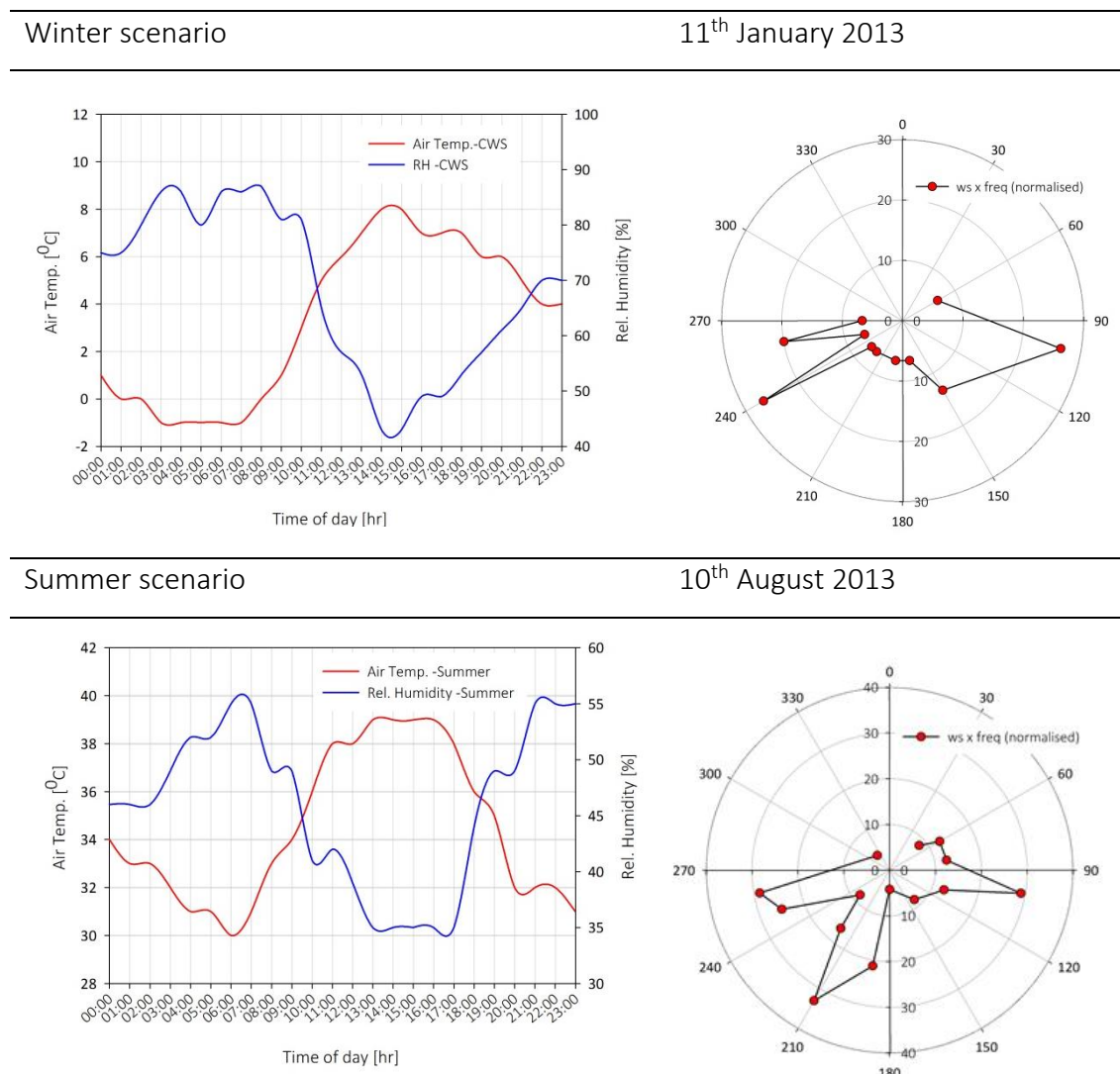


Figure 6.7. Hourly weather conditions (Left) and the prevalent normalised wind direction (wind speed x frequency) (Right) for the winter scenario (11th January 2013, Top) and the summer scenario (10th August 2013, Bottom). Data Source: The Weather Underground (2014a).

On the 10th of August 2013 the mean temperature was 36 °C. The average RH was 44% and the wind was blowing from a South – South West direction with an average speed of about 2 m/s (The Weather Underground, 2014a) (Figure 6.7). The sky was clear. The previous four days had been dry with 41 °C maximum air temperature and similar to the day in the summer scenario weather conditions. The analysis was conducted for the diurnal conditions (i.e. 24 hours) from 00:00 China standard time (CST) to 23:00 CST for the days in the scenarios.

The sensitivity to the computational grid size analysis has showed that a step increase of the horizontal resolution to 6 m (black square in Figure 6.8 & Figure 6.9) and 3m (black x in Figure 6.8 & Figure 6.9) delivered no significant change in the model output. The results from the case studies in both scenarios showed that the air temperature differences between the cases are less than 0.5°C (Figure 6.8) and for RH the difference was in the range of 2-3% RH units (Figure 6.9).

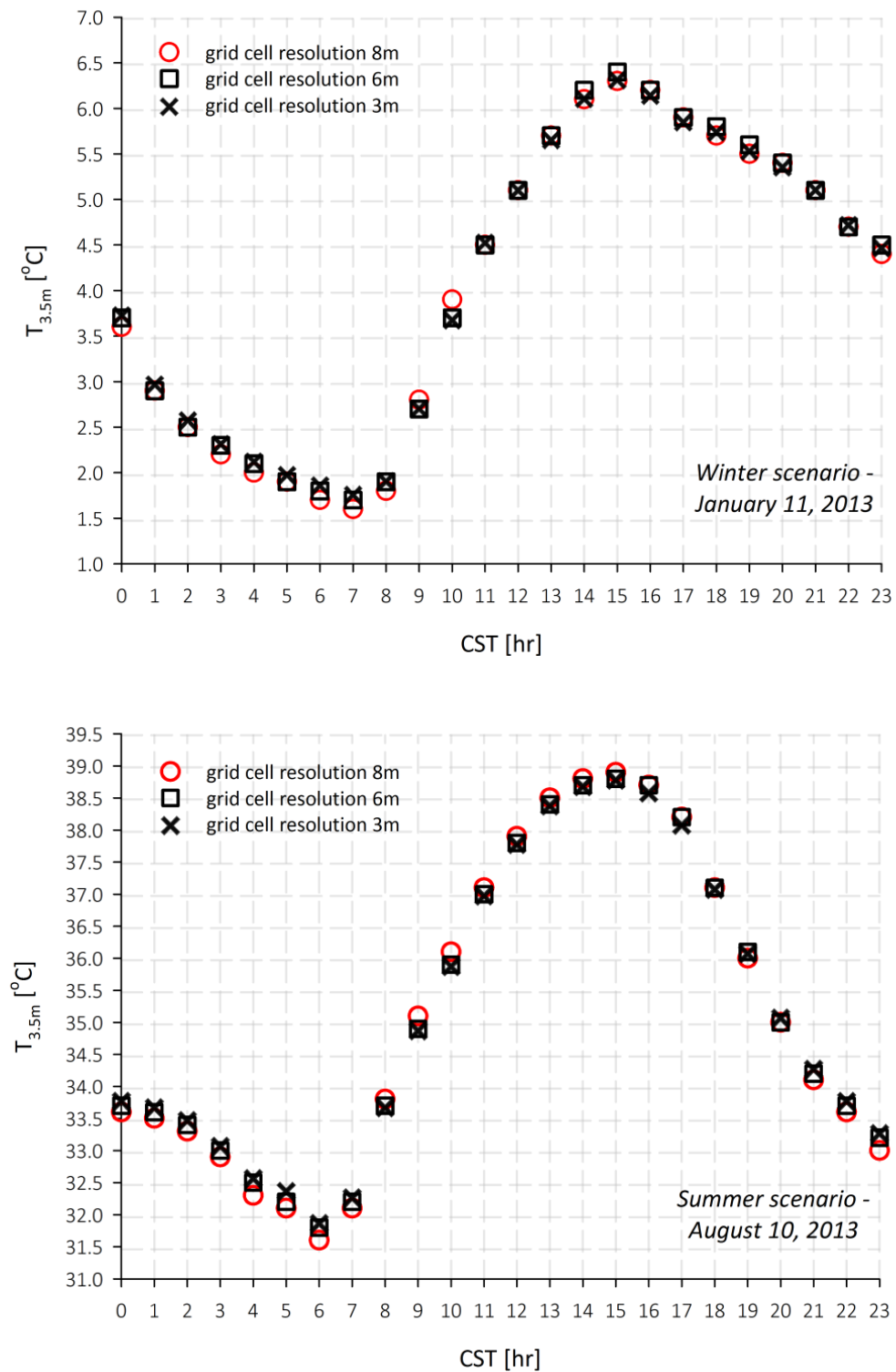


Figure 6.8. Sensitivity of simulated air temperature to computational grid resolution of 8m (red circle), 6m (black square) and 3m (black x).

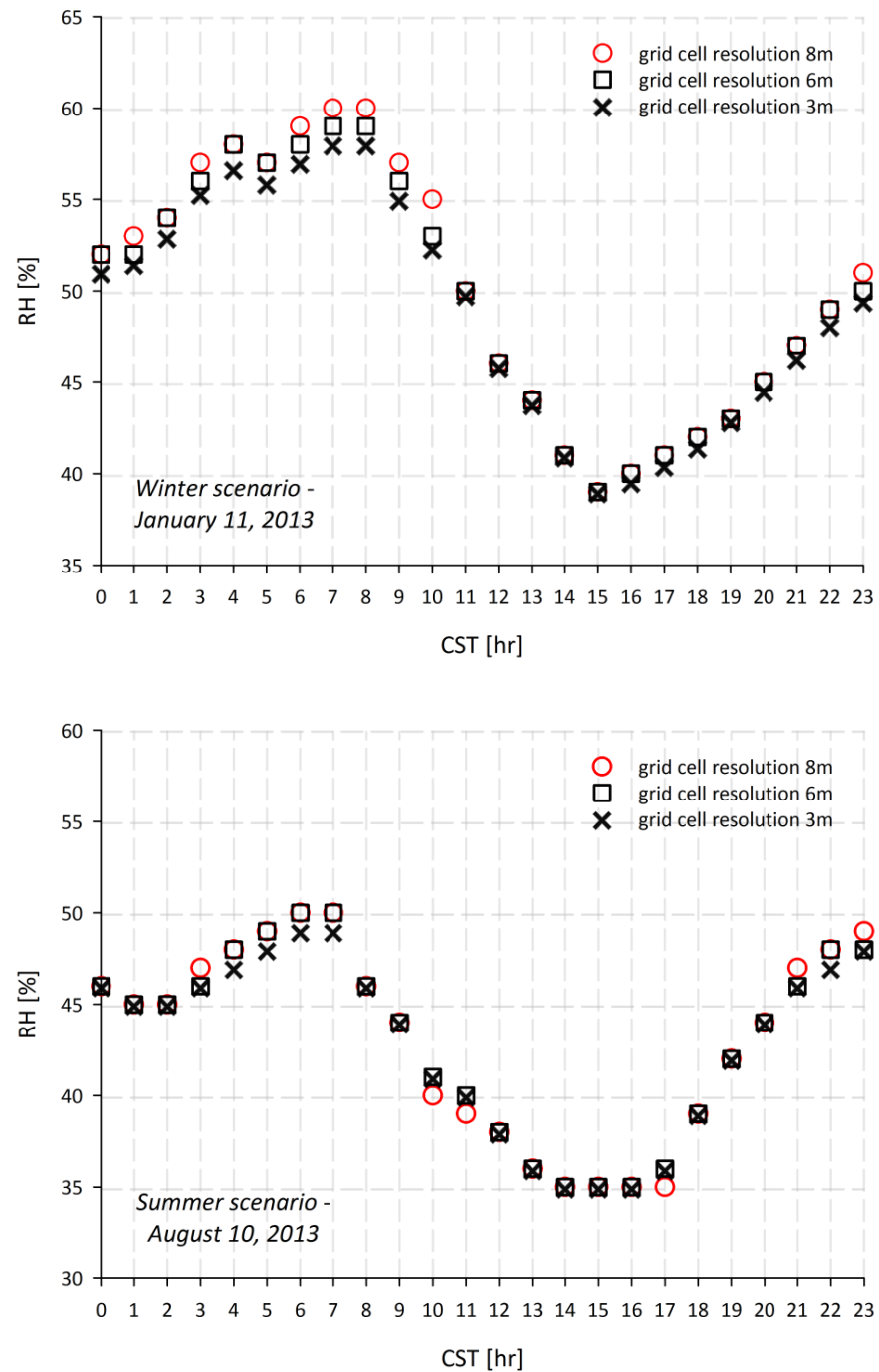


Figure 6.9. Sensitivity of simulated relative humidity to computational grid resolution of 8m (red circle), 6m (black square) and 3m (black x).

In addition, two scenarios have been investigated for assessing the sensitivity of the model to the distribution and the amount of green-space in the model. The first scenario (Scenario 1) investigated the impact of vegetation's location in relation to the air temperature development (T3.5m) at the middle of the idealised urban unit. Scenario

1 compared the air temperature at 3.5m height above ground ($T_{3.5m}$) in Case 1, where the vegetation was distributed according to the statistical results from the land surface analysis, with Case 2, where all the vegetation surface area was moved to the centre of the urban unit and Case 3 where the vegetated area was moved towards the outer annuli (Figure 6.10). The pervious surface area ratio (i.e. 0.15) remained the same for the urban unit model.

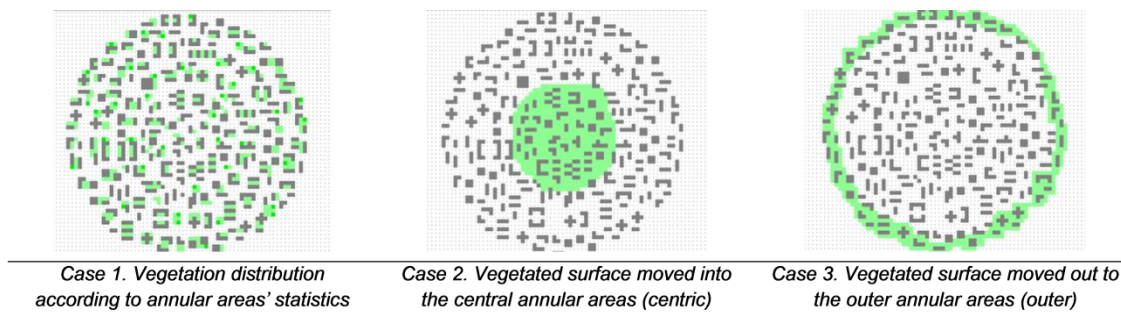


Figure 6.10. Distribution of the vegetated surface area in the urban unit for the cases considered in Scenario 1 of the green-space sensitivity analysis.

Scenario 2 compared the air temperature ($T_{3.5m}$) from Case 1 with 5 additional Cases (4 to 8) that had increasing ratios of pervious surface area that was distributed evenly (same percentage) in each annular area (Figure 6.11). Each case had 5% P_r points more vegetated surface area (i.e. in the form of grass) than the previous one up to a maximum of $P_r = 0.4$ which represents the upper limit for the “Local Climate Zone 5” classification.

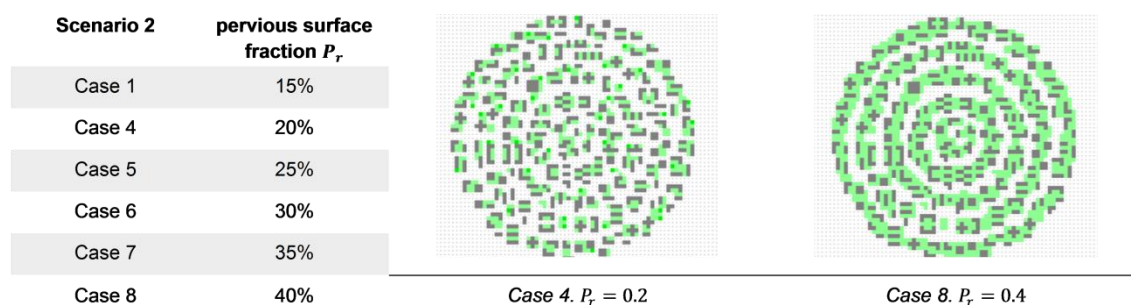


Figure 6.11. The different percentages of vegetated surface area in the “urban unit” for the cases in Scenario 2 of the green-space sensitivity analysis. Top plan view of the computational domain (Right) for the cases with $P_r = 0.2$ and $P_r = 0.4$.

The air temperature development in the idealised “urban unit” for both scenarios was simulated with ENVI-met (Version 4) for August 10, 2013 which represented a sunny hot day in Hangzhou (Table 6.2). In both scenarios (green-space amount and distribution) the modelled temperature varied less than 0.5°C between the cases showing that the solution is relatively insensitive to the distribution of the green-space in the model and the model performs as expected regarding the differences in the amount of vegetation.

Specifically, the assessment of the impact of the vegetation’s location on the air temperature development in the urban canopy revealed that the proximity to “green” – vegetated space can decrease the urban heat island intensity during night-time and the maximum day-time air temperature. The marginal difference between the cases with a central allocation of the vegetated surface area and those where the vegetation was positioned at the outer border of the urban unit is an indication that the distance to a vegetated area is not enough to alone produce large cooling benefits during the day and attenuate the night-time urban heat island intensity. In Scenario 2 (amount of green-space), an increase to the urban unit’s permeable surface area showed a small decrease in the average air temperature across the urban unit. The case with the largest vegetated surface area had the lowest daily air temperatures. A shift was noted in the air temperature distribution towards a higher occurrence frequency of temperatures at the cooler end. The differences between the cases were more evident in the average surface temperatures. The results suggest that high percentages of vegetated space can reduce the surface temperatures within the cities. There were, however, strong indications that in places with a humid sub-tropical climate such as Hangzhou, in the case of successive hot, dry summer days, a reduction in soil water content will negate, to a large extent, the cooling benefits of the added vegetation.

2.1.3 Boundary conditions

The flow field at the inlet, the outlet and the lateral (i.e. vertical domain “walls”) boundaries was simulated with an open type boundary (i.e. the values of the closest to the border grid cell are copied to the border) (Bruse & Fleer, 1998). The vertical flow profiles in the inlet and the top boundary were calculated by the 1D boundary layer

model (Figure 6.12). A fixed zero-gradient Neumann condition (velocity profile normal to the boundary has a zero gradient (Nabla Ltd, 2007)) is assumed at the outflow and the lateral walls of the domain (Bruse, 2004). A closed; no slip condition is applied to the bottom boundary of the model (i.e. $u=v=w=0$). At the top boundary, vertical motions are assumed to be zero (Table 6.3). Air temperature and relative humidity at a 2 m level are forced with hourly observations from the reference weather station at Mantou Mountain as described before. Turbulence related profiles are copied to the inlet from the outflow with the use of cyclic boundary conditions.

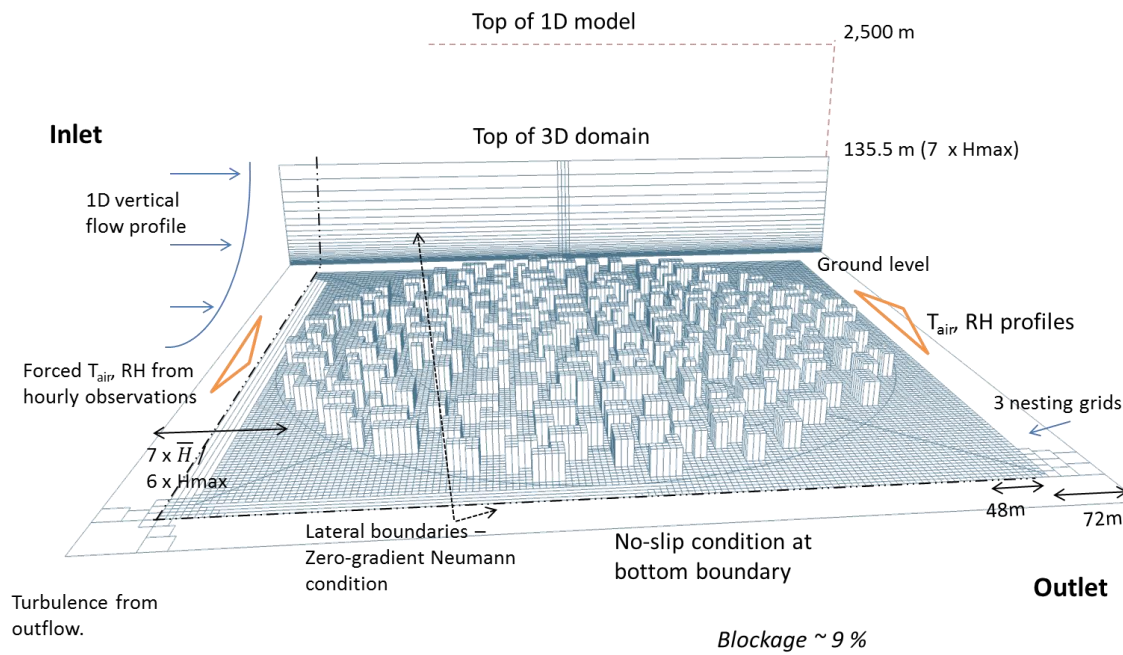


Figure 6.12. The computational modelling domain and the boundary conditions. \bar{H} (m) denotes the average building footprint-area-weighted height over the urban unit.

At the bottom boundary, the surface temperatures are used as the physical boundaries (Bruse, 2004). The production and dissipation of the turbulent kinetic energy are a function of the local tangential friction velocity (Bruse, 2004). The model is positioned at the centre of the computational domain. This allows the simulation to be run for different wind directions without any changes to the computational grid. The minimum distance to the inlet, the outlet and the lateral boundaries is $7 \times \bar{H}$ or $6 \times H_{\max}$ where \bar{H} is the average building footprint-area-weighted height (~ 18 m) and H_{\max} the maximum building height (20 m) (Figure 6.12). A 9% blockage ratio was estimated (i.e. model's frontal area to total cross section area ratio).

A distance of five times the building height from the inflow and 15 x the building height from the outflow is proposed respectively in the case of a single building (COST Action 732, 2007). On the other hand, the VDI German technical guide recommends that for a single building and a blockage below 10% a distance of 2 x the building height from the inflow is adequate (Verein Deutscher Ingenieure (VDI) 3783, 2005).

Table 6.3. Boundary conditions of the 3D computational domain. Table adapted from (Ashie & Kono, 2011).

Variable	Top boundary	Lateral boundaries	Inlet	Outlet	Bottom boundary
wind velocity	Constant u, v (horizontal). w=0 (vertical)	zero-gradient Neumann condition	Constant u, v, w (from 1D model)	Constant u, v, w – zero gradient	no-slip condition (u=v=w=0)
Temperature	Constant potential temperature* from 1D model	zero potential temperature gradient	Forced T at 2m level (reference observations)	zero potential temperature gradient	Heat transfer
Humidity	Constant specific humidity from 1D model	zero specific humidity gradient	Forced RH at 2m level (reference observations)	zero specific humidity gradient	Moisture transfer
E and ϵ	Constant from 1D model	zero gradient	from outflow	zero gradient	tangential friction velocity

* Potential temperature is the temperature that unsaturated air would have if brought adiabatically from its current conditions to standard pressure p_0 (American Meteorological Society, 2013a).

The top boundary of the computational domain is suggested to be positioned at a height of 5 x H_{\max} above ground. The same distance is generally recommended for the lateral boundaries of the domain too (COST Action 732, 2007). In the case of urban areas with multiple buildings though, the lateral boundaries can be closer to the model (COST Action 732, 2007). In this study, the top boundary of the 3D computational domain is positioned at 7 x H_{\max} height above the ground and the lateral boundaries of the computational domain at a distance of 6 x H_{\max} away from the model.

2.1.4 Surface parameters

Initial values for the ground, soil, vegetation and building surface parameters are required for the solution of the thermal and evapotranspiration sub-models. These sub-models update the surface temperatures and regulate the moisture transfer from and to the atmosphere during the simulation. The surface temperature affects the thermal stratification of the atmosphere and the production of local turbulent energy (Bruse, 2004). The radiative fluxes are calculated with the use of the Sky View Factor in order to distinguish between the shaded and the unshaded fraction of the surfaces.

The soil profile comprises 14 layers with the upper layer being the surface and the lower at a 2 m depth (Bruse, 2004). The initial temperature and relative soil humidity are required at three levels below the ground surface (i.e. 0 – 20cm; 20 – 50cm; 50cm to 2m). The temperature below the 2 m depth remains constant during the simulation (Bruse, 2008a). The surface related parameters were initialised with data obtained by the Final Operational Global Analysis Data Assimilation System (GDAS) dataset. The GDAS dataset contains the simulation results from the National Centers for Environmental Prediction (NCEP) global weather forecasting model at 4 time snapshots daily (i.e. 02:00, 08:00, 14:00, 20:00 Hangzhou local time).

The model is calibrated over 6 hour cycles with observations from the Global Telecommunications System (GTS) and other sources globally (NCEP/NCAR US, 2000). The use of reanalysis data (i.e. data created by a consistent data assimilation method and models that are updated with real observations every 6-12 hours (Dee et al., 2014)) sets realistic boundary conditions to the forecasting model and increases the reliability of its output (Carter, 2007).

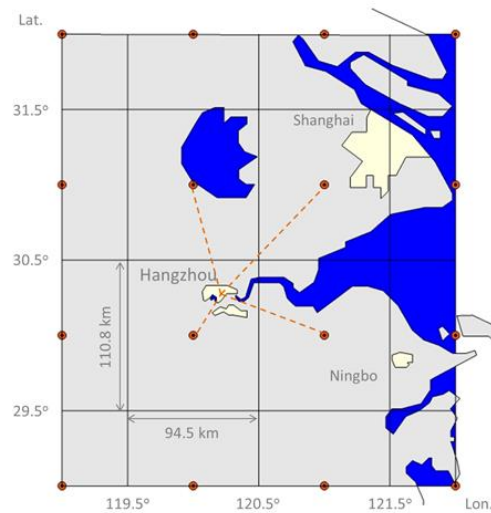


Figure 6.13. The computational grid of the generic circulation model for the region of Hangzhou (major cities outlined with white). The centre of each grid box (model output available) is marked with an orange bullet. The dashed orange lines show the four grid boxes closest to Hangzhou.

This study used the NCER/NCAR operational generic circulation model outputs from the 4 grid points closest to Hangzhou (Carter, 2007) (Figure 6.13). The values of these outputs were interpolated with the Grid Analysis and Display System (GrADS COLA/IGES, 2011) in order to create contour lines. The results of the interpolation as depicted by the contour lines over the region of Hangzhou were used for initialising the simulations. The relative soil humidity required for the simulation in ENVI-met is the water content of the soil at field capacity (Bruse, 2008a). The field capacity is the water content of the soil after the drainage of excess water and the decrease of any downward flow (Sun & Yang, 2013).

There were no field observations available regarding the soil profile characteristics at the studied sites in Hangzhou. The data from the NCEP global weather forecasting model are not expected to be representative of the real soil conditions within the city (i.e. under the asphalt or pavements). Nonetheless it is expected that these data are a good approximation of the soil conditions in “open” (i.e. unsealed soil) areas inside the city. All the initial underground soil parameters were updated according to the ground surface cover properties and the ground heat flux during the model’s spin-up and simulation period.

The sealed ground surfaces in the “urban unit model” were represented with the “asphalt” soil profile. The ground surface in the rest of the computational domain

(i.e. excluding the core “urban unit model” of 250 m radius) was represented with the “concrete pavement, used/dirty” soil profile (Figure 6.14).

A concrete pavement surface was favoured against unsealed loam soil in order to achieve a more realistic approximation of the heat fluxes in the urban environment. The use of the default unsealed soil would result in higher water content and lower thermal conductivity values and would not be true in the case of a neighbourhood within a large city.

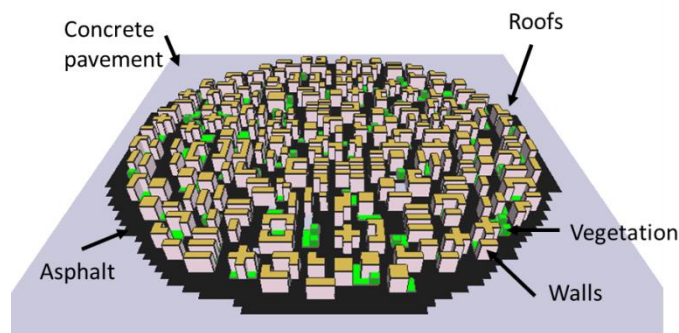


Figure 6.14. Ground surface types used in the simulations with the “urban unit model”.

In addition, the ENVI-met default unsealed loam soil profile was selected for the ground below any vegetated surfaces and for the nested grids. A summary of the main properties of the ground surface materials used in the simulations can be seen in Table 6.4.

Table 6.4. Ground surface material properties used in the simulations with the “urban unit model”.

Ground surface	Thermal conductivity [W m ⁻¹ K ⁻¹]	Heat capacity 10 ⁶ [J m ⁻³ K ⁻¹]	Albedo
Asphalt	0.90*	2.25*	0.10**
Concrete pavement	1.63*	2.08*	0.23**
Building surface	Thermal transmittance [W m ⁻² K ⁻¹]	Heat capacity 10 ⁶ [J m ⁻³ K ⁻¹]	Albedo
Walls (30 cm)	1.4 [0.56^]	0.8	0.4**
Roofs (25 cm)	0.9 [0.26^]	1.5	0.3**

Data Source: * ENVI-met default database (Bruse, 2008a), **Yang et al. (2013b). ^ Conductivity [W m⁻¹ K⁻¹]

The thermal characteristics and the albedo of walls and roofs are common to all buildings in the model. The buildings' surfaces are distinguished by walls and roofs. Each wall/roof surface has 3 nodes, on the inner, outer surfaces and the middle of the wall/roof elements (Figure 6.15) (Huttner, 2012). The energy balance for each element is calculated with a transient model. The heat stored and transferred between the 3 nodes of the building elements is calculated at each time step. The air volume inside the buildings does not store or produce any heat (Huttner, 2012).

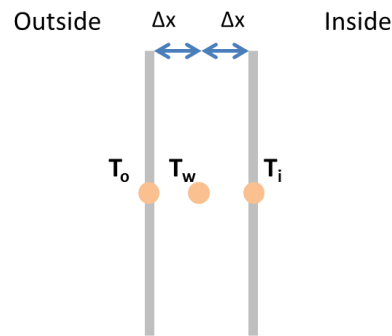


Figure 6.15. The 3 nodes model for the calculation of the wall/roof surface temperature and the internal building air temperature. T_o is the node at the outer surface, T_w at the middle and T_i at the internal surface of the building element. Image Adapted from Huttner (2012).

At the beginning of the simulation the internal building temperature is set to the initial temperature of the environment. The buildings in the simulation are considered to be free-running (i.e. without any heating, cooling and mechanical ventilation systems).

The Chinese National Building Guidelines for residential buildings in the Cold winter Hot summer climate zone specify a wall thermal transmittance of $U_o = 1.5 \text{ W m}^{-2} \text{ K}^{-1}$ and a roof thermal transmittance of $U_r = 1 \text{ W m}^{-2} \text{ K}^{-1}$ (MIT Building Technology Group, 2000). The Design Standard for the Energy Efficiency of Public Buildings 2005 recommends for the same zone a wall thermal transmittance of $U_o = 1.0 \text{ W m}^{-2} \text{ K}^{-1}$ and roof transmittance $U_r = 0.7 \text{ W m}^{-2} \text{ K}^{-1}$ (Yang et al., 2008; Wang et al., 2014). In 2008 the public buildings' floor area in China accounted approximately for 17% of the total buildings' floor area (Bin & Jun, 2012). Therefore it was assumed that 20% of the building roof and wall area in the urban unit model corresponds to public buildings. A detailed floor to wall area ratio analysis for individual buildings was not an objective of this study. The area of commercial buildings was not considered separately as the majority of the measurement sites have a primarily residential use where commercial

activity takes place at the ground floors of residential buildings. The mean thermal transmittance was estimated to be $U_o = 1.5 \times 0.8 + 1 \times 0.2 = 1.4 \text{ W m}^{-2} \text{ K}^{-1}$ for the walls and $U_r = 1 \times 0.8 + 0.2 \times 0.7 = 0.9 \text{ W m}^{-2} \text{ K}^{-1}$ for the roofs.

Vegetation modelling is based on the Leaf Area Density (LAD) at ten levels with different height. LAD is defined as the area covered by leaves per cubic meter of the plant canopy's volume [$\text{m}^2 \text{ leaves/m}^3 \text{ canopy (leaves and air)}$] (Bruse, 2008a; Peng & Jim, 2013). The leaf canopy levels start from a normalised height of $z/H=0.1$ and end at $z/H=1$ above ground, where z is the beginning of the leaf area (e.g. trees with a distinct leaf crown that begins at a 2 m height above ground) and H is the total height of the plant (Bruse, 2008a). The stem of the trees is not modelled explicitly. The dimensions of the vegetated surface (green area) are restricted by the computational grid size. In this study, the tree canopy covered a minimum area of 64 m^2 . Regarding the vertical grid dimension, the grass used in the urban unit model had a minimum height equal to the height of the first vertical grid cell (i.e. 0.50 m). The use of a finer vertical grid resolution would have resulted in the top boundary of the computational domain being lower, closer to the buildings' roof tops due to the 30 vertical grid cells limitations. This would have resulted, in turn, in a higher blockage rate. Trees were assumed to cover part of the pervious surface area. All tree species were represented by a 10m tall tree with a distinctive crown and a Leaf Area Density (LAD) equal to 2. These were randomly distributed across the pervious surface area in the annular areas.

2.2 Anthropogenic heat emissions

The average total anthropogenic heat flux profile in the urban unit was estimated from literature data and with the use of the Large scales Urban Consumption of energy model (LUCY) (Allen et al., 2011; Lindberg et al., 2013). Sailor and Lu (2004) studied the anthropogenic heat emissions profile for 6 large cities in the U.S.A. (i.e. Atlanta, Salt Lake City, Chicago, San Francisco, Los Angeles and Philadelphia) (Table 6.5). It has been previously established with the urban analysis that cities in China grow by following a pattern similar to the U.S.A. paradigm (Figure 5.9; Chapter 5 Section 2.3). In the Sailor and Lu (2004) study, Atlanta and Philadelphia have the same humid sub-tropical climate classification as Hangzhou in China. However,

Philadelphia's population density is five times lower than the population density in Hangzhou and Atlanta's population density is even lower (Wendell Cox Consultancy, 2014).

Table 6.5. Comparison of population density and climate classification between the cities in Sailor and Lu (2004) and this study.

City	Urban population density [persons/km ²]	Köppen Climate classification (Rubel & Kottek, 2010)
Hangzhou, China	5,600 *	Cfa – humid sub-tropical
Shanghai, China	6,200 *	Cfa – humid sub-tropical
Ningbo, China	4,600 *	Cfa – humid sub-tropical
Atlanta, U.S.A.	700 *	Cfa – humid sub-tropical
Salt Lake City, U.S.A.	1,500 *	Dsa – dry summer continental
Chicago	1,300 *	Dfa – humid continental
San Francisco	2,100 *	Csb – sub-tropical Med.
Los Angeles	2,400 *	Csb / Csa – sub-tropical Med.
Philadelphia	1,100 *	Cfa – humid sub-tropical

* Data Source: Wendell Cox Consultancy (2014).

Sailor and Lu (2004) estimated for Philadelphia a daily average wintertime anthropogenic heat flux in the order of 42 W m^{-2} and a daily summertime average flux in the order of 25 W m^{-2} . However, the correlation between population density and anthropogenic heat emissions is not expected to be linear due to the underlying differences between the two countries in the daily traffic patterns, fuel consumption, heating fuel type and levels of building insulation. Energy consumption in China is not correlated with population density to the same degree as energy consumption in the U.S.A. is (Yang et al., 2014). Table 6.6 attempts a comparative review of anthropogenic heat flux estimations for Hangzhou and Philadelphia. The anthropogenic heat flux in Hangzhou according to published studies is 4 to 8 times lower than Philadelphia's heat emission levels (references are provided in Table 6.6) but this can be explained by the underlying data, reference scale and resolution used in each study. In general, at the administrative areas (low resolution) the anthropogenic heat flux can be considerably lower than the areas within the city (high resolution), with cities typically having a flux range from 20 to 100 W m^{-2} (Lu et al., 2016).

The LUCY model incorporates population density (Global Rural-Urban Mapping Project (GRUMP v.1), Center for International Earth Science Information Network et al. (2011)), total primary energy consumption and traffic datasets into the calculation of

hourly sensible heat flux (Lindberg et al., 2013). In order to calculate the building heat emissions, LUCY normalises the national total net primary energy consumption for the population, time of day and monthly average temperature. A building thermal comfort set point of 18°C was assumed (Allen et al., 2011).

Table 6.6. Anthropogenic heat flux reference values for Hangzhou, China and Philadelphia, U.S.A..

City	Anthropogenic heat flux [W m^{-2}]	Reference study
Hangzhou, China	50 (daily mean)	Yan et al. (2008)
Philadelphia, U.S.A.	25 (daily summertime mean)	Sailor and Lu (2004)
Hangzhou, China	2.7 (annual mean, 0.5x0.5 (lon x lat) degrees)	Flanner (2009)
Philadelphia, U.S.A.	8.5 (annual mean, 0.5x0.5 (lon x lat) degrees)	Flanner (2009)
Hangzhou, China	17.4 (annual mean, 2.5x2.5 (lon x lat) minute degrees)	Yang et al. (2014)
Hangzhou, China	9.1 (annual mean, 2.5x2.5 (lon x lat) minute degrees)	Flanner (2009)
Philadelphia, U.S.A.	77.3 (annual mean, 2.5x2.5 (lon x lat) minute degrees)	Flanner (2009)

A temperature scaling factor is used to correspond for seasonal energy demand changes (Allen et al., 2011). The scaling factor is a function of the Heating and Cooling Degree days and the country's annual income in order to distinguish between countries with different income levels (Lindberg et al., 2013). It is expected that the total energy consumption is positively correlated with income; countries with the same annual total heating and cooling demand but different income levels will have a different energy consumption (Lindberg et al., 2013).

The anthropogenic heat emissions as calculated with the LUCY tool for this study were based on monthly average temperature observations from the period between 1970-2000 and population density data from 2000 (Allen et al., 2011). The energy consumption data were from the year 2011 and the number of cars, motorcycles and freight vehicles were from the year 2005. An average speed of 40 km/h was assumed. The average hourly estimations for each month are shown in Figure 6.16. The anthropogenic heat flux peaks in the early afternoon and drops during the night to its minimum value ($\sim 2\text{-}3 \text{ W m}^{-2}$). The diurnal pattern exhibits a seasonal

variation between summer/winter and spring/autumn indicating higher primary energy consumption during the summer months.

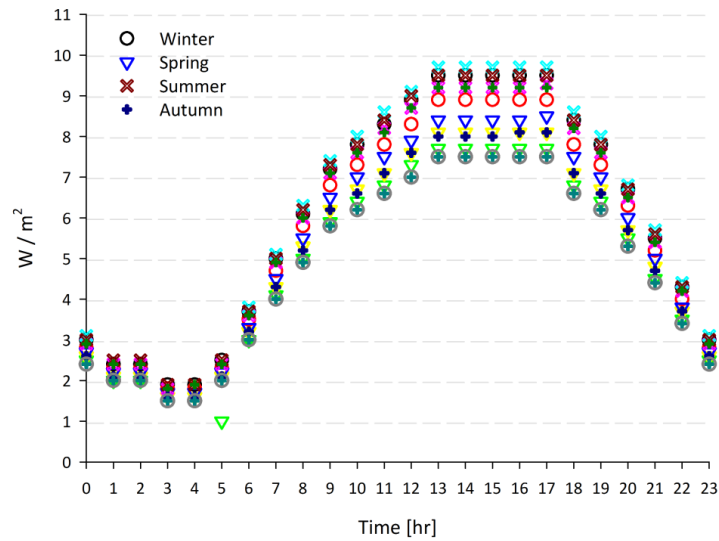


Figure 6.16. The monthly anthropogenic heat emissions as calculated for Hangzhou with the LUCY model. Data Source: Allen et al. (2011), Lindberg et al. (2013)

The small difference between summer and winter heat emissions can be explained by the large number of Cooling Degree Days and higher cooling and dehumidification load than the heating load in winter (Lindberg et al., 2013). However, these results were used only as an indication of the expected diurnal and seasonal profile. The fluxes were calculated based on old census data (i.e. ambient temperature from the period 1970-2000 and traffic from 2005) and they are not representative of dense urban locations at the modelled scale within the city centre (Lindberg et al., 2013).

In the scale of this study and for locations within the city such as the LCZ5 sites in Hangzhou, the anthropogenic heat flux was estimated to be in the range of 70 W m^{-2} in 2010 (Lu et al., 2016). The same study estimated an anthropogenic heat flux of about 120 W m^{-2} for downtown Shanghai (Lu et al., 2016). During the study period the anthropogenic heat flux in Hangzhou was estimated to be about 90 W m^{-2} to account for further development.

The estimated anthropogenic heat flux could not be directly incorporated into the ENVI-met model with the addition of heat sources. Instead, the hourly global solar radiation levels were statistically inflated to include the additional energy by heat

emissions. The main drawback of this technique is that night time forcing was neglected as the solar radiation in the model is zero. The night time values were extrapolated and added to the daylight hours in order to represent the total daily heat emissions.

2.3 Solar radiation

In the case of cities at latitudes near the equator and in the temperate zones, solar radiation is the most important energy input to the urban energy balance. The levels of incident solar irradiation define the magnitude of the sensible and latent heat fluxes and the heat storage in the urban environment. Consequently, the development of surface and air temperature and relative humidity with time is directly linked to the solar radiation net energy balance (Figure 6.17). The net radiation is a key factor in efforts for the alleviation of the urban heat island effects (Synnefa et al., 2008; Santamouris et al., 2011). One of these effects with great relevance to this study is the impact on the cooling and heating loads of buildings.

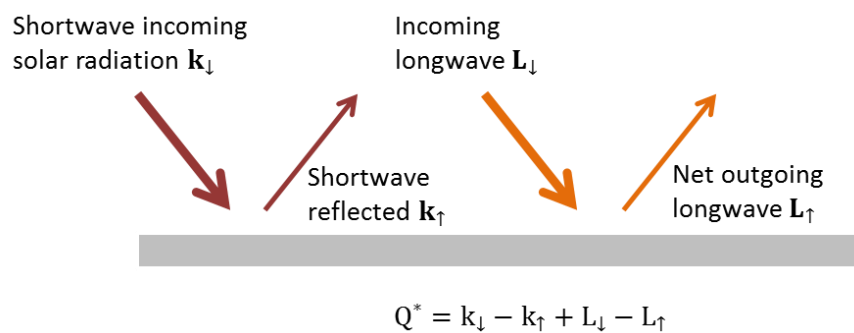


Figure 6.17. Schematic representation of the solar radiation net energy Q^* balance at the ground surface. Shortwave and longwave radiation are denoted with k and L respectively. Image modified from Foken (2008).

ENVI-met estimates the incoming shortwave and longwave radiation at the model top with an approximation of the clear sky total radiation and then it applies corrections for humidity, cloudiness and visibility levels (Taesler & Andersson, 1984; Bruse, 2004). The diurnal cycle (not separate hours) of the incoming total shortwave global horizontal radiation can be adjusted with the use of an adjustment factor (i.e. 50% to 150%) in order to fit to the measured levels at the location of the model. This

adjustment affects the global horizontal radiation (GHR) which is calculated as the total incoming direct and diffuse shortwave radiation received on a horizontal surface. Site specific solar radiation data are required to accurately set up the solar radiation input for the simulation model. However, solar radiation data with high spatial and time resolution are sparse. There were not any solar radiation data available from Hangzhou for the period of the observations. Therefore, this study developed and assessed the use of an artificial neural network (Appendix E) for the generation of hourly global horizontal radiation time series in the context of micro-climatic simulations for the city of Hangzhou in China.

Initially, a multi-layer (i.e. with hidden layers) perceptron (MLP), feed-forward back-propagation Artificial Neural Network (ANN) was developed for the prediction of global horizontal radiation (GHR) (Appendix E). Artificial neural networks are information processing systems that learn by training so that they can provide projections when the network is applied to new data (Stergiou & Siganos, 2004). ANNs for solar radiation prediction perform better compared to empirical and other statistical models (i.e. linear, nonlinear, fuzzy logic) (Behrang et al., 2010; Yadav & Chandel, 2014). The accuracy of the prediction depends largely on the selection of the input parameters with sunshine duration and air temperature having the highest correlation with solar radiation (>0.95) (Yadav & Chandel, 2014). The final ANN configuration in this study had a large mean absolute percent error (MAPE) and poor performance in the prediction of hourly GHR (see in E.3 Validation of the ANN model and conclusions on its use).

In a sunny winter scenario (SWS, 11/01/2013), the solar radiation model used in ENVI-met estimated a maximum hourly global horizontal solar radiation (GHR) equal to 530 W m^{-2} , a minimum GHR value of 90 W m^{-2} and a daily average GHR on the order of 350 W m^{-2} . The hourly global solar radiation modelled with ENVI-met for Hangzhou was compared with the hourly GHR ANN results, the GHR historical data from the typical meteorological year (TMY) weather data file (WMO 584570) and the NCEP/NCAR US (2000) 6 hourly downward shortwave solar radiation model output (i.e. output at 08:00 and 14:00) for Hangzhou (Figure 6.18).

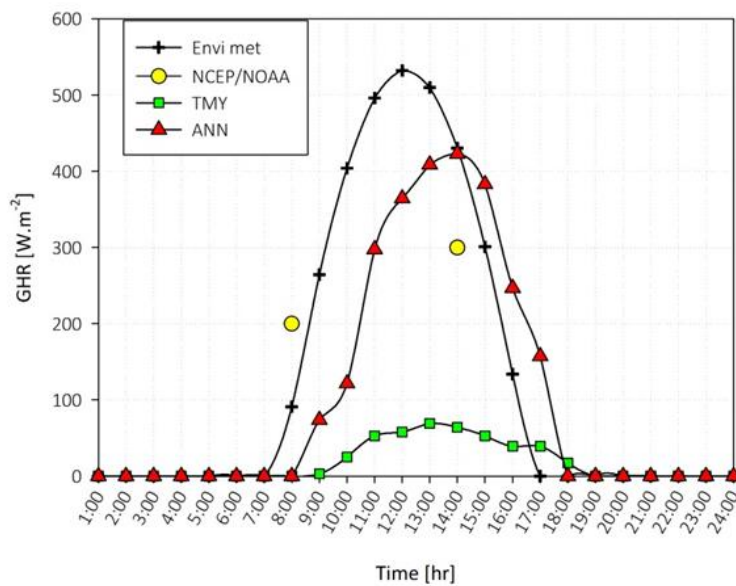


Figure 6.18. Comparison of the hourly global horizontal solar radiation (GHR) [W m^{-2}] for the winter scenario between different datasets. ENVI-met estimations (black cross), NCEP/NOAA model (yellow points) output, TMY (WMO 584570) file (green square) and the ANN results (red triangle) for Hangzhou are shown respectively. Data Source: Bruse (2004), NCEP/NCAR US (2000).

The ENVI-met value of global solar radiation at noon peaked 25% to 50% higher than the ANN and the NCEP/NOAA model outputs (Figure 6.18). A two hour phase shift was noticed between the diurnal GHR results from ENVI-met and the ANN results. This phase shift was expected to be matched by a similar phase shift between the simulated air temperature and the on-site air temperature observations (Middel et al., 2014). The daily average GHR from the ANN model was 25% lower than the daily average GHR as modelled with the ENVI-met tools.

On the 10th of August 2013 (sunny summer scenario) the maximum hourly GHR according to ENVI-met solar radiation modelling was 880 W m^{-2} while the daily average global solar radiation was 520 W m^{-2} and the minimum 30 W m^{-2} respectively. The comparison between ENVI-met and NCEP/NCAR US (2000) model outputs with the GHR data from the typical meteorological year (TMY) weather data file and the GHR ANN results (Figure 6.19) showed that the ENVI-met GHR prediction is a very good fit to the NCEP/NOAA model output at 08:00. On the other hand, the ANN results showed a good fit to the TMY data in the morning (06:00 to 09:00) and early afternoon (15:00 to 20:00) and to the NCEP/NOAA solar radiation output at early afternoon (14:00) hours (Figure 6.19). The daily average GHR predicted with ENVI-met is 20% higher than the ANN daily GHR results. The estimated GHR levels from both the ANN and the GCM models are lower than the ENVI-met calculations in both winter and summer.

However, the solar radiation levels estimated by the ANN and GCM models are either not available on every hour or they have a relatively high error.

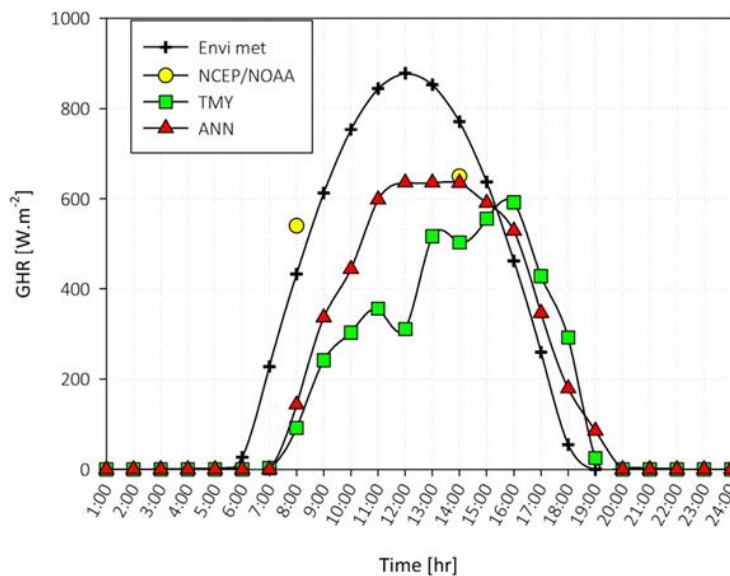


Figure 6.19. Comparison of the hourly global horizontal solar radiation (GHR) [W m^{-2}] for the summer scenario between different datasets. ENVI-met estimations (black cross), NCEP/NOAA model (yellow points) output, TMY (WMO 584570) file (green square) and the ANN results (red triangle) for Hangzhou are shown respectively. Data Source: Bruse (2004), NCEP/NCAR US (2000).

In the “urban unit model” simulations therefore, the hourly GHR modelled with ENVI-met was used with an adjustment to include the anthropogenic heat emissions and fitted to the solar radiation profiles of the three distinct weather forcing groups. As a result of distributing the total daily anthropogenic heat fluxes into the daylight hours, the anthropogenic heat emissions were overrepresented in morning and underrepresented during the afternoon when they peak. In order to overcome this issue the solar radiation profile was extended to the afternoon. The modelled GHR was adjusted to fit the hourly solar radiation levels in the groups (statistically estimated by the TMY file reference GHR values) during the peak of the anthropogenic heat emissions (15:00 – 16:00) and as late as possible in the day. This adjustment led to the use of scaling factors that offset upwards or downwards the total diurnal solar radiation curve. The largest scaling factors (~ 1.3) were used as expected in the weather forcing case of Group 3 (clear sky, hot weather) and the smallest (~ 0.5) in the case of Group 1 (cloudy/rainy weather). In most months the Group 2 weather forcing case (clear sky/average weather conditions) did not need a solar radiation adjustment. The total annual solar radiation in the model represented the annual solar radiation levels for Hangzhou including an average daily anthropogenic heat flux in the range of 90 W m^{-2} as discussed in Chapter 6, Section 2.2 Anthropogenic heat emissions.

2.4 Meteorological data for the simulations

ENVI-met (version 4) allows for the hourly weather forcing of relative humidity and air temperature with external data. Wind velocity at the top boundary of the 1 dimensional model (i.e. 2,500 m) is constant during the simulation. The initial meteorological data should be representative of the daily average weather conditions during the simulation (Bruse, 2008a). The main input weather parameters are (Appendix F; example in Table 6.7): a) specific humidity [g Water per 1 kg air] at 2,500m above ground, b) the mean potential air temperature [K] that is not influenced by surface layer processes (Chow & Brazel, 2012), c) wind speed and direction at 10 m above ground and d) the roughness length z_0 at the location where the wind velocity was measured.

The specific humidity [g water per 1 kg air] at 2,500 m (750 mbar isobaric pressure) above ground (ab. gr.) was estimated by the NCEP/NCAR US (2000) model daily outputs (i.e. total 3 values per day, data available every six hours (on the hour, not a six hour average; 08:00, 14:00, 20:00 China Standard Time) for each date and weather forcing group) from the 4 grid boxes closest to Hangzhou (Figure 6.13). In the validation simulations the data at 20:00 CST from days with a similar profile to the date of the simulation characteristics were used to calculate the specific humidity and initialise the simulations. For the generation of the “urban weather projections” daily average values (average of 3 values per day) were used from a minimum of 4 days from the weather forcing groups respectively. The initial air temperature profile was calculated from the daily average of the hourly forcing weather data at the 2 m height above ground. The hourly air temperature and RH forcings in the case of validations were the observed hourly data from the reference weather station (TMY source; Mantou Mountain National Principle station, WMO 584570) adjusted with the weather forcing group’s UHI intensity (and not the observed UHI during the simulated day). In the case of the “urban weather projection” simulations the hourly forcing was the hourly average data from the days in the weather forcing groups adjusted for the group’s UHI intensity.

Chapter 6 Urban weather projections

Table 6.7. Overview of key forcing for the validation simulations and the “urban weather projections” generation. An example is shown for June, weather forcing Group 2.

Input parameter	Validation	Urban weather projections	Source
Specific humidity 2,500m (750 mbar) <i>gr w/kg dry air</i>	12	9.90	NCEP/NCAR US (2000)
Prevalent wind direction (N = 0 clockwise)		90	The Weather Underground (2014b)
Wind speed 10m ab. gr. <i>m/s</i>		2.8	The Weather Underground (2014b)
Roughness length z_0		0.10	Stewart and Oke (2012)
Mean wall albedo		0.23	Yang et al. (2013b)
Mean roof albedo		0.50	Yang et al. (2013b)
Wall heat transmittance $Wm^{-2}K^{-1}$		1.40	
Roof heat transmittance $Wm^{-2}K^{-1}$		0.90	
Underground soil temperature (Upper-Middle-Deep layer) <i>K</i>	299-294-291	297.5-292.7-290.5	NCEP/NCAR US (2000);
Underground soil humidity (Upper-Middle-Deep layer)	39%-37%-36%	37%-37%-36%	NCEP/NCAR US (2000);
Hourly T and RH	Reference weather station observations for the simulated day adjusted with group UHII	Average hourly observations from the days in group adjusted with group UHII	

Low night time air temperature can significantly affect the daily average temperature (over 24 hours). A low initial value could mean that the model needs a long spin-up period in order to minimise the influence of the initial conditions. However, during the simulation spin-up parameters such as the heat storage and soil moisture change too. The dynamic change of these parameters with time raised considerations for the use of a spin-up period longer than the 4 hours finally used in this study. This time period was deemed satisfactory in this case because the initialisation parameters were based on real-time observations.

The specific humidity [kg water/kg dry air] at 2,500 m above ground was calculated for moist air by the equations for relative humidity and the water vapour partial pressure (The Engineering Toolbox, 2014):

$$p_{ws} = e^{(77.3450 + 0.0057 \times T - 7235/T)} / T^{8.2} \quad [\text{Pa}] \quad (6.11)$$

$$RH = (p_w / p_{ws}) \times 100 \quad [\%] \quad (6.12)$$

$$Sp. H. = m_w / m_{da} = R_{da} / R_w \times p_w / (p - p_w) \quad [\text{kg water/kg dry air}] \quad (6.13)$$

where p_{ws} is the saturation pressure [Pa] of water vapour, T is the absolute temperature [K] of moist air, RH is the relative humidity [%], p_w is the partial pressure of water vapour in the moist air mixture [Pa]. $Sp. H.$ is the specific humidity [kg water/kg dry air], m_w and m_{da} are the mass of water vapour and dry air [kg] respectively. R_w (~461.5 J/kg/K) and R_{da} (~286.9 J/kg/K) are the water vapour and dry air gas constants respectively and p is the total air pressure at 2,500 m (~750 mbar = 75,000 Pa).

The wind velocity at 10 m above ground was obtained from observations at the Mantou Mountain official weather station in Hangzhou. The prevalent wind direction was estimated by the highest wind direction frequency normalised with the wind speed (frequency x wind speed) for the weather forcing groups in each month. The wind speed is the daily average of the observations from the same weather station (The Weather Underground, 2014b). The roughness length z_0 at the location of the weather station was not known. Images and description of the weather station site (Shen et al., 2014) indicated that it is a site with low plant cover and few buildings. There are trees farther away from the site. According to the LCZ classification scheme a roughness length $z_0=0.1$ (Stewart & Oke, 2012) was appropriate. This is also the maximum value in ENVI-met version 4. The key forcing differences between the validation and the “urban weather projection” simulations are shown in Table 6.7.

3. Validation of the simulations with the “urban unit model”

The “urban unit model” methodology was validated for each of the 4 seasons and 3 different weather forcing conditions against the hourly average air temperature and RH observations from the 9 studied sites on a given day representative of the weather forcing conditions. The main parameters for the “urban unit model” validation are shown in Appendix F. Looking at the dates given in Appendix F the “urban unit model” validation simulations were forced with the hourly weather data from the reference weather station (TMY source) overlaid with the representative urban heat island effect of the weather forcing group as calculated from the 10 “sample” sites’ observations (and not the observed UHI during the simulated day) (see also Figure 6.1 and Figure 6.2). The hourly weather forcing for the “urban weather projections” simulations was undertaken with the hourly average air temperature and RH for the respective weather forcing group in the TMY file, adjusted by the representative bulk hourly UHI intensity (same as in the validation case) for the weather forcing groups.

This evaluation of the model’s performance (Figure 6.20 - Figure 6.23) has showed that urban micro-climatic simulations using the idealised “urban unit model” captures to within 1 °C the main characteristics of the diurnal air temperature development in all seasons. If the model output is a perfect prediction we would expect the observed temperatures (black line; average of hourly observations from the nine “LCZ5” sites, see Figure 6.20 - Figure 6.23) to be identical to the modelled temperatures (red line in Figure 6.20 - Figure 6.23). In this case the UHI effect experienced by the 9 LCZ5 sites and the 10 “sample” weather stations within the city would have to be identical. The ENVI-met model would have to perfectly forecast the average temperature / RH development at street level.

In the weather forcing group 1 winter scenario (January 13, 2013; Figure 6.20 (top)) the modelled air temperature at 3.5 m above ground (Air Temp. [°C]; red line) is a very good fit to the observed temperature (black line; RMSE: 0.4, MAPE: 5%, Table 6.8). The simulation results predict the night-time UHI better than the reference weather station (TMY source station) observations (circles in Figure 6.20 - Figure 6.23). The RH results (red line in Figure 6.20 (right)) are representative of the observed RH diurnal trend.

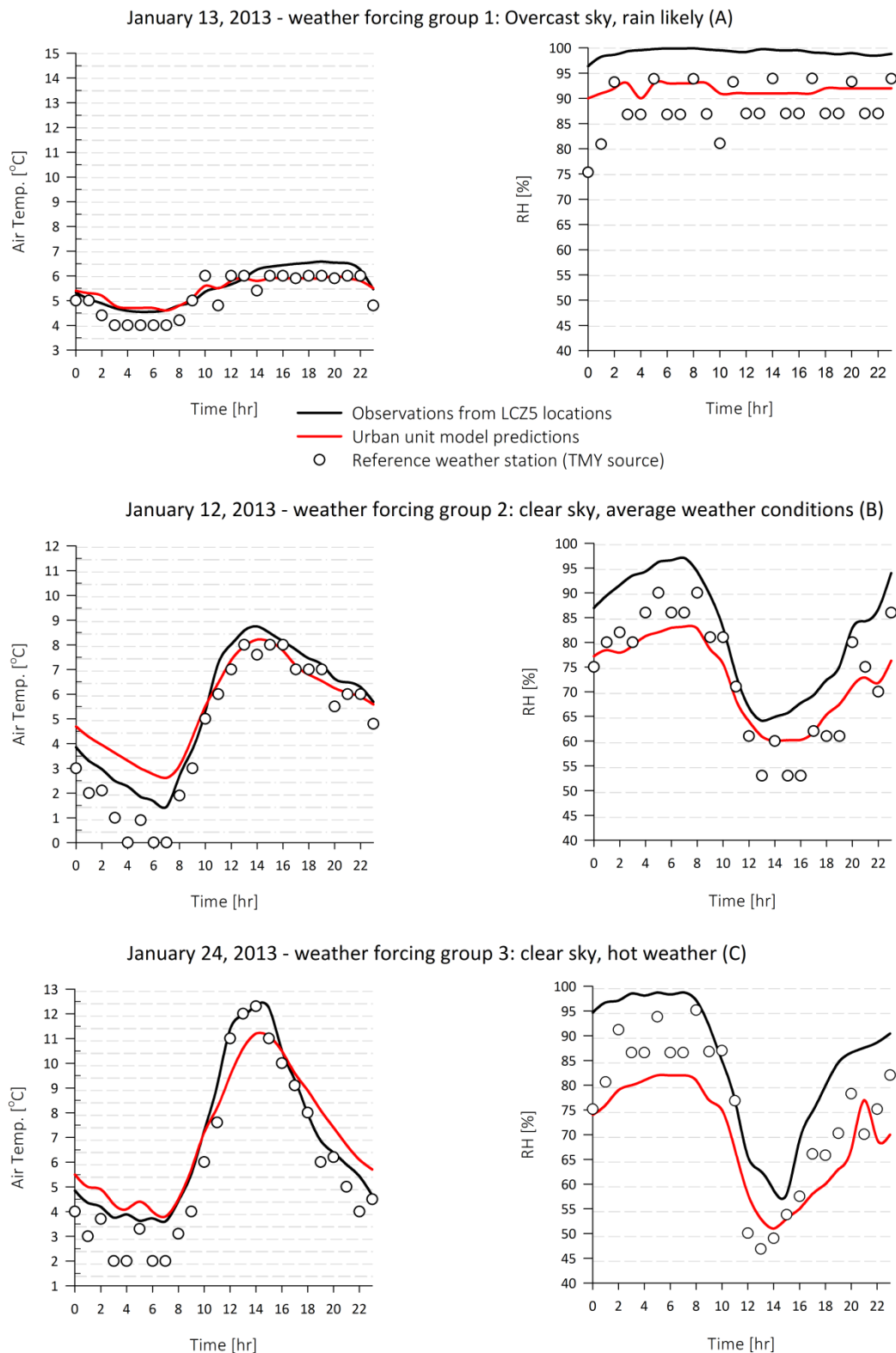


Figure 6.20. Comparison of the observed (black line) and the modelled air temperature (left) and RH (right) at 3.5m above ground for the 3 days in January 2013 (winter) representative for the weather forcing groups. (Time given in China Standard Time – CST: GMT+8).

The simulated RH values are low compared to the average of the hourly observations but still represent an improvement in the urban weather conditions' prediction when compared to the reference weather station. In the case of weather forcing group 2 the simulated air temperature is a good fit to the observations for most hours of the day (Figure 6.20 (middle)). The air temperature is overestimated early in the morning but the high values potentially better represent the urban conditions than the measured data from the reference weather station. In the weather forcing group 3 case, winter daytime air temperatures are underestimated with the model failing to predict the temperature peak around 13:00 h.

Table 6.8. Model performance indices determined for the heating season simulations with the novel urban unit model.

Model performance indices	T (RH) - Heating season (January)			T (RH) - Heating season (October)		
	Group 1	Group 2	Group 3	Group 1	Group 2	Group 3
Mean Squared Error (MSE)	0.13 (56.1)	0.55 (116.1)	0.70 (258.5)	0.50 (61.6)	0.31 (261.2)	0.39 (287.1)
Mean Bias Error (MBE)	-0.14 (-7.4)	0.12 (-10)	0.16 (-15.4)	-0.42 (-7.5)	-0.17 (-15.9)	-0.02 (-15.3)
MSE systematic	0.11 (55.8)	0.49 (112.5)	0.40 (246.3)	0.33 (56.7)	0.22 (255.4)	0.23 (280.9)
Root Mean Squared Error (RMSE)	0.36 (7.50)	0.74 (10.75)	0.84 (16.05)	0.70 (7.85)	0.56 (16.16)	0.63 (16.95)
RMSE systematic	0.33 (7.47)	0.70 (10.61)	0.64 (15.70)	0.58 (7.53)	0.47 (15.98)	0.48 (16.76)
MSE unsystematic	0.02 (0.73)	0.05 (3.05)	0.30 (11.17)	0.17 (4.89)	0.09 (5.85)	0.16 (6.26)
RMSE unsystematic	0.15 (0.85)	0.23 (1.75)	0.55 (3.34)	0.41 (2.21)	0.31 (2.42)	0.40 (2.50)
Mean Absolute Percentage Error (MAPE)	5% (8%)	21% (12%)	11% (18%)	3% (9%)	2% (21%)	2% (21%)
Index of agreement d	0.92 (0.13)	0.97 (0.78)	0.98 (0.72)	0.95 (0.68)	0.99 (0.48)	0.99 (0.77)

Nevertheless, the simulation results fit the observed data relatively well at night-time, in the early morning and afternoon. The failure to accurately predict the peak could be a result of an inaccurate representation of thermal mass and heat storage in the model (Middel et al., 2014) and the modelling of thermal diffusivity by ENVI-met (Maggiotto et al., 2014).

The simulated RH in January for both the weather forcing group 2 and group 3 cases (Figure 6.20), again replicates the daily observed trend and the RH predicted levels are comparable with the reference weather station observations (especially when considering the 5% units RH sensor accuracy) for the largest part of the day. The model underestimates the RH during early morning before 08:00 o'clock indicating a possible discrepancy between the modelled vegetation properties (i.e. amount and type of trees, grass) and reality. However, this difference is not expected to have a significant effect on the model's application because 1) the predicted RH values are relatively close to the reference weather station observations and 2) the largest discrepancy is early in the morning and late at night in winter when typically dehumidification is not an option when split AC units operate in heating mode (or auxiliary heating sources are used instead). The satisfactory prediction of the expected urban heat island during the night ($\Delta T_{\text{Case} - \text{reference}}$) in all three cases is a further indication that this level of inaccuracy is not detrimental to the overall function of the model.

In the spring scenario (May 2013, Figure 6.21) the air temperature was overestimated during night and early morning. The simulated air temperature in the afternoon was representative of the observed air temperature across all three weather forcing groups. The reference weather station observations were consistently very close to the urban observations showing the existence of a rather small urban heat island effect in Hangzhou during spring. The RH in the urban unit model was again underestimated with the error being tolerable (RMSE: 7, MAPE:7%, Table 6.9) in the case that represents overcast sky conditions (group 1, Figure 6.21 (top)) but significant (RMSE:15, MAPE:20%, Table 6.9) in the weather forcing group 3 case (i.e. clear sky, hot weather).

Overall, in the spring scenario the night-time urban heat island intensity was overestimated across all the weather forcing groups. However, in May night-time the air temperature is still low and the air-conditioning demand if any is expected to be minimal (see next chapter for cooling profiles).

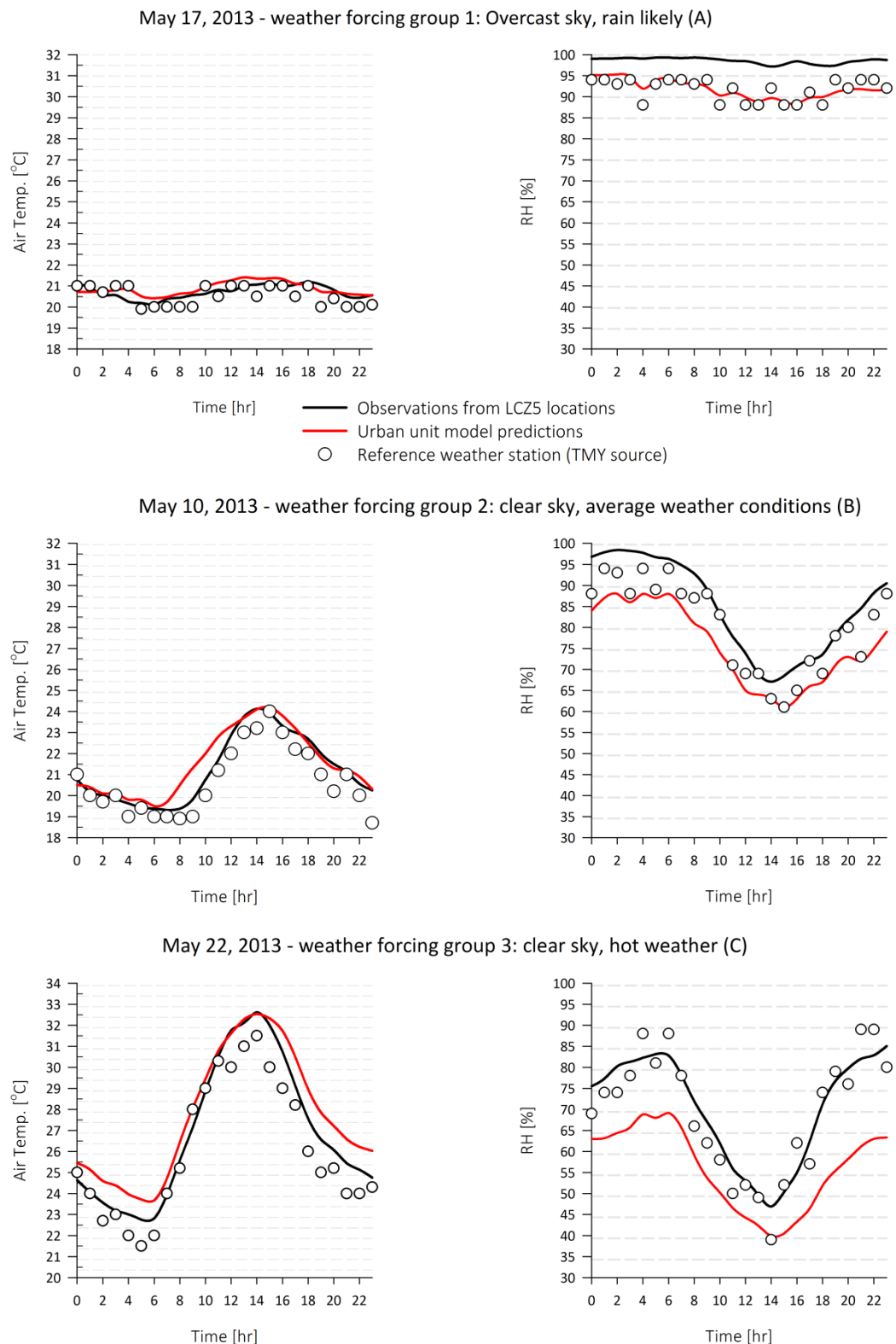


Figure 6.21. Comparison of the observed (black line) and the modelled air temperature (left) and RH (right) at 3.5m above ground for the 3 days in May 2013 (spring) representative for the weather forcing groups. (Time given in China Standard Time – CST: GMT+8).

Table 6.9 Model performance indices determined for the cooling season simulations with the novel urban unit model.

Model performance indices	T (RH) - Cooling season (May)			T (RH) - Cooling season (June)		
	Group 1	Group 2	Group 3	Group 1	Group 2	Group 3
Mean Squared Error (MSE)	0.08 (48.5)	0.31 (91.3)	0.90 (226.5)	0.15 (77.2)	0.52 (65.2)	0.67 (88.3)
Mean Bias Error (MBE)	0.15 (-6.8)	0.31 (-9.2)	0.84 (-14.4)	-0.11 (-8.4)	0.23 (-6.9)	0.75 (-8.9)
MSE systematic	0.04 (46)	0.11 (89.8)	0.80 (219.4)	0.04 (73.5)	0.08 (53.6)	0.56 (84.0)
Root Mean Squared Error (RMSE)	0.29 (6.9)	0.56 (9.6)	0.95 (15.1)	0.38 (8.8)	0.72 (8.1)	0.82 (9.4)
RMSE systematic	0.19 (6.78)	0.33 (9.47)	0.89 (14.81)	0.20 (8.56)	0.27 (7.32)	0.75 (9.17)
MSE unsystematic	0.05 (1.96)	0.20 (2.45)	0.10 (8.37)	0.11 (3.71)	0.45 (11.60)	0.11 (4.73)
RMSE unsystematic	0.22 (1.40)	0.45 (1.57)	0.32 (2.89)	0.33 (1.93)	0.67 (3.41)	0.33 (2.17)
Mean Absolute Percentage Error (MAPE)	1% (7%)	2% (11%)	3% (20%)	2% (9%)	2% (9%)	2% (13%)
Index of agreement d	0.78 (0.17)	0.97 (0.82)	0.98 (0.73)	0.94 (0.29)	0.98 (0.89)	0.98 (0.85)

In the weather forcing group 3 case (Figure 6.21 (bottom)) the high air temperature at noon suggests that indoor temperatures are highly likely to exceed the comfort band threshold of 27 °C (Nikolou, 2011) creating a demand for cooling. The simulated air temperature peaks are a good fit to the urban observations and in most cases they represent the urban weather development better than the reference weather station measurements.

In the summer scenario (June, Figure 6.22), the air temperature predictions from all three weather forcing groups fit the observations from the studied LCZ5 sites (Figure 6.22) reasonably well (RMSE: 0.4 to 0.8, MAPE: 2%, Table 6.9). In June 2013, in the weather forcing group 3 case, the air temperature is over predicted at noon and early morning.

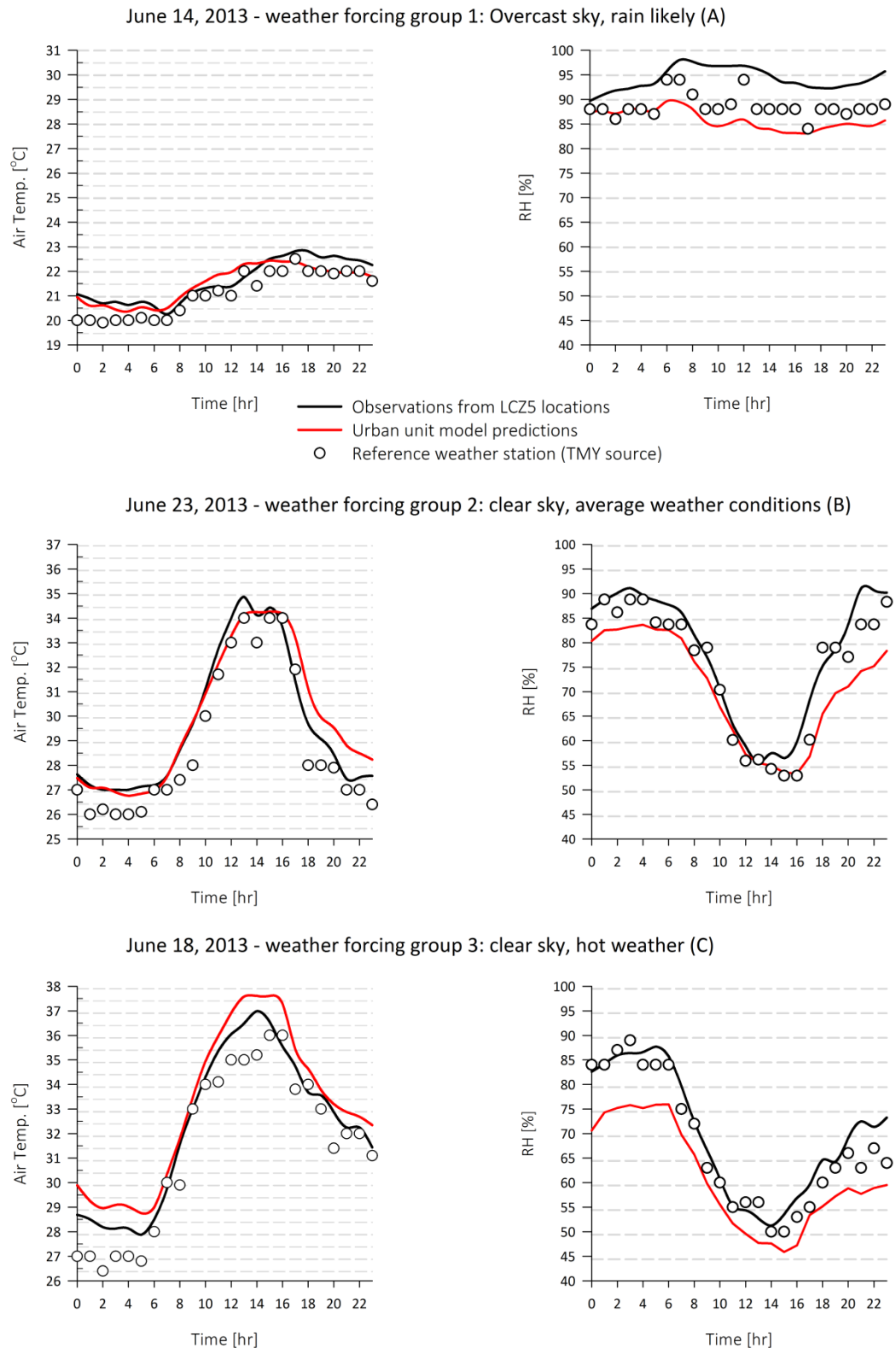


Figure 6.22. Comparison of the observed (black line) and the modelled (red line) air temperature (left) and RH (right) at 3.5m above ground for the 3 days in June 2013 (summer) representative for the weather forcing groups. (Time given in China Standard Time – CST: GMT+8).

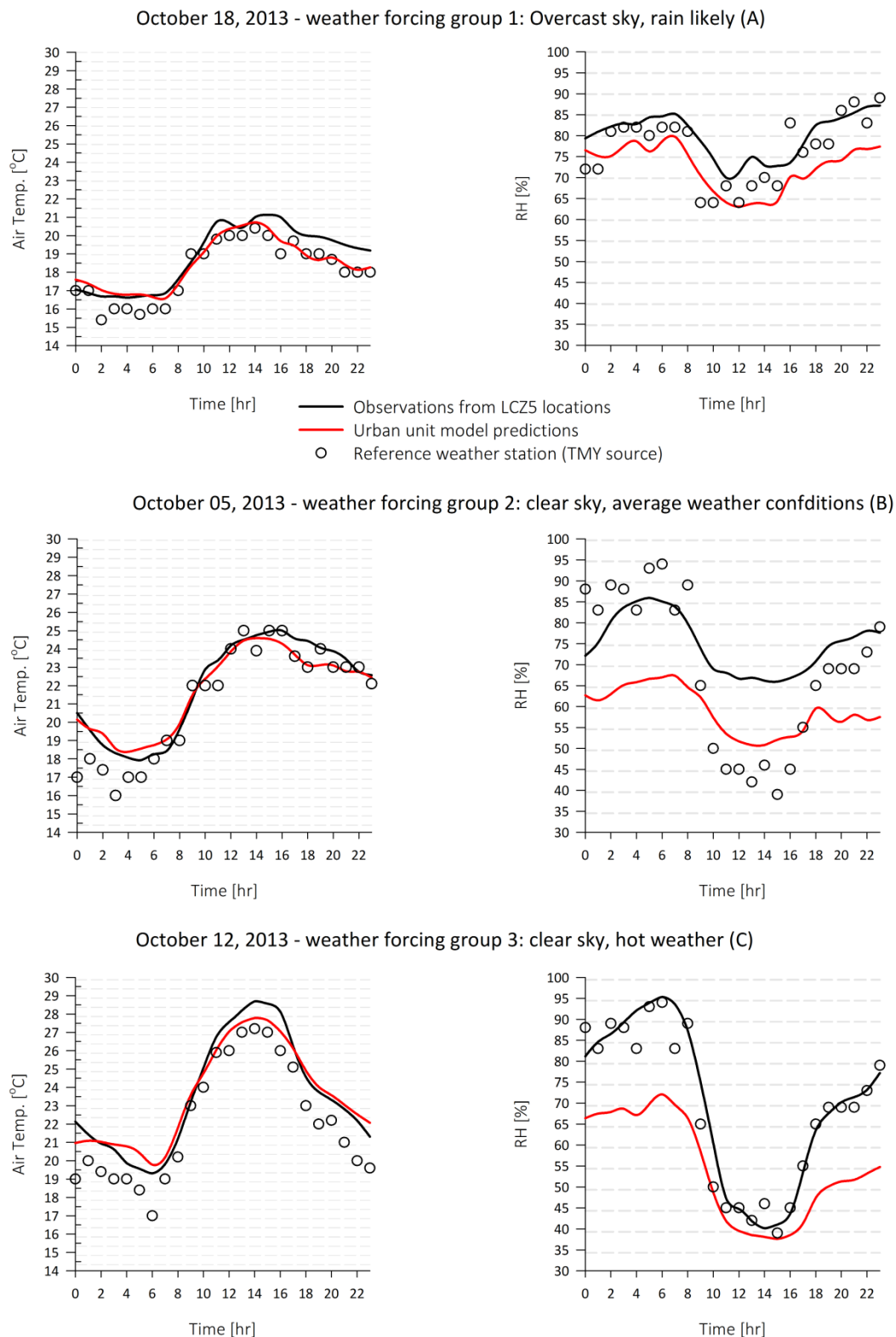


Figure 6.23. Comparison of the observed (black line) and the modelled (red line) air temperature (left) and RH (right) at 3.5m above ground for the 3 days in October 2013 (autumn) representative for the weather forcing groups. (Time given in China Standard Time – CST: GMT+8).

This recurring pattern in the simulation of hot weather conditions in spring and summer can be the result of underrepresentation of the permeable surface and soil water content in the model (Maggiotto et al., 2014). The RH simulation results support this argument with the error of the simulated RH in morning being in the range of 15 RH percentage units. Overall, the RH is underestimated during large parts of the day but the simulated RH levels are comparable with the observations with a RMSE around 10 RH units and MAPE of 10% (Table 6.9).

In October (autumn, Figure 6.23) the model simulates the urban heat island development during the night with the simulated air temperature being close to the observations from the LCZ5 sites. The modelled air temperature development is more realistic for the urban environment than the measured reference temperature. At noon and under hot weather conditions (weather forcing group 3), the model fails to accurately predict the peak but the simulated temperature is still an improvement in comparison with the reference air temperature observations. In general, domestic buildings in October are expected to be free-running (no heating or cooling). There is a demand for cooling in September and for heating from mid-November onwards. The validation of the model showed that cooling demand in autumn is likely to be underestimated at noon and in the early afternoon but its prediction is largely improved at night when the air temperature simulation results fit the urban observations very well (RMSE: 0.6 to 0.7, MAPE: ~2%, Table 6.8).

The simulated RH follows the observed diurnal RH trend but in weather forcing groups 2 and 3 the error is large with the RMSE equal to 16 and 17 RH % units respectively and the MAPE in the range of 20%. This discrepancy might be a result of weather events that ENVI-met cannot simulate such as mist, haze and rain. Specifically on the 12th of October there was mist until 08:00 in the morning when it dispersed and at the same time the model's prediction accuracy increased. In the evening the large error in the RH prediction can be attributed to the modelled soil water content and the position of some of the LCZ5 sites being close to large water bodies. In late autumn the RH plays little role as there is no dehumidification load associated with heating. In addition, the largest RH error in October was noticed early in the morning and during the evening when the temperature is expected to be within the comfort dead band of the thermostat and there will be no cooling requirement.

Overall, the accuracy of the model can be viewed as satisfactory in relation to its purpose, considering the uncertainties involved in the initialisation of the model and the simulation itself. Furthermore, the model performance evaluation indices' scores for air temperature (Table 6.8 and Table 6.9) are comparable to other published work (Yang et al., 2013b; Middel et al., 2014). The index of agreement d takes values in the range $\{0, 1\}$ with a value of 1 indicating a perfect match between the model prediction and the observations (Willmott, 1982; Middel et al., 2014). The index of agreement scores low in the weather forcing group 1 results for all seasons. However the Mean Absolute Percentage Error of the air temperature was consistently less than 10% in almost all cases and the systematic component of the root mean square error (RMSEs) was lower than 0.5 °C in most cases and always lower than 1 °C. The systematic component of the error (i.e. RMSEs), which represents the error attributed to the simulation and the error integrated into the initialisation estimates, should approach 0 (Middel et al., 2014). The unsystematic component should approach the value of RMSE (Willmott, 1982). The relatively low RMSE values in conjunction with the fact that the model results were closer to the urban observations than the reference measured values show that the model's performance is acceptable.

The accuracy of the RH prediction is most important during the cooling season when dehumidification is required. In Hangzhou and other similar cities with a humid sub-tropical climate the full cooling season is expected to last from June to September (Hu et al., 2013; Shen et al., 2014). The validation showed that in June and for the summer scenario the error is below 10 RH percentage units. However, the measured RH from the reference weather station fits better to the urban observations than the simulated RH. Furthermore there is only a marginal RH difference between the urban and the reference sites. Therefore, the urban weather projections were used to adapt the air temperature only in the TMY file and not the relative humidity.

A full scale error analysis was not undertaken due to lack of available data / input parameters notably the hourly global solar radiation and soil properties. The validation has been restricted to days that are typical for the weather forcing groups' conditions. The main sources of systematic error are the input initialisation parameters, in particular hourly global solar radiation. Other sources of systematic error include the initial boundary conditions, building and vegetation properties. Unsystematic errors might be a result of the thermal diffusivity (Maggiotto et al., 2014)

and turbulence modelling, the modelling of evapotranspiration and the total heat advection to the atmosphere.

Chapter 7 Case studies of building energy performance in Hangzhou, China

1. Urban weather adapted TMY file

Following the “urban unit model” validation the TMY file for Hangzhou (584570_CSWD) was adapted to include the “urban weather projections” (UWP) according to the methods outlined above. This enabled the assessment of any improvement in the potential change in building energy consumption through heating and cooling loads for domestic and non-domestic building scenarios. An initial comparison between the “urbanised” (TMY-UWP) and the reference TMY (TMYref) files showed an increase in the range of 1 °C in the daily average urban temperature trend (Figure 7.1).

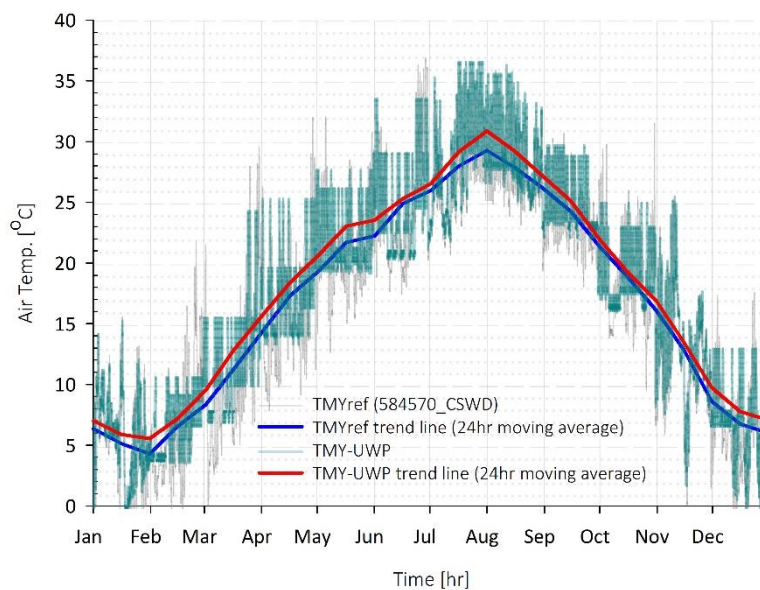


Figure 7.1. The air temperature trend line (24 hr moving average) for the reference TMY file (TMYref, blue, 584570_CSWD) and the TMY file adapted for the urban weather projections (TMY-UWP, red).

The 24 hr moving average trend shows that the temperature difference between the reference TMY file (TMYref, blue line in Figure 7.1) and the “urbanised” TMY file (TMY-UWP, red line in Figure 7.1) peaks in late May and August while it is

minimal during June and autumn. The 24 hr moving average trend comparison points out the importance of hourly data in the context of energy performance modelling. While the air temperature trend suggests a difference less than 1 °C between the two datasets, it is the hourly diurnal temperature fluctuations that in conjunction with the occupancy and the air-conditioning profiles determine the cooling and heating demand.

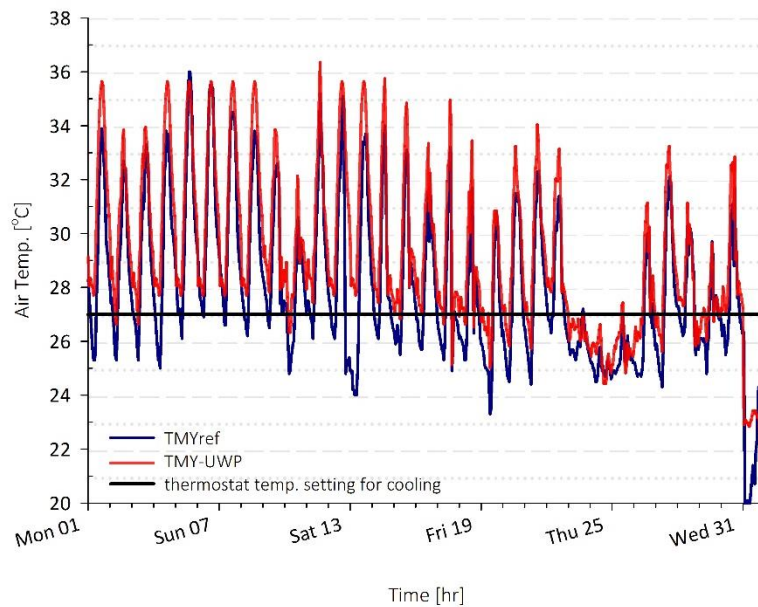


Figure 7.2. The importance of hourly air temperature profiles in cooling demand. The air temperature difference in August between the reference TMY file (TMYref, blue, 584570_CSWD) and the local - specific TMY file (TMY-UWP, red) is in the range of 2°C and above at noon and during night. The 27°C thermostat set point for cooling is shown with a black line.

For example, in August the higher temperature peaks at noon as compared to the original TMY file are expected to have a noticeable effect on daytime air conditioning loads and the peak electricity demand. High night-time temperatures will negatively impact the cooling potential via natural ventilation and the occupants' thermal comfort especially during the first two weeks of August (Figure 7.2).

The impact of the change in HDD and CDD was assessed in terms of heating and cooling loads for a domestic (Case 1) and a non-domestic (Case 2) building scenario in Hangzhou. For this purpose, the “urbanised” (TMY-UWP) and the reference TMY files were used within a dynamic thermal simulation tool (TRNSYS Version 17.1) to model the annual heating and cooling load for both scenarios.

2. Case study of a domestic building in Hangzhou, China

The case study for the domestic building considers an apartment block in Hangzhou at a city location classified as LCZ5. A “typical” apartment was selected with an average floor area of 80 m² (Chen et al., 2009; Nikolou, 2011; Chow et al., 2013). The material properties were assumed to comply with the current Chinese residential regulation JGJ134-2010 “Design standard for the energy efficiency of residential buildings in hot summer and cold winter zone”. The material properties of the modelled apartment are shown in Table 7.1. The windows were modelled as double glazed with aluminium frames and a thermal transmittance value of 3.5 W/m² K (Chow et al., 2013).

Table 7.1. Thermal properties of the building elements in the domestic building case study. Data source: Chow et al. (2013).

Building elements	Composition layers (Outside to inside)	U-value [W/m ² K]
External walls	10mm plaster 200mm reinforced concrete 15mm XPS insulation 200mm hollow concrete blocks 10mm plaster	1.0
Floor/ceiling	10mm ceramic tiles 100mm cast concrete 10mm plaster	1.47
Windows	Double glazing Aluminium frame	3.5

The total apartment space was modelled with 1 unified zone and all the rooms were considered air-conditioned. A survey of 56 apartments in Guangzhou, China (Nikolou, 2011) found that the average “typical” apartment had a glazing to wall ratio of 0.3. This glazing to wall ratio was used in the TRNSYS model of the apartment in Hangzhou. The floor, the ceiling and any internal walls shared with building communal areas were assumed to be adiabatic surfaces (i.e. no heat transfer through the building elements) for the purposes of this study. It was assumed that the apartment has a rectangular shape and the main long facades of the apartment have a North/South orientation.

Heating and cooling loads were both served by a split air-conditioning unit. The heating season was from the 15th of November until the 15th of March and the cooling

season was from the 1st of June to the 1st of October (Figure 7.3) (Hu et al., 2013). The hourly operation profile of the heating system during winter had a small peak in the morning from 06:00 to 08:00 local time and then it was on again from 17:00 to midnight (Hu et al., 2013). The hours of air-conditioning in the hourly cooling profile in summer were from 12:00 to 04:00 (Figure 7.3) (Hu et al., 2013). The apartment was considered occupied from 17:00 to 08:00 during weekdays and from 15:00 to 10:00 in the weekends.

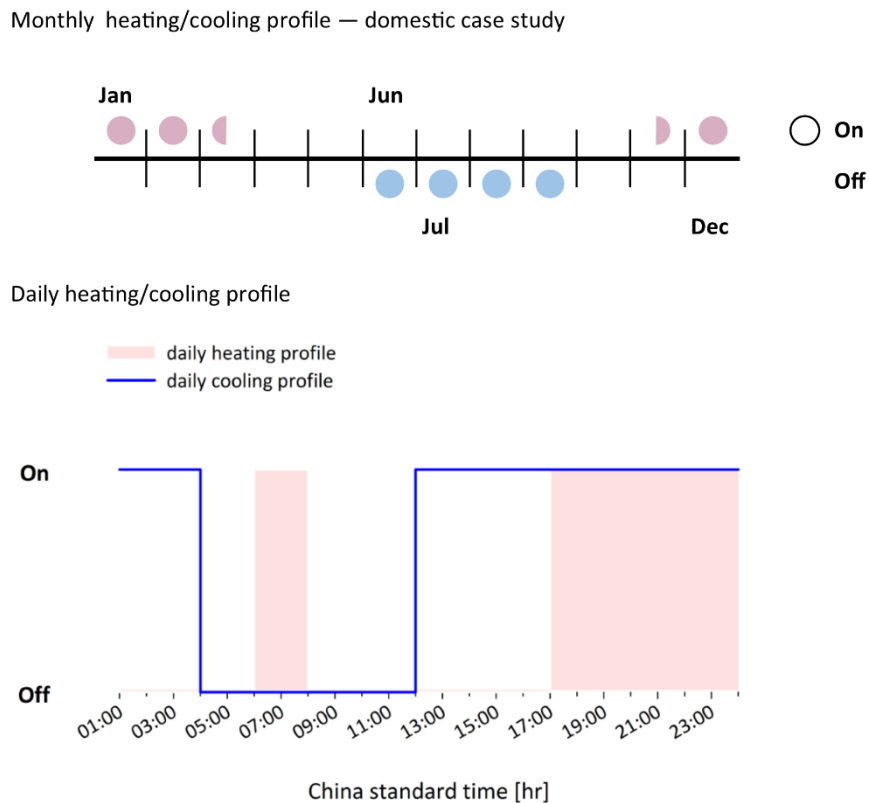


Figure 7.3. The monthly (top) and daily (week day) (bottom) heating (red) and cooling (blue) profile for the domestic apartment case study in Hangzhou. Data source: Hu et al. (2013).

The infiltration rate was set to 1 air change per hour (ac/h). The internal gains profile followed the hourly occupancy schedule. The internal gains were set to 14 W/m² when the apartment was occupied and 2.5 W/m² when empty (Table 7.2) (Nikolou, 2011). The comfort band for the heating / cooling system thermostat range was set to 18 °C – 27 °C (Nikolou, 2011; Chow et al., 2013). This means that the heating system is on when the room temperature is equal to or below 18 °C and the cooling system is on when the room temperature is equal to or exceeds 27 °C. When the room temperature is between the thermostat range set-points the system is set to off.

Table 7.2. Main characteristics of the TRNSYS model for the heating and cooling load simulations in the domestic building case study.

Characteristics	Settings	Source
Orientation	North/South	
Occupancy profile	Weekdays: 17:00 to 08:00 Weekends: 00:00 to 10:00 and 15:00 to 00:00	
Internal gains profile	14 W/m ² when occupied 2.5 W/m ² when empty Hourly profile follows the occupancy	Nikolou (2011)
Infiltration rate	1 air change h ⁻¹	Nikolou (2011)
Heating/cooling system thermostat comfort range set- points	Heating on: ≤18 °C Cooling on: ≥27 °C	Nikolou (2011); Chow et al. (2013)

3. Case study of a non-domestic building in Hangzhou, China

An office building in Hangzhou was selected for this case study. The building was assumed to comply with the 2007 building code for fully air-conditioned public buildings (Shen et al., 2014). The thermal properties of the building elements are shown in Table 7.3. The total building floor area was assumed to be 75,000 m², the height of the building 140m and each floor's area 1,000 m² (Pan et al., 2003). A central air-conditioning system was used for heating and cooling (Han et al., 2014). The total installed capacity of the air-conditioning system was 120 W/m² (Han et al., 2014).

Table 7.3. Thermal properties of the building elements in the non-domestic building case study (Shen et al., 2014).

Building elements	U-value [W/m ² K]	
External walls	0.7	
Floor/ceiling	0.5	
Windows	2.0	shading coefficient 0.4 glazing to wall ratio 0.5

The heating/cooling comfort band range for the thermostatic control set-points was set to 18 °C for heating and 26 °C for cooling (Shen et al., 2014). This means that

the heating system is on when the room temperature is equal to or below 18 °C and the cooling system is on when the room temperature is equal to or exceeds 26 °C.

The air infiltration rate was 0.4 air changes h⁻¹ and the fresh air ventilation rate was 10 litres per second per person (Pan et al., 2003). The internal loads during the occupied hours were 20 W/m² from lighting and 30 W/m² from equipment (Pan et al., 2003). It was assumed that during out of occupation hours these loads were halved.

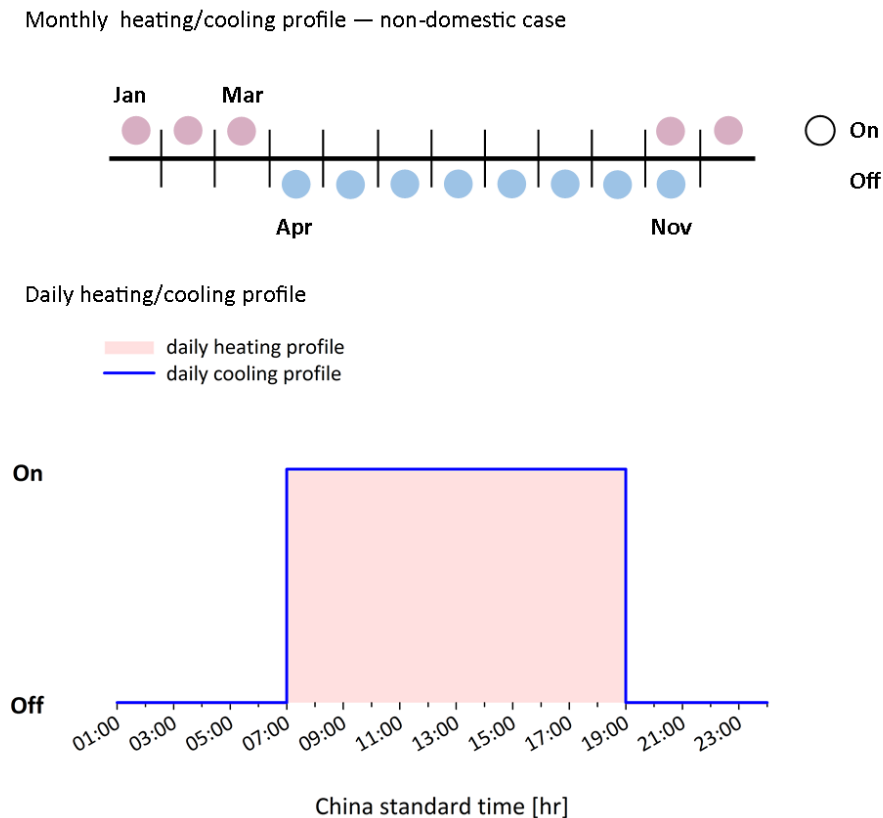


Figure 7.4. The monthly (top) and daily (week day) (bottom) heating (red) and cooling (blue) profile for the non-domestic apartment case study in Hangzhou.

The floor space was modelled with one uniform zone. It was assumed to have a square floorplan with the lift shafts, corridors and staircases in the middle. The ceiling, the floor and the internal walls were considered to be adiabatic elements. The glazing to wall ratio was set at 0.5 and the windows were not openable. The monthly and daily air-conditioning operation profiles are shown in Figure 7.4.

The cooling period was from April to November and the heating period was from November to March (Huang et al., 2007). In November the operation of the air-conditioning system in heating or cooling mode was determined by the thermostat set-

point temperatures. The main characteristics of the TRNSYS model can be found in Table 7.4.

Table 7.4. Main characteristics of the TRNSYS model for the heating and cooling load simulations in the non-domestic building case study.

Characteristics	Settings	Source
Orientation	North/South	
Occupancy profile	Weekdays: 07:00 to 19:00 Weekends: 10:00 to 16:00	
Internal gains profile	50 W/m ² when occupied 25 W/m ² when empty Hourly profile follows the occupancy	Pan et al. (2003)
Occupants per floor	150 persons	
Infiltration rate	0.4 air change h ⁻¹	Dai et al. (2014)
Ventilation rate	10 l/s pp	Pan et al. (2003)
Heating/cooling system thermostat comfort range set-points	Heating on: ≤18 °C Cooling on: ≥26 °C	Shen et al. (2014)

4. Results from the case studies

Following the “urban unit model” validation the TMY file for Hangzhou (584570_CSWD) was adapted to include the “urban weather projections” (UWP) according to the methods outlined above. A comparison amongst the reference TMY, the TMY overlaid with the bulk “city” UHI effect (TMY+UHI) and the micro-scale “urban weather projections” (TMY-UWP) is shown in Figure 7.5. In the “TMY+UHI” HDD have decreased by 6% from 1598 days in the reference TMY and in the “TMY-UWP” file by 13% showing that the local specific micro-climate attributes an additional 7% heating load reduction to the bulk UHI effect of the city. This difference between the “TMY-UWP” and the “TMY+UHI” files is a reflection of the thermal characteristics of the specific urban morphology of the studied sites compared to the wider city. CDD in the “TMY+UHI” file are 17% more than the reference TMY file (207 days). The “TMY-UWP” file shows an additional 14% increase in comparison with the “TMY+UHI” file. This assessment indicates that cooling loads can be significantly underestimated in the

business as usual case of using the reference TMY file and that the urban effect on air temperature should not be neglected.

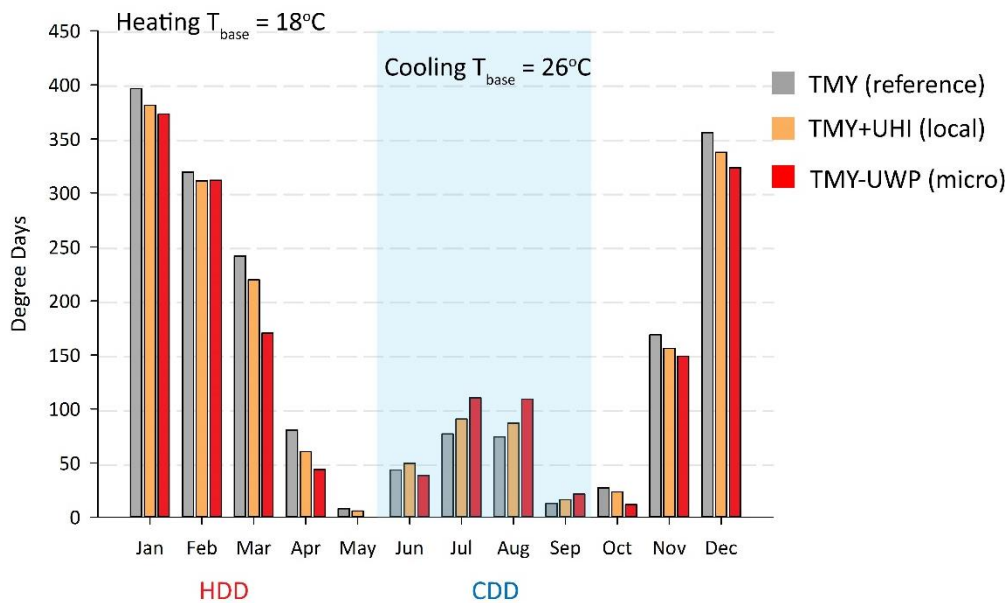


Figure 7.5. Comparison of the degree days in the reference TMY (TMY reference, gray; 1598 HDD, 207 CDD) with the TMY overlaid with the bulk “city” UHI effect (TMY+UHI, orange; 1495 HDD, 243 CDD) and the micro-scale “urban weather projections” (TMY-UWP, red; 1383 HDD, 279 CDD). T_{base} is the temperature threshold used for the calculation of the HDD and CDD. The area with the light blue background marks the cooling period.

The heating and cooling demand has been further calculated for a domestic and a non-domestic building cases in Hangzhou. The total heating load calculated with the TMY reference file is 30 kWh/m² for the domestic and 62 kWh/m² for the non-domestic building cases. The cooling loads are 9 kWh/m² and 23 kWh/m² respectively. The heating and cooling demand calculated with the TMY-UWP file are 25 kWh/m² for heating and 11 kWh/m² for cooling in the domestic building case. In the non-domestic building case the heating demand is 51 kWh/m² and the cooling load is 27 kWh/m².

It has been shown that in both cases there is approximately 20% increase of the cooling load and a 20% decrease of the heating load. If typical coefficient of performance (COP) values for a reversible air-conditioning system are taken as 2.0 for heating and 3.5 for cooling then the total electricity consumption estimated with the use of the “urban weather projections” TMY file developed here will be decreased by 11% in comparison with the “business as usual” (i.e. reference TMY) case. This result shows the impact highly efficient heat pumps and air-conditioning systems can have

on the electricity consumption of cities with a humid sub-tropical climate. However, this assumes a cooling set-point of 26°C. If a lower set-point is used the predicted energy savings will be lost.

Chapter 8 Conclusions

It is to be expected that in developing countries with fast growing economies the thermal comfort perception of people in the buildings will change as people become richer. The existence of more people with upper-middle and high incomes means that more people will afford to heat and cool their space to a higher degree, increasing the annual total energy consumption (Lindberg et al., 2013). This “rebound” effect (Haas & Biermayr, 2000) can be detrimental to any policies and efforts for reducing energy consumption and the carbon emissions of cities.

Cities, urban planners and engineers need to transform the urban environment and promote air quality, functionality and people’s well-being. The urban micro-climate is a very good starting point from which to formulate policies and measures that can enhance people’s positive experience in a city. It can also be a valuable tool to engineer a low carbon, flourishing city-scape.

This work is an approach to assessing the development of urban micro-climates and evaluate how specific urban morphologies can impact air temperature development at street level and the energy consumption of buildings. This thesis introduced a simplified urban representation for use in micro-climatic simulations to produce building simulation weather data files for locations within a city. A methodology has been developed that uses statistical spatial analysis to produce an “urban unit model” representative of the complex urban environment and the energy balance at street level. This methodology has demonstrated its applicability to the downscaling of the above-the-city canopy and non-rural temperature measurements to the street level in the urban micro-scale. The “urban unit model” was used in micro-climatic simulations to create a dataset, the “urban weather projections”, for the air temperature development in the neighbourhood scale under three different weather forcing groups for each month of a year. The “urban weather projections” dataset has incorporated the urban heat island effect of the city and the effect of local-specific morphology at street level. The results were used to adapt a typical meteorological year (TMY) data file for the urban micro-climate as exhibited by the morphology of a city neighbourhood.

Chapter 8 Conclusions

The validation of the “urban unit model” and the results of its implementation into micro-climatic simulations show that there is a potential for the simplification of urban site modelling and for the wider application of the method introduced in this thesis as a tool for adapting typical meteorological weather data files to represent the neighbourhood micro-scale of cities with a humid sub-tropical climate.

In the majority of cases it would be difficult to justify the additional level of analysis described here to develop the localised weather data file over the generic bulk “city” UHI file. That is, single / smaller residential buildings can take the bulk UHI correction approach. However, the method presented delivers an enhancement which in large developments is justified. In addition, the developed methodology would also benefit initial stages of urban planning and could inform decisions on the use and the urban form of existing and new developments in the city.

1. Contribution to knowledge

- **A methodology is introduced for the analysis of urban morphology in the scale of neighbourhoods.** This study developed a method for the estimation of common morphological parameters by widely available metadata. A circular urban unit (250m radius) is introduced that is expected to represent the main urban characteristics that impact on the local specific energy balance and the generation of the city - “neighbourhood” micro-climate. The permeable surface to the total urban unit’s surface area ratio and the density of the buildings are the two main parameters in the modelling of urban sites regarding the local specific micro-climate.
- **An idealised “urban unit model” of 250m radius is presented for use in micro-climatic simulations.** This idealised “urban unit model” is based on the main thermal and morphological characteristics of nine sites with residential / institutional (university) use in Hangzhou, China. The area of the urban unit was determined by the region of influence on the air temperature signal at the centre of the unit. The “urban unit model” was then implemented into micro-climatic simulations using a Computational Fluid Dynamics – Surface Energy Balance analysis tool (ENVI-met, Version 4). The “urban unit model” approach used here in the simulations delivered results with satisfactory performance. The simplified “urban unit model” approach contributes to the research on the urban modelling and its requirements to adequately capture the physical processes involved in micro-scale weather development.
- **A data cleaning procedure is examined in the context of urban measurement datasets.** This analysis concluded that the most appropriate methods for the replacement of erroneous and missing weather data are (1) the replacement with the average value from observations collected at locations near the place of interest and (2) with direct replacement with data collected from the reference weather station even if it is not representative of the urban location.

- **Knowledge on the impact of vegetation's location and density on the air temperature development in the urban canopy.** This work revealed that the proximity to “green” – vegetated space can decrease the urban heat island intensity during night-time and the maximum day-time air temperature. The marginal difference between the cases with a central allocation of the vegetated surface area and those where the vegetation was positioned at the outer border of the urban unit is an indication that the distance to a vegetated area is not enough to alone produce large cooling benefits during the day and attenuate the night-time urban heat island intensity. The results suggest that high percentages of vegetated space can reduce the surface temperatures within the cities. There are, however, strong indications that in places with a humid sub-tropical climate such as Hangzhou, in the case of successive hot, dry summer days, a reduction in soil water content will negate, to a large extent, the cooling benefits of the added vegetation.
- **An Artificial Neural Network (ANN) is developed for the prediction of hourly global horizontal radiation (GHR) when only air temperature and RH data are available.** This study showed that the air temperature and RH only are not sufficient for the training of ANNs for the estimation of solar radiation. The ANN has a large MAPE and poor performance in the prediction of hourly GHR. The use of this ANN model is only recommended as a generic indication of the solar radiation levels in the case where real solar radiation observations or parameters other than air temperature and RH meteorological data are missing.
- **A method is proposed for the micro-climatic adaptation of typical simulation weather data files.** The “urban unit model” was used in micro-climatic simulations to create a dataset, the “urban weather projections”, for the air temperature development in the city-neighbourhood scale under three different weather forcing groups for each month of a year. The “urban weather projections” dataset has incorporated the urban heat island effect of the city and the effect of local-specific morphology at street level. This methodology has demonstrated its applicability to the downscaling of the above-the-city canopy and non-rural temperature measurements to the street level in the urban micro-scale. The results were used to adapt a typical

Chapter 8 Conclusions

meteorological year (TMY) data file for the urban micro-climate as exhibited by the morphology of a city-neighbourhood.

This thesis concludes that cooling loads can be significantly underestimated in the business as usual case of using the reference TMY file and that the urban effect on air temperature should not be neglected. Most importantly it is showed that in the case of air-conditioned buildings, efficient building services systems and the human behaviour-comfort levels are the key factors determining the final energy consumption and any potential savings.

2. Further work

This study has shown that urban morphology can be simplified to model the development of the urban micro-climate at the “neighbourhood” scale. However, it has also highlighted the necessity of more detailed field observations for the initialisation of micro-climatic simulations. Specifically, solar radiation and anthropogenic heat emissions data that are the main input in the energy balance. In this study these are modelled as field data from the period of temperature monitoring were not available. Further studies are required for the assessment of the model’s function under specific weather events such as rainfall showers and its validation under different weather forcings.

The “urban unit model” was implemented into micro-climatic simulations using a Computational Fluid Dynamics – Surface Energy Balance analysis tool (ENVI-met, Version 4). The use of the model with different analysis tools may reveal additional benefits and drawbacks of its implementation into specific types of simulation. It would be of particular interest to evaluate the model's function regarding the temperature and wind field representation at different heights in the urban canopy layer. It would also be interesting to assess if it could be used to simplify the urban morphology representation for air pollution simulations at the "neighbourhood" scale.

In this thesis, a humid sub-tropical climate context has been considered. The transferability of this methodology to other climate types should be further investigated. The development of the idealised "urban unit model" was based on the

Chapter 8 Conclusions

characteristics of nine sites with residential / institutional (university) use in Hangzhou, China. It is expected that there will be differences to the characteristics of sites with similar use in other countries. Furthermore, sites with different use have only been briefly considered during the site analysis and the urban classification. The "urban unit model" can be further modified to represent sites with diverse thermal and morphological characteristics and it can also be expanded to other cities with different urban layouts.

An "under the canopy" approach has been used for the representation of vegetation. This approach does not consider the effect of different types of vegetation and their impact on wind, air quality, water drainage and people's wellbeing. Further studies could investigate the integration of different types of vegetation in the model and their effect to the micro-climate.

Experimental investigations are required with dense weather station networks in cities to further assess and model the mechanisms responsible for the local specific micro-climatic development. The sites for the experiments and the position of the monitoring equipment must be carefully selected to ensure the measurements are representative of the roughness sub-layer and the urban canopy layer. Sensors should be strategically deployed to monitor the synchronous development of the physical processes at different heights above the ground. Field measurements would allow further validation of the model's function and "urban weather projections" representative of the local specific micro-climate. The methodology for the adaptation of the TMY files should be simplified and integrated in an automated software application. The results of the simulations with the "urban unit model" could be used to create an extensive database with hourly weather data offsets according to urban morphology classification and the location of the site. This database would feed in an algorithm that would adapt the TMY for the studied site's characteristics with the minimum input from the user of the application; ideally only the latitude and longitude of the site.

Appendices

Appendix A

Performance indices for the assessment of the models
examined for the replacement of missing air temperature
values in weather data files

Scenario 1 - January

<i>Jan night</i>	Case 1	Case 2	Case 3	Case 4	Case 5A	Case 5B	Case 6A	Case 6B	Case 7	Case 8
MSE	0.007	0.017	0.034	0.566	0.041	0.004	0.038	0.029	2.272	0.538
MBE	-0.014	0.074	0.121	0.673	0.178	-0.052	0.167	-0.113	-1.45	-0.717
MAPE	1.4	2.3	3.3	14.1	3.7	1	3.5	2.3	29.7	14.5

Scenario 1 - March

<i>Mar night</i>	Case 1	Case 2	Case 3	Case 4	Case 5A	Case 5B	Case 6A	Case 6B	Case 7	Case 8
MSE	0.225	1.124	0.159	9.809	1.287	0.686	0.188	0.055	92.98	2.198
MBE	0.083	1.003	0.185	2.973	1.108	0.812	0.368	0.178	-9.617	-1.383
MAPE	2.3	6.8	1.9	18.2	6.7	4.9	2.3	1.1	57.5	8.1

Scenario 2 - January

<i>Jan day</i>	Case 1	Case 2	Case 3	Case 4	Case 5A	Case 5B	Case 6A	Case 6B	Case 7	Case 8
MSE	0.56	3.056	2.739	0.224	0.072	0.021	0.126	0.011	0.117	0.187
MBE	0.633	1.663	1.553	-0.303	-0.2	-0.095	-0.300	-0.072	-0.033	-0.233
MAPE	11	34.2	32.1	6.7	3.3	1.9	4.7	1.1	3.7	6.3

Scenario 2 - March

<i>Mar day</i>	Case 1	Case 2	Case 3	Case 4	Case 5A	Case 5B	Case 6A	Case 6B	Case 7	Case 8
MSE	10.812	6.87	7.078	9.516	7.916	0.603	9.436	0.533	294.06	2.325
MBE	2.783	1.823	1.84	-2.703	-2.488	-0.112	-2.952	-0.615	-17.083	-1.35
MAPE	9.7	3.9	7.7	9.1	8.3	2.3	9.8	2	57.5	4.7

MSE is the Mean Squared Error, MBE is the Mean Bias Error and MAPE is the Mean Absolute Percentage Error.

IV

Performance indices for the assessment of the models examined for the replacement of missing air temperature values in weather data files

Appendix B

Sky View factor calculations

Sky view factor (SVF) estimations have been made with the methods of Holmer et al. (2001) and Johnson and Watson (1984). The SVF_{summer} and the SVF_{winter} value are the average values of the two methods. The annual SVF is the average of the seasonal values. Weather station numbers correspond to the locations shown in the figures at the end of Appendix B.

Weather station No. - Hangzhou	SVF_{summer}	SVF_{winter}	Average SVF_{annual}
1	0.85	0.85	0.85
2	0.48	0.70	0.59
3	0.20	0.95	0.58
4	0.75	0.90	0.83
5	0.71	0.83	0.77
6	0.52	0.65	0.58
7	0.23	0.66	0.45
8	0.55	0.56	0.55
9	0.49	0.97	0.73
10	0.44	0.86	0.65
11	0.30	0.93	0.61
12	0.48	0.81	0.64
13	0.88	0.93	0.90
14	0.27	0.84	0.55
15	0.19	0.75	0.47
16	0.92	0.95	0.93
17	0.68	0.95	0.81
18	0.34	0.60	0.47
19	0.54	0.56	0.55
20	0.83	0.97	0.90
21	0.58	0.58	0.58
22	0.69	0.94	0.81
23	0.93	0.94	0.93
24	0.34	0.94	0.64
25	0.66	0.66	0.66
26	0.29	0.97	0.63

Weather station No. - Ningbo	SVF _{summer}	SVF _{winter}	Average SVF _{annual}
1	0.62	0.68	0.65
2	0.34	0.47	0.40
3	0.46	0.47	0.46
4	0.82	0.95	0.89
5	0.69	0.98	0.84
6	0.51	0.72	0.61
7	0.83	0.98	0.90
8	0.26	0.95	0.60
9	0.56	0.96	0.76
10	0.58	0.89	0.73
11	0.21	0.43	0.32
12	0.94	0.96	0.95
13	0.91	0.91	0.91
14	0.31	0.96	0.64
15	0.55	0.59	0.57
16	0.56	0.71	0.63
17	0.85	0.94	0.89
18	0.77	0.77	0.77
19	0.63	0.66	0.64
20	0.74	0.94	0.84
21	0.91	0.92	0.91
22	0.79	0.95	0.87
23	0.88	0.88	0.88
24	0.55	0.60	0.57
25	0.44	0.52	0.48
26	0.98	0.99	0.98
27	0.99	0.99	0.99
28	0.82	1.00	0.91

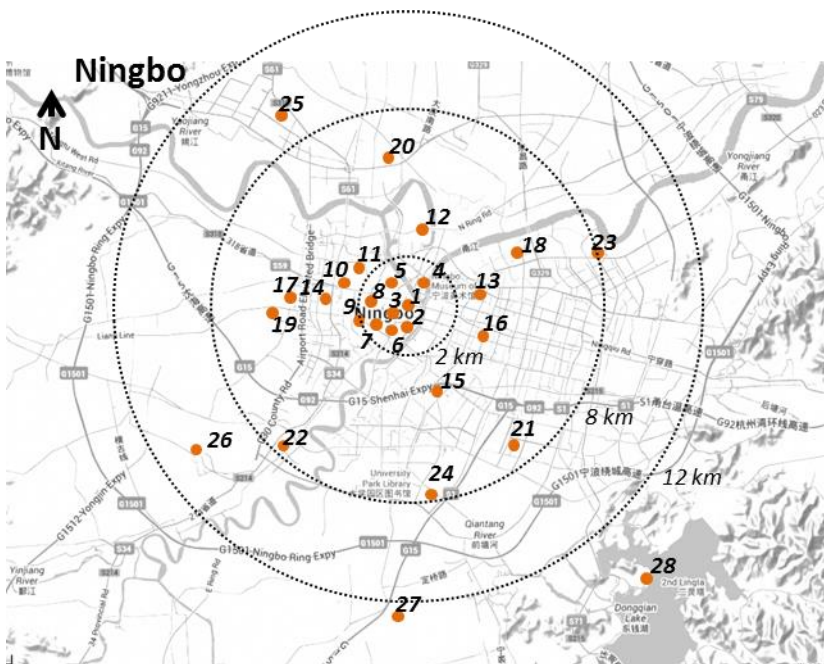
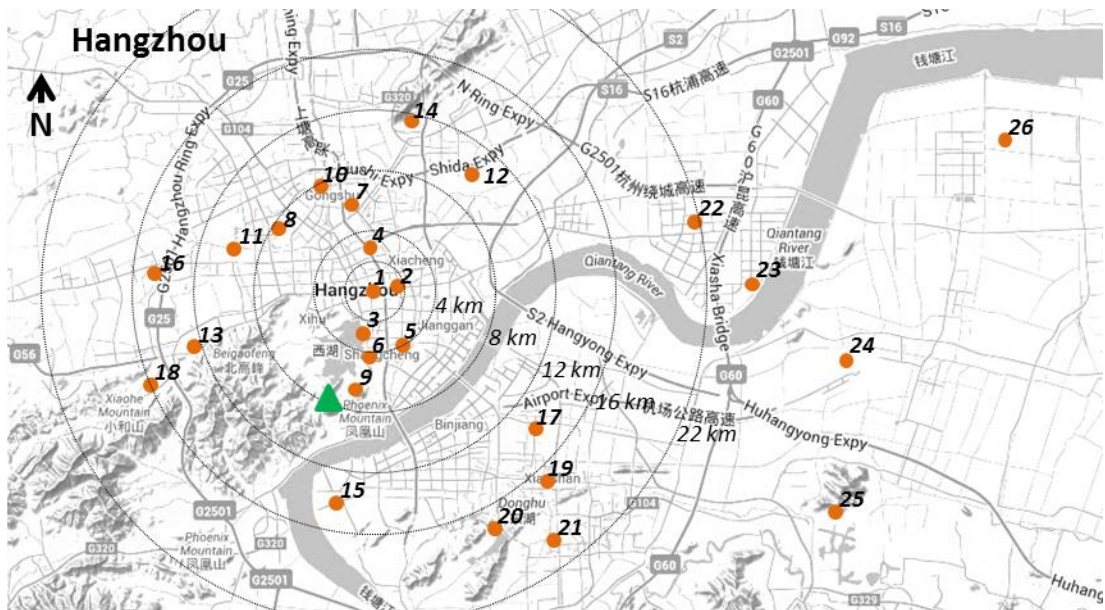


Figure B.1. The location of the sensors in Hangzhou (Top) and Ningbo (Bottom).

Appendix C

Local Climate Zones urban classification scheme Tables adapted from Stewart and Oke (2012)

LCZ	Zone name
Zone Definition	
Form	Building geometry and materials, land cover, vegetation and human activity.
Function	Most likely land uses. Location in a city (e.g. periphery, city core)
Zone properties	
Sky View Factor [0 – 1]	The ratio of the amount of the sky hemisphere visible from the level of interest to the total sky hemisphere. Relevant to the street canyon where the sensor sits.
Aspect Ratio H/W [0 – 3 ⁺]	Mean Height to Width ratio of the street canyon where the sensor is. In the case of sparsely built areas it is equal to building spacing. Affects airflow characteristics and amount of solar radiation to and from building surfaces. Relevant to the street canyon where the sensor sits.
Mean building height \bar{H} [0 – 50+ m]	Area weighted average of building heights. Affects the exposure of surfaces to solar radiation, air flow and heat dispersion above ground. Relevant to the urban unit.
Terrain roughness class [1 – 8]	According to Davenport et al. (2000) effective terrain roughness classification scheme (based on the roughness length z_0). Affects the exposure of surfaces to solar radiation, air flow and heat dispersion above ground. Relevant to the urban unit.
Building surface fraction F_r [0-100%]	Proportion of ground surface covered by buildings. Affects the exposure of surfaces to solar radiation, air flow and heat dispersion above ground. Relevant to the urban unit.
Impervious surface fraction I_r [0-100%]	Proportion of ground surface covered by roads, rock and pavements. Affects the exposure of surfaces to solar radiation, air humidity and heating/cooling potential. Relevant to the urban unit. Relevant to the urban unit.
Pervious surface fraction P_r	Proportion of ground surface covered by soil, vegetation and water. Affects the exposure of surfaces to solar radiation, air humidity and heating/cooling potential. Relevant to the urban unit. Relevant to the urban unit.
Surface admittance μ [500 – 2,500+ J.m ⁻² .s ^{-1/2} .K ⁻¹]	The ability of a surface to allow heat flow through it. Relevant to the urban unit. Unknown in the case of dense tree canopies. Affects heat storage and heating / cooling rates.
Albedo α [0.02 – 0.5]	Surface reflectivity at midday under clear sky. Relevant to the urban unit.
Anthropogenic heat flux Q_F [0 – 400 W.m ⁻²]	Mean annual anthropogenic heat flux. Relevant to the urban unit.

LCZ 1		Compact high-rise
Zone Definition		
Form		Tall buildings (>10 floors). High density. Buildings with variable height, free-standing and closely built. Steel, concrete and glass. Few or no trees. Heavy traffic flow.
Function		Commercial (office buildings, hotels), residential (apartment towers). Central business district.
Zone properties		
Sky View Factor [0 – 1]		0.2 to 0.4
Aspect Ratio H/W [0 – 3 ⁺]		>2
Mean building height \bar{H} [0 – 50+ m]		>25 m
Terrain roughness class [1 – 8]		8 – Chaotic ($z_0 \geq 2$)
Building surface fraction F_r [0-100%]		40 - 60 %
Impervious surface fraction I_r [0-100%]		40 - 60 %
Pervious surface fraction P_r		<10 %
Surface admittance μ [500 – 2,500+ J.m ⁻² .s ^{-1/2} .K ⁻¹]		1,500 - 1,800 J.m ⁻² .s ^{-1/2} .K ⁻¹
Albedo α [0.02 – 0.5]		0.10 – 0.20
Anthropogenic heat flux Q_F [0 – 400 W.m ⁻²]		50 – 300 W.m ⁻²

LCZ 2	Compact mid-rise
Zone Definition	
Form	Buildings 3 – 9 stories tall. Buildings with uniform height, Attached or closely spaced. Stone, concrete and brick. Few or no trees. Moderate to heavy traffic flow.
Function	Commercial (office buildings, hotels, retail shops), residential (multi-unit housing), industrial (warehouses). Central business district, old town.
Zone properties	
Sky View Factor [0 – 1]	0.3 to 0.6
Aspect Ratio H/W [0 – 3 ⁺]	0.75 - 0.2
Mean building height \bar{H} [0 – 50+ m]	10 - 25 m
Terrain roughness class [1 – 8]	6 - 7 – Very rough to Skimming ($0.5 \leq z_0 \leq 1$)
Building surface fraction F_r [0-100%]	40 - 70 %
Impervious surface fraction I_r [0-100%]	30 - 50 %
Pervious surface fraction P_r	<20 %
Surface admittance μ [500 – 2,500+ $\text{J.m}^{-2}.\text{s}^{-1/2}.\text{K}^{-1}$]	1,500 - 2,200 $\text{J.m}^{-2}.\text{s}^{-1/2}.\text{K}^{-1}$
Albedo α [0.02 – 0.5]	0.10 – 0.20
Anthropogenic heat flux Q_F [0 – 400 W.m^{-2}]	<75 W.m^{-2}

LCZ 3	Compact low-rise
Zone Definition	
Form	Buildings 1 – 3 stories tall. Small and tightly packed along narrow streets. Stone, concrete and brick. Few or no trees. Low to Moderate traffic flow.
Function	Commercial (small retail shops), residential (single-unit housing, terrace). Old or densely populated cities, old towns or villages. City core, periphery (high-density sprawl).
Zone properties	
Sky View Factor [0 – 1]	0.2 to 0.6
Aspect Ratio H/W [0 – 3 ⁺]	0.75 - 1.5
Mean building height \bar{H} [0 – 50+ m]	3 - 10 m
Terrain roughness class [1 – 8]	6 – Very rough ($z_0 \approx 0.5$)
Building surface fraction F_r [0-100%]	40 - 70 %
Impervious surface fraction I_r [0-100%]	20 - 50 %
Pervious surface fraction P_r	<30 %
Surface admittance μ [500 – 2,500+ $\text{J.m}^{-2}.\text{s}^{-1/2}.\text{K}^{-1}$]	1,200-1,800 $\text{J.m}^{-2}.\text{s}^{-1/2}.\text{K}^{-1}$
Albedo α [0.02 – 0.5]	0.10 – 0.20
Anthropogenic heat flux Q_F [0 – 400 W.m^{-2}]	<75 W.m^{-2}

LCZ 4		Open high-rise
Zone Definition		
Form		Tall Buildings >10 stories tall. Open, geometric arrangements. Uniform height, width and spacing. Steel, concrete and glass. Scattered trees, grass, plants. Moderate traffic flow.
Function		Residential (high-rise housing estates, apartment blocks). Periphery.
Zone properties		
Sky View Factor [0 – 1]		0.5 to 0.7
Aspect Ratio H/W [0 – 3 ⁺]		0.75 - 1.25
Mean building height \bar{H} [0 – 50+ m]		>25 m
Terrain roughness class [1 – 8]		7 - 8 – Skimming to Chaotic ($1 \leq z_0 \leq 2$)
Building surface fraction F_r [0-100%]		20 - 40 %
Impervious surface fraction I_r [0-100%]		30 - 40 %
Pervious surface fraction P_r		30 - 40 %
Surface admittance μ [500 – 2,500+ $\text{J.m}^{-2}.\text{s}^{-1/2}.\text{K}^{-1}$]		1,400 - 1,800 $\text{J.m}^{-2}.\text{s}^{-1/2}.\text{K}^{-1}$
Albedo α [0.02 – 0.5]		0.15 – 0.25
Anthropogenic heat flux Q_F [0 – 400 W.m^{-2}]		<50 W.m^{-2}

LCZ 5	Open mid-rise
Zone Definition	
Form	Buildings 3-9 stories tall. Open arrangement. Steel, concrete and stone. Scattered trees, grass, plants. Low traffic flow.
Function	Commercial (office buildings, hotels), residential (multi-unit housing), institutional (business parks, campuses). Periphery.
Zone properties	
Sky View Factor [0 – 1]	0.5 to 0.8
Aspect Ratio H/W [0 – 3 ⁺]	0.3 - 0.75
Mean building height \bar{H} [0 – 50+ m]	10 - 25 m
Terrain roughness class [1 – 8]	5 - 6 – Rough to Very rough ($0.25 \leq z_0 \leq 0.50$)
Building surface fraction F_r [0-100%]	20 - 40 %
Impervious surface fraction I_r [0-100%]	30 - 50 %
Pervious surface fraction P_r	20 - 40 %
Surface admittance μ [500 – 2,500+ $\text{J.m}^{-2}.\text{s}^{-1/2}.\text{K}^{-1}$]	1,400 - 2,000 $\text{J.m}^{-2}.\text{s}^{-1/2}.\text{K}^{-1}$
Albedo α [0.02 – 0.5]	0.15 – 0.25
Anthropogenic heat flux Q_F [0 – 400 W.m^{-2}]	<25 W.m^{-2}

LCZ 6 Open low-rise	
Zone Definition	
Form	Buildings 1 – 3 stories tall. Detached or terrace in grid patterns. Wood, brick, stone. Scattered trees, grass, plants. Low traffic flow.
Function	Commercial (small retail shops), residential (single or multi-unit housing, low density terrace). Medium density cities, periphery (suburban).
Zone properties	
Sky View Factor [0 – 1]	0.6 to 0.9
Aspect Ratio H/W [0 – 3 ⁺]	0.3 - 0.75
Mean building height \bar{H} [0 – 50+ m]	3 - 10 m
Terrain roughness class [1 – 8]	5 - 6 – Rough to Very rough ($0.25 \leq z_0 \leq 0.50$)
Building surface fraction F_r [0-100%]	20 - 40 %
Impervious surface fraction I_r [0-100%]	20 - 50 %
Pervious surface fraction P_r	30 - 60 %
Surface admittance μ [500 – 2,500+ $\text{J.m}^{-2}.\text{s}^{-1/2}.\text{K}^{-1}$]	1,200 - 1,800 $\text{J.m}^{-2}.\text{s}^{-1/2}.\text{K}^{-1}$
Albedo α [0.02 – 0.5]	0.12 – 0.25
Anthropogenic heat flux Q_F [0 – 400 W.m^{-2}]	<25 W.m^{-2}

LCZ 7	Lightweight low-rise
Zone Definition	
Form	Buildings 1 storey tall. Attached or detached in compact arrangement. Few or no trees. Low traffic flow.
Function	Commercial (small retail shops), residential (low-cost housing estates, mobile housing, informal settlements). Periphery of large, developing cities, rural towns.
Zone properties	
Sky View Factor [0 – 1]	0.2 to 0.5
Aspect Ratio H/W [0 – 3 ⁺]	1 - 2
Mean building height \bar{H} [0 – 50+ m]	2 - 4 m
Terrain roughness class [1 – 8]	4-5 – Roughly open to Rough ($0.10 \leq z_0 \leq 0.25$)
Building surface fraction F_r [0-100%]	60 - 90 %
Impervious surface fraction I_r [0-100%]	<20 %
Pervious surface fraction P_r	<30 %
Surface admittance μ [500 – 2,500+ $\text{J.m}^{-2}.\text{s}^{-1/2}.\text{K}^{-1}$]	800-1,500 $\text{J.m}^{-2}.\text{s}^{-1/2}.\text{K}^{-1}$
Albedo α [0.02 – 0.5]	0.15 – 0.35
Anthropogenic heat flux Q_F [0 – 400 W.m^{-2}]	<35 W.m^{-2}

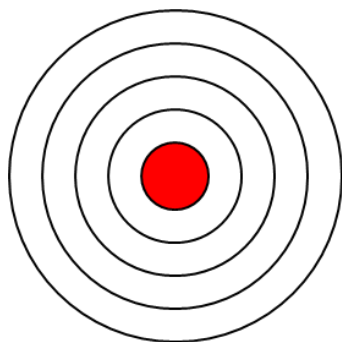
LCZ 8	Large low-rise
Zone Definition	
Form	Large low buildings 1-3 stories tall. Separated by extensive paved surfaces. Few or no trees. Moderate to heavy traffic flow.
Function	Commercial (shopping centres, storage facilities), transportation (airport, railway station), light industrial. Periphery.
Zone properties	
Sky View Factor [0 – 1]	>0.7
Aspect Ratio H/W [0 – 3 ⁺]	0.1 - 0.3
Mean building height \bar{H} [0 – 50+ m]	3 - 10 m
Terrain roughness class [1 – 8]	5 – Rough ($z_0 \approx 0.25$)
Building surface fraction F_r [0-100%]	30 - 50 %
Impervious surface fraction I_r [0-100%]	40 - 50 %
Pervious surface fraction P_r	<20 %
Surface admittance μ [500 – 2,500+ $\text{J.m}^{-2}.\text{s}^{-1/2}.\text{K}^{-1}$]	1,200-1,800 $\text{J.m}^{-2}.\text{s}^{-1/2}.\text{K}^{-1}$
Albedo α [0.02 – 0.5]	0.15 – 0.25
Anthropogenic heat flux Q_F [0 – 400 W.m^{-2}]	<50 W.m^{-2}

LCZ 9	Sparsely built
Zone Definition	
Form	Small or medium sized buildings. Widely spaced across natural landscape. Wood, brick, stone. Scattered trees, grass, plants. Low traffic flow.
Function	Residential (Single or multi-unit housing), institutional (campuses), agricultural (country estates). Periphery (low-density suburban), rural towns, villages.
Zone properties	
Sky View Factor [0 – 1]	>0.8
Aspect Ratio H/W [0 – 3 ⁺]	0.1 – 0.25
Mean building height \bar{H} [0 – 50+ m]	3 – 10 m
Terrain roughness class [1 – 8]	5 - 6 – Rough to Very rough ($0.25 \leq z_0 \leq 0.50$)
Building surface fraction F_r [0-100%]	10 - 20 %
Impervious surface fraction I_r [0-100%]	<20 %
Pervious surface fraction P_r	60 - 80 %
Surface admittance μ [500 – 2,500+ J.m ⁻² .s ^{-1/2} .K ⁻¹]	1,000-1,800 J.m ⁻² .s ^{-1/2} .K ⁻¹
Albedo α [0.02 – 0.5]	0.12 – 0.25
Anthropogenic heat flux Q_F [0 – 400 W.m ⁻²]	<10 W.m ⁻²

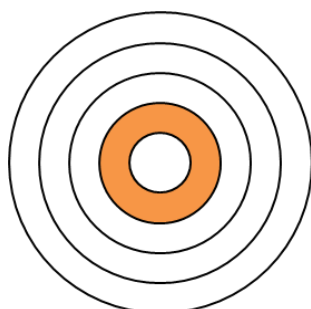
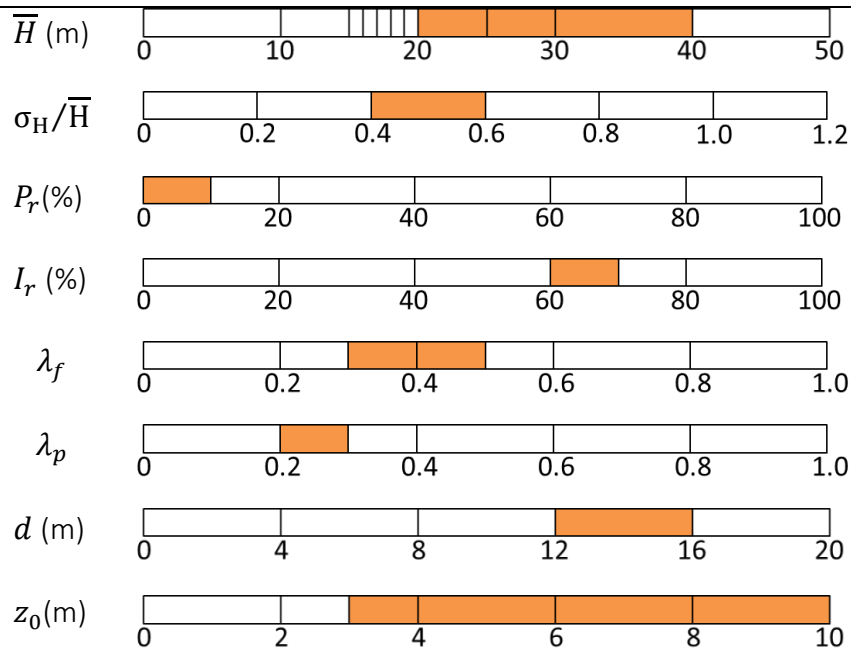
LCZ 10	Heavy industry
Zone Definition	
Form	Irregular mix of low and mid-rise structures (tanks, towers). Open spaced. Steel, concrete, metal. Few or no trees. Low traffic flow. Waste heat and atmospheric pollution.
Function	Industrial (factories, mills, refineries). City periphery or country.
Zone properties	
Sky View Factor [0 – 1]	0.6 – 0.9
Aspect Ratio H/W [0 – 3 ⁺]	0.2 – 0.5
Mean building height \bar{H} [0 – 50+ m]	5 – 15 m
Terrain roughness class [1 – 8]	5 - 6 – Rough to Very rough ($0.25 \leq z_0 \leq 0.50$)
Building surface fraction F_r [0-100%]	20 - 30 %
Impervious surface fraction I_r [0-100%]	20 - 40 %
Pervious surface fraction P_r	40 - 50 %
Surface admittance μ [500 – 2,500+ $\text{J.m}^{-2}.\text{s}^{-1/2}.\text{K}^{-1}$]	1,000-2,500 $\text{J.m}^{-2}.\text{s}^{-1/2}.\text{K}^{-1}$
Albedo α [0.02 – 0.5]	0.12 – 0.20
Anthropogenic heat flux Q_F [0 – 400 W.m^{-2}]	>300 W.m^{-2}

Appendix D

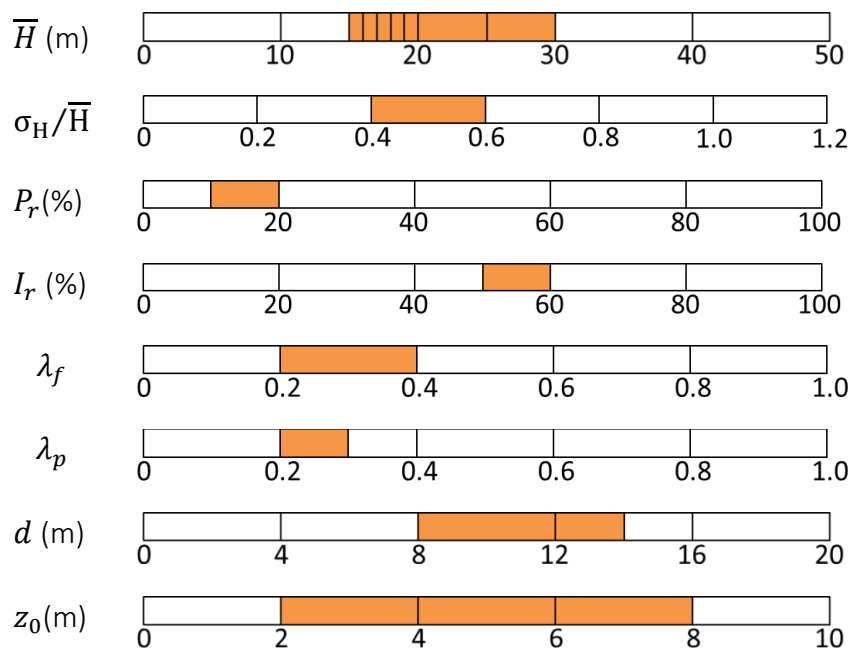
Morphology characteristics of the annuli areas in the idealised “urban unit” model.

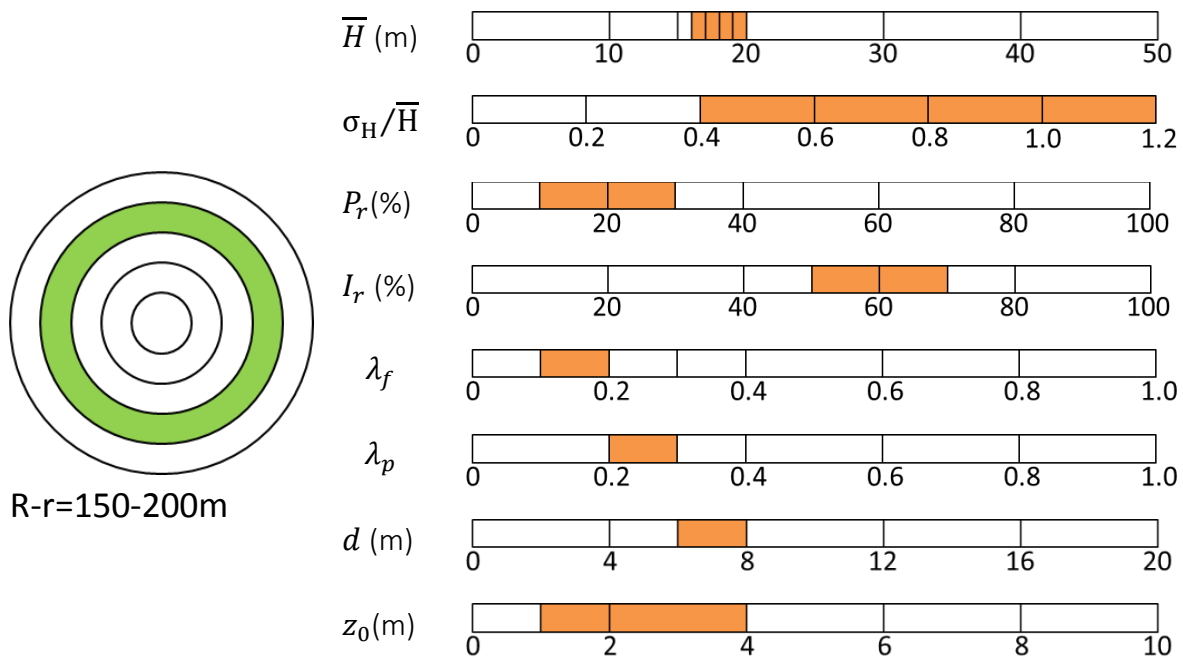
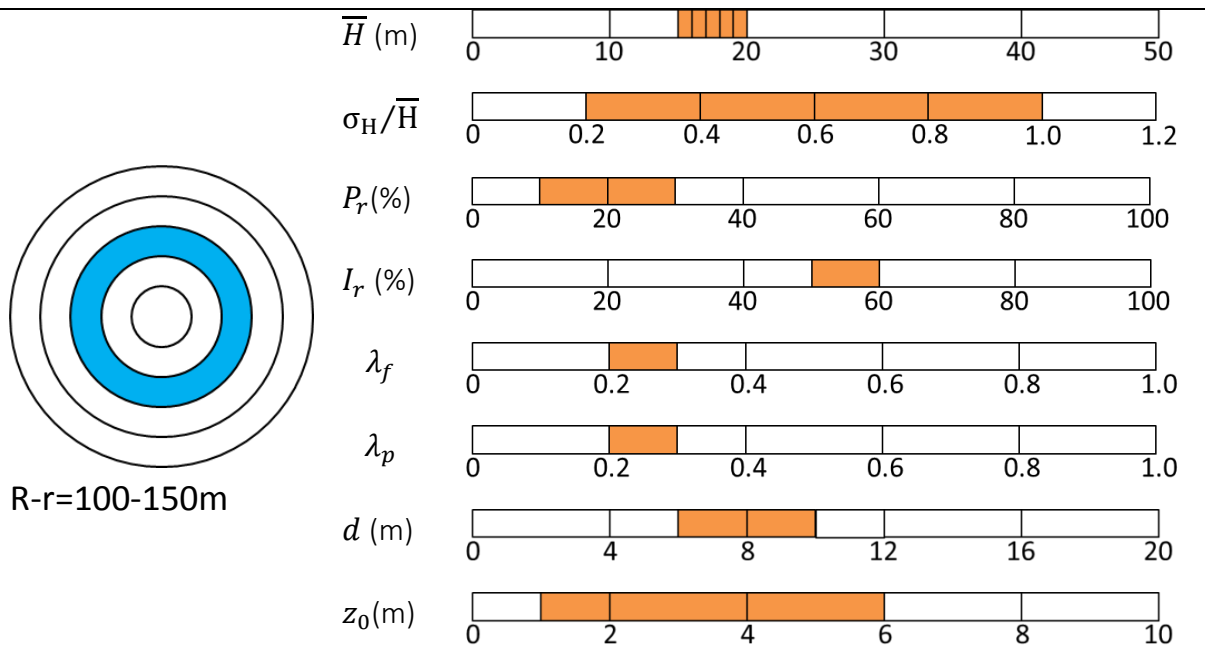


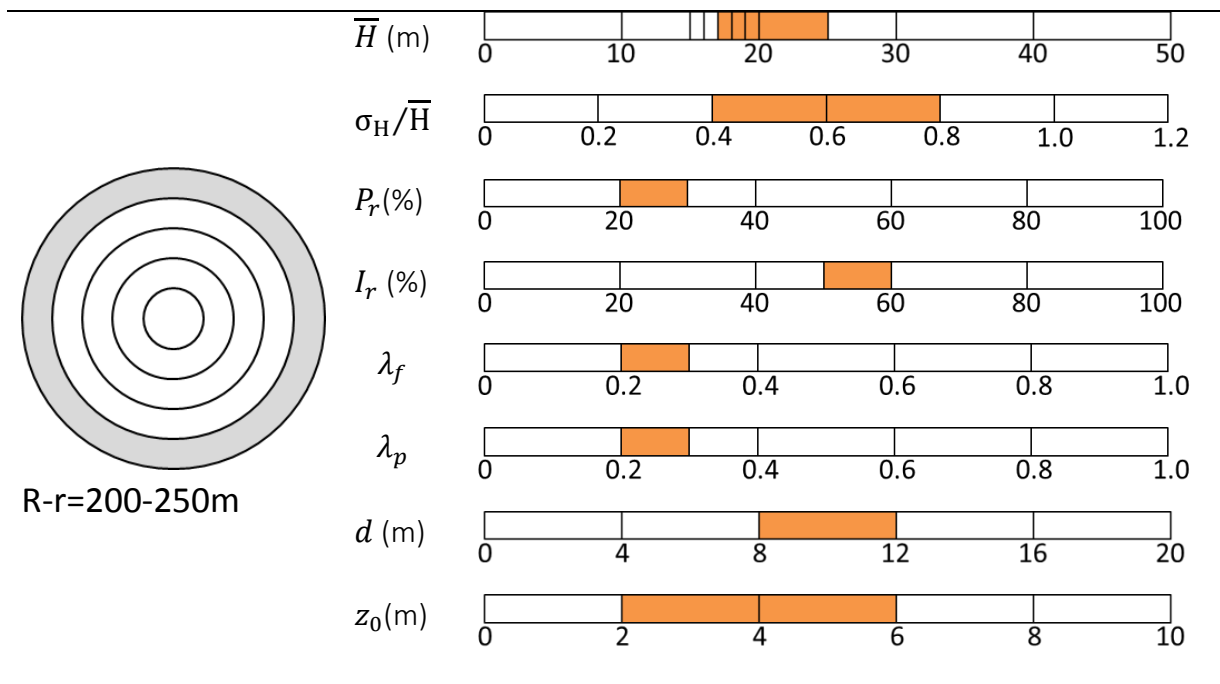
R-r=0-50m



R-r=50-100m







Appendix E

Development of a ANN for the prediction of hourly solar radiation values from typical meteorological parameters

The feed-forward back-propagation multilayer perceptron network consists of the input layer (predictors or independent variables), the hidden layers (hidden units are functions of the weighted sums of the predictors according to the network type and set up) and the output layer (units are functions of the weighted sums of the hidden units) (Figure E.1) (IBM Corp, 2010). The units in the input layer do not consist of any function and they are used only for signal distribution (Mihalakakou et al., 2000). In feed forward networks the connections between the units are only forward and there is no feedback between them (Colton, 2004). Back-propagation refers to the algorithm that is used to reduce the error function between the sampled output and the network's output (Rumelhart et al., 1986; Gershenson, 2003). In order to minimise the error, the initial random weights are adjusted with the use of the Scaled conjugate gradient (SCG) training algorithm (Moller, 1993). The activation functions for the units used in the model are the hyperbolic tangent for the hidden layer and the identity function for the output layer (Figure E.1).

The layers are connected with different synaptic weights. Hidden units (neurons) receive information (signal) from the input. Each hidden unit in this model has a hyperbolic tangent activation function with the form (IBM Corp, 2010):

$$\gamma(c) = \tanh(c) = (e^c - e^{-c}) / (e^c + e^{-c}) \quad (\text{E.1})$$

The hyperbolic tangent function transforms arguments with real values to the range (-1,1) (IBM Corp, 2010).

The activation function in the output layer is the identity function and takes the form (IBM Corp, 2010):

$$\gamma(c) = c \quad (\text{E.2})$$

where c is the weighted sum function from the previous layer. The identity function means that the activation equals the output and the arguments are returned unchanged.

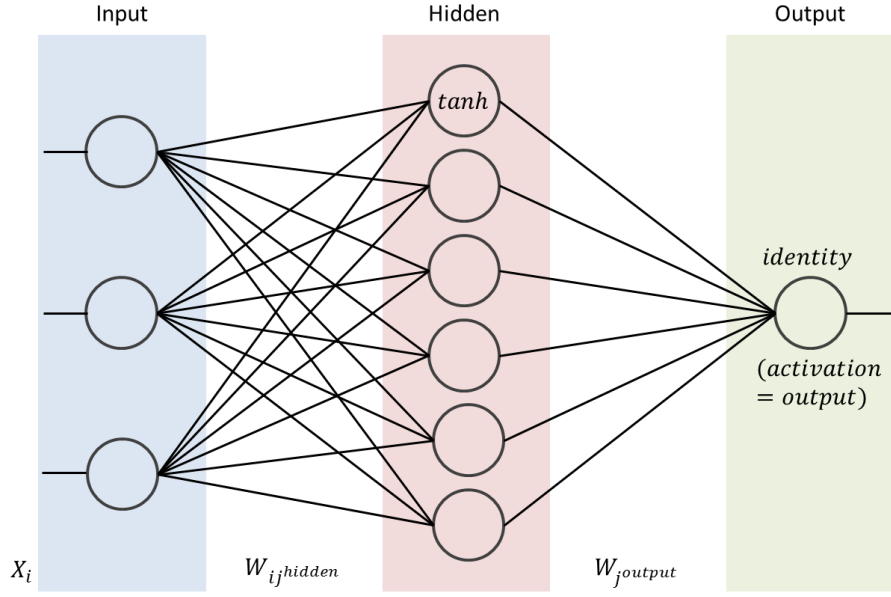


Figure E.1. Feed forward ANN model architecture. X_i refers to the input parameters. W_{ij}^{hidden} and $W_{joutput}$ denote the synaptic weights between the input and the output. The black lines represent the synaptic weights (here equal for display purposes). Data Source: Gershenson (2003), Bosch et al. (2008).

The output Y_j can be defined after Bosch et al. (2008) as:

$$Y = \sum_{j=1}^{N_h} W_{joutput} * \tanh \sum_{i=1}^N W_{ij}^{hidden} X_i \quad (E.3)$$

The explanation for the terms of equation (6.5) is provided in the caption of Figure E.1.

Training is an important stage in the generation of the neural network. Initially, random weights were assigned to the input variables X_i . The hidden units sum the products of the weights and the input arguments $\sum_{i=1}^N (W_{ij}^{hidden} X_i)$ where N is the number of input variables (Figure E.2). The weighted sum was then transformed according to the activation function. In this case a hyperbolic tangent function $\tanh \sum_{i=1}^N (W_{ij}^{hidden} X_i)$ was selected. This choice follows the recommendations of Bosch et al. (2008) that are based on the benefits of the tanh function for network training due to its non-linearity, the set boundaries and the production of both positive and negative numbers (Bosch et al., 2008). New weights $W_{joutput}$ were assigned to the hidden layer output (Figure E.2).

The unit in the output layer subsequently estimated the weighted sum of the input arguments as

$$\sum_{j=1}^{N_h} W_{joutput} * \tanh \sum_{i=1}^N (W_{ijhidden} X_i) \quad (E.4)$$

where N_h denotes the number of the hidden units (Bosch et al., 2008).

It then applied the activation function to the final weighted sum. The identity function selected in this model is a linear function that returns the argument without any transformation (Bosch et al., 2008; IBM Corp, 2010). The identity function was favoured because of the output data characteristics; Global solar radiation is a scale variable that takes real (instead of nominal) values with a physical meaning. The output of the ANN must be in a form that allows the direct comparison with observations and other models' results. In SPSS, the other functions available would have returned values in the range of (-1,1) for the case of the hyperbolic tangent or in the range of (0,1) for the logistic sigmoid function. The estimation of the real value from the results of these functions requires knowing the exact synaptic weights used for the network and the number of hidden units. The additional transformation adds to the complexity of the calculations and the uncertainty of the model.

At the final stage of the training process, the output values for several cases are compared with the target variable values in the data sample (i.e. the dataset used for the training). An error function is calculated to assess the difference between the values. In this model the error function is equal to the squared residual (Sarle, 1997a; IBM Corp, 2010). The synaptic weights are updated and the output is recalculated repeatedly until an optimum solution is reached (Figure E.2).

E.1 Artificial Neural Network model development

A Batch learning method was favoured because it processes all the training data in order to update the synaptic weights (Sarle, 1997a). Each time that all the training data are processed an epoch is finished. Incremental methods such as the mini-batch and online method were rejected because they update the weights after the process of each individual case or for a small set of cases in the dataset (Sarle, 1997a). The

training dataset consists of hourly values of meteorological parameters for the duration of a month. In the incremental methods, the random subsampling during the update of the synaptic weights could increase the bias in the results and there is no control over which and how many hours are used in total during the training.

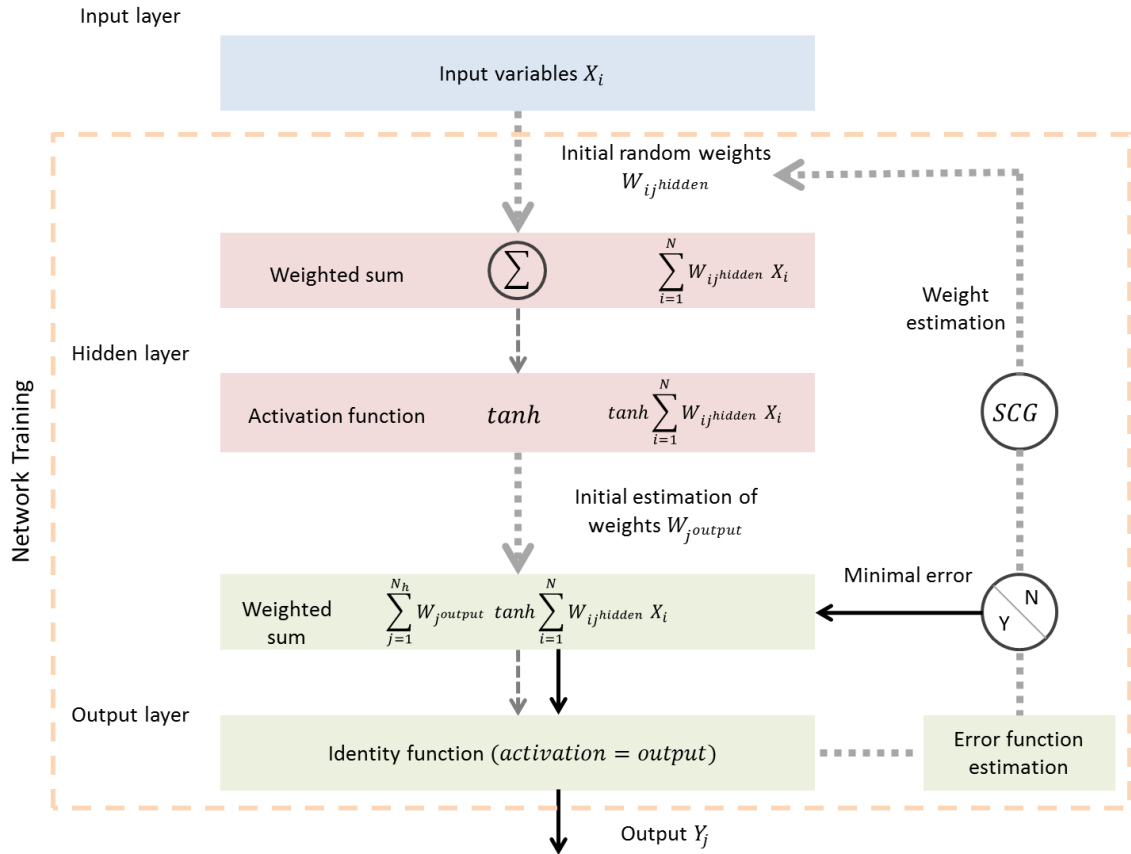


Figure E.2. The neural network function and the training process. SCG denotes the Scale conjugate gradient algorithm. Grey dashed arrows mark the training loop. Bold black arrows show the end of the loop and the final output.

A Scaled conjugate gradient was used for the determination of a global optimum (minimisation of the error function). Conjugate gradients use more second order information than descent gradients and can help to prevent ill-conditioning (i.e. small errors in data can have large effects on the solution's accuracy) (Sarle, 1997a). Input values were standardised by subtracting the mean and dividing by the standard deviation of the dataset ($X = (x - mean)/sd$). The standardisation of the values was found to largely improve the solution. It helps to alleviate ill-conditioning (Sarle, 1997a) and transforms data of different order to the same range (Stack Exchange Inc.,

2011) avoiding any bias in the synaptic weights due to the scale of the variables. For example, 80% RH and 500 W m⁻² h⁻¹ solar radiation should not implicitly have a larger weight than 8 °C air temperature. It must be noted that any scale input variables were standardised before each model generation according to the statistics (mean, standard deviation) of the whole dataset (i.e. Standardisation in SPSS is an integrated step in the network generation. It only standardises the variables according to statistics from the current for each run training dataset). Standardisation was preferred over normalisation (i.e. values are turned in the range of (0,1), $X = (x - \min)/(\max - \min)$) because it does not cut off any outliers that in our case were valid values. In this case standardisation was a good representation of the change of global horizontal radiation in relation to the changes in the independent variables (IBM Corp, 2010; Stack Exchange Inc., 2011).

Table E.1. Model architecture of the ANN for the generation of global solar radiation time series.

Multilayer perceptron model architecture			
<i>Activation Functions:</i> Hyperbolic tangent (Hidden layer) Identity (Output layer)		<i>Rescaling of covariates:</i> Standardised before ANN generation	
		<i>Number of hidden layers:</i> One	
<i>Learning method:</i> Batch		<i>Number of hidden units:</i> Automatically computed	
<i>Optimisation algorithm:</i> Scaled conjugate gradient ($\lambda=5 \times 10^{-7}$, $\sigma=5 \times 10^{-5}$)		<i>Simulated annealing:</i> Interval center 0, Interval offset +/- 0.5	
<i>Stopping rules:</i>	Max steps without decrease in error: 800	Max training time: off	Max training epochs: 10,000
	Min relative change in training error: 1×10^{-5}	Min relative change in training error ratio: 1×10^{-4}	
Random Number Generator: Mersenne Twister, Starting point = 20			

The use of simulated annealing during the determination of initial weights (IBM Corp, 2010) is a technique that helps to avoid local minima. Simulated annealing generates random initial weight vectors between user defined intervals. Then the

XXX

Development of a ANN for the prediction of hourly solar radiation values from typical meteorological parameters

training error is estimated and the initial weights are adjusted by adding different noise in an iterative process (IBM Corp, 2010). The iterations stop when the minimum error is found between the different weights and a set of training error criteria is satisfied (IBM Corp, 2010). A summary of the final network architecture is presented in Table E.1.

E.2 Data structure and results

In ANN modelling the data are divided into Training, Test and Holdout datasets. The Training dataset is used for the training of the network. The Test dataset is an independent sample that is used for integral feedback to the training's progress. Its role is important because it can prevent overtraining. Overtraining or overfitting refers to the situation where the neural network loses its generalisation in an effort to reduce further the error function (Sarle, 1997b). In practice this means that the final model will fit the noise or extreme data instead of the generic trend (Sarle, 1997b). The Holdout sample is not involved at any stage of the network's development and it is only used for validation of the final network's results (IBM Corp, 2010). The holdout error is the relative error between the ANN prediction of global solar radiation and the GHR observations from the typical meteorological year file for Hangzhou.

The partition of data to the different sets can be randomised according to a ratio between samples. For example, a ratio of 6:2:2 between the samples means that 60% of the data are randomly allocated to the training sample, 20% to the testing sample and 20% to the holdout sample. In this case, the randomness of this allocation would have mixed the subsets of the data in a way that would not have allowed comparison with other datasets and the validation of the network. The main reason for this is the complete lack of control over what part of the data from the initial dataset ends up in each sample. For the generation of the solar radiation time series for use in simulations with the "urban unit model" it was important to know which dataset was the one from Hangzhou and to ensure that there would be equal representation of the hours in a day of the training and testing samples. Therefore, the partitioning was made manually with the use of a partition variable.

The typical meteorological year files of nine cities were used for the analysis. One of the cities was Hangzhou while the other cities are within an interval of ± 2 degrees of latitude difference from Hangzhou (Lat. 30.23' N). All the cities have a humid sub-tropical climate with a Cfa classification (the same as Hangzhou) in the Köppen-Geiger climate system (Rubel & Kottek, 2010). The Cfa classification denotes a warm temperate (C), fully humid (f) climate with hot summer (a) (Rubel & Kottek, 2010). The location of the weather stations for the typical meteorological year files is shown in Table E.2. The location of the cities can be seen in Figure E.3.

Table E.2. Cities and the TMY origin weather stations used for the development of the ANN.

Province - City	Longitude*	Latitude*	Elevation (m)	Köppen Climate classification**	WMO ID code
Anhui – Anqing	117.05	30.53	20	Cfa	584240
Anhui - Hefei	117.23	31.87	27	Cfa	583210
Anhui - Huoshan	116.32	31.40	68	Cfa	583140
Henan - Xinyang	114.05	32.13	115	Cfa	572970
Hubei - Wuhan	114.13	30.62	23	Cfa	574940
Jiangsu - Nanjing	118.80	32.83	7	Cfa	582380
Shanghai - Shanghai	121.45	31.40	6	Cfa	583620
Zhejiang - Dinghai	122.10	30.03	36	Cfa	584770
Zhejiang - Hangzhou	120.17	30.23	42	Cfa	584570

*(decimal degrees, -W +E: -180 to +180), **Rubel and Kottek (2010)

The dataset from Hangzhou was only used in the holdout sample for the validation of the ANN results. A scenario was examined where the data from Hangzhou alone were used for network training, testing and validation. The ANN model returned very good results but there were two drawbacks; (1) A prerequisite to manually dividing the data into partitions is for the subsets to have a similar distribution which is not valid when the data come from the same city. (2) When the data are randomly partitioned there are issues with the process as has been discussed previously. As a

result this scenario was dropped. The datasets from the eight cities excluding Hangzhou were allocated to the training and testing samples in different scenarios.

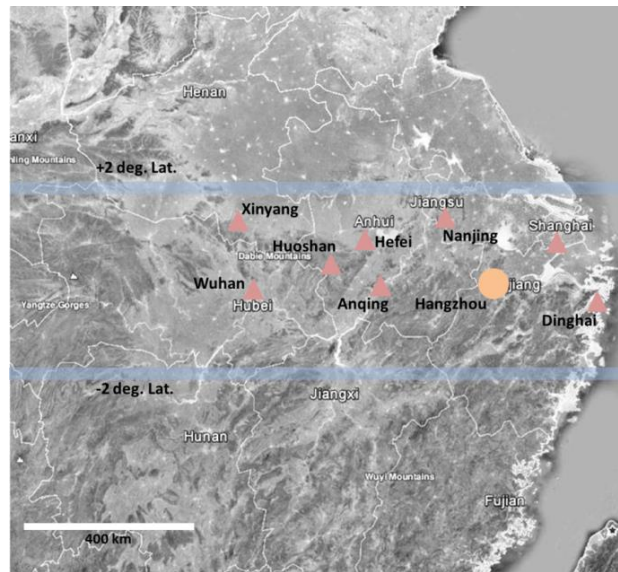


Figure E.3. Location of the cities (marked as red triangles) used for the development of the ANN model. Blue lines give an approximation of the ± 2 degrees latitude distance to Hangzhou (marked as orange bullet point). Background Image source: Google Earth (2013).

A wide range of input parameters and network configurations have been used previously in studies for the prediction of solar radiation (Table E.3). The input variables for this ANN model have been restricted to weather data that can be found in a typical meteorological year weather data file and are widely available online. At the beginning, the hour of the day (0-23) (Hr), dry bulb temperature ($^{\circ}\text{C}$) (DBT), sky cover (0-9) (SC), relative humidity (%) (RH) and wind speed (m/s) (WS) were tested as input for the development of the ANN. Sky cover and wind speed were eliminated because they had a very low normalised importance ($<20\%$) on the network training and the ANN was performing better without them.

In summary, several network configurations were tested with a different number of datasets (TMY files for the cities above). The allocation of datasets to the sampling subsets was varied, along with the input variables and changes were made in the order of the input variables. Different random starting points were used (Figure E.4). The optimisation of the random starting point is considered to solve any issues related to the order of the cases (i.e. hours of days) in the training dataset (i.e. Batch

methods are sensitive to case order because the random initialisation of weights is based on subsampling (IBM Corp, 2010)). The different order of the input parameters can also affect the training of the network.

Table E.3. Input parameters and ANN architecture used for the prediction of global solar radiation.

Input parameters	ANN configuration / activation function (hidden layer) / training algorithm	Reference study
L, m, MP, MT, MVP, MRH, MWS, MDS	MLP-BP / LSF / GD	(Al-Alawi & Al-Hinai, 1998)
(H)TSR (zero values omitted)	MLP-BP / LSF / GD	(Mihalakakou et al., 2000)
Lat, Lon, Alt, m, MDS, MT	MLP-BP / LSF / SCG; CGP; LM	(Sözen et al., 2004)
DS, m, MaxT, TSR	MLP-BP / LSF / GD	(Tymvios et al., 2005)
Alt, doy, K_t (most relevant)	MLP-BP / tanh / SCG	(Bosch et al., 2008)
Lat, Lon, Alt, DS, CC, MaxT	MLP-BP / tanh / LM	(Mubiru & Banda, 2008)
doy, MT, RH, DS, WS, Ev	MLP-BP (RBF) / LSF (GDF) / GD	(Behrang et al., 2010)
Lat, Lon, doy, Max/Min T, Max/Min RH, DS, CEW	MLP-BP / LSF; tanh / BFGS; CG	(Mejdoul et al., 2013)

MLP: multilayer perceptron, RBF: radial basis function, BP: back-propagation, GDF: Gaussian distribution function, tanh: hyperbolic tangent, LSF: logistic sigmoid transfer function, GD: gradient descent, (S)CG: (scaled) conjugate gradient, CG(P): (Pola-Ribiere) conjugate gradient, LM: Levenberg-Marquardt, BFGS: Broyden-Fletcher-Goldfarb-Shanno quasi-Newton method, L: Location, Lat: Latitude, Lon: Longitude, Alt: Altitude, m: month, doy: day of year, MP: mean pressure, MT: mean temperature, MVP: mean vapour pressure, MRH: mean relative humidity, MWS: mean wind speed, (M)DS: (mean) sunshine duration, K_t : clearness index, CC: cloud cover, MaxT: maximum temperature, (H)TSR: (hourly) total solar radiation, CEW: column of evaporating water, Ev: evaporation

The performance of the different ANN configurations was assessed with the estimation of the holdout error. The training error and the test error (i.e. the relative error for the training and testing sample respectively) had also been evaluated in relation to the holdout error. Large discrepancies between the relative errors from the different samples is an indication of overfitting (IBM Corp, 2010).

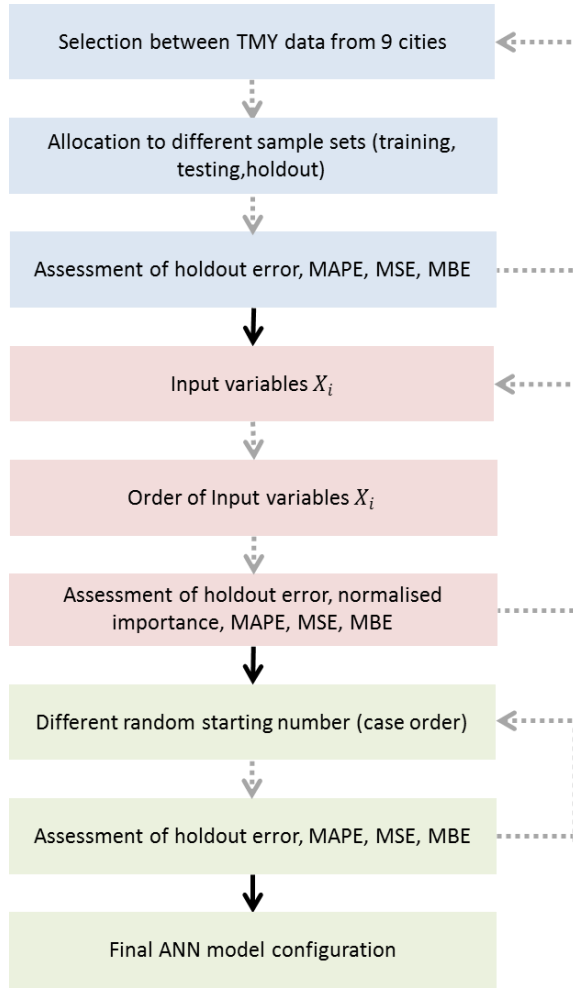


Figure E.4. The ANN optimisation in different stages during its development. Grey dashed arrows mark the training loop. Bold black arrows show the end of the loop and the output.

The final ANN model was assessed in terms of the mean squared error (MSE), the mean absolute percent error (MAPE) and the mean bias error (MBE) of the results as follows:

$$Holdout\ RE = \frac{1}{N} \sum_{i=1}^N \left(\frac{GHR_{ANN,i}}{GHR_{obs,i}} - 1 \right) \quad (E.5)$$

$$MSE = \frac{1}{N} \sum_{i=1}^N (GHR_{obs,i} - GHR_{ANN,i})^2 \quad (E.6)$$

$$MAPE = \frac{100\%}{N} \sum_{i=1}^N \frac{|GHR_{obs,i} - GHR_{ANN,i}|}{GHR_{obs,i}} \quad (E.7)$$

$$MBE = \frac{\sum_{i=1}^N (GHR_{obs,i} - GHR_{ANN,i})}{N} \quad (E.8)$$

where N is the total number of cases (the hour for a day of month), $GHR_{obs,i}$ is the i_{th} hour observation and $GHR_{ANN,i}$ is the ANN prediction for the GHR at the i_{th} hour respectively.

The artificial neural network with the best performance was selected through a vigorous trial and error optimisation process (Figure E.4). The selected network architecture was used to train a network for each month. This was deemed as essential in the process due to the seasonal levels of solar radiation and the differences in the monthly weather trends. A summary of the main ANN configurations that had been tested and their performance for the month of January is available in Appendix E. The MSE, MAPE and MBE were calculated only for the hours in the TMY file for Hangzhou with a global horizontal radiation value higher than zero ($GHR > 0$). The estimated GHR values for the night time hours were set to zero regardless of the ANN model's results. However, zero radiation values have not been excluded from the training and testing datasets as the model performed better when they were included. The selected model's configuration along with its performance statistics is shown for each month in Table E.4.

The final ANN model was used to predict the global horizontal radiation in Hangzhou according to the weather data input from the TMY weather data file for Hangzhou. The TMY weather data file for Hangzhou had not been used in the training or testing of the ANN model (holdout). The calculation of the error statistics was based on a comparison of the ANN generated GHR with the GHR observations from the TMY file for Hangzhou.

E.3 Validation of the ANN model and conclusions on its use

The prediction accuracy of the ANN model is poor when its MAPE is compared directly with other models in the relevant literature (Table E.5). However almost all the models in this review predict monthly or daily values of GHR, not hourly as the ANN does. The model developed by Mihalakakou et al. (2000) predicts hourly GHR with a reported MAPE of 0.2% and a % RMSE of 6.05% for the first day. Their model was developed as a solar radiation forecasting model and it was trained with long historical time series

of solar radiation collected from the same station that was used for the model forecast's validation. The MAPE increases to levels >70% in the forecast of the 14th day (Mihalakakou et al., 2000).

Table E.4. Input data and variables for the final ANN model and its performance at hourly GHR prediction for each month.

Partitioning	Input variables (in order)	Random starting number	Holdout Error (%)	MAPE (%)	MSE (W/m ² h)	MBE (W/m ² h)
Training: 7 cities +/- 2 deg. Lat. Test: Shg Holdout: Hz (Table 5.2)	Factors: Hr	20	JAN : 20.5	130	12298	1.3
	Covariates: ZDBT, ZRH		FEB : 16.8	97	13528	1.3
	Dependent: GHR		MAR : 15.9	163	18548	5.4
			APR : 20.4	152	25239	1
			MAY : 17.3	128	20988	-0.6
			JUN : 16.2	93	22131	50.7
			JUL : 9.6	71	12845	19.5
			AUG : 12.2	112	14502	0.2
			SEP : 19.4	129	20299	-13
			OCT : 9.5	65	7414	-0.2
			NOV : 18.4	118	13042	15.9
			DEC : 15.8	72	10191	27
			Mean Annual	16	111	16203
(RMSE: 127 Wh m ⁻² h ⁻¹ or 0.46 MJ m ⁻² h ⁻¹)						

Shg : Shanghai, Hz : Hangzhou, 7 cities see Table , Hr : hour, ZDBT : standardised dry bulb temperature, ZRH : standardised relative humidity, GHR : global horizontal radiation, MAPE : Mean absolute percent error, MSE : Mean squared error, MBE : Mean bias error, RMSE : Root mean square error. For definition of the errors refer to text.

The ANN developed in this study is not recommended for the hourly prediction of GHR but its daily function was further evaluated. The hourly GHR values generated with the ANN were summed up daily. The daily sums were compared with the daily GHR observations sums from the TMY data file for Hangzhou (Figure E.5).

The daily ANN results for Hangzhou show that the MAPE is still (when compared with the hourly results) high at 58% but the RMSE is 917 Wh m⁻² which is comparable to Deng et al. (2010) for locations in China (Table E.5). The ANN model under predicts the global horizontal radiation at high radiation levels (>2,500 Wh m⁻²) (Figure E.5). The increase in the error of the compared solar radiation values with increase in solar

radiation levels indicates a decrease of the ANN predictive capability for high solar radiation levels (Figure E.5).

Table E.5. Comparison of the mean absolute percent error (MAPE) in this study with other models in the literature.

Location	Network type	Resolution	MAPE (%)	Reference study
S. Arabia	MLP	daily	4.5	(Rehman & Mohandes, 2008)
Turkey	MLP	monthly	6.7	(Sözen et al., 2004)
Uganda	MLP	daily	0.3	(Mubiru & Banda, 2008)
n.a.	MLP	daily	0.12 (Mubiru & Banda, 2008)	(Tymvios et al., 2005)
Greece	MLP	hourly	0.2 (Mubiru & Banda, 2008)	(Mihalakakou et al., 2000)
Iran	MLP	daily	5.21	(Behrang et al., 2010)
Oman	MLP	monthly	7.3	(Al-Alawi & Al-Hinai, 1998)
Morocco	MLP	daily	1	(Mejdoul et al., 2013)
China	MLP	daily	n.a. (RMSE< 944 Wh m ⁻² d ⁻¹)	(Deng et al., 2010)
China	MLP	hourly	111	this study
MLP : Multilayer perceptron, MAPE : Mean absolute percent error, RMSE : Root mean square error. For definition of the errors refer to text. n.a. denotes not available.				

In an effort to assess the transferability of the ANN model, the ANN was run with hourly air temperature and relative humidity observations from the Hongqiao airport in Shanghai (WMO 583670, international code ZSSS, elevation 7 m, 31 10' N, 121 26') (The Weather Underground, 2012). The daily sum of the ANN GHR results for Shanghai were compared with GHR observations from the WMO weather station 583620 (Baoshan airport, elevation 4 m, 31 24' N, 121 27' E) in Shanghai (World Radiation Data Centre, 2014)(Figure E.6).

The horizontal distance between the two airport sites (Baoshan and Hongqiao) is 28 km. It was considered that the global solar radiation levels would be similar at the two weather stations due to the short distance and the similar elevation. This mismatch between the source and the validation weather stations happened due to data availability. Air temperature and RH data were available from Hongqiao airport in

Shanghai but the GHR values were collected from the Baoshan airport. Four days (i.e. the 1st, 7th, 14th and 21st) in each month were selected for the period from January 2012 to December 2012. The selection of the time period was a compromise between the available meteorological data and the solar radiation records. If meteorological data were missing for any of these days in a month, the next day was selected until a day that contains data for all the hours was found.

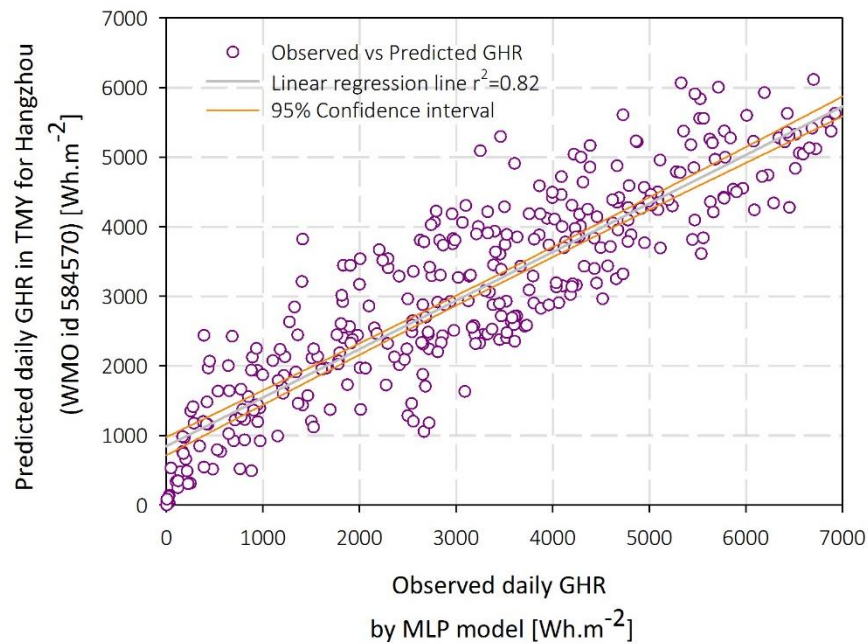


Figure E.5. Comparison of the ANN (MLP model) GHR results for Hangzhou with the observed daily GHR from Hangzhou TMY file (TMY WMO 584570) for 365 days (a year).

The MAPE for the daily total GHR results in Shanghai remained significant at 34%. The RMSE in Shanghai remained the same as the RMSE in the case of Hangzhou (917 Wh m⁻²), showing a small increase to 1,140 Wh m⁻². The ANN model over predicts the values for total solar radiation levels below 4,000 Wh m⁻² d⁻¹ and under predicts the GHR values for daily total solar radiation levels above this threshold (Figure E.6).

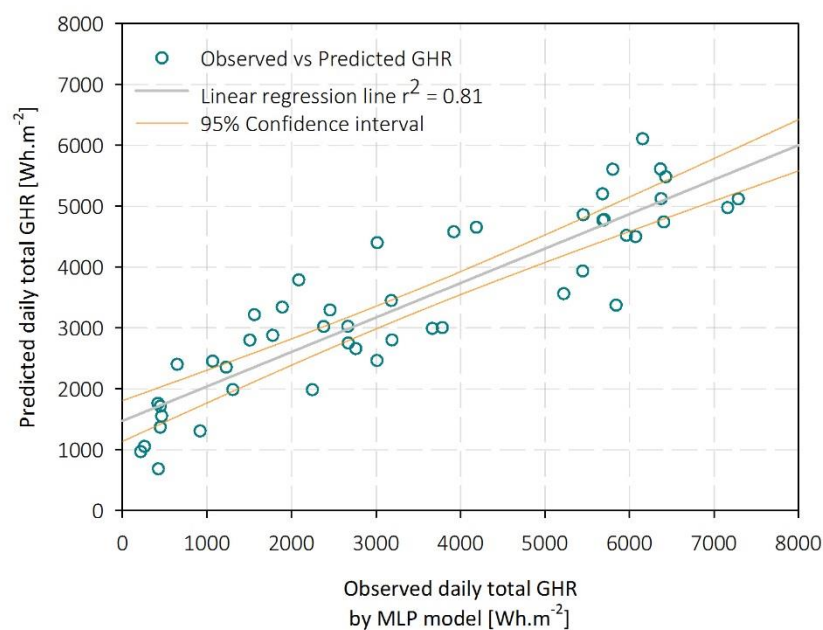


Figure E.6. Comparison of the ANN (MLP model) results for Shanghai (Hongqiao, WMO 583670) with the total daily GHR observations from Baoshan Shanghai(WMO 583620) for 4 days in each month in 2012.

The different ANN configurations considered and the error analysis of their predictions are shown in the tables below (Table E.6, Table E.7, Table E.8):

XL

Development of a ANN for the prediction of hourly solar radiation values from typical meteorological parameters

Table E.6. ANN modelling results for different input variables.

TMY files	Partitioning	Input variables (in order)	Random starting number	Holdout Error (%)	MAPE (%)	MSE	MBE (Wh/m²)
Hz, Shg, Ang, Dng	Training: Ang, Dng Test: Shg Holdout: Hz	Factors: Hr, Covariates: ZDBT,ZRH Dependent: GHR	10 ⁶	27.5	188	15522	-0.9
Hz, Shg, Ang, Dng, Nnj	Training: Shg, Nnj, Dng Test: Ang Holdout: Hz	Factors: Hr, Covariates: ZDBT,ZRH Dependent: GHR	10 ⁶	25.6	157	14546	-7.4
Hz, Shg, Ang, Dng, Nnj	Training: Shg, Nnj, Ang Test: Dng Holdout: Hz	Factors: Hr, Covariates: ZDBT,ZRH Dependent: GHR	10 ⁶	26.9	147	15633	1.5
All	Training: 7 cities +/- 2 deg. Lat. Test: Shg Holdout: Hz	Factors: Hr, Covariates: ZDBT,ZRH Dependent: GHR	10 ⁶	21.6	141	12622	-1.9
Hz : Hangzhou, Shg : Shanghai, Ang : Anqing, Dng : Dinghai, Nnj : Nanjing Hr : Hour of day (0-23), SC : Sky cover (decas), ZDBT: standardised dry bulb temperature (-1,1), ZRH: standardised relative humidity (-1,1), ZWS: standardised wind speed (-1,1), GHR: global horizontal radiation (Wh/m ²)							

Table E.7. ANN modelling results for different input variables.

TMY files	Partitioning	Input variables (in order)	Random starting number	Holdout Error (%)	MAPE (%)	MSE	MBE (Wh/m²)
All	Training: 7 cities +/- 2 deg. Lat. Test: Shg Holdout: Hz	Factors: SC, Hr, Covariates: ZDBT, ZRH, ZWS Dependent: GHR	10 ⁶	25.1	550	46200	-0.2
All	Training: 7 cities +/- 2 deg. Lat. Test: Shg Holdout: Hz	Factors: Hr, Covariates: ZDBT, ZRH, ZWS Dependent: GHR	10 ⁶	21.3	580	38527	-13
All	Training: 7 cities +/- 2 deg. Lat. Test: Shg Holdout: Hz	Factors: SC, Hr Covariates: ZDBT, ZRH Dependent: GHR	10 ⁶	23.6	467	31677	-6
Hz : Hangzhou, Shg : Shanghai, Ang : Anqing, Dng : Dinghai, Nnj : Nanjing Hr : Hour of day (0-23), SC : Sky cover (decas), ZDBT: standardised dry bulb temperature (-1,1), ZRH: standardised relative humidity (-1,1), ZWS: standardised wind speed (-1,1), GHR: global horizontal radiation (Wh/m ²)							

Table E.8. ANN modelling with different random number generator starting points.

TMY files	Partitioning	Input variables (in order)	Random starting number	Holdout Error (%)	MAPE (%)	MSE	MBE (Wh/m²)
All	Training: 7 cities +/- 2 deg. Lat. Test: Shg Holdout: Hz	Factors: Hr, Covariates: ZDBT, ZRH, Dependent: GHR	10 ⁷	22.1	137	12857	-1.3
All	Training: 7 cities +/- 2 deg. Lat. Test: Shg Holdout: Hz	Factors: Hr, Covariates: ZDBT, ZRH, ZWS Dependent: GHR	10	21.5	136	12624	-2.2
All	Training: 7 cities +/- 2 deg. Lat. Test: Shg Holdout: Hz	Factors: Hr Covariates: ZDBT, ZRH Dependent: GHR	20	20.5	126	11838	1.2
All	Training: 7 cities +/- 2 deg. Lat. Test: Shg Holdout: Hz	Factors: Hr Covariates: ZDBT, ZRH Dependent: GHR	2,000	21.8	143	12723	-2.8
Hz : Hangzhou, Shg : Shanghai, Ang : Anqing, Dng : Dinghai, Nnj : Nanjing Hr : Hour of day (0-23), SC : Sky cover (decas), ZDBT: standardised dry bulb temperature (-1,1), ZRH: standardised relative humidity (-1,1), ZWS: standardised wind speed (-1,1), GHR: global horizontal radiation (Wh/m ²)							

Appendix F

Main input parameters for the “urban unit model”
validation and the simulation of the “urban weather
projections”

Main input parameters for the urban unit model validation in January 2013 (heating season).

Input parameter	Jan 13, 2013	Jan 12, 2013	Jan 24, 2013	Source
Weather forcing Group	Group 1	Group 2	Group 3	
Specific humidity 2,500 m (750 mbar) <i>gr w/kg dry air</i>	3.3	2.0	1.1	NCEP/NCAR US (2000)
Prevalent wind direction (N = 0 clockwise)	22	225	225	The Weather Underground (2014b)
Wind speed 10m ab. <i>gr. m/s</i>	3.2	2.1	2.5	The Weather Underground (2014b)
Roughness length z_0	0.1	0.1	0.1	Stewart and Oke (2012)
Mean wall albedo	0.23	0.23	0.23	Yang et al. (2013b)
Mean roof albedo	0.50	0.50	0.50	
Wall heat transmittance $W. m^{-2}. K^{-1}$	1.4	1.4	1.4	
Roof heat transmittance $W. m^{-2}. K^{-1}$	0.9	0.9	0.9	
Underground soil temperature (Upper-Middle-Deep layer) K	278.4 279.6 282.6	277.3 279.5 283.0	280.6 281.4 282.4	NCEP/NCAR US (2000)
Underground soil humidity (Upper-Middle-Deep layer)	38% 38% 36%	36% 36% 35%	34% 35% 35%	NCEP/NCAR US (2000) “

Main input parameters for the urban unit model validation in June 2013 (cooling season).

Input parameter	Jun 14, 2013	Jun 23, 2013	Jun 18, 2013	Source
Weather forcing Group	Group 1	Group 2	Group 3	
Specific humidity 2,500 m (750 mbar) <i>gr w/kg dry air</i>	8.9	12	11.3	NCEP/NCAR US (2000)
Prevalent wind direction (N = 0 clockwise)	45	90	225	The Weather Underground (2014b)
Wind speed 10m ab. <i>gr. m/s</i>	3.1	2.8	3.1	The Weather Underground (2014b)
Roughness length z_0	0.1	0.1	0.1	Stewart and Oke (2012)
Mean wall albedo	0.23	0.23	0.23	Yang et al. (2013b)
Mean roof albedo	0.50	0.50	0.50	
Wall heat transmittance $W. m^{-2}. K^{-1}$	1.4	1.4	1.4	
Roof heat transmittance $W. m^{-2}. K^{-1}$	0.9	0.9	0.9	
Underground soil temperature (Upper-Middle-Deep layer) K	294.3 292.7 290.6	299 294 291	300 293 291	NCEP/NCAR US (2000)
Underground soil humidity (Upper-Middle-Deep layer)	38% 38% 37%	39% 37% 36%	38% 38% 37%	NCEP/NCAR US (2000) “

Main input parameters for the urban weather projections simulations in January (heating season).

Input parameter	Jan, 2013	Jan, 2013	Jan, 2013	Source
Weather forcing Group	Group 1	Group 2	Group 3	
Specific humidity 2,500 m (750 mbar) <i>gr w/kg dry air</i>	3.3	2.0	1.1	NCEP/NCAR US (2000)
Prevalent wind direction (N = 0 clockwise)	22	225	225	The Weather Underground (2014b)
Wind speed 10m ab. <i>gr. m/s</i>	3.2	2.1	2.5	The Weather Underground (2014b)
Roughness length z_0	0.1	0.1	0.1	Stewart and Oke (2012)
Mean wall albedo	0.23	0.23	0.23	Yang et al. (2013b)
Mean roof albedo	0.50	0.50	0.50	
Wall heat transmittance $W. m^{-2}. K^{-1}$	1.4	1.4	1.4	
Roof heat transmittance $W. m^{-2}. K^{-1}$	0.9	0.9	0.9	
Underground soil temperature (Upper-Middle-Deep layer) <i>K</i>	277.3 279.6 283	277.3 279.4 283	279 280.2 283	NCEP/NCAR US (2000)
Underground soil humidity (Upper-Middle-Deep layer)	36% 36% 36%	36% 36% 35%	35% 35% 35%	NCEP/NCAR US (2000) “

Main input parameters for the urban weather projections simulations in June (cooling season).

Input parameter	June, 2013	June, 2013	June, 2013	Source
Weather forcing Group	Group 1	Group 2	Group 3	
Specific humidity 2,500 m (750 mbar) <i>gr w/kg dry air</i>	8.9	9.9	11.3	NCEP/NCAR US (2000)
Prevalent wind direction (N = 0 clockwise)	45	90	225	The Weather Underground (2014b)
Wind speed 10m ab. <i>gr. m/s</i>	3.1	2.8	3.1	The Weather Underground (2014b)
Roughness length z_0	0.1	0.1	0.1	Stewart and Oke (2012)
Mean wall albedo	0.23	0.23	0.23	Yang et al. (2013b)
Mean roof albedo	0.50	0.50	0.50	
Wall heat transmittance $W. m^{-2}. K^{-1}$	1.4	1.4	1.4	
Roof heat transmittance $W. m^{-2}. K^{-1}$	0.9	0.9	0.9	
Underground soil temperature (Upper-Middle-Deep layer) <i>K</i>	294.3 292.7 290.6	297.5 292.7 290.5	300 293 291	NCEP/NCAR US (2000)
Underground soil humidity (Upper-Middle-Deep layer)	38% 38% 37%	37% 37% 36%	38% 38% 37%	NCEP/NCAR US (2000) “

Appendix G

Publication list

<http://scholar.google.co.uk/citations?user=2EnjYjgAAAAJ&hl=en&oi=ao>

Citations 49, h-index 2, i10-index 1 as of 10/05/2017

Articles

- [1] Bourikas L., James P.A.B., Bahaj A.S., Jentsch M.F., Shen T., Chow D.H.C., Darkwa J. (2016) Transforming typical hourly simulation weather data files to represent urban locations by using a 3D urban unit representation with micro-climate simulations. *Future Cities and Environment*, vol. 2, p.p. 1-23
- [2] Jentsch M.F., James P.A.B., Bourikas L. and Bahaj A.S. (2013) Transforming existing weather data for worldwide locations to enable energy and building performance simulation under future climates. *Renewable Energy*, vol. 55, p.p. 514-524
- [3] Bourikas L., Shen T., James P.A.B., Chow D.H.C., Jentsch M.F., Darkwa J. and Bahaj A.S. (2013) Addressing the Challenge of Interpreting Microclimatic Weather Data Collected from Urban Sites. *Journal of Power and Energy Engineering*, vol. 1, p.p. 7-15. First presented to the 2nd International Conference on New Energy and Sustainable Development (NESD 2013), 29 Nov – 1 Dec 2013, Sanya, China.

Conferences

- [1] Bourikas, L., James, P.A.B., Bahaj, A.S., Jentsch, M.F., Shen, T., Chow, D.H.C. and Darkwa, J. (2015) A simplified 3D urban unit representation for urban microclimate simulations: A case study in China's 'Hot Summer and Cold Winter' climate zone. In, *SET2015: 14th International Conference on Sustainable Energy Technologies*, 25-27 Aug 2015, Nottingham, UK

References

- Akbari H., Shea Rose L. and Taha H. (2003) Analyzing the land cover of an urban environment using high-resolution orthophotos. *Landscape and Urban Planning*, vol. 63 (1), p.p. 1-14
- Al-Alawi S.M. and Al-Hinai H.A. (1998) An ANN-based approach for predicting global radiation in locations with no direct measurement instrumentation. *Renewable Energy*, vol. 14 (1-4), p.p. 199-204
- Al-Sallal K.A., Aboulmaga M.M. and Alteraifi A.M. (2001) Impact of Urban Spaces and Building Height on Airflow Distribution: Wind Tunnel Testing of an Urban Setting Prototype in Abu-Dhabi City. *Architectural Science Review*, vol. 44 (3), p.p. 227-232
- Allen L., Lindberg F. and Grimmond C.S.B. (2011) Global to city scale urban anthropogenic heat flux: model and variability. *International Journal of Climatology*, vol. 31 (13), p.p. 1990-2005
- American Meteorological Society (2013a) "Definition of potential temperature." *Glossary of meteorology*.
- American Meteorological Society (2013b) "Monin-Obukhov similarity theory." *Glossary of Meteorology*.
- American Society of Heating Refrigerating and Air-Conditioning Engineers (ASHRAE). Technical Committee 4.2 (2009) *Frequently Asked Questions, Climatic Information: Weather years for energy simulations and how they differ from other types of weather or climate data*. Available from: <http://tc42.ashraetcs.org/faq.html#6> [Accessed]
- Arnfield A.J. (2003) Two decades of urban climate research: A review of turbulence, exchanges of energy and water, and the urban heat island. *International Journal of Climatology*, vol. 23 (1), p.p. 1-26
- Ashie Y. and Kono T. (2011) Urban-scale CFD analysis in support of a climate-sensitive design for the Tokyo Bay area. *International Journal of Climatology*, vol. 31 (2), p.p. 174-188
- Atkinson B. (2003) Numerical Modelling of Urban Heat-Island Intensity. *Boundary-Layer Meteorology*, vol. 109 (3), p.p. 285-310
- Bahaj A.S., James P.A.B. and Jentsch M.F. (2008) Potential of emerging glazing technologies for highly glazed buildings in hot arid climates. *Energy and Buildings*, vol. 40 (5), p.p. 720-731
- Baik J.-J., Park S.-B. and Kim J.-J. (2009) Urban Flow and Dispersion Simulation Using a CFD Model Coupled to a Mesoscale Model. *Journal of Applied Meteorology and Climatology*, vol. 48 (8), p.p. 1667-1681
- Baklanov A., Ching J., Grimmond C.S.B. and Martilli A. (2009) Model Urbanization Strategy: Summaries, Recommendations and Requirements In: Baklanov A., Sue G., Alexander M. and Athanassiadou M. (eds) *Meteorological and Air Quality Models for Urban Areas*. Springer Berlin Heidelberg 151-162
- Baklanov A., Martilli A., Grimmond C.S.B., Mahura A., Ching J., Calmet I., Clark P., Esau I., Dandou A., Zilitinkevich S., Best M.J., Mestayer P., Santiago J.L., Tombrou M., Petersen C., Porson A., Salamanca F. and Amstrup B. (2010) *Hierarchy of Urban Canopy Parameterisations for different scale models. MEGAPOLI Project Scientific Report 10-04* Copenhagen: Danish Meteorological Institute, DMI. Available from: http://megapoli.dmi.dk/publ/MEGAPOLI_sr10-04.pdf
- Baklanov A., Mestayer P.G., Clappier A., Zilitinkevich S., Joffre S., Mahura A. and Nielsen N.W. (2008) Towards improving the simulation of meteorological fields in urban areas through updated/advanced surface fluxes description. *Atmospheric Chemistry and Physics*, vol. 8 (3), p.p. 523-543
- Barlow J., Harman I. and Belcher S. (2004) Scalar fluxes from urban street canyons. Part I: Laboratory simulation. *Boundary-Layer Meteorology*, vol. 113 (3), p.p. 369-385

References

- Basara J.B., Hall P.K., Jr., Schroeder A.J., Illston B.G. and Nemunaitis K.L. (2008) Diurnal cycle of the Oklahoma City urban heat island. *J. Geophys. Res.*, vol. 113 (D20), p.p. D20109
- Bechtel B. (2011) Multitemporal landsat data for urban heat island assessment and classification of local climate zones. Paper presented at Joint Urban Remote Sensing Event. Munich, Germany
- Behrang M.A., Assareh E., Ghanbarzadeh A. and Noghrehabadi A.R. (2010) The potential of different artificial neural network (ANN) techniques in daily global solar radiation modeling based on meteorological data. *Solar Energy*, vol. 84 (8), p.p. 1468-1480
- Best M.J. (1998) A Model to Predict Surface Temperatures. *Boundary-Layer Meteorology*, vol. 88 (2), p.p. 279-306
- Best M.J. (2005) Representing urban areas within operational numerical weather prediction models. *Boundary-Layer Meteorology*, vol. 114 (1), p.p. 91-109
- Best News (2013) Hangzhou Ranked New "Four Furnaces" Third Old Foundation Hangzhou Sign. 2013 Available from: <http://www.best--news.us/news-4918452-Hangzhou-ranked-new-four-furnaces-third-old-foundation-Hangzhou-sigh.html> [Accessed 16 July 2013]
- Bin S. and Jun L. (2012) *Building energy efficiency policies in China*. Paris, France: American Council for an Energy-Efficient Economy (ACEEE) and Global Buildings Performance Network (GBPN). Available from: http://www.gbpn.org/sites/default/files/08.%20China%20Report_0.pdf
- Bohnenstengel S.I., Evans S., Clark P.A. and Belcher S.E. (2011) Simulations of the London urban heat island. *Quarterly Journal of the Royal Meteorological Society*, vol. 137 (659), p.p. 1625-1640
- Bosch J.L., López G. and Batlles F.J. (2008) Daily solar irradiation estimation over a mountainous area using artificial neural networks. *Renewable Energy*, vol. 33 (7), p.p. 1622-1628
- Bourikas L., James P.A.B., Bahaj A.S., Jentsch M.F., Shen T., Chow D.H.C. and Darkwa J. (2015) A simplified 3D urban unit representation for urban micro-climate simulations: A case study in China's "Hot Summer and Cold Winter" climate zone. Paper presented at 14th International Conference on Sustainable Energy Technologies. Nottingham, UK
- Bourikas L., James P.A.B., Bahaj A.S., Jentsch M.F., Shen T., Chow D.H.C. and Darkwa J. (2016) Transforming typical hourly simulation weather data files to represent urban locations by using a 3D urban unit representation with micro-climate simulations. *Future Cities and Environment*, vol. 2 (1), p.p. 7
- Bourikas L., Shen T., James P.A.B., Chow D.H.C., Jentsch M.F., Darkwa J. and Bahaj A.S. (2013) Addressing the challenge of interpreting microclimatic weather data from urban sites *Journal of Power and Energy Engineering*, vol. 1, p.p. 7-15
- Bouyer J., Inard C. and Musy M. (2011) Microclimatic coupling as a solution to improve building energy simulation in an urban context. *Energy and Buildings*, vol. 43 (7), p.p. 1549-1559
- Bowler D.E., Buyung-Ali L., Knight T.M. and Pullin A.S. (2010) Urban greening to cool towns and cities: A systematic review of the empirical evidence. *Landscape and Urban Planning*, vol. 97 (3), p.p. 147-155
- Britter R.E. and Hanna S.R. (2003) Flow and dispersion in urban areas. *Annual Review of Fluid Mechanics*, vol. 35, p.p. 469-496
- Bruse M. (2004) *ENVI-met 3.0: Updated model overview*. www.envi-met.com.
- Bruse M. (2008a) *ENVI-met 3.1 Manual*. Available from: <http://www.envi-met.com/htmlhelp/helpindex.htm> [Accessed 10 July 2014]
- Bruse M. (2008b) *ENVI-met 3.1 Manual: Vertical Grid Layout*. Available from: <http://www.envi-met.com/htmlhelp/helpindex.htm> [Accessed 12 February]
- Bruse M. (2008c) *ENVI-met 3: Model architecture*. Available from: <http://www.envi-met.com/> [Accessed 12 February]
- Bruse M. (2008d) *ENVI-met 3: Overview model data flow* Available from: <http://www.envi-met.com> [Accessed]

References

- Bruse M. (2008e) *ENVI-met 3: Overview model layout*. Available from: <http://www.envi-met.com/> [Accessed]
- Bruse M. and Fleer H. (1998) Simulating surface–plant–air interactions inside urban environments with a three dimensional numerical model. *Environmental Modelling & Software*, vol. 13 (3–4), p.p. 373-384
- Brutsaert W. (1982) *The Surface Sublayer Evaporation into the Atmosphere: Theory, History and Applications*. Dordrecht, Holland: D.Reidel Publishing Company 64-67
- Bueno B., Norford L., Hidalgo J. and Pigeon G. (2012) The urban weather generator. *Journal of Building Performance Simulation*, vol. 6 (4), p.p. 269-281
- Burdick A. (2011) *Strategy Guideline: Accurate heating and cooling load calculations*. Oak Ridge, USA.
- Burian S., Brown J.F. and Linger S.P. (2002) *Building morphology analysis of downtown Los Angeles*. (Tech. Rep. LA-UR-02-0781):67 California.
- Carter T.R. (2007) *General guidelines on the use of scenario data for climate impact and adaptation assessment - Version 2, Intergovernmental Panel on Climate Change - Task Group on Data and Scenario Support for Impact and Climate Assessment (TGICA)*. Available from: http://www.ipcc-data.org/guidelines/TGICA_guidance_sdciaa_v2_final.pdf
- Center for International Earth Science Information Network C.C.U., International Food Policy Research Institute I., The World B. and Centro Internacional De Agricultura Tropical C. (2011) Global Rural-Urban Mapping Project, Version 1 (GRUMPv1): Population Density Grid. Palisades, NY: NASA Socioeconomic Data and Applications Center (SEDAC)
- Chan A.L.S. (2011) Developing a modified typical meteorological year weather file for Hong Kong taking into account the urban heat island effect. *Building and Environment*, vol. 46 (12), p.p. 2434-2441
- Chen F., Kusaka H., Bornstein R., Ching J., Grimmond C.S.B., Grossman-Clarke S., Loridan T., Manning K.W., Martilli A., Miao S., Sailor D., Salamanca F.P., Taha H., Tewari M., Wang X., Wyszogrodzki A.A. and Zhang C. (2011) The integrated WRF/urban modelling system: development, evaluation, and applications to urban environmental problems. *International Journal of Climatology*, vol. 31 (2), p.p. 273-288
- Chen S., Yoshino H., Levine M.D. and Li Z. (2009) Contrastive analyses on annual energy consumption characteristics and the influence mechanism between new and old residential buildings in Shanghai, China, by the statistical methods. *Energy and Buildings*, vol. 41 (12), p.p. 1347-1359
- Cheng H. and Castro I. (2002a) Near-Wall Flow Development After A Step Change In Surface Roughness. *Boundary-Layer Meteorology*, vol. 105 (3), p.p. 411-432
- Cheng H. and Castro I.P. (2002b) Near wall flow over urban-like roughness. *Boundary-Layer Meteorology*, vol. 104 (2), p.p. 229-259
- Cheung H.K.W., Levermore G.J. and Watkins R. (2010) A Low Cost, Easily Fabricated Radiation Shield for Temperature Measurements to Monitor Dry Bulb Air Temperature in Built Up Urban Areas. *Building Services Engineering Research and Technology*, vol. 4 (31), p.p. 371-380
- Cheung J.O.P. and Liu C.-H. (2011) CFD simulations of natural ventilation behaviour in high-rise buildings in regular and staggered arrangements at various spacings. *Energy and Buildings*, vol. 43 (5), p.p. 1149-1158
- China Daily (2013) Summer Heat Leaves Cities Gasping as Mercury Rises. 2013 Available from: http://www.chinadaily.com.cn/cndy/2013-07/17/content_16786059.htm [Accessed 27 July 2013]
- Chow D.H.C., Kelly M. and Darkwa J. (2013) The Effects of Future Climate Change on Energy Consumption in Residential Buildings in China. *Journal of Power and Energy Engineering*, vol. Vol.01No.05, p.p. 9
- Chow W.T.L. and Brazel A.J. (2012) Assessing xeriscaping as a sustainable heat island mitigation approach for a desert city. *Building and Environment*, vol. 47 (0), p.p. 170-181

References

- Collier C.G. (2006) The impact of urban areas on weather. *Quarterly Journal of the Royal Meteorological Society*, vol. 132 (614), p.p. 1-25
- Colton S. (2004) *Lecture 13: Multi-layer artificial neural networks* London, UK Imperial College London. Available from: <http://www.doc.ic.ac.uk/~sgc/teaching/pre2012/v231/lecture13.html> [Accessed 29 May 2014]
- Comet® Cooperative Program for Operational Meteorology Education and Training (2002) *How mesoscale models work* University Corporation for Atmospheric Research (UCAR), funded by the National Weather Service. Available from: <http://meted.ucar.edu/> [Accessed 25 May 2012]
- Cost Action 732 (2007) *Best practice guideline for the CFD simulation of flows in the urban environment*. Hamburg, Germany: Meteorological Institute, University of Hamburg
- Council on Tall Buildings and Urban Habitat (2014) *CTBUH Tall building Height calculator*. Available from: <http://www.ctbuh.org/TallBuildings/HeightStatistics/HeightCalculator/tabid/1007/language/en-US/Default.aspx> [Accessed 17 March]
- Coutts A.M., Beringer J. and Tapper N.J. (2007) Impact of Increasing Urban Density on Local Climate: Spatial and Temporal Variations in the Surface Energy Balance in Melbourne, Australia. *Journal of Applied Meteorology and Climatology*, vol. 46 (4), p.p. 477-493
- Crawley D.B. (1998) *Which weather data should you use for energy simulations of commercial buildings?* ASHRAE Transactions 104 Part 2:498-515 Atlanta, USA: ASHRAE.
- Dai C., Lan L. and Lian Z. (2014) Method for the determination of optimal work environment in office buildings considering energy consumption and human performance. *Energy and Buildings*, vol. 76, p.p. 278-283
- Dandou A., Tombrou M., Akylas E., Soulakellis N. and Bossioli E. (2005) Development and evaluation of an urban parameterization scheme in the Penn State/NCAR Mesoscale Model (MM5). *J. Geophys. Res.*, vol. 110 (D10), p.p. D10102
- Davenport A.G., Grimmond C.S.B., Oke T.R. and Wieringa J. (2000) Estimating the roughness of cities and sheltered country. Paper presented at 12th Conference on Applied Climatology. Asheville, NC
- De La Flor F.S. and DomíNquez S.A. (2004) Modelling microclimate in urban environments and assessing its influence on the performance of surrounding buildings. *Energy and Buildings*, vol. 36 (5), p.p. 403-413
- Dee D., Fasullo J., Shea D., Walsh J. and Ncar (2014) *"The Climate Data Guide: Atmospheric Reanalysis: Overview and Comparison Tables."* Available from: <https://climatedataguide.ucar.edu/climate-data/atmospheric-reanalysis-overview-comparison-tables>. [Accessed]
- Deng F., Su G., Liu C. and Wang Z. (2010) Global Solar Radiation Modeling Using The Artificial Neural Network Technique. In: *Asia-Pacific Power and Energy Engineering Conference (APPEEC)* Asia-Pacific. 1-5
- Design H.a.O.U.P. (2006) *Hangzhou general planning map*. Hangzhou, China:
- Devon (2010) *Devon Laser measuring equipment* Nanjing, China. Available from: <http://www.devon.com.cn/en/> [Accessed 16 June 2014]
- Di Sabatino S., Leo L.S., Cataldo R., Ratti C. and Britter R.E. (2010) Construction of Digital Elevation Models for a Southern European City and a Comparative Morphological Analysis with Respect to Northern European and North American Cities. *Journal of Applied Meteorology and Climatology*, vol. 49 (7), p.p. 1377-1396
- Dimitriou T., Teli D., James P.A.B., Bahaj A.S., Ellison L. and Waggott A. (2014) Impact of current occupant behaviour on potential carbon savings in a council owned tower block undergoing retrofit.
- Drew D.R., Barlow J.F. and Cockerill T.T. (2013) Estimating the potential yield of small wind turbines in urban areas: A case study for Greater London, UK. *Journal of Wind Engineering and Industrial Aerodynamics*, vol. 115 (0), p.p. 104-111

References

- Dupont S., Otte T.L. and Ching J.K.S. (2004) Simulation of meteorological fields within and above urban and rural canopies with a mesoscale model (MM5). *Boundary-Layer Meteorology*, vol. 113, p.p. 111-158
- Eames M.E. (2016) An update of the UK's design summer years: Probabilistic design summer years for enhanced overheating risk analysis in building design. *Building Services Engineering Research and Technology*, vol. 37 (5), p.p. 503-522
- Ellefsen R. (1991) Mapping and measuring buildings in the canopy boundary layer in ten U.S. cities. *Energy and Buildings*, vol. 16 (3-4), p.p. 1025-1049
- Emporis GmbH (2014) *Building heights database for cities worldwide. Public website data for Hangzhou in China*. Available from: <http://www.emporis.com/city/hangzhou-china> [Accessed]
- Erell E., Pearlmuter D. and Williamson T. (2011) *Urban microclimate: designing the spaces between buildings*. (1st Edition) London: Earthscan
- Erell E. and Williamson T. (2006) Simulating air temperature in an urban street canyon in all weather conditions using measured data at a reference meteorological station. *International Journal of Climatology*, vol. 26, p.p. 1671-1694
- Esdu (1980) Mean Fluid Forces and Moments on Rectangular Prisms: Surface-Mounted Structures in Turbulent Shear Flow. *Engineering Sciences Data*.
- Evans S. (2009) 3D cities and numerical weather prediction models: An overview of the methods used in the LUCID project. University College London, London: CASA, Centre of Advanced Spatial Analysis
- Flagg D.D. and Taylor P.A. (2011) Sensitivity of mesoscale model urban boundary layer meteorology to the scale of urban representation. *Atmospheric Chemistry and Physics*, vol. 11 (6), p.p. 2951-2972
- Flanner M.G. (2009) Integrating anthropogenic heat flux with global climate models. *Geophysical Research Letters*, vol. 36 (2),
- Foken T. (2008) *Micrometeorology*. Berlin Heidelberg: Springer-Verlag
- Forejt L., Hensen J., Drkal F. and Barankova P. (2006) Weather data around the world for design of field hospital HVAC. In: *17th International Air-Conditioning and Ventilation Conference Prague*. STP - Society of Environmental Engineering 6
- Gaitani N., Spanou A., Saliari M., Synnefa A., Vassilakopoulou K., Papadopoulou K., Pavlou K., Santamouris M., Papaioannou M. and Lagoudaki A. (2011) Improving the microclimate in urban areas: a case study in the centre of Athens. *Building Services Engineering Research and Technology*, vol. 32 (1), p.p. 53-71
- Georgakis C. and Santamouris M. (2008) On the estimation of wind speed in urban canyons for ventilation purposes—Part 1: Coupling between the undisturbed wind speed and the canyon wind. *Building and Environment*, vol. 43 (8), p.p. 1404-1410
- Gershenson C. (2003) Artificial Neural Networks for Beginners. 2003 Available from: arxiv.org/ftp/cs/papers/0308/0308031.pdf [Accessed 30 May 2014]
- Google Earth (2013) *Satellite Images of Hangzhou and Ningbo*. [Accessed]
- GrADS Cola/Iges (2011) The Grid Analysis and Display System (GrADS) Version 2.0.:
- Grimmond C.S.B., Blackett M., Best M.J., Baik J.J., Belcher S.E., Beringer J., Bohnenstengel S.I., Calmet I., Chen F., Coutts A., Dandou A., Fortuniak K., Gouvea M.L., Hamdi R., Hendry M., Kanda M., Kawai T., Kawamoto Y., Kondo H., Krayenhoff E.S., Lee S.H., Loridan T., Martilli A., Masson V., Miao S., Oleson K., Ooka R., Pigeon G., Porson A., Ryu Y.H., Salamanca F., Steeneveld G.J., Tombrou M., Voogt J.A., Young D.T. and Zhang N. (2011) Initial results from Phase 2 of the international urban energy balance model comparison. *International Journal of Climatology*, vol. 31 (2), p.p. 244-272
- Grimmond C.S.B., Blackett M., Best M.J., Barlow J., Baik J.J., Belcher S.E., Bohnenstengel S.I., Calmet I., Chen F., Dandou A., Fortuniak K., Gouvea M.L., Hamdi R., Hendry M., Kawai T., Kawamoto Y., Kondo H., Krayenhoff E.S., Lee S.H., Loridan T., Martilli A., Masson V., Miao S., Oleson K., Pigeon G., Porson A., Ryu Y.H., Salamanca F., Shashua-Bar L., Steeneveld G.J., Tombrou M., Voogt J., Young D. and Zhang N. (2010) The International

References

- Urban Energy Balance Models Comparison Project: First Results from Phase 1. *Journal of Applied Meteorology and Climatology*, vol. 49 (6), p.p. 1268-1292
- Grimmond C.S.B. and Oke T.R. (1999) Aerodynamic Properties of Urban Areas Derived from Analysis of Surface Form. *Journal of Applied Meteorology*, vol. 38 (9), p.p. 1262-1292
- Grimmond C.S.B. and Oke T.R. (2002) Turbulent Heat Fluxes in Urban Areas: Observations and a Local-Scale Urban Meteorological Parameterization Scheme (LUMPS). *Journal of Applied Meteorology*, vol. 41 (7), p.p. 792-810
- Haas R. and Biermayr P. (2000) The rebound effect for space heating empirical evidence from Austria. *Energy Policy*, vol. 28 (6-7), p.p. 403-410
- Hacker J., Capon R. and Mylona A. (2009) Use of climate change scenarios for building simulation: the CIBSE future weather years. London, UK: The Chartered Institution of Building Services Engineers
- Hamilton I.G., Davies M., Steadman P., Stone A., Ridley I. and Evans S. (2009) The significance of the anthropogenic heat emissions of London's buildings: A comparison against captured shortwave solar radiation. *Building and Environment*, vol. 44 (4), p.p. 807-817
- Hamlyn D. and Britter R. (2005) A numerical study of the flow field and exchange processes within a canopy of urban-type roughness. *Atmospheric Environment*, vol. 39 (18), p.p. 3243-3254
- Han X., Chen J., Huang C., Weng W., Wang L. and Niu R. (2014) Energy audit and air-conditioning system renovation analysis on office buildings using air-source heat pump in Shanghai. *Building Services Engineering Research and Technology*, vol. 35 (4), p.p. 376-392
- Hangzhou Statistical Bureau (2011) *Statistical yearbook of Hangzhou*. Beijing.
- Harman I.N. (2003) *The energy balance of urban areas*. Unpublished, Doctor of Philosophy Thesis, University of Reading, Reading, UK
- Hirst E. and Brown M. (1990) Closing the efficiency gap: barriers to the efficient use of energy. *Resources, Conservation and Recycling*, vol. 3, p.p. 267-281
- Holmer B., Postgard U. and Eriksson M. (2001) Sky view factors in forest canopies calculated with IDRISI. *Theoretical and Applied Climatology*, vol. 68, p.p. 33-40
- Hu T., Yoshino H. and Jiang Z. (2013) Analysis on urban residential energy consumption of Hot Summer & Cold Winter Zone in China. *Sustainable Cities and Society*, vol. 6, p.p. 85-91
- Huang D., He S., She X. and Lin B. (2007) *Pre-feasibility study of GSHP application. Eco-Building International Club for advanced European sustainable energy technology dissemination in Europe and China*: ZERI.
- Huang H., Ooka R. and Kato S. (2005) Urban thermal environment measurements and numerical simulation for an actual complex urban area covering a large district heating and cooling system in summer. *Atmospheric Environment*, vol. 39 (34), p.p. 6362-6375
- Huttner S. (2012) *Further development and application of the 3D microclimate simulation ENVI-met*. Unpublished, Doktor der Naturwissenschaften Thesis, Johannes Gutenberg Universität, Mainz, Germany
- Ibm Corp (2010) *IBM SPSS Statistics 19.0*. Armonk, NY: IBM Corp.,
- Information Office of the State Council of the People's Republic of China (2008) *China's policies and actions for addressing climate change*. Available from: http://www.gov.cn/english/2008-10/29/content_1134544.htm [Accessed]
- Jaffe A.B. and Stavins R.N. (1994) The energy-efficiency gap. What does it mean? *Energy policy*, vol. 22 (10), p.p. 804-810
- James P.A.B., Sissons M.F., Bradford J., Myers L.E., Bahaj A.S., Anwar A. and Green S. (2010) Implications of the UK field trial of building mounted horizontal axis micro-wind turbines. *Energy Policy*, vol. 38 (10), p.p. 6130-6144
- Järvi L., Grimmond C.S.B. and Christen A. (2011) The Surface Urban Energy and Water Balance Scheme (SUEWS): Evaluation in Los Angeles and Vancouver. *Journal of Hydrology*, vol. 411 (3-4), p.p. 219-237

References

- Jentsch M.F., James P.A.B., Bourikas L. and Bahaj A.S. (2013) Transforming existing weather data for worldwide locations to enable energy and building performance simulation under future climates. *Renewable Energy*, vol. 55 (0), p.p. 514-524
- Jentsch M.F., Levermore G.J., Parkinson J.B. and Eames M.E. (2014) Limitations of the CIBSE design summer year approach for delivering representative near-extreme summer weather conditions. *Building Services Engineering Research and Technology*, vol. 35 (2), p.p. 155-169
- Ji Z., Yunhao C., Jinfei W. and Wenfeng Z. (2011) Maximum Nighttime Urban Heat Island (UHI) Intensity Simulation by Integrating Remotely Sensed Data and Meteorological Observations. *Selected Topics in Applied Earth Observations and Remote Sensing, IEEE Journal of*, vol. 4 (1), p.p. 138-146
- Johansson E. (2006) Influence of urban geometry on outdoor thermal comfort in a hot dry climate: A study in Fez, Morocco. *Building and Environment*, vol. 41 (10), p.p. 1326-1338
- Johnson G. and Watson I. (1984) The Determination of View-Factors in Urban Canyons. *Journal of Climate and Applied Meteorology*, vol. 23, p.p. 329-335
- Jusuf S.T.W., N.H. (2009) Development of empirical models for an estate level air temperature prediction in Singapore. Paper presented at 7th International Conference on Urban Climate. June 29 - July 3, Yokohama, Japan
- Kanda M. (2006) Progress in the scale modeling of urban climate: Review. *Theoretical and Applied Climatology*, vol. 84 (1-3), p.p. 23-33
- Kanda M., Kawai T., Kanega M., Moriwaki R., Narita K. and Hagishima A. (2005) A Simple Energy Balance Model for Regular Building Arrays. *Boundary-Layer Meteorology*, vol. 116 (3), p.p. 423-443
- Kanda M. and Moriizumi T. (2009) Momentum and Heat Transfer over Urban-like Surfaces. *Boundary-Layer Meteorology*, vol. 131 (3), p.p. 385-401
- Kassomenos P.A. and Katsoulis B.D. (2006) Mesoscale and macroscale aspects of the morning Urban Heat Island around Athens, Greece. *Meteorology and Atmospheric Physics*, vol. 94 (1), p.p. 209-218
- Kershaw T., Sanderson M., Coley D. and Eames M. (2010) Estimation of the urban heat island for UK climate change projections. *Building Services Engineering Research and Technology*, vol. 31 (3), p.p. 251-263
- Kljun N., Rotach M.W. and Schmid H.P. (2002) A Three-Dimensional Backward Lagrangian Footprint Model For A Wide Range Of Boundary-Layer Stratifications. *Boundary-Layer Meteorology*, vol. 103 (2), p.p. 205-226
- Kolokotroni M., Giannitsaris I. and Watkins R. (2006) The effect of the London urban heat island on building summer cooling demand and night ventilation strategies. *Solar Energy*, vol. 80 (4), p.p. 383-392
- Kolokotroni M., Zhang Y. and Watkins R. (2007) The London Heat Island and building cooling design. *Solar Energy*, vol. 81 (1), p.p. 102-110
- Kondo H., Genchi Y., Kikegawa Y., Ohashi Y., Yoshikado H. and Komiyama H. (2005) Development of a Multi-Layer Urban Canopy Model for the Analysis of Energy Consumption in a Big City: Structure of the Urban Canopy Model and its Basic Performance. *Boundary-Layer Meteorology*, vol. 116 (3), p.p. 395-421
- Kusaka H. and Kimura F. (2004) Coupling a Single-Layer Urban Canopy Model with a Simple Atmospheric Model: Impact on Urban Heat Island Simulation for an Idealized Case. *Journal of the Meteorological Society of Japan*, vol. 82 (1), p.p. 67-80
- Kusaka H., Kondo H., Kikegawa Y. and Kimura F. (2001) A Simple Single-Layer Urban Canopy Model For Atmospheric Models: Comparison With Multi-Layer And Slab Models. *Boundary-Layer Meteorology*, vol. 101 (3), p.p. 329-358
- Levermore G.J. and Parkinson J.B. (2006) Analyses and algorithms for new Test Reference Years and Design Summer Years for the UK. *Building Services Engineering Research and Technology*, vol. 27 (4), p.p. 311-325

References

- Li J., Song C., Cao L., Zhu F., Meng X. and Wu J. (2011) Impacts of landscape structure on surface urban heat islands: A case study of Shanghai, China. *Remote Sensing of Environment*, vol. 115 (12), p.p. 3249-3263
- Li X.-X., Liu C.-H., Leung D.Y.C. and Lam K.M. (2006) Recent progress in CFD modelling of wind field and pollutant transport in street canyons. *Atmospheric Environment*, vol. 40 (29), p.p. 5640-5658
- Lindberg F., Grimmond C.S.B., Yogeswaran N., Kotthaus S. and Allen L. (2013) Impact of city changes and weather on anthropogenic heat flux in Europe 1995–2015. *Urban Climate*, vol. 4 (0), p.p. 1-15
- Liu Z., He C., Zhou Y. and Wu J. (2014) How much of the world's land has been urbanized, really? A hierarchical framework for avoiding confusion. *Landscape Ecology*, vol. 29 (5), p.p. 763-771
- Loridan T. and Grimmond C.S.B. (2011) Characterization of Energy Flux Partitioning in Urban Environments: Links with Surface Seasonal Properties. *Journal of Applied Meteorology and Climatology*, vol. 51 (2), p.p. 219-241
- Loridan T., Grimmond C.S.B., Offerle B.D., Young D.T., Smith T.E.L., Järvi L. and Lindberg F. (2010) Local-Scale Urban Meteorological Parameterization Scheme (LUMPS): Longwave Radiation Parameterization and Seasonality-Related Developments. *Journal of Applied Meteorology and Climatology*, vol. 50 (1), p.p. 185-202
- Lu Y., Wang Q.G., Zhang Y., Sun P. and Qian Y. (2016) An estimate of anthropogenic heat emissions in China. *International Journal of Climatology*, vol. 36 (3), p.p. 1134-1142
- Macdonald R.W., Griffiths R.F. and Hall D.J. (1998) An improved method for the estimation of surface roughness of obstacle arrays. *Atmospheric Environment*, vol. 32 (11), p.p. 1857-1864
- Maggiotto G., Buccolieri R., Santo M.A., Leo L.S. and Di Sabatino S. (2014) Validation of temperature-perturbation and CFD-based modelling for the prediction of the thermal urban environment: the Lecce (IT) case study. *Environmental Modelling & Software*, vol. 60 (0), p.p. 69-83
- Martilli A. (2002) Numerical Study of Urban Impact on Boundary Layer Structure: Sensitivity to Wind Speed, Urban Morphology, and Rural Soil Moisture. *Journal of Applied Meteorology*, vol. 41 (12), p.p. 1247-1266
- Martilli A. (2007) Current research and future challenges in urban mesoscale modelling. *International Journal of Climatology*, vol. 27 (14), p.p. 1909-1918
- Martilli A. (2009) On the Derivation of Input Parameters for Urban Canopy Models from Urban Morphological Datasets. *Boundary-Layer Meteorology*, vol. 130 (2), p.p. 301-306
- Martilli A., Clappier A. and Rotach M.W. (2002) An Urban Surface Exchange Parameterisation for Mesoscale Models. *Boundary-Layer Meteorology*, vol. 104 (2), p.p. 261-304
- Martilli A. and Santiago J. (2007) CFD simulation of airflow over a regular array of cubes. Part II: analysis of spatial average properties. *Boundary-Layer Meteorology*, vol. 122 (3), p.p. 635-654
- Massachusetts Institute of Technology (2015) *Urban heat island effect modelling software: Urban Weather Generator version 3.0.0* MIT. Available from: <http://urbanmicroclimate.scripts.mit.edu/uwg.php> [Accessed 26 Feb]
- Masson V. (2000) A Physically-Based Scheme For The Urban Energy Budget In Atmospheric Models. *Boundary-Layer Meteorology*, vol. 94 (3), p.p. 357-397
- Masson V. (2006) Urban surface modeling and the meso-scale impact of cities. *Theoretical and Applied Climatology*, vol. 84 (1), p.p. 35-45
- Masson V., Grimmond C.S.B. and Oke T.R. (2002) Evaluation of the Town Energy Balance (TEB) Scheme with Direct Measurements from Dry Districts in Two Cities. *Journal of Applied Meteorology*, vol. 41 (10), p.p. 1011-1026
- Maxim Integrated (2013) *iButton Temperature / Humidity logger with 8 kb data logger memory*. Available from: <http://www.maximintegrated.com/products/ibutton/data-logging/> [Accessed]

References

- Mejdoul R., Taqi M. and Belouaggadia N. (2013) Artificial neural network based prediction model of daily global solar radiation in Morocco. *Journal of Renewable and Sustainable Energy*, vol. 5 (6),
- Memon R.A., Leung D.Y.C. and Chunho L. (2008) A review on the generation, determination and mitigation of Urban Heat Island. *Journal of Environmental Sciences*, vol. 20 (1), p.p. 120-128
- Memon R.A., Leung D.Y.C. and Liu C.-H. (2009) An investigation of urban heat island intensity (UHII) as an indicator of urban heating. *Atmospheric Research*, vol. 94 (3), p.p. 491-500
- Memon R.A., Leung D.Y.C. and Liu C.-H. (2010) Effects of building aspect ratio and wind speed on air temperatures in urban-like street canyons. *Building and Environment*, vol. 45 (1), p.p. 176-188
- Miao S., Chen F., Lemone M.A., Tewari M., Li Q. and Wang Y. (2009) An Observational and Modeling Study of Characteristics of Urban Heat Island and Boundary Layer Structures in Beijing. *Journal of Applied Meteorology and Climatology*, vol. 48 (3), p.p. 484-501
- Middel A., Häb K., Brazel A.J., Martin C.A. and Guhathakurta S. (2014) Impact of urban form and design on mid-afternoon microclimate in Phoenix Local Climate Zones. *Landscape and Urban Planning*, vol. 122 (0), p.p. 16-28
- Mihalakakou G., Santamouris M. and Asimakopoulos D.N. (2000) The total solar radiation time series simulation in Athens, using neural networks. *Theoretical and Applied Climatology*, vol. 66 (3-4), p.p. 185-197
- Millward-Hopkins J.T., Tomlin A.S., Ma L., Ingham D.B. and Pourkashanian M. (2013) Aerodynamic Parameters of a UK City Derived from Morphological Data. *Boundary-Layer Meteorology*, vol. 146 (3), p.p. 447-468
- Mirzaei P.A. and Haghighat F. (2010a) Approaches to study Urban Heat Island – Abilities and limitations. *Building and Environment*, vol. 45 (10), p.p. 2192-2201
- Mirzaei P.A. and Haghighat F. (2010b) A novel approach to enhance outdoor air quality: Pedestrian ventilation system. *Building and Environment*, vol. 45 (7), p.p. 1582-1593
- Mit Building Technology Group (2000) *Sustainable urban housing in China: China Building Code* Cambridge MA 02139, USA MIT Building Technology Group. Available from: <http://chinahousing.mit.edu/english/resources/BuildingCode.html> [Accessed 17 March]
- Mochida A. and Lun I.Y.F. (2008) Prediction of wind environment and thermal comfort at pedestrian level in urban area. *Journal of Wind Engineering and Industrial Aerodynamics*, vol. 96 (10–11), p.p. 1498-1527
- Moller M.F. (1993) Scaled conjugate gradient algorithm for fast supervised learning. *Neural Networks*, vol. 6 (4), p.p. 525-533
- Morris C.J.G., Simmonds I. and Plummer N. (2001) Quantification of the Influences of Wind and Cloud on the Nocturnal Urban Heat Island of a Large City. *Journal of Applied Meteorology*, vol. 40 (2), p.p. 169-182
- Mubiru J. and Banda E.J.K.B. (2008) Estimation of monthly average daily global solar irradiation using artificial neural networks. *Solar Energy*, vol. 82 (2), p.p. 181-187
- Mylona A. (2012) The use of UKCP09 to produce weather files for building simulation. *Building Services Engineering Research and Technology*, vol. 33 (1), p.p. 51-62
- Nabla Ltd (2007) *FOAM programmer's guide. Section 2.6 Boundary Conditions*. Available from: <http://www.foamcfd.org/Nabla/guides/ProgrammersGuidese11.html> [Accessed 07 July 2014]
- National Oceanic and Atmospheric Administration (Noaa)-National Climatic Data Center (2014) Climate Data Online, Daily weather observations from Hangzhou and Ningbo, China. Boulder Colorado, U.S.A.: NOAA, National Climatic Data Centre
- Ncep/Ncar Us (2000) National Centers for Environmental Prediction (NCEP)/National Weather Service/NOAA/U.S. Department of Commerce. NCEP Final Operational Model Global Tropospheric Analyses, continuing from July 1999. Research Data Archive at the National Center for Atmospheric Research, Computational and Information Systems Laboratory. Boulder CO.,: National Center for Atmospheric Research,

References

- Nikolou S. (2011) *Low carbon city living in Guangzhou, China*. Unpublished, MSc Thesis, University of Southampton, Southampton, UK
- Ningbo Municipal Statistics Bureau (2012) *Ningbo Statistical YearBook 2012*. Beijing: China Statistical Press
- Ningbo Urban Planning Bureau (2003) *Ningbo general planning map (2004-2020)*. Ningbo, China:
- Nist/Sematech e-Handbook of Statistical Methods.
- Offerle B., Eliasson I., Grimmond C.S.B. and Holmer B. (2007) Surface heating in relation to air temperature, wind and turbulence in an urban street canyon. *Boundary-Layer Meteorology*, vol. 122 (2), p.p. 273-292
- Offerle B., Grimmond C.S.B., Fortuniak K., Kłysik K. and Oke T.R. (2006) Temporal variations in heat fluxes over a central European city centre. *Theoretical and Applied Climatology*, vol. 84 (1-3), p.p. 103-115
- Oke T.R. (1973) City size and the urban heat island. *Atmospheric Environment (1967)*, vol. 7 (8), p.p. 769-779
- Oke T.R. (1982) The energetic basis of the urban heat island. *Quarterly Journal of the Royal Meteorological Society*, vol. 108 (455), p.p. 1-24
- Oke T.R. (1987) *Boundary Layer Climates*. Methuen, London and New York
- Oke T.R. (2006) Initial guidance to obtain representative meteorological observations at urban sites. *Instruments and observing methods 2006* (WMO/TD-No. 1250):47 Available from: <http://www.wmo.int/pages/prog/www/IMOP/publications/IOM-81/IOM-81-UrbanMetObs.pdf>
- Oleson K.W., Bonan G.B., Feddema J., Vertenstein M. and Grimmond C.S.B. (2008) An Urban Parameterization for a Global Climate Model. Part I: Formulation and Evaluation for Two Cities. *Journal of Applied Meteorology and Climatology*, vol. 47 (4), p.p. 1038-1060
- Orlanski I. (1975) A rational subdivision of scales for atmospheric processes. *Bulletin of the American Meteorological Society*, vol. 56 (5), p.p. 527-530
- Pan Y., Zhou H., Huang Z., Zeng Y. and Long W. (2003) Measurement and simulation of indoor air quality and energy consumption in two Shanghai office buildings with variable air volume systems. *Energy and Buildings*, vol. 35 (9), p.p. 877-891
- Papadopoulos A.M. (2001) The influence of street canyons on the cooling loads of buildings and the performance of air conditioning systems. *Energy and Buildings*, vol. 33 (6), p.p. 601-607
- Papangelis G., Tombrou M., Dandou A. and Kontos T. (2012) An urban “green planning” approach utilizing the Weather Research and Forecasting (WRF) modeling system. A case study of Athens, Greece. *Landscape and Urban Planning*, vol. 105 (1–2), p.p. 174-183
- Park M., Hagishima A., Tanimoto J. and Narita K.-I. (2012) Effect of urban vegetation on outdoor thermal environment: Field measurement at a scale model site. *Building and Environment*, vol. 56 (0), p.p. 38-46
- Pearlmutter D., Berliner P. and Shaviv E. (2007) Urban climatology in arid regions: current research in the Negev desert. *International Journal of Climatology*, vol. 27 (14), p.p. 1875-1885
- Pearlmutter D., Bitan A. and Berliner P. (1999) Microclimatic analysis of “compact” urban canyons in an arid zone. *Atmospheric Environment*, vol. 33 (24–25), p.p. 4143-4150
- Peng L.L.H. and Jim C.Y. (2013) Green-Roof effects on neighborhood microclimate and human thermal sensation. *Energies*, vol. 6, p.p. 598-618
- Piringer M., Joffre S., Baklanov A., Christen A., Deserti M., De Ridder K., Emeis S., Mestayer P., Tombrou M., Middleton D., Baumann-Stanzer K., Dandou A., Karppinen A. and Burzynski J. (2007) The surface energy balance and the mixing height in urban areas—activities and recommendations of COST-Action 715. *Boundary-Layer Meteorology*, vol. 124 (1), p.p. 3-24
- Porson A., Clark P.A., Harman I.N., Best M.J. and Belcher S.E. (2010) Implementation of a new urban energy budget scheme in the MetUM. Part I: Description and idealized

References

- simulations. *Quarterly Journal of the Royal Meteorological Society*, vol. 136 (651), p.p. 1514-1529
- Poskanzer J. (2000) *ACME Laboratories Mapper Version 2.1. Maps from Google for China*. Available from: <http://mapper.acme.com/> [Accessed 14 June]
- Ramamurthy P., Bou-Zeid E., Smith J.A., Wang Z., Baeck M.L., Saliendra N.Z., Hom J.L. and Welty C. (2014) Influence of Subfacet Heterogeneity and Material Properties on the Urban Surface Energy Budget. *Journal of Applied Meteorology and Climatology*, vol. 53 (9), p.p. 2114-2129
- Ramponi R. and Blocken B. (2012) CFD simulation of cross-ventilation for a generic isolated building: Impact of computational parameters. *Building and Environment*, vol. 53 (0), p.p. 34-48
- Ratti C., Di Sabatino S. and Britter R. (2006) Urban texture analysis with image processing techniques: winds and dispersion. *Theoretical and Applied Climatology*, vol. 84 (1-3), p.p. 77-90
- Ratti C., Di Sabatino S., Caton F. and Britter R. (2000) Morphological parameters for urban dispersion models. In: *Third Symposium for Urban Environment* Davis, CA. American Meteorological Society P2.3.
- Raupach M.R. (2001) Combination theory and equilibrium evaporation. *Quarterly Journal of the Royal Meteorological Society*, vol. 127 (574), p.p. 1149-1181
- Rehman S. and Mohandes M. (2008) Artificial neural network estimation of global solar radiation using air temperature and relative humidity. *Energy Policy*, vol. 36 (2), p.p. 571-576
- Rotach M.W. (2001) Simulation Of Urban-Scale Dispersion Using A Lagrangian Stochastic Dispersion Model. *Boundary-Layer Meteorology*, vol. 99 (3), p.p. 379-410
- Rotach M.W., Vogt R., Bernhofer C., Batchvarova E., Christen A., Clappier A., Feddersen B., Gryning S.E., Martucci G., Mayer H., Mitev V., Oke T.R., Parlow E., Richner H., Roth M., Roulet Y.A., Ruffieux D., Salmond J.A., Schatzmann M. and Voogt J.A. (2005) BUBBLE – an Urban Boundary Layer Meteorology Project. *Theoretical and Applied Climatology*, vol. 81 (3), p.p. 231-261
- Roth M. (2000) Review of atmospheric turbulence over cities. *Quarterly Journal of the Royal Meteorological Society*, vol. 126 (564), p.p. 941-990
- Rubel F. and Kottek M. (2010) Observed and projected climate shifts 1901-2100 depicted by world maps of the Köppen - Geiger climate classification. *Meteorologische Zeitschrift*, vol. 19 (2), p.p. 135-141
- Rumelhart D.E., Hinton G.E. and Williams R.L. (1986) Learning internal representations by error propagation. In: Rumelhart D.E. and McClelland J.L. (eds) *Parallel distributed processing*. Cambridge: MIT Press 318-362
- Sailor D.J. and Lu L. (2004) A top-down methodology for developing diurnal and seasonal anthropogenic heating profiles for urban areas. *Atmospheric Environment*, vol. 38 (17), p.p. 2737-2748
- Salagoor J. (1990) *The influence of building regulations on urban dwelling in Jeddah*. Unpublished, PhD Thesis, University of Newcastle upon Tyre, Newcastle upon Tyre, UK
- Salamanca F., Martilli A., Tewari M. and Chen F. (2011) A Study of the Urban Boundary Layer Using Different Urban Parameterizations and High-Resolution Urban Canopy Parameters with WRF. *Journal of Applied Meteorology and Climatology*, vol. 50 (5), p.p. 1107-1128
- Sanderse B., Van Der Pijl S.P. and Koren B. (2011) Review of computational fluid dynamics for wind turbine wake aerodynamics. *Wind Energy*, vol. 14, p.p. 799-819
- Santamouris M. (2001a) Heat-island effect In: Santamouris M. (ed) *Energy and climate in the urban built environment*. London, UK: James & James 48-68
- Santamouris M. (2001b) Thermal balance in the urban environment In: Santamouris M. (ed) *Energy and climate in the urban built environment*. London, UK: James & James 39-47
- Santamouris M., Georgakis C. and Niachou A. (2008) On the estimation of wind speed in urban canyons for ventilation purposes—Part 2: Using of data driven techniques to calculate

References

- the more probable wind speed in urban canyons for low ambient wind speeds. *Building and Environment*, vol. 43 (8), p.p. 1411-1418
- Santamouris M., Synnefa A. and Karlessi T. (2011) Using advanced cool materials in the urban built environment to mitigate heat islands and improve thermal comfort conditions. *Solar Energy*, vol. 85 (12), p.p. 3085-3102
- Santiago J., Martilli A. and Martín F. (2007) CFD simulation of airflow over a regular array of cubes. Part I: Three-dimensional simulation of the flow and validation with wind-tunnel measurements. *Boundary-Layer Meteorology*, vol. 122 (3), p.p. 609-634
- Sarle W.S. (1997a) *Neural Network FAQ, part 2 of 7: Learning*. Available from: <ftp://ftp.sas.com/pub/neural/FAQ.html> [Accessed]
- Sarle W.S. (1997b) *Neural Network FAQ, part 3 of 7: Generalisation*. Available from: <ftp://ftp.sas.com/pub/neural/FAQ.html> [Accessed 2 June 2014]
- Schlünzen K.H. (2010) Joint modelling of obstacle induced and mesoscale changes-current limits and challenges. Paper presented at The Fifth International Symposium on Computational Wind Engineering (CWE2010). May 23-27, 2010, Chapel Hill, North Carolina, USA
- Schmid H.P. and Oke T.R. (1990) A model to estimate the source area contributing to turbulent exchange in the surface layer over patchy terrain. *Quarterly Journal - Royal Meteorological Society*, vol. 116 (494), p.p. 965-988
- Shen T., Chow D.H.C., Cui T. and Darkwa J. (2013) Generating a modified weather data file for urban building design and sustainable urban planning accounting for the Urban Heat Island (UHI) effect. Paper presented at 12th International Conference on Sustainable Energy Technologies. Hong Kong Polytechnic University
- Shen T., Chow D.H.C., Darkwa J. and Yao R. (2014) Impact of Urban Heat Island on Building Cooling Energy Consumption in Hangzhou. Paper presented at 13th International Conference on Sustainable Energy Technologies. 25-28 August 2014, Geneva, Switzerland
- Sogou Maps (2014) *Three dimensional street view maps for major cities in China*. Available from: <http://map.sogou.com/> [Accessed]
- Souch C. and Grimmond S. (2006) Applied climatology: urban climate. *Progress in Physical Geography*, vol. 30 (2), p.p. 270-279
- Sözen A., Arcaklioğlu E., Özalp M. and Kanit E.G. (2004) Use of artificial neural networks for mapping of solar potential in Turkey. *Applied Energy*, vol. 77 (3), p.p. 273-286
- Stack Exchange Inc. (2011) *What's the difference between Normalisation and Standardisation?* Cross Validated, Stack Exchange inc. Available from: <http://stats.stackexchange.com/questions/10289/whats-the-difference-between-normalization-and-standardization> [Accessed 04 June 2014]
- Stergiou C. and Siganos D. (2004) Neural Networks, Final Reports. *SURPRISE 96 Journal* 2004 4 Available from: http://www.doc.ic.ac.uk/~nd/surprise_96/journal/vol4/cs11/report.html [Accessed 30 May 2014]
- Stewart I.D. and Oke T.R. (2012) Local Climate Zones for Urban Temperature Studies. *Bulletin of the American Meteorological Society*, vol. 93 (12), p.p. 1879-1900
- Stewart I.D., Oke T.R. and Scott Kravenhoff E. (2014) Evaluation of the 'local climate zone' scheme using temperature observations and model simulations. *International Journal of Climatology*, vol. 34, p.p. 1062-1080
- Sun H. and Yang J. (2013) Modified Numerical Approach to Estimate Field Capacity. *Journal of Hydrologic Engineering*, vol. 18 (4), p.p. 431-438
- Synnefa A., Dandou A., Santamouris M., Tombrou M. and Soulakellis N. (2008) On the Use of Cool Materials as a Heat Island Mitigation Strategy. *Journal of Applied Meteorology and Climatology*, vol. 47 (11), p.p. 2846-2856
- Taeschler R. and Andersson C. (1984) A method for solar radiation computations using routine meteorological observations. *Energy and Buildings*, vol. 7 (4), p.p. 341-352

References

- Taha H., Konopacki S. and Gabersek S. (1999) Impacts of Large-Scale Surface Modifications on Meteorological Conditions and Energy Use: A 10-Region Modeling Study. *Theoretical and Applied Climatology*, vol. 62 (3), p.p. 175-185
- Tencent (2013) *Street view maps for China*. Available from: map.qq.com [Accessed 16 June 2014]
- Tewari M., Kusaka H., Chen F., Coirier W.J., Kim S., Wyszogrodzki A.A. and Warner T.T. (2010) Impact of coupling a microscale computational fluid dynamics model with a mesoscale model on urban scale contaminant transport and dispersion. *Atmospheric Research*, vol. 96 (4), p.p. 656-664
- The Carbon Trust (2012) *Closing the gap. Lessons learned on realising the potential of low carbon building design. Sharing our experience* London. Available from: <http://www.carbontrust.com/media/81361/ctg047-closing-the-gap-low-carbon-building-design.pdf>
- The Engineering Toolbox (2014) *Humidity ratio of Air. Water Vapor and Saturation Pressure in Humid Air*. Available from: <http://www.engineeringtoolbox.com/> [Accessed 17 July 2014]
- The Weather Underground (2012) Shanghai weather data from airport, WMO stations and hobbyists.:
- The Weather Underground (2014a) Hangzhou weather data from Mantou mountain's National Principle WMO-listed weather station.
- The Weather Underground (2014b) Hangzhou weather data from Mantou mountain's National Principle WMO-listed weather station
- Thomas P.C. and Moller S. (2006) *HVAC system size - getting it right. Clients Driving Innovation: Moving Ideas into Practice* Brisbane, Australia: Cooperative Research Centre for Construction Innovation.
- Trimble Navigation Limited (2013) *SketchUp 3D CAD software*. Available from: <http://www.sketchup.com/> [Accessed]
- Tymvios F.S., Jacovides C.P., Michaelides S.C. and Scouteli C. (2005) Comparative study of Ångström's and artificial neural networks' methodologies in estimating global solar radiation. *Solar Energy*, vol. 78 (6), p.p. 752-762
- U.S. Department of Energy (2012) EnergyPlus Energy Simulation Software. Weather Data.:
- Verein Deutscher Ingenieure (Vdi) 3783 (2005) Part 9: Environmental meteorology - Prognostic microscale wind field models - Evaluation for flow around buildings and obstacles. Dusseldorf VDI
- Virk D. and Eames M. (2016) CIBSE weather files 2016 release: Technical briefing and testing. London, UK: The Chartered Institution of Building Services Engineers
- Wang H., Wu H., Ding Y., Feng J. and Wang S. (2014) Feasibility and optimization of aerogel glazing system for building energy efficiency in different climates. *International Journal of Low-Carbon Technologies*, vol.,
- Watkins R., Palmer J., Kolokotroni M. and Littlefair P. (2002) The London heat island: results from summertime monitoring. *Building Services Engineering Research and Technology*, vol. 23 (2), p.p. 97-106
- Wendell Cox Consultancy (2014) *Demographia World Urban Areas*. Available from: <http://www.demographia.com/db-worldua.pdf>
- Willmott C.J. (1982) Some comments on the evaluation of model performance. *Bulletin of the American Meteorological Society*, vol. 63 (11), p.p. 1309-1313
- Wong N.H., Jusuf S.K., Syafii N.I., Chen Y., Hajadi N., Sathyanarayanan H. and Manickavasagam Y.V. (2011) Evaluation of the impact of the surrounding urban morphology on building energy consumption. *Solar Energy*, vol. 85 (1), p.p. 57-71
- World Meteorological Organisation (1996) *Guide to meteorological instruments and methods of observation*. Geneva: World Meteorological Organisation
- World Meteorological Organisation (2008) *Guide to meteorological instruments and methods of observation*. In: Organisation W.M. (ed) Seventh Edition Edition Geneva:

References

- World Meteorological Organisation (2014) *Climate observation networks and systems* Geneva, Switzerland WMO. Available from: http://www.wmo.int/pages/themes/climate/climate_observation_networks_systems.php [Accessed 07 June 2014]
- World Radiation Data Centre (2014) Solar radiation and radiation balance data (The World Network). .
- Xie Z. and Castro I.P. (2006) Large-eddy simulation for urban micro-meteorology. *Journal of Hydrodynamics, Ser. B*, vol. 18 (3, Supplement), p.p. 259-264
- Yadav A.K. and Chandel S.S. (2014) Solar radiation prediction using Artificial Neural Network techniques: A review. *Renewable and Sustainable Energy Reviews*, vol. 33 (0), p.p. 772-781
- Yamada T. and Koike K. (2011) Downscaling mesoscale meteorological models for computational wind engineering applications. *Journal of Wind Engineering and Industrial Aerodynamics*, vol. 99 (4), p.p. 199-216
- Yamada T. and Mellor G. (1975) A Simulation of the Wangara Atmospheric Boundary Layer Data. *Journal of the Atmospheric Sciences*, vol. 32 (12), p.p. 2309-2329
- Yan C., Weimei J. and Ning Z. (2008) Numerical Study of Anthropogenic Heat Impact on Boundary Layer Characteristics. In: *Bioinformatics and Biomedical Engineering, 2008. ICBBE 2008. The 2nd International Conference on* 16-18 May 2008. 4043-4045
- Yang F., Lau S.S.Y. and Qian F. (2010) Summertime heat island intensities in three high-rise housing quarters in inner-city Shanghai China: Building layout, density and greenery. *Building and Environment*, vol. 45 (1), p.p. 115-134
- Yang F., Lau S.S.Y. and Qian F. (2011) Urban design to lower summertime outdoor temperatures: An empirical study on high-rise housing in Shanghai. *Building and Environment*, vol. 46 (3), p.p. 769-785
- Yang F., Qian F. and Lau S.S.Y. (2013a) Urban form and density as indicators for summertime outdoor ventilation potential: A case study on high-rise housing in Shanghai. *Building and Environment*, vol. 70 (0), p.p. 122-137
- Yang L., Lam J.C. and Tsang C.L. (2008) Energy performance of building envelopes in different climate zones in China. *Applied Energy*, vol. 85 (9), p.p. 800-817
- Yang W., Chen B. and Cui X. (2014) High - resolution mapping of anthropogenic heat in China from 1992 to 2010. *International Journal of Environmental Research and Public Health*, vol. 11, p.p. 4066-4077
- Yang X., Zhao L., Bruse M. and Meng Q. (2013b) Evaluation of a microclimate model for predicting the thermal behavior of different ground surfaces. *Building and Environment*, vol. 60, p.p. 93-104
- Yongzhu X., Zhengdong Z., Feng C. and Run W. (2010) Estimation of urbanization effect on climatic warming over the recent 30 years in Guangzhou, South China. In: *Geoinformatics, 2010 18th International Conference on* 18-20 June 2010. 1-6
- Zero Carbon Hub (2014) *Closing the gap between design and as-built performance. End of term report*. London. Available from: http://www.zerocarbonhub.org/sites/default/files/resources/reports/Design_vs_As_Built_Performance_Gap_End_of_Term_Report_0.pdf
- Zhao C., Fu G., Liu X. and Fu F. (2011) Urban planning indicators, morphology and climate indicators: A case study for a north-south transect of Beijing, China. *Building and Environment*, vol. 46 (5), p.p. 1174-1183